

UNIVERSITY OF CALIFORNIA

Los Angeles

Seismic Evidence for Small Scale Mantle Convection  
under the Baikal Rift Zone, Siberia

A dissertation submitted in partial satisfaction of the  
requirements for the degree Doctor of Philosophy  
in Geophysics and Space Physics

by

Shangxing Gao

1995

The dissertation of Shangxing Gao is approved.



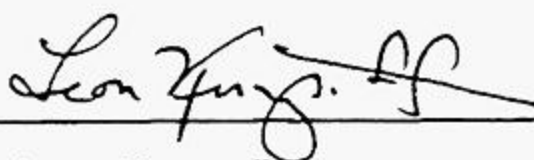
---

David D. Jackson



---

William M. Kaula



---

Leon Knopoff



---

Paul M. Davis, Committee Chair

1995

To my wife Hong Liu

## TABLE OF CONTENTS

<b>List of Figures</b> .....	<b>vi</b>
<b>List of Tables</b> .....	<b>viii</b>
<b>Acknowledgements</b> .....	<b>ix</b>
<b>Vita</b> .....	<b>x</b>
<b>Abstract of the dissertation</b> .....	<b>xii</b>
<b>Chapter 1. Introduction</b> .....	<b>1</b>
1.1 Purpose of the study .....	3
1.2 The Baikal rift zone of Siberia .....	4
1.3 The Baikal 1991-92 teleseismic experiment .....	5
1.4 Russian permanent seismic network .....	7
1.5 Participants .....	8
1.6 Structure of the thesis .....	10
Figure captions .....	12
<b>Chapter 2. Interpretation of Teleseismic P-wave Travel Time</b>	
<b>Residuals by Assuming an Isotropic Upper Mantle</b> .....	<b>15</b>
2.1 Introduction .....	15
2.2 Data .....	17
2.3 Model construction .....	23
2.4 Nonlinear Bayesian inversion: the theory .....	27
2.5 Nonlinear Bayesian inversion: results .....	30
Figure captions .....	39

<b>Chapter 3. SKS Splitting Measurements and Interpretation</b>	<b>----- 85</b>
3.1 Introduction	----- 85
3.2 Method	----- 88
3.3 Data	----- 95
3.4 Measurements	----- 98
3.5 Results	----- 105
3.6 Tectonic implications	----- 107
Figure captions	----- 110
<b>Chapter 4. Interpretation of Teleseismic Quasi_P-wave Travel</b>	
<b>Time Residuals by Assuming an Anisotropic Upper Mantle</b>	<b>-- 158</b>
4.1 Introduction	----- 158
4.2 Model construction	----- 161
4.3 Method of computation	----- 165
4.4 Nonlinear Bayesian inversion: results	----- 166
Figure captions	----- 172
<b>Chapter 5. A Small Scale Mantle Convection Model for</b>	
<b>the Baikal Rift Zone</b>	<b>----- 188</b>
5.1 Introduction	----- 188
5.2 A small-scale mantle convection model derived from this study	- 188
5.3 Applications of the model	----- 189
Figure captions	----- 199
<b>Chapter 6. Conclusions and Future Studies</b>	<b>----- 205</b>
6.1 Conclusions	----- 205
6.2 Proposed future studies and predicted results	----- 207
<b>References</b>	<b>----- 210</b>

## List of Figures

Figure 1.2.1: Asia topography and study area .....	13
Figure 1.3.1: Station locations .....	14
Figure 2.2.1: P-wave travel time residuals .....	42
Figure 2.2.2: Location of stations used for travel time inversion .....	44
Figure 2.2.3: Example seismograms .....	45
Figure 2.2.4: P-wave travel time residuals from 1992 event groups .....	46
Figure 2.2.5: P-wave travel time residuals from 1991 event groups .....	52
Figure 2.2.6: Mean travel time residual curves for 1992 event groups .....	59
Figure 2.2.7: Mean travel time residual curves for 1991 event groups .....	60
Figure 2.3.1: Examples of the function $f(x)$ defined in Eq. 2.3.1 .....	61
Figure 2.3.2: Coordinate systems for travel time tomography .....	62
Figure 2.5.1: Sum of squared residuals at each iteration for model 1 .....	63
Figure 2.5.2: Inverted velocity model 1, original and fitted data .....	64
Figure 2.5.3: Cross correlation coefficients of parameters for model 1 .....	66
Figure 2.5.4: Sum of squared residuals at each iteration for model 2 .....	67
Figure 2.5.5: Inverted velocity model 2, original and fitted data .....	68
Figure 2.5.6: Cross correlation coefficients of parameters for model 2 .....	70
Figure 2.5.7: Sum of squared residuals at each iteration for model 3 .....	71
Figure 2.5.8: Inverted velocity model 3, original and fitted data .....	72
Figure 2.5.9: Cross correlation coefficients of parameters for model 3 .....	74
Figure 2.5.10: Sum of squared residuals at each iteration for model 4 .....	75
Figure 2.5.11: Inverted velocity model 4, original and fitted data .....	76
Figure 2.5.12: Cross correlation coefficients of parameters for model 4 .....	77
Figure 3.1.1: Ray path of the SKS phase .....	113
Figure 3.1.2: P-wave velocity of an olivine crystal .....	114

Figure 3.1.3: Preferred orientation of olivine axes in flow fields .....	115
Figure 3.1.4: SKS splitting measurements in the Rio Grande rift .....	116
Figure 3.1.5: SKS splitting measurements in the East African rift .....	117
Figure 3.2.1: Geometric relations of un-split and split SKS .....	118
Figure 3.2.2: Synthetic tests of the method for $f = 0.4$ Hz .....	119
Figure 3.2.3: Synthetic tests of the method for $f = 0.1$ Hz .....	123
Figure 3.2.4: Modeling the maximum depth of anisotropy contrast .....	127
Figure 3.2.5: Fast directions calculated using synthetic seismograms .....	128
Figure 3.3.1: Location of stations used in SKS splitting studies .....	129
Figure 3.3.2: Epicenter of events used in SKS splitting studies .....	130
Figure 3.4.1: Original and corrected seismograms and particle motions ..	131
Figure 3.4.2: SKS splitting measurement results .....	153
Figure 4.2.1: Anisotropic model & travel times for vertical incidence .....	174
Figure 4.2.2: Examples of $f(\theta) = c_1 \cos(2\theta) + c_2 \cos(4\theta)$ .....	175
Figure 4.4.1: Anisotropic model & travel times for non-vertical incidence	178
Figure 4.4.2: Averaged P-wave isotropic 1D velocity model from DSS .....	181
Figure 4.4.3: Sum of squared residuals at each iteration .....	182
Figure 4.4.4: Anisotropic velocity model from Bayesian inversion .....	183
Figure 4.4.5: Fitted and original data .....	184
Figure 4.4.6: Estimated vertical anisotropy along the 1992 profile .....	186
Figure 4.4.7: Cross correlation coefficients of parameters .....	187
Figure 5.2.1: A small-scale convection model for the Baikal rift zone .....	201
Figure 5.3.1: Generalized structures and stress fields of the BRZ .....	202
Figure 5.3.2: Regional stress fields of the BRZ .....	203
Figure 5.3.3: Seismic anisotropy measurements in Asia .....	204

## List of Tables

Table 2.2.1: Events used in travel time residual studies .....	78
Table 2.2.2: Location of stations used for travel time inversion .....	82
Table 2.2.3: Event group information .....	84
Table 3.3.1: SKS splitting measurement results .....	155
Table 3.3.2: Events used in SKS splitting studies .....	157

## ACKNOWLEDGEMENTS

I am deeply indebted to my academic advisor Prof. Paul Davis for providing constant guidance, support, assistance, and encouragement throughout this study. I am grateful to my committee members Profs. Paul Davis, Dave Jackson, Bill Kaula, and Leon Knopoff for their suggestions and criticisms.

This work could not have been done without the help from our Russian colleagues at Institute of Earth's Crust (IEC), Irkutsk. During the nine months when I was in Siberia, their hospitality eliminated all the inconvenience in my work and personal life, in spite of the fact that the only sentence I could speak in Russian was "*Ya nyet gavalju pa ruski*" (I don't speak Russian). Special thanks are given to Prof. Yuliy Zorin, Drs. Valya Mordvinova and Volodia Kozhevnikov.

This study has benefited from discussion and cooperation with our colleagues at the University of Wisconsin, Madison (Prof. Bob Meyer and his group), and with Prof. Ron Girdler of University of Newcastle (UK). Helps provided by colleagues especially by M. Benthien, P. Fang, J. Gardner, X. Ge, D. Guo, P. Jögi, Y. Kagan, F. Leader, R. Mehlman, G. Pei, H. Rendon, A. Rigor, Z. Shen, P. Slack, J. Somers, M. Winter, X. Yang, O. Youn, and K. Zhou are gratefully acknowledged.

Thanks are given to my parents, sisters, and brother for their support.

Finally, I would like to thank the one who is most deserving of acknowledgement, my wife Hong Liu. The fact that both of us are UCLA seismology graduate students made her support and encouragement professional.

The study was supported by DARPA under contracts F2901-91-K-DB17 & F49620-94-1-0161 to UCLA, and by ISF under grants RLN000 & RLN300 to IEC.

## VITA

March, 1964      Born, Shandong Province, P.R. China

1984              B.S., Marine Geophysics  
                    Qingdao Institute of Oceanography, P.R. China

1984-1989        Faculty of Geophysics  
                    China Petroleum University, P.R. China

1989-1990        Visiting scholar  
                    Department of Earth and Space Sciences  
                    University of California, Los Angeles

1990-1995        Graduate research assistant  
                    Department of Earth and Space Sciences  
                    University of California, Los Angeles

1993              M.S., Geophysics and Space Physics  
                    University of California, Los Angeles

## Publications

- Davis, P.M., S. Gao, H. Liu, and P. Slack (1992), Seismic array study of the Baikal rift zone, Siberia, Proceedings of the 14th Annual PL/DARPA Seismic Research Symposium: 99-110.
- Gao, S., P.M. Davis, H. Liu, P. Slack, Y.A. Zorin, N.A. Logatchev, M. Kogan, P. Burkholder, and R.P. Meyer (1994), Asymmetric upwarp of the Asthenosphere beneath the Baikal Rift zone, Siberia, J. Geophys. Res., 99: 15,319-15,330.

- Gao, S., P.M. Davis, H. Liu, P.D. Slack, Yu.A. Zorin, V.V. Mordvinova, V.M. Kozhevnikov, and R.P. Meyer (1994), Seismic anisotropy and mantle flow beneath the Baikal rift zone, Nature, 371: 149-151.
- Gao, S., P.M. Davis, H. Liu, P.D. Slack, Yu.A. Zorin, N.A. Logatchev, M.G. Kogan, P.D. Burkholder, and R.P. Meyer (1994), Preliminary results of teleseismic studies of the mantle of the Baikal rift, (in Russian), Fizika Zemli (Physics of the Earth), N7-8: 113-122, Moscow, Russia.
- Gao, S., H. Liu, P.M. Davis, and L. Knopoff, Localized amplification of seismic waves and correlation with damage due to the Northridge earthquake: evidence for focusing in Santa Monica, Bull. Seismo. Soc. Ame. (accepted), 1996.
- Liu, H., P.M. Davis, and S. Gao (1995), SKS splitting beneath southern California, Geophys. Res. Lett., 22: 767-770.
- Zorin, Yu. A., V.G. Belichenko, E.Kh. Turutanov, V.V. Modvinova, V.M. Kozhevnikov, P. Khozbayar, O. Tomurtogoo, N. Arvisbaatar, S. Gao, and P. Davis (1994), Baikalo-Mongolian transect, (in Russian), Geology and Geophysics, 35: 94-110, Nauka, Novosibirsk, Russia.

## ABSTRACT OF THE DISSERTATION

Seismic Evidence for Small Scale Mantle Convection

under the Baikal Rift Zone, Siberia

by

Shangxing Gao

Doctor of Philosophy in Geophysics and Space Physics

University of California, Los Angeles, 1995

Professor Paul M. Davis, Chair

The Baikal rift zone (BRZ) in Siberia is a major continental rift zone. The 1500 km en echelon system of rift depressions, which originated about 30 million years ago, is the most seismically active continental rift in the world.

We use seismic data that we collected at about 100 stations to study the upper mantle structure and search for the existence of small-scale convection. Positive (late) teleseismic P-wave travel time residuals of about 0.7 s corresponding to the BRZ have been observed using 153 teleseismic events. The location of the peak of the positive residuals lies on the rift axis and is almost stationary for incoming rays from different directions; Negative (early) teleseismic P-wave travel time residuals relative to the Siberian platform of about 0.5 s at a mean location of about 250 km on each side of the rift axis have been observed. The location of the peaks of the negative residuals shifts as much as 200 km for event groups from different azimuths.

The travel time residuals were interpreted by Bayesian nonlinear inversion using a traditional isotropic upper mantle model, and a new anisotropic upper mantle model. Thermal upwarp of the asthenosphere could explain the central peak in both models. The P-wave velocity contrast across the lithosphere/asthenosphere boundary ranges from 2% to 4%, depending on the model type (isotropic or anisotropic) and prior estimates of the parameters.

The upper mantle in the study area is anisotropic as revealed by SKS splitting of about 1 second. In the Siberian platform and the northern part of the Mongolian fold belt, the fast SKS polarization directions are mostly perpendicular to the rift axis; in the southern part of the fold belt the fast directions are mostly E-W; in the central part of the BRZ the observed fast directions are mostly either parallel or perpendicular to the rift.

A small-scale mantle convection model was constructed and used to interpret the observations, such as the existence of the rift zone and the lake, the travel time residuals and SKS splitting results.

# CHAPTER 1

## Introduction

A continental rift is a region where the crust has split apart, usually marked by a rift valley [Fowler, 1990]. Some common features of a typical continental rift zone include: 1) the central part of rift valley subsides and the edges of the adjacent blocks are uplifted; 2) flanking normal faults; 3) negative Bouguer gravity anomalies; 4) higher than normal heat flow; 5) shallow, tensional and higher than normal seismicity; 6) thinning of the crust beneath the rift valley [Fowler, 1990; Turcotte and Schubert, 1982]. Continental rifting is the first stage in a Wilson cycle, although some rifts never evolve into an ocean [e.g., Turcotte and Schubert, 1982].

The major continental rift zones are the Baikal rift zone in Siberia, the East African rift zone, the Rio Grande rift zone in North America, the Rhine graben in Europe, and the Shanxi graben in northern China. The Baikal rift zone is the least familiar to, and most poorly studied by, western geophysicists.

This study intends to review the geophysics of the Baikal rift zone (BRZ), and to significantly deepen our understanding of it by combining existing data sets and a new seismic data set recorded by a large digital seismic network that we installed and operated during the summers of 1991 and 1992.

There are several models for the formation and development of the BRZ. The two most commonly cited models are the so-called "active rifting" model [Zorin, 1971; 1981; Logatchev et al., 1983a; 1983b; Turcotte and Emerman, 1983; Logatchev and Zorin, 1992] and the "passive rifting" model [Molnar and Tapponnier, 1975;

Tapponnier and Molnar, 1979; Zonenshain and Savostin, 1981; Kiselev and Popov, 1992].

In an active rifting model the formation and development of the BRZ is thought to be the result of the active intrusion of an asthenospheric diapir. Small scale mantle convection in the the diapir causes thermal thinning of the subcrustal lithosphere [Logatchev and Florensov, 1978;Logatchev, 1984; Logatchev and Zorin, 1992].

The passive rifting model of Molnar and Tapponnier [1975] suggests that the India-Asia collision generated most of the large scale tectonics of Asia, and that the collision perhaps ripped open Lake Baikal more than 3000 km away. In eastern Mongolia and China they note that deformation takes place in a shear zone of east-west, left lateral, strike slip faults. They suggest that Baikal rifting results from a mechanism equivalent to the development of tension cracks near the ends of and oblique to shear zones. They interpret the BRZ as a manifestation of the India-Eurasia collision, and therefore driven by the forces causing the collision, not by the forces directly beneath the rift.

The existence of the small-scale mantle convection would represent important evidence for the active rifting model. Using the shear-wave splitting technique, Gao and others [1994a] present evidence for the direction of asthenospheric flow beneath the BRZ. The study was the "first detailed study of asthenospheric flow across a continental rift" [Savage, 1994]. Small-scale mantle convection is not required by the passive rifting model.

Another important criterion for the active model is that the accompanying small-scale convection is associated with a broad asthenospheric upwarp. A broad

asthenospheric upwarp, which extends at least 300 km on each side of the BRZ was inferred using gravity data [e.g. Zorin et al., 1989] and teleseismic travel time residuals [Gao et al., 1994b]. For the passive rifting model, extension reduces the upper mantle pressure and generates ascending of asthenospheric materials. However, the horizontal dimension of the upwarp should be relatively small, possibly limited to beneath the rift zone.

The present study combines our previous studies [Gao et al., 1994a; 1994b] on shear-wave splitting and teleseismic travel time inversion using an extended data set, in order to deepen our understanding of the formation and geodynamics of the BRZ and other major continental rift zones.

### **1.1 Purpose of the study**

The specific purpose of the study is:

- 1). to introduce the tectonics of the BRZ and adjacent areas and the Baikal seismic experiment;
- 2). to present newly obtained teleseismic P-wave travel time residuals;
- 3). to invert for the velocity structure using the travel time residuals under the assumption of an isotropic upper mantle;
- 4). to demonstrate the existence of, and to find the characteristics of, anisotropic upper mantle layers using the SKS phase;
- 5). to invert for the velocity structure using the travel time residuals under the assumption of an anisotropic upper mantle;
- 6). to form a geodynamic model that can explain most of the observations made in the BRZ and adjacent areas;

- 7). to use the geodynamic model to explain some observations made in other areas, such as other major continental rift zones and subduction zones; and
- 8). to suggest future study topics and predict results based on the current study.

## **1.2 The Baikal rift zone of Siberia**

The Baikal rift zone lies along the junction of the stable Siberian platform and the Sayan-Baikal mobile fold belt (Figure 1.2.1). Collision of the Amurian plate with the Siberian plate occurred south of the future Lake Baikal in the middle Jurassic. Rotation of the Amurian plate relative to Siberia is thought to have closed the sea of Okhotsk in the middle Jurassic [Zonenshain et al., 1990]. This was followed by folding in the Trans-Baikal area. Southeast of Lake Baikal, faulting near the Mongolian border generated a series of northeast trending elongated rift depressions filled by early Cretaceous sediments. Rifting at Baikal began about 30 million years ago, approximately at the time of the start of the collision between India and Eurasia [Zonenshain and Savostin, 1981].

The 1500 km en echelon system of rift depressions is the most seismically active continental rift in the world [Golenetsky and Misharina, 1978; Golenetsky, 1990] (Figure 1.2.1). During the past 270 years, 13 earthquakes with magnitude larger than 6.5 have occurred within the area [Doser, 1991].

Lake Baikal is the deepest lake on the Earth. It contains 1/5 of the world's fresh water, with the maximum depth of 1620 m. The maximum width of the lake is about 50 km. The lake is filled with sediments up to 6 km deep [Zorin, 1971; Logatchev and Florensov, 1978].

It is a region of high heat flow: 75-120 mW/m<sup>2</sup> compared to 38-42 mW/m<sup>2</sup> on the Siberian platform and 40-60 mW/m<sup>2</sup> on the fold belts [Lubimova, 1969; Morgan, 1982; Lysak, 1984; 1987].

It is a region of low  $Q$ . Using the method of Halderman and Davis [1991], Gao et al. [1994b] determined that the  $Q$  value [Knopoff, 1964] beneath the rift zone is  $132 \pm 20$  by assuming that the  $Q$  in the lithosphere is 200.

Estimates of total horizontal extension across the rift range from 10 km [Logatchev and Florensov, 1978] to 20 km [Zorin and Cordell, 1991]. Gravity anomalies and deep seismic soundings (DSS) reveal that crustal thickness increases from 34-35 km beneath the rift axis to 42-46 km beneath the adjacent margins [Zorin et al., 1989].

### **1.3 The Baikal 1991-92 teleseismic experiment**

During the 90 days between July 7 and October 4, 1991, and the 117 days between June 11 and October 5, 1992, researchers from two United States universities (University of California, Los Angeles, and University of Wisconsin, Madison), and two institutes of Russian (Soviet Union in 1991) Academy of Sciences (Institute of Earth's Crust at Irkutsk, and Institute of Physics of the Earth at Moscow) conducted a joint seismic array study in the territory of the BRZ (Figure 1.3.1). Approximately 100 sites were occupied.

All the stations were equipped with three-dimensional short period sensors with central frequencies ranging from 0.5 to 2 Hz and about 12 of the stations were co-sited with broadband (Guralp and STS2) seismometers. All seismographs synchronized their internal clocks to signals from the Omega navigation system

(locked to either Norway or Japan) which ensured that the timing error for most of the seismograms was less than 20 ms.

All the station locations were determined by using a GPS Path-finder receiver (borrowed from UCLA's GPS group). The errors of the measurement for horizontal coordinates were less than 50 meters. Due to the poor accuracy of GPS in determining elevation, the ETOPO5 elevation data-base is used to get the elevations for the stations. Station locations can be found in Chapters two and three.

Installation and servicing were carried out using a combination of land vehicles, Aeroflot helicopters, boats on lake Baikal, and the Beijing-Moscow international train. Stations were serviced once about every 20 days for about 7 months. Extremely tricky roads and shortage of gasoline limited the frequency of services. Cloudy and rainy weather in the short summer of Siberia caused some recorder power failures. All of these conditions made a final rate of success about 75%.

For most of the stations we programmed a 10 sample per second (sps) continuous data stream to record teleseismic events; a 25 sps (for STS2 stations) or 50 sps triggering stream to record high frequency local and regional events; and for those stations co-sited with broadband sensors, another data stream with 1 sps and wide dynamic range (32 bit data words) was programmed to record surface waves.

Data dumped from the station disks were converted to SEG-Y format by using the REF2SEG-Y routine written by the PASSCAL Instrument Center. The resulting SEG-Y format data can easily be converted to other formats such as SAC, AH, and SIERRA by using routines provided by the Instrument Center.

Data from these digital stations will be used for travel time residual studies in Chapters two and four. The 1992 stations and the Russian analog stations (see

section 1.4) will be used for SKS splitting studies in Chapter three. No SKS signals suitable for splitting studies were recorded by the 1991 stations.

The total amount of data recorded is about 20 Gigabytes. All the data have been submitted to IRIS Data Management Center (DMC) and became a public data set. More information regarding the data set can be found in our data reports submitted to IRIS DMC [Davis et al., 1993; 1994], and the annual report submitted to the funding agency [Davis, 1992].

#### **1.4 Russian permanent seismic network**

In September, 1994 H. Liu and S. Gao of UCLA made their third trip to Russia to visit the Institute of Earth's Crust at Irkutsk, Russia, to select and copy analog seismograms recorded by 27 Russian seismic stations in the Baikal area (Figure 1.3.1). The purpose of the trip was to collect SKS signals recorded by these stations since 1980. All the stations were equipped with 3D short period sensors with central frequencies ranging from 0.2 to 1.2 Hz. Most of the stations have been operated at least since 1980. Timing errors as large as 10 seconds were frequent before 1985. Significant improvement in timing has been made during the past decade. Most of the timing errors can be easily corrected using radio signals recorded on the seismograms every hour. Since all the 3 channels were timed by a single clock, the timing errors have little effect on SKS splitting studies.

The stations were well-maintained and the sensors and seismographs were calibrated every year. The resulting parameters and calibration curves were published in a booklet named "Parameters, amplitude and phase characteristics of instruments of seismic network of Siberia" every year.

The analog seismograms were scanned and digitized at 100 samples per second. Station locations and example seismograms can be found in Chapter three. Data from these analog stations will be used for SKS splitting study in Chapter three.

## 1.5 Participants

Many people from several institutions contributed greatly to the acquisition and analysis of the data sets used by this study. Their names and titles during the field experiment are listed below in an alphabetic order. It must be mentioned that in addition to those listed below, many other people also made essential contributions to the field work, e.g., more than 20 vehicle drivers and several cooks from IEC, and helicopter pilots from Aeroflot.

•*Institute of Earth's Crust of Russian Academy of Sciences, Irkutsk:*

Artyomov, O., Engineer

Baduev, A., Engineer and head of field team two

Kochetkov, V., Geophysicist and head of seismology section

Kozhevnikov, V., Geophysicist

Logatchev, N., Academician and head of the Institute

Masalsky, O., Geophysicist and manager of the expedition for Russian side

Mordvinov, D., Volunteer

Mordvinova, I., Volunteer

Mordvinova, V., Geophysicist and head of field team one

Naiditch, V., Geophysicist and head of field team four

Perepelova, T., Interpreter

Tairov, V., Geophysicist and head of field team three

Zorin, Yu., Professor and scientific head of the expedition for Russian side

• *Institute of Physics of the Earth, Russian Academy of Sciences, Moscow:*

Karpachov, M., Graduate student

Kogan, M., Professor and head of gravity lab

Panasyuk, S., Graduate student

• *Institute of Geophysics, Mongolian Academy of Sciences, Ulan-Bator:*

Berlek, E., Geophysicist

• *PASSCAL Instrument Center at Lamont-Doherty Earth Observatory:*

Busby, R., Engineer

• *United States Air Force:*

Johnston, J., Researcher

• *University of Wisconsin, Madison:*

Abernathy, R., Engineer

Burkholder, P., Graduate student

Delitsin, L., Graduate student

Green, V., Graduate student

Lord, N., Engineer

Meyer, M., Volunteer

Meyer, R., Professor and principal investigator

Powell, L., Engineer

Unger, W., Engineer

• *University of California, Los Angeles:*

Benthien, M., Undergraduate student

Daniels, D., Volunteer

Davis, C., Volunteer

Davis, P.M., Professor and principal investigator  
Gao, S., Graduate student and author of this thesis  
Liu, H., Graduate student  
Rigor, A., Undergraduate student  
Slack, P., Graduate student  
Winter, M., Undergraduate student

## **1.6 Structure of the thesis**

The objectives of the study are listed in the first section of Chapter one. The following sections introduce the BRZ and describe the data set that is going to be used to accomplish the goals, and acknowledge the participants of the project who helped in the acquisition and analysis of the data sets. The structure of the entire thesis is described at the end of Chapter one (this section).

The first section of Chapters two through five is an introduction to the subject that is going to be dealt with in the chapter. The introduction usually summarizes previous studies, introduces related background material, and lays out the major goals of the chapter.

In Chapter two the teleseismic travel time residuals are interpreted using a traditional isotropic upper mantle model. The azimuthal variation of the residuals is illustrated and a function is selected based on the major features of the residual curves to represent the asthenosphere-lithosphere boundary. The theory of the inverse method to be used in this chapter and Chapter four, i.e., nonlinear Bayesian inversion, is summarized. An expected asthenospheric upwarp beneath the BRZ is revealed.

If the upwarp of the asthenosphere is caused by mantle flow, the upper mantle beneath the BRZ might be anisotropic, since the upper mantle is composed of highly anisotropic minerals and upper mantle flow can lead to preferred orientation of crystallographic axes and cause velocity anisotropy. Using SKS phases, Chapter three finds that the upper mantle beneath the study area is indeed anisotropic. The characteristic parameters of the anisotropy are obtained and interpreted. The method to obtain the parameters is described.

Given that the mantle is anisotropic, the velocity structure obtained from Chapter two, which was made under the assumption of isotropy, must be modified using an anisotropic model. This is the main task of Chapter four.

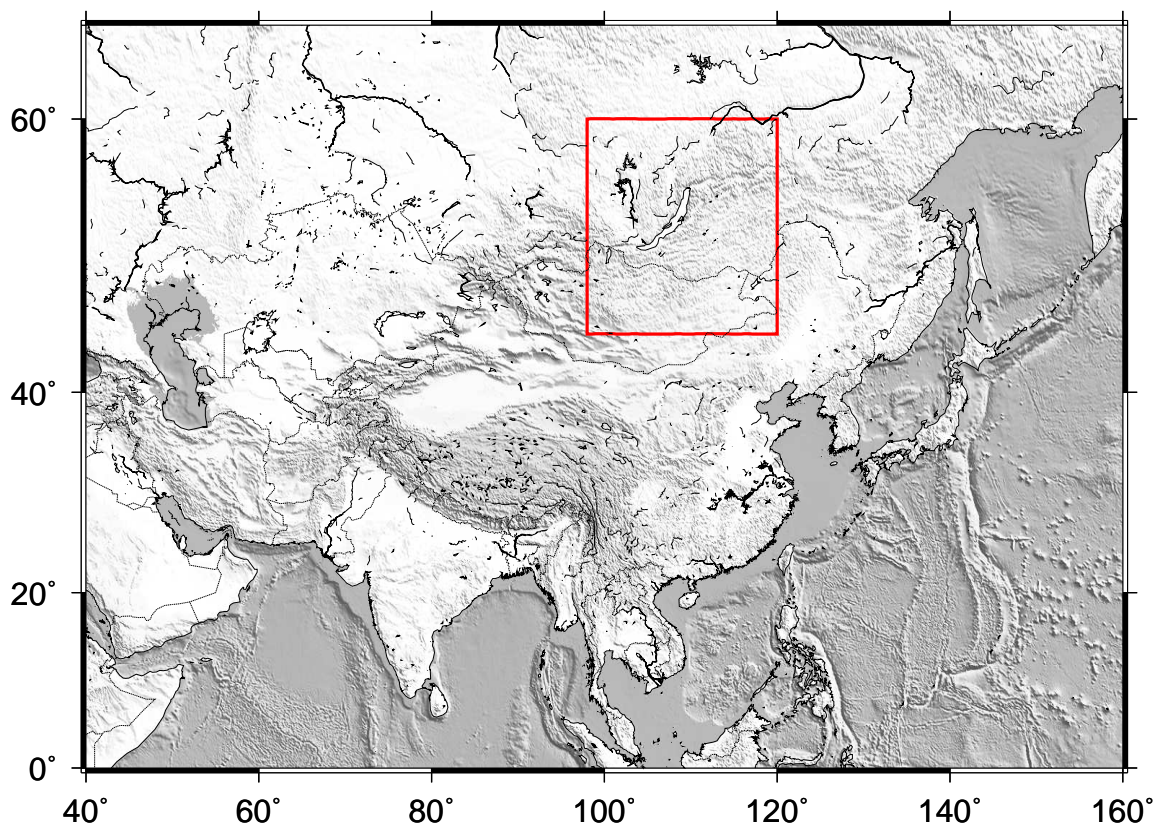
Chapter five summarizes the main results from travel time inversion and anisotropy studies and proposes that rifting is associated with small-scale mantle convection. The model can explain almost all the major features on the travel time residual curves and the spatial variation of anisotropy parameters. The model is described and used to make some alternate interpretations for the previous SKS splitting observations made in other areas.

Chapter six summarizes the main results and points out possible future study topics.

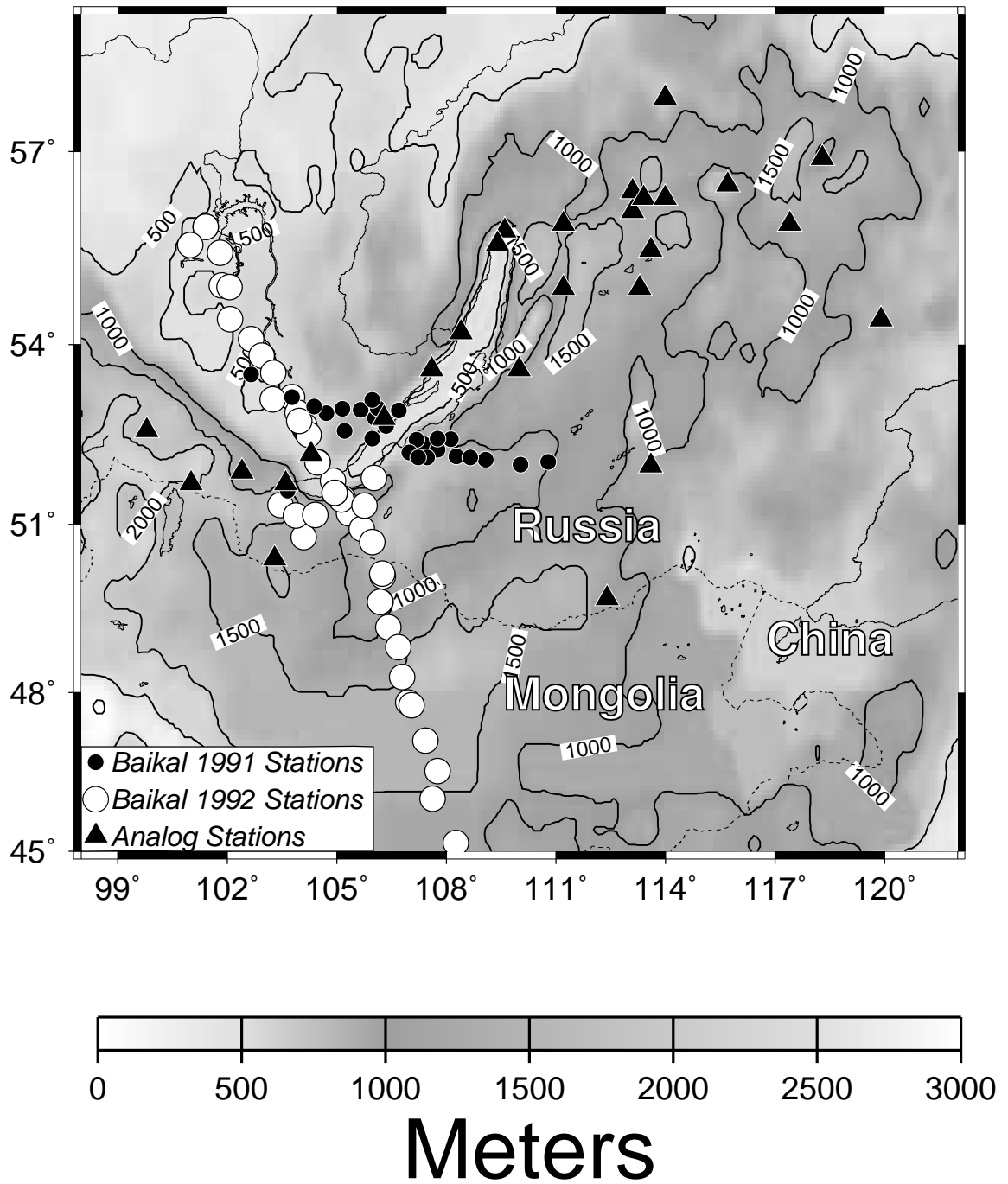
## FIGURE CAPTIONS

Figure 1.2.1: A Mercator projection map showing topography and seismicity (open circles, 1965-1992,  $m_b \geq 5.0$ ) of Asia, and location of the study area (confined area). The size of the circles is proportional to the magnitude of the event. The diagram, as well as most of the other diagrams in the dissertation, is produced using Generic Mapping Tool (GMT) Version 3.0 [Wessel and Smith, 1991], a free software for mapping and displaying data.

Figure 1.3.1: A Mercator projection map showing location of stations used in this study and topography of the study area. Elevations are part of the global ETOPO-5 data set and are smoothed with a two-dimensional boxcar filter.



**Figure 1.2.1**



**Figure 1.3.1**

# CHAPTER 2

## Interpretation of Teleseismic P-wave Travel Time Residuals by Assuming an Isotropic Upper Mantle

### 2.1 Introduction

Teleseismic travel-time residuals are suited for upper mantle studies because they are essentially not affected by small-scale inhomogeneities [Wylegalla et al., 1988]. Over the last 30 years, the deep seated structure beneath the Baikal rift zone (BRZ) and its adjacent regions has been studied by using various kinds of geologic and geophysical measurements, such as deep seismic sounding [Puzyrev et al., 1978], gravimetric investigation [Zorin et al., 1989], modeling of heat flow [Lysak, 1984; 1987; Zorin and Osokina, 1984; Zorin and Lepina, 1985], spectral ratio methods [Mordvinova, 1983; 1988], magnetotelluric measurements [Popov, 1990], and teleseismic travel time tomography [Gao et al., 1994b].

The deep seismic sounding experiment started in 1968. Since then in an area of over 400,000 km<sup>2</sup> a total length of profiles of more than 4000 km has been completed [Puzyrev et al., 1978]. Along one such profile across the southern Baikal area, the Moho depth varies from 37 to 39 km beneath the Siberian platform, decreases to 35 km beneath the rift and increases south-eastward in the mobile belt area [Puzyrev et al., 1978; Logatchev and Florensov, 1978; Zorin and Rogozhina, 1978; Zamarayev and Ruzhich, 1978]. The investigation discovered a low velocity upper mantle layer in the area. It also indicated that the P-wave velocity is around 6.4 km/s in the crust; 8.15 km/s in the subcrustal lithosphere; 7.4-7.8 km/s in an anomalous upper mantle layer [Puzyrev et al., 1978] immediately beneath the Moho under the BRZ.

Another interpretation of the DSS data revealed that the P-wave velocities of the subcrustal lithosphere is 8.1 to 8.2 km/s and beneath the rift zone decreases to 7.7 km/s, i.e., a 5% variation [Puzyrev, 1981; Logatchev and Zorin, 1987]. The thickness of the lithosphere was determined as about 120 km beneath the Siberian platform, 100 km in the Trans-Baikal region SE of the rift zone. Beneath the rift zone, the upwarped asthenosphere reaches the Moho discontinuity. The upwarp was found to have an asymmetric shape with the NW edge being steeper.

Recent gravity and seismic studies suggested that the lithospheric thickness beneath the rift zone is about 40-50 km; beneath the Siberian platform it increases to 200 km; and in the Trans-Baikal region it ranges from 75 to 160-175 km [Zorin et al., 1989; Logatchev and Zorin, 1992; Egorkin et al., 1984].

Magnetotelluric experiments indicated that in the southern part of the Baikal rift zone, the depth of a mantle conductive layer, which was referred to as the asthenosphere, was found to be about 110 km [Popov, 1990; Kiselev and Popov, 1992]. The asthenosphere-lithosphere boundary was found to be about 200 km beneath the Siberian platform.

Using teleseismic data from the 1991 experiment, Gao et al. [1994b] suggested that the upwarp has an asymmetric shape with the NW edge being steeper, and the lithosphere-asthenosphere P-wave velocity contrast is 4.9%. In the inversion of the travel time data, Gao et al. constrained the top of the upwarped asthenosphere to the Moho due to poor vertical resolution of the non-linear inversion. At a distance of about 300 km NW of the rift axis, the thickness of the lithosphere beneath the Siberian platform was about 100 km and appears to be still increasing at the end of

the profile. The profile was not long enough to find the thickness of the lithosphere beneath the platform.

This chapter will invert for the velocity structure by combining some of the previous and our our new and high quality travel time residual data, under the assumption of an isotropic upper mantle. An anisotropic model will be dealt with in Chapter four. Several models will be presented using different starting parameters.

## 2.2 Data

The data set consists of 2128 P-wave travel time measurements from 153 teleseismic events (Figure 2.2.1 and Table 2.2.1) recorded by 63 digital seismic stations suitable for travel time residual studies (Figure 2.2.2 and Table 2.2.2).

Theoretical arrival times were calculated by using the International Association of Seismology and Physics of the earth's Interior (IASPEI) 1991 Earth model [Kennett and Engdahl, 1991]. Residuals were found by subtracting these theoretical arrival times from observed ones, and relative residuals were formed for each event by subtracting the event's mean residual from the raw residuals.

The relative residuals were further corrected by removing the slope for each event. The slopes for the events in the subduction zone areas are the greatest, with maximum value of about 1 ms/km, which results in a travel time difference of about 1.5 s between the two ends of the 1992 profile. We believe that the slopes on the travel time residual curves are not the result of earth structure beneath the stations, but of mis-location of hypocenters [Gao et al., 1994b], because

- 1). Events with slopes of larger than 0.2 ms/km all occurred in subduction zones. The near-source stations used to locate these events were almost all at one side of the event, and hence a systematic mislocation is plausible [Dziewonski and

Anderson, 1981]. The error in the position and the origin time must be compensated by an equivalent error in depth, which can lead to the tilt of a derived travel time curve [Dziewonski and Anderson, 1981]. We calculated that [Gao et al., 1994b] for an earthquake of intermediate focal depth, at  $40^\circ$  from the center of the array, a 50-km depth mislocation causes a slope error in the travel time residual curves of 0.3 ms/km. Anisotropy in the subduction area [e.g. Kendall and Thomson, 1993] can also cause systematic mislocation of events, when an isotropic model is used.

2). Events show near zero slopes along the 1992 profile occurred in non-subduction zone areas such as California, where sufficient local seismic stations were available to accurately determine the hypocenters of the events.

It must be pointed out that events occurred in California show significant travel time slopes along the 1991 profile [Gao et al., 1994b], which crossed the middle part of BRZ; and show near zero slopes along the 1992 profile, which crossed the southern part. It could indicate that in the middle part of BRZ, the structure is asymmetric; while in the southern part, the asthenospheric structure is close to symmetric.

The final data after these corrections are plotted in Figure 2.2.1.

The digital seismographs that we used synchronize internal clocks to signals from the Omega navigation system, which ensured that the timing error for most of the data was less than 20 ms. Figure 2.2.3 shows a record section of a New Guinea event on vertical sensors. The traces were aligned using the IASPEI 1991 theoretical arrival times. The waveform is coherent over a distance of 1200 km. The sampling rate for the seismograms was 10 samples per seconds or greater. The picking error for most of the measurements was between 0.1-0.2 seconds.

To study the event location dependence of the relative travel time residuals, we group the events by azimuth ( $\phi$ ) and epicentral distance ( $\Delta$ ) of the sources relative to station 9224 (For 1992 events) and 9106 (For 1991 events). The Earth's surface is divided into 24 areas. Events within area  $(i, j)$  satisfy

$$(i - 1) * 30^\circ \leq \phi < i * 30^\circ, (i = 1, 2, \dots, 12), \quad (2.2.1)$$

$$(j - 1) * 60^\circ \leq \Delta < j * 60^\circ, (j = 1, 2). \quad (2.2.2)$$

The 77 events recorded by the 1992 network occurred within 12 of the 24 areas (Figure 2.2.4) and the 76 events recorded by the 1991 network occurred inside 14 of the areas (Figure 2.2.5). Therefore the data set is divided into 26 groups. Detailed information about each group is indicated in Table 2.2.3. The average number of events within each group is six. Seven groups have only one event. The maximum number of events in a group is 20 (group 92G). Events that belong to the same group have similar epicentral locations, as indicated by the small standard deviations of the mean longitude (less than  $5^\circ$ ) and latitude (less than  $4^\circ$ ). The incident angles ( $\theta$ ) were computed using the IASPEI 1991 Earth model. Events within a group show similar residual curves.

• *Group 92A*

The two northern California events in this group show consistent travel time residual patterns (Figure 2.2.4a). Both events are 10 km deep. The peak of the travel time residual curve which is about 1.0 second, is located at distance 50 km. There are two valleys in the curve on each side of the peak, with magnitudes of 0.3-0.4 seconds and located at  $-190$  km and  $280$  km, respectively. Most of the groups described below have such an one-peak-and-two-valley feature on their mean travel

time curves. The location of the peaks remains relatively stationary from group to group, while that of the valleys varies considerably.

- *Group 92B*

The seven events in this group are located along the NE Pacific subduction zone, in the Aleutian trench area (Figure 2.2.4b). The depths of these events are less than 56 km. Although the one-peak-and-two-valley feature is still clear, the magnitudes of the peak and the two valleys are smaller than group 92A. The epicentral distance for this group is about  $50^\circ$ , which is much smaller than that of group 92A, which is about  $75^\circ$ .

- *Group 92C*

This group is the nearest event cluster with an epicentral distance of  $28^\circ$  and consequently has the largest angle of incidence ( $31.5^\circ$ ). The lowest point reached by the rays from the 15 events is about 800 km. The travel time residuals from this group are different from other groups in the following features 1). The magnitudes of the peak are small compared with other groups; 2). The valleys in the travel time curves are unobservable; 3). The stations at the two ends show early arrivals of about 0.7 seconds.

The difference in the travel time residuals might be due to the fact that the rays from these events travel mainly through the upper mantle, which is more heterogeneous than the lower mantle. The rays can also be influenced by some shallow heterogeneities on the east side of the profile. These heterogeneities cannot be sampled by the rays from other groups because of more vertical incidence.

- *Group 92D*

There is only one event in this group (Figure 2.2.4d). This Tonga trench event is the most distant and one of the deepest events among the events used for travel time residual studies. The magnitude of the peak reduces to nearly zero, and the magnitude of the right valley is large.

• *Group 92E*

The travel time residuals from the two events occurred in the Mariana trench resume the one-peak-and-two-valley pattern observed in group 92A and 92B. The locations of the two valleys shift about 100 km and that of the peak shift about 50 km toward the left (NW) relative to group 92A. The distance between the two valleys is approximately the same as that of group 92A and 92B.

• *Group 92F*

The 13 events in this group occurred in New Guinea and surrounding areas. The back azimuths of the events are similar to that of Group 92E, but the epicentral distances are about  $20^\circ$  larger. The mean residual curve for this group is similar to that of Group 92E, except that the magnitude of the right valley is greater and that of the peak is smaller than those observed in the mean curve of Group 92E.

• *Group 92G*

This group consists of 20 events from the Banda Sea and adjacent areas. Relative to Group 92F, the location of the right valley shifts about 100 km toward the left (NW), while that of the left valley shifts about 30 km.

• *Group 92H*

The travel time residuals from this group, which consists of 5 events that occurred in the eastern Java trench and NW Australia regions, are similar to those of Group 92G. The rays from this group arrive approximately along the profile.

- *Group 92I*

The 7 events occurred in the NW part of the Java trench. The magnitudes of the peak and the valleys in the mean residual curve is larger than those on 92G and 92H, despite the fact that the epicentral distance and hence the angle of incidence is almost the same as that of 92G. The right valley covers a relatively small distance of about 150 km and is bounded by a peak on its right side.

- *Group 92J*

The only event in this group occurred inside the central valley of the Mid-oceanic ridge of the Indian Ocean. While the location of the right valley is not well determined due to lack of data, that of the left valley shifts towards the SE about 80 km relative to that of Group 92I.

- *Group 92K*

The event in this group is from the Persian Gulf area and is recorded by about half of the stations. Compared to Group 92J, the location of the valleys shifts about 50 km toward the right (SE). The magnitude and location of the peak cannot be determined due to lack of data.

- *Group 92L*

The two events in this group occurred along the north end of the Atlantic mid-ocean ridge. The magnitude of the peak is the largest among all the 12 groups described above. The location of the two valleys shifts further SE, approximately to the same location observed for Group 92A.

- *Groups 91A-91N*

The event location and travel time residuals of the 14 event groups from the 1991 network are shown in Figure 2.2.5. The length of the 1991 array is about

570km, which is less than half of the 1992 profile’s length. The array is more two-dimensional than the 1992 one. Positive residuals can be observed on some of the groups. Several groups show the two valleys in their travel time residual curves as observed along the 1992 profile, e.g., group 91A, 91B, 91J, and 91L. The location of the valleys, whenever observable, is approximately the same as that observed in the 1992 groups having similar back azimuth and epicentral distance.

Figures 2.2.6 and 2.2.7 show the mean residual curves together with error bars. When there is only one event in a group, the errors are taken as 0.2 seconds, which is approximately the accuracy of our picking; when the number of events in a group is more than one, the error for a station is taken as the standard deviation of the mean value for the station, i.e.,

$$\sigma_{\bar{t}} = \frac{1}{\sqrt{N}} \left[ \frac{1}{N-1} \sum_{i=1}^N (t_i - \bar{t})^2 \right]^{1/2}, \quad (2.2.3)$$

where  $\bar{t}$  is the mean residual,  $N$  is the number of available events for the station,  $t_i$  is the residual from the  $i$ th event.

The direction of the arriving rays from each group is shown on the upper-right insert of Figures 2.2.6 and 2.2.7.

### 2.3. Model construction

The isotropic velocity structure in the study area will be computed using nonlinear Bayesian inversion method, which requires a starting model. The starting model is constructed using both the results from previous studies and the major features of the travel time residuals described in section 2.2. The following facts are used as guidelines:

1). Most of the event clusters (Figures 2.2.4 and 2.2.5) display a peak on their travel time residual curves approximately in the region  $-30 \text{ km} < x < 60 \text{ km}$ . The existence and the appearance of the peaks imply a upwarped low-velocity structure.

2). The two valleys on travel time residual curves on each side of the rift, the relatively uniform distance between them, and the large location shift for events from different azimuths imply two high velocity structures located around  $\pm 200 \text{ km}$ . The depth of the high velocity structures should be about  $250 \text{ km}$  in order to create the observed  $200 \text{ km}$  location shift of the valleys on travel time residual curves.

3). Previous studies indicated that the top of the asthenosphere might reach the Moho [e.g., Zorin et al., 1989; Gao et al., 1994b]. Other studies suggest that it doesn't reach the Moho but lies a greater depth, about  $110 \text{ km}$  in this area [Popov, 1990; Kiselev and Popov, 1992].

4). Studies in the BRZ [e.g., Logatchev and Zorin, 1992; Gao et al., 1994b] and in other rift zones [e.g., Parker et al., 1984; Dahlheim et al., 1989; Davis, 1991; Davis et al., 1984; 1993b; Slack et al., 1994; Slack, 1994] reveal that the velocity contrast between the low velocity structure, which is generally believed to be upwarped asthenosphere, and the velocity of the surrounding areas is about  $4\% - 8\%$ .

5). Using the data from the 1991 experiment, Gao et al. [1994b] show that the upwarp of the asthenosphere is asymmetric in the middle part of BRZ with the NW edge being steeper. The study also indicates that the highest position of the upwarp is not aligned with the lake axis but is shifted about  $50 \text{ km}$  toward the SE.

By utilizing the above prior information, we represent the geometry of the upper boundary of the asthenosphere using the combination of a cosine and a Gaussian function, i.e.

$$f(x) = -h_0 + f1(x) * f2(x), \quad (2.3.1)$$

where

$$f1(x) = \begin{cases} a_1 * \cos(2\pi x/\lambda) & \text{if } |x| \leq 3/4\lambda; \\ 0 & \text{elsewhere.} \end{cases}, \quad (2.3.2)$$

and

$$f2(x) = \exp(-0.5x^2/\sigma^2), \quad (2.3.3)$$

where  $h_0$  is the depth of the normal lithosphere, i.e., lithosphere outside the upwarp region,  $a_1$  is the magnitude of the upwarp,  $\lambda$  is the wavelength of the cosine function, and  $\sigma$  is the standard deviation of the Gaussian function.

As shown in Figure 2.3.1,  $f(x)$  is a function with great versatility. The examples shown in Figure 2.3.1 indicate that 1). the two minima occur at  $x \leq \lambda/2$ ; 2). when  $\lambda/\sigma > 6$  (Figure d and e), the magnitude of the two minima reduces to nearly zero; 3). the magnitude of the maxima  $\geq$  that of the minima.

To illustrate the possible asymmetric shape of the upwarp, each side will be given an independent pair of  $\lambda$  and  $\sigma$ . An example of such an asymmetric shape could be formed by replacing the right side of Figure (a) with the right side of Figure (d).

The strike and location of the vertex line of the two-dimensional structure will also be treated as unknown parameters.

The coordinate systems are shown in Figure 2.3.2. The origin for  $X'O'Y'$  is at station 9224, which is on the southern shore of the Lake.  $+X'$ ,  $+Y'$ , and  $+Z'$

point East, South, and downward, respectively. The origin for  $XOY$  is along the  $Y'$  axis,  $b$  km from  $O'$ .  $+X$ ,  $+Y$ , and  $+Z$  directions are along the vertex line of the 2D velocity structure, perpendicular to it, and downward, respectively.

In summary, there are nine unknown parameters to be solved, they are:

1.  $a_1$ : magnitude of the upwarp;
2.  $\lambda_1$ : wavelength of the left cosine function;
3.  $\sigma_1$ : standard deviation of the left Gaussian function;
4.  $\lambda_2$ : wavelength of the right cosine function;
5.  $\sigma_2$ : standard deviation of the right Gaussian function;
6.  $\gamma$ : asthenospheric-lithospheric velocity contrast;
7.  $\phi_0$ : strike of the structure measured anti-clockwise from the East;
8.  $b$ : location of the vertex line of the 2D structure (see Figure 2.3.2);
9.  $h_0$ : depth of normal lithosphere.

In the coordinate system ( $XOY$ ) (Figure 2.3.2), the location of a station at  $(x', y')$  in the original system ( $X'O'Y'$ ) is found using

$$x = x' \cos(\phi_0) - (y' - b) \sin(\phi_0), \quad (2.3.4)$$

$$y = x' \sin(\phi_0) + (y' + b) \cos(\phi_0). \quad (2.3.5)$$

The time needed for a ray to travel from a depth  $z_0$  to the station is

$$t(y) = \int_0^{z_0} \frac{\sqrt{1 + \sin^2 \theta(y, z)}}{\cos \theta(y, z)} \frac{dz}{v(y, z)}, \quad (2.3.6)$$

where  $\theta$  is the angle of incidence of the ray,  $v(y, z)$  is the P-wave velocity.

Note that because the velocity structure is two-dimensional, the travel time is independent of  $x$ . Since the velocity contrast between the lithosphere and the

asthenosphere is in an order of 5%, in this study we use the straight ray assumption. Under such an assumption,  $\theta$  in Eq. 2.3.6 becomes a constant for a given station-event pair.

## 2.4 Nonlinear Bayesian inversion: the theory

The method that we used to search for the optimal parameters is nonlinear Bayesian inversion [Jackson and Matsu'ura, 1985; Jackson, 1972]. The procedure summarized below is part of my term paper for the course *Inverse Theory and Data Interpretation* conducted by Prof. D. D. Jackson at UCLA.

Consider a nonlinear parametric inverse problem of the form

$$y = f(x, t) + e \quad (2.4.1)$$

and some prior information of the form

$$z = g(x, t) + d, \quad (2.4.2)$$

where  $y$  is an  $n$ -vector of observed data,  $x$  is an  $m$ -vector of unknown parameters,  $t$  is the independent variables,  $f$  is an  $n$ -vector of known functions,  $z$  is a vector of prior data,  $g$  is a vector of known functions of the  $m$  unknown parameters, and  $e$  and  $d$  are vectors of Gaussian errors with zero means and known covariance for the observed and prior data, respectively.

Expansion of (1) and (2) in Taylor series about the starting parameters  $\{x_{01}, x_{02}, \dots, x_{0m}\}$  gives

$$y_k = f(x_{01}, x_{02}, \dots, x_{0m}, t_k) + \frac{\partial f}{\partial x_i} \Big|_{x_i=x_{0i}} (x_i - x_{0i}) + \delta_1 + e_k \quad (2.4.3)$$

$$z_k = g(x_{01}, x_{02}, \dots, x_{0m}, t_k) + \frac{\partial g}{\partial x_i} \Big|_{x_i=x_{0i}} (x_i - x_{0i}) + \delta_2 + d_k, \quad (2.4.4)$$

where  $\delta_1$  and  $\delta_2$  are negligible higher order terms.

Let

$$y'_k = y_k - f(x_{01}, x_{02}, \dots, x_{0m}, t_k) \quad (2.4.5)$$

$$x'_k = (x_k - x_{0k}) \quad (2.4.6)$$

$$A'_{ij} = \left. \frac{\partial f}{\partial x_j} \right|_{t=t_i, x=x_j} \quad (2.4.7)$$

$$z'_k = z_k - g(x_{01}, x_{02}, \dots, x_{0m}, t_k), \quad (2.4.8)$$

and

$$B'_{ij} = \left. \frac{\partial g}{\partial x_j} \right|_{t=t_i, x=x_j} . \quad (2.4.9)$$

By ignoring higher order terms  $\delta_1$  and  $\delta_2$ , (3) and (4) can be written as the following linear forms

$$Y' = A'X' + e \quad (2.4.10)$$

$$Z' = B'X' + d. \quad (2.4.11)$$

To standardize, applying two diagonal matrices  $F$  and  $G$  to (10) and (11) so that

$$F^T F = E^{-1} \quad (2.4.12)$$

and

$$G^T G = D^{-1}. \quad (2.4.13)$$

where  $E$  and  $D$  are covariance matrices satisfying

$$E = \overline{ee^T} \quad (2.4.14)$$

and

$$D = \overline{dd^T}. \quad (2.4.15)$$

Let

$$Y'' = \begin{pmatrix} FY' \\ \dots \\ GZ' \end{pmatrix} \quad (2.4.16)$$

$$A'' = \begin{pmatrix} FA' \\ \dots \\ GB' \end{pmatrix}, \quad (2.4.17)$$

the problem becomes the most general linear form

$$Y'' = A''X' + e', \quad e' \sim N(0, I) \quad (2.4.18)$$

The estimated parameters are calculated using

$$\hat{x} = H''Y'' = H'Y' + K'Z', \quad (2.4.19)$$

where the inverse matrices

$$H'' = (A''^T A'')^{-1} A''^T \quad (2.4.20)$$

$$H' = (A'^T E^{-1} A' + B'^T D^{-1} B')^{-1} A'^T E^{-1} \quad (2.4.21)$$

$$K' = (A'^T E^{-1} A' + B'^T D^{-1} B')^{-1} B'^T D^{-1} \quad (2.4.22)$$

The sensitivity of parameter  $\hat{x}_k$  to observed datum point  $y_i$  is given by

$$\frac{\partial \hat{x}_k}{\partial y_i} = H'_{ki}, \quad (2.4.23)$$

and that to prior datum  $z_i$  is given by

$$\frac{\partial \hat{x}_k}{\partial z_i} = K'_{ki}, \quad (2.4.24)$$

The covariance matrix for the estimate  $\hat{x}$  is

$$X = (A''^T A'')^{-1}. \quad (2.4.25)$$

The matrix describing the resolution provided by observed data is

$$R_a = X A'^T E^{-1} A', \quad (2.4.26)$$

and the resolution matrix related with prior data is

$$R_b = X B'^T D^{-1} B'. \quad (2.4.27)$$

Obviously,

$$R_a + R_b = I, \quad (2.4.28)$$

whence  $Trace(R_a) + Trace(R_b) = m$ , the number of parameters.

## 2.5 Nonlinear Bayesian inversion: results

### • *Input data*

The distribution of the epicenters are highly uneven with the majority in the Banda Sea and adjacent areas (Figures 2.2.4F-H; 2.2.5E-I). For instance, 96 of the 153 events (63%) occurred in the back azimuthal range of  $120^\circ - 180^\circ$ , which covers only 16.7% of the  $360^\circ$  total back azimuthal range. The result of the inversion would be dominated by those events from the south if the original travel time residuals were used. For a more even azimuthal coverage, we use the mean residuals (Figures 2.2.6 and 2.2.7) in the inversion.

Totally 517 mean travel time residuals from 26 groups are used in the inversion. In model 4 below we use only the data from the 1992 array.

We will present several models below. Each of them is derived using a different set of starting parameters and constraints.

### • *Model 1*

The starting parameters and their standard deviations are chosen based on previous studies and our data set as described in section 2.3, as well as some forward modelling.

$h_0$ , the depth of the normal asthenosphere, is set to be 200 km with standard deviation 60 km.

$a_1$ , the magnitude of the cosine function in Eq. 2.3.2, is set to be 150 km with standard deviation 45 km. Therefore the depth of the shallowest part of the asthenosphere upwarp is  $h_0 - a_1 = 50$  km.

$\lambda_1$  and  $\lambda_2$ , the wavelength of the cosine function in Eq. 2.3.2 for  $y < 0$  and  $y > 0$  (see Figure 2.3.2), respectively, are chosen as 500 km with standard deviation 150 km.

$\sigma_1$  and  $\sigma_2$ , the standard deviation of the Gaussian function in Eq. 2.3.3 for  $y < 0$  and  $y > 0$  (see Figure 2.3.2), respectively, are chosen as 125 km with standard deviation 37.5 km.

$\phi_0$ , the orientation of the two-dimensional structure measured anti-clockwise from the East, is set to be  $45^\circ$ , which is approximately the orientation of the surface expression of the rift. Its standard deviation is set to be 15 degrees.

$b$ , the offset of the vertex line (Figure 2.3.2), is set to be zero with standard deviation 50 km.

$\gamma$ , the velocity contrast between the lithosphere and the asthenosphere, is chosen as 5% with standard deviation 1.5%.

The thickness and P-wave velocity of the crust are kept as constant and are chosen as 40 km, 6.5 km/s, respectively; the velocity of the lithosphere is set to be 8.1 km/s.

The result of the inversion is obtained after 100 iterations. Figure 2.5.1 shows the sum of squared residuals (SSR) at each iteration. After 100 iterations, the SSR dropped from 58 to 26. No significant decreasing on SSR is observed after the 90th iteration, implying that 100 iterations is enough. The resulting parameters are:

1.  $a_1 = 152 \pm 10$  km
2.  $\lambda_1 = 495 \pm 15$  km
3.  $\sigma_1 = 145 \pm 10$  km
4.  $\lambda_2 = 500 \pm 15$  km
5.  $\sigma_2 = 145 \pm 10$  km
6.  $\gamma = (2.16 \pm 0.024)\%$
7.  $\phi_0 = 52.9 \pm 0.2^\circ$
8.  $b = 27 \pm 5$  km
9.  $h_0 = 198 \pm 15$  km

The fitted and original data, as well as the final velocity model are shown in Figure 2.5.2. The results indicate that

- 1). the asthenosphere reaches to a depth of  $h_0 - a_1 = 46 \pm 10$  km;
- 2). the two lithospheric downwarps occur approximately in the range of  $120 \text{ km} < |y| < 300 \text{ km}$  with the maxima at  $y = \pm 200$  km;
- 3). the velocity contrast between the lithosphere and the asthenosphere is 2.16%.
- 4). the strike of the structure is  $52.9^\circ$  measured anti-clockwise from the East.

Using the covariance matrix defined in Equation 2.4.25, the cross correlation coefficients between the parameters can be calculated using

$$C_{ij} = \frac{X_{ij}}{\sqrt{X_{ii}X_{jj}}} \quad (2.5.1)$$

where  $C_{ij}$  is the cross correlation coefficient between the  $i$ th and the  $j$ th parameter, and  $X_{ij}$  is the element at the  $i$ th row and the  $j$ th column. Figure 2.5.3 shows the resulting coefficients. While most of the parameters are highly independent of each other, some parameter pairs have large absolute coefficients. The significant positive correlation between  $\phi_0$  and  $b$  ( $C_{7-8} = 0.86$ ) indicates that rotating the 2D structure anti-clockwise has a similar effect to moving the offset of the vertex line southward. The significant negative correlation between  $a_1$  and  $\gamma$  ( $C_{1-6} = -0.55$ ) indicates that increasing the height of the upwarp has a similar effect to decreasing the velocity contrast. The significant negative correlation between  $a_1$  and  $h_0$  ( $C_{6-9} = -0.51$ ) indicates that increasing the thickness of the lithosphere has a similar effect to decreasing the velocity contrast. The reasons for the large negative correlation between  $\gamma$  and  $\sigma_2$  ( $C_{5-6} = -0.79$ ) and the small negative correlation between  $\gamma$  and  $\sigma_1$  ( $C_{3-6} = -0.19$ ) are not obvious.

The trace of the matrix describing the resolution provided by observed data is (Equation 2.4.26)  $R_a = 8.993$ , and the trace of the matrix describing the resolution provided by prior data is (Equation 2.4.27)  $R_b = 0.007$ , implying that the observed data contributed to almost all of the solution of the parameters.

• *Model 2*

Some of the previous studies suggested that the thickness of the normal lithosphere in this area is about 120 km [Puzyrev, 1981; Logatchev and Zorin, 1987] and the asthenosphere reaches the Moho. To use this information, we use the following prior information:

$h_0$ , the depth of the normal asthenosphere, is set to be 120 km with standard deviation 36 km.

$a_1$ , the magnitude of the cosine function in Eq. 2.3.2, is set to be 70 km with standard deviation 21 km. Therefore the depth of the shallowest part of the asthenosphere upwarp is  $h_0 - a_1 = 50$  km.

$\lambda_1$  and  $\lambda_2$  are set to be the same as in Model 1.

$\sigma_1$  and  $\sigma_2$  are set to be the same as in Model 1.

$\phi_0$  is set to be the same as in Model 1.

$b$ , is set to be the same as in Model 1.

$\gamma$  is set to be the same as in Model 1.

The result of the inversion is obtained after 100 iterations. Figure 2.5.4 shows the sum of squared residuals (SSR) at each iteration. After 100 iterations, the SSR dropped from 29 to 27. The resulting parameters are:

1.  $a_1 = 70 \pm 10$  km
2.  $\lambda_1 = 517 \pm 15$  km
3.  $\sigma_1 = 130 \pm 10$  km
4.  $\lambda_2 = 490 \pm 20$  km
5.  $\sigma_2 = 120 \pm 10$  km
6.  $\gamma = (3.91 \pm 0.073)\%$
7.  $\phi_0 = 50.5 \pm 0.3^\circ$
8.  $b = 13 \pm 35$  km
9.  $h_0 = 118 \pm 30$  km

The fitted and original data, as well as the final velocity model are shown in Figure 2.5.5. The results indicate that

- 1). the asthenosphere reaches to a depth of  $h_0 - a_1 = 48$  km; 2). the two lithospheric downwarps occur approximately in the range of  $120 \text{ km} < |y| < 300 \text{ km}$

with the maxima at  $y = \pm 180$  km; 3). the velocity contrast between the lithosphere and the asthenosphere is 3.9%. 4). the strike of the structure is  $50.5^\circ$  measured anti-clockwise from the East.

Figure 2.5.6 shows the cross correlation coefficients between the resulting parameters. The significant negative correlation between  $a_1$  and  $\gamma$  ( $C_{1-6} = -0.91$ ) indicates that increasing the height of the upwarp has almost the same effect as decreasing the velocity contrast. The significant negative correlation between  $a_1$  and  $h_0$  ( $C_{6-9} = -0.54$ ) indicates that increasing the thickness of the lithosphere has a similar effect to decreasing the velocity contrast.

The trace of the matrix describing the resolution provided by observed data is (Equation 2.4.26)  $R_a = 8.985$ , and the trace of the matrix describing the resolution provided by prior data is (Equation 2.4.27)  $R_b = 0.015$ , implying that the observed data contributed to almost all of the solution of the parameters.

• *Model 3*

Some of the previous studies suggested that the thickness of the normal lithosphere in this area is about 200 km [Egorkin et al., 1984; Logatchev and Zorin, 1992] and the depth of the asthenosphere beneath BRZ is about 110 km. [Popov, 1990; Kiselev and Popov, 1992]. To use these information, we use the following prior information:

$h_0$ , the depth of the normal asthenosphere, is set to be 200 km with standard deviation 60 km.

$a_1$ , the magnitude of the cosine function in Eq. 2.3.2, is set to be 90 km with standard deviation 27 km. Therefore the depth of the shallowest part of the asthenosphere upwarp is  $h_0 - a_1 = 110$  km.

$\lambda_1$  and  $\lambda_2$  are set to be the same as in Model 1.

$\sigma_1$  and  $\sigma_2$  are set to be the same as in Model 1.

$\phi_0$  is set to be the same as in Model 1.

$b$ , is set to be the same as in Model 1.

$\gamma$  is set to be the same as in Model 1.

The result of the inversion is obtained after 100 iterations. Figure 2.5.7 shows the sum of squared residuals (SSR) at each iteration. After 100 iterations, the SSR dropped from 31 to 27.

1.  $a_1 = 79 \pm 10$  km
2.  $\lambda_1 = 512 \pm 10$  km
3.  $\sigma_1 = 171 \pm 15$  km
4.  $\lambda_2 = 528 \pm 15$  km
5.  $\sigma_2 = 139 \pm 10$  km
6.  $\gamma = (3.06 \pm 0.05)\%$
7.  $\phi_0 = 51.7 \pm 0.3^\circ$
8.  $b = 22 \pm 10$  km
9.  $h_0 = 180 \pm 40$  km

The fitted and original data, as well as the final velocity model are shown in Figure 2.5.8. The results indicate that

- 1). the asthenosphere reaches to  $h_0 - a_1 = 101 \pm 20$  km;
- 2). the magnitudes of the two valleys are about 20 km;
- 3). the velocity contrast between the lithosphere and the asthenosphere is 3.1%.
- 4). the strike of the structure is  $51.7^\circ$  measured anti-clockwise from the East.

Figure 2.5.9 shows the cross correlation coefficients between the resulting parameters. The significant negative correlation between  $a_1$  and  $\gamma$  ( $C_{1-6} = -0.83$ ) indicates that increasing the height of the upwarp has a similar effect to decreasing the velocity contrast.

• *Model 4*

As shown in Figure 2.2.2, the 1991 profile was short and located around the central part of the BRZ, while the 1992 profile was long and located across the southern part of the BRZ. The upper mantle structure beneath the two profiles may not be the same. To invert for the structure beneath the southern part of the BRZ, in this model we use the 1992 profile alone. Results from this model are dominated by structure beneath the 1992 profile while those from the previous models are averaged structure beneath southern-central parts of the BRZ.

The starting parameters and their errors are exactly the same as those in model 1.

The result of the inversion is obtained after 100 iterations. Figure 2.5.10 shows the sum of squared residuals (SSR) at each iteration. After 100 iterations, the SSR dropped from 26 to 14.6.

1.  $a_1 = 153 \pm 10$  km
2.  $\lambda_1 = 518 \pm 15$  km
3.  $\sigma_1 = 171 \pm 10$  km
4.  $\lambda_2 = 505 \pm 25$  km
5.  $\sigma_2 = 132 \pm 10$  km
6.  $\gamma = (2.4 \pm 0.05)\%$
7.  $\phi_0 = 31.6 \pm 0.7^\circ$

8.  $b = 14 \pm 25$  km

9.  $h_0 = 198 \pm 25$  km

1). the asthenosphere reaches to  $h_0 - a_1 = 45 \pm 15$  km; 2). the magnitudes of the downwarps are about 120 km for the left one and 40 km for the right one; 3). the velocity contrast between the lithosphere and the asthenosphere is 2.4%. 4). the strike of the structure is  $31.6^\circ$  measured anti-clockwise from the East; This value is smaller than the general direction of the strike of the BRZ, but is close to the local strike of the BRZ. 5). the vertex line of the 2D structure is about 14 km south of the origin of coordinate system  $X'O'Y'$  (Figure 2.3.2).

Figure 2.5.12 shows the cross correlation coefficients between the resulting parameters. The significant positive correlation between  $a_1$  and  $h_0$  ( $C_{1-9} = 0.98$ ) indicates that increasing the height of the upwarp has almost the same effect as increasing the thickness of the lithosphere. The significant negative correlation between  $a_1$  and  $\gamma$  ( $C_{1-6} = -0.59$ ) indicates that increasing the height of the upwarp has a similar effect to decreasing the velocity contrast. The significant negative correlation between  $h_0$  and  $\gamma$  ( $C_{6-9} = -0.74$ ) indicates that increasing the thickness of the lithosphere has a similar effect to decreasing the velocity contrast.

## FIGURE CAPTIONS

Figure 2.2.1: The top diagrams show teleseismic travel time delays relative to the IASPEI91 Earth model for the Baikal 1992 (A) and 1991 (B) networks. For (A) the reference station is 9224, which was a station in the Baikal 1992 profile and was on the southern shore of Lake Baikal; For (B) the reference station is 9106, which was a station in the Baikal 1991 profile and was on the southeastern shore of Lake Baikal. The diagrams at the bottom show locations of the earthquakes, as well as their azimuths and epicentral distances relative to the reference stations.

Figure 2.2.2: Map showing the location of stations used for travel time studies. The stations were installed and operated by the University of California, Los Angeles (UCLA), University of Wisconsin, Madison (UW), and Russian Academy of Sciences Baikal in the summers of 1991 & 1992. Circles are 1992 stations and triangles are 1991 stations.

Figure 2.2.3: Sample seismograms recorded by the vertical components along the 1992 profile. Event time: 1992:229:10:23; mb: 6.0; depth: 237 km; location:  $146.659^{\circ}\text{E}$ ,  $5.393^{\circ}\text{S}$ . Positive direction is to the southeast.

Figure 2.2.4: Location of events (left diagrams), P-wave travel time residuals (circles, right diagrams), and the mean residuals (solid line, right diagrams) from the 1992 network. Events are separated into clusters having similar azimuths and epicentral angles. Center of the polar map is station 9224. Relative residual curves within these event clusters have similar patterns. Delay patterns show strong dependence on hypocentral locations.

Figure 2.2.5: Location of events (left diagrams), P-wave travel time residuals (circles, right diagrams), and the mean residuals (solid line, right diagrams) from the 1991 network. Events are separated into clusters having similar azimuths and epicentral angles. Center of the polar map is station 9106. Relative residual curves within these event clusters have similar patterns. Delay patterns show strong dependence on hypocentral locations.

Figure 2.2.6: Mean travel time residual curves from the 1992 event groups. One vertical unit represents one second. Each horizontal grid line is the zero line of a group, with its name being written on the right side of the diagram. The two vertical curves connect the location of the two minima on the residual curves. The insert on top shows average arrival direction of each event group.

Figure 2.2.7: Mean travel time residual curves from the 1991 event groups. One vertical unit represents one second. Each horizontal grid line is the zero line of a group, with its name being written on the right side of the diagram. The two vertical curves connect the location of the two minima on the residual curves. The insert on top shows average arrival direction of each event group.

Figure 2.3.1: Examples of the function  $f(x)$  defined in Eq. 2.3.1.

Figure 2.3.2. Coordinate systems for the calculation of travel time residuals. The origin for  $X'O'Y'$  is at station 9224, which is on the southern shore of the Lake.  $+X'$ ,  $+Y'$ , and  $+Z'$  directions are toward the East, South, and downward, respectively. The origin for  $XOY$  is along the  $Y'$  axis

and  $b$  km from  $O'$ .  $+X$ ,  $+Y$ , and  $+Z$  directions are along the vertex line of the 2D velocity structure, perpendicular to it, and downward, respectively.  $\phi_0$  is the strike of the 2D structure measured anti-clockwise from the East.

Figure 2.5.1: Sum of squared residuals at each iteration during the inversion for Model 1.

Figure 2.5.2: Inverted velocity model 1 (upper-right insert), fitted (solid lines) and original (dots) data, as well as arrival direction of the rays (upper-left insert) for the 1992 (a) and 1991 (b) networks. The velocity model is plotted along the  $+Y$  direction, and the travel time residuals are plotted along the 1992 and 1991 profiles for figure (a) and (b), respectively.

Figure 2.5.3: Cross correlation coefficients between resulting parameters for Model 1.

Figure 2.5.4: Same as Figure 2.5.1 but for Model 2.

Figure 2.5.5: Same as Figure 2.5.2 but for Model 2.

Figure 2.5.6: Same as Figure 2.5.3 but for Model 2.

Figure 2.5.7: Same as Figure 2.5.1 but for Model 3.

Figure 2.5.8: Same as Figure 2.5.2 but for Model 3.

Figure 2.5.9: Same as Figure 2.5.3 but for Model 3.

Figure 2.5.10: Same as Figure 2.5.1 but for Model 4.

Figure 2.5.11: Same as Figure 2.5.2 but for Model 4.

Figure 2.5.12: Same as Figure 2.5.3 but for Model 4.

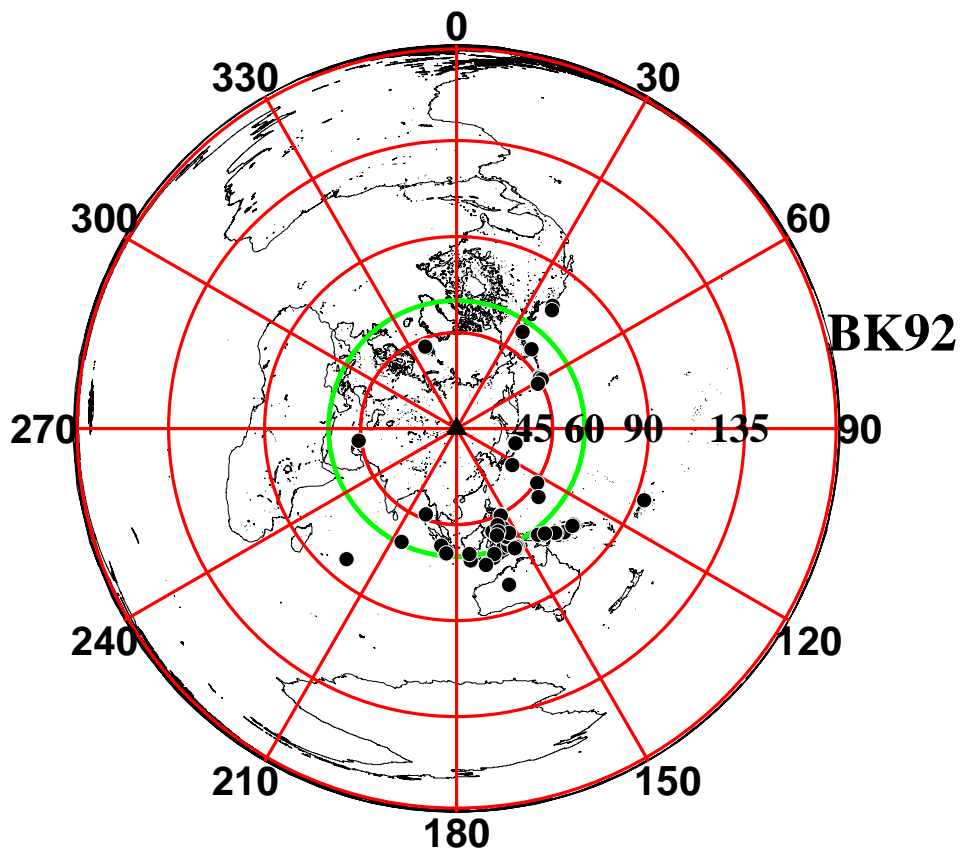
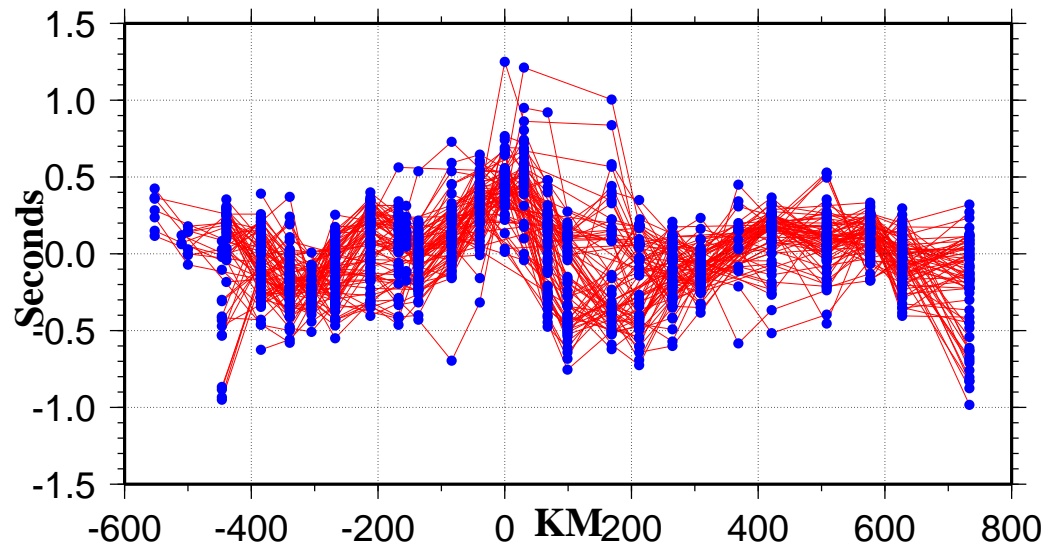


Figure 2.2.1 (A)

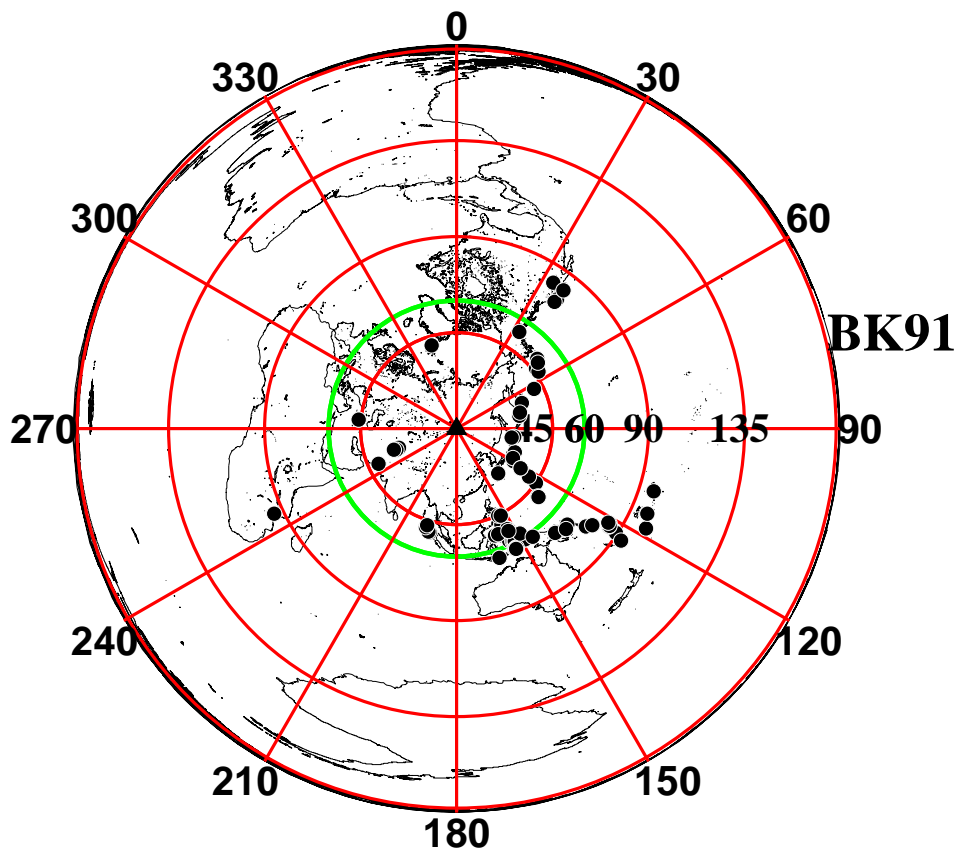
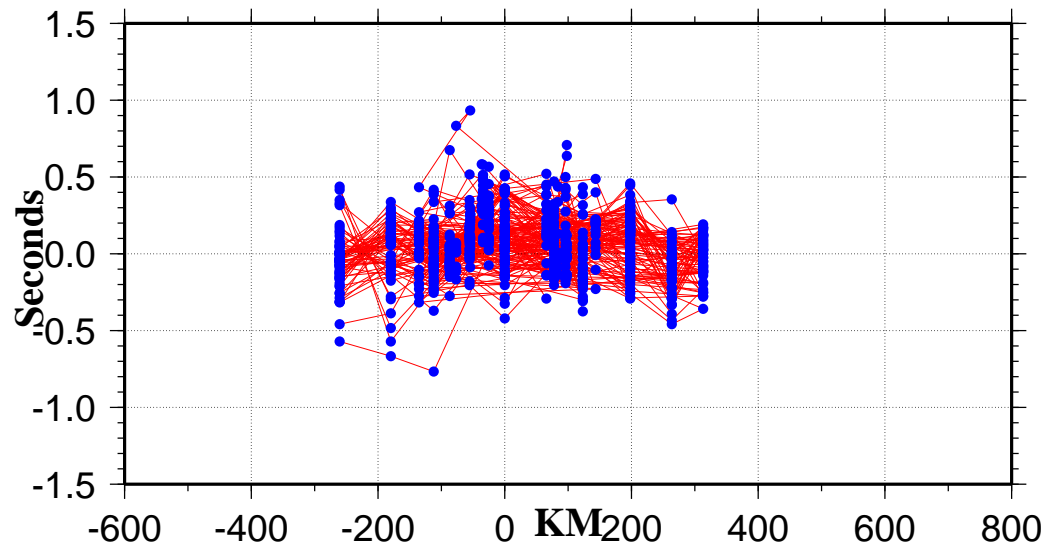
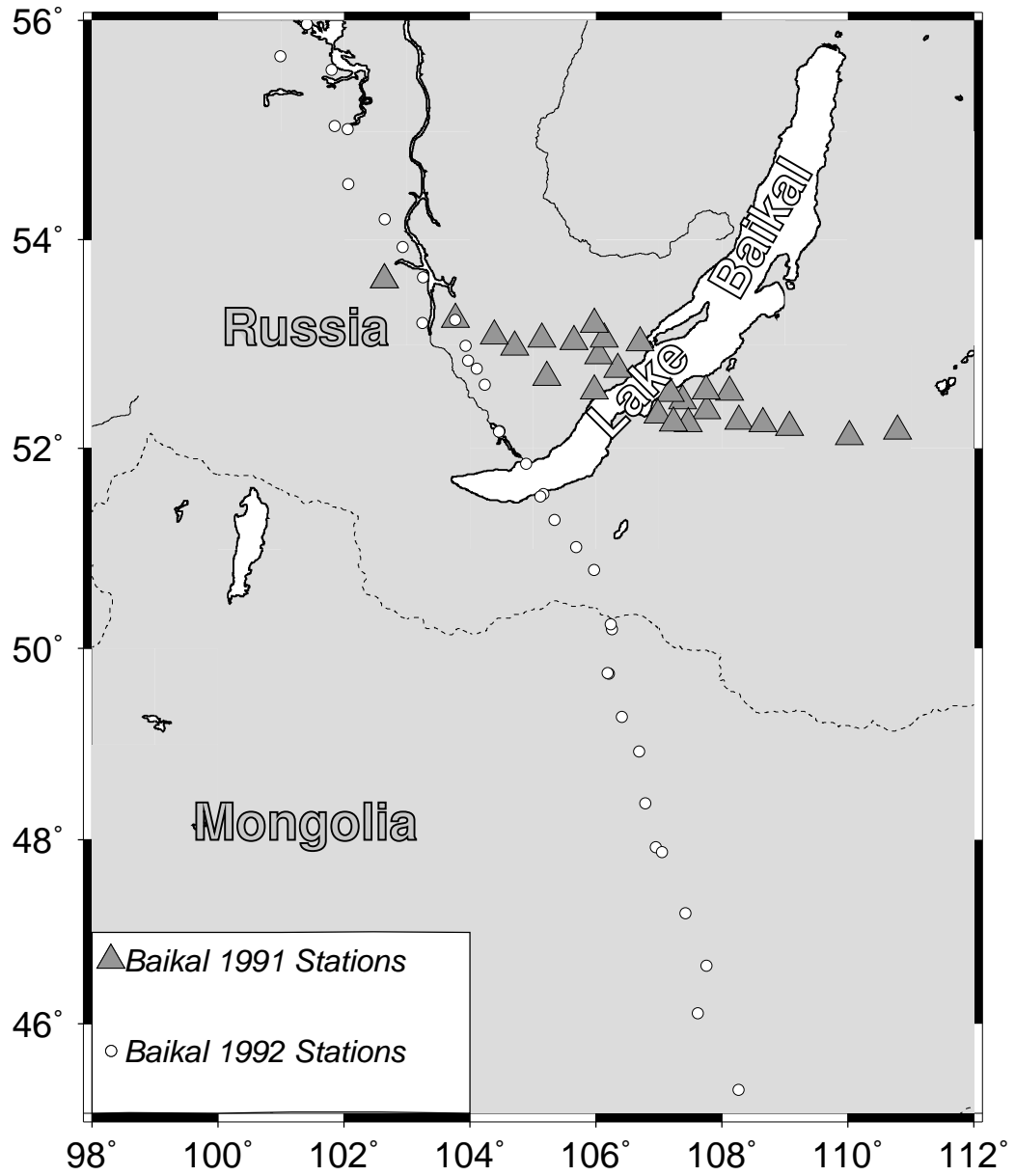
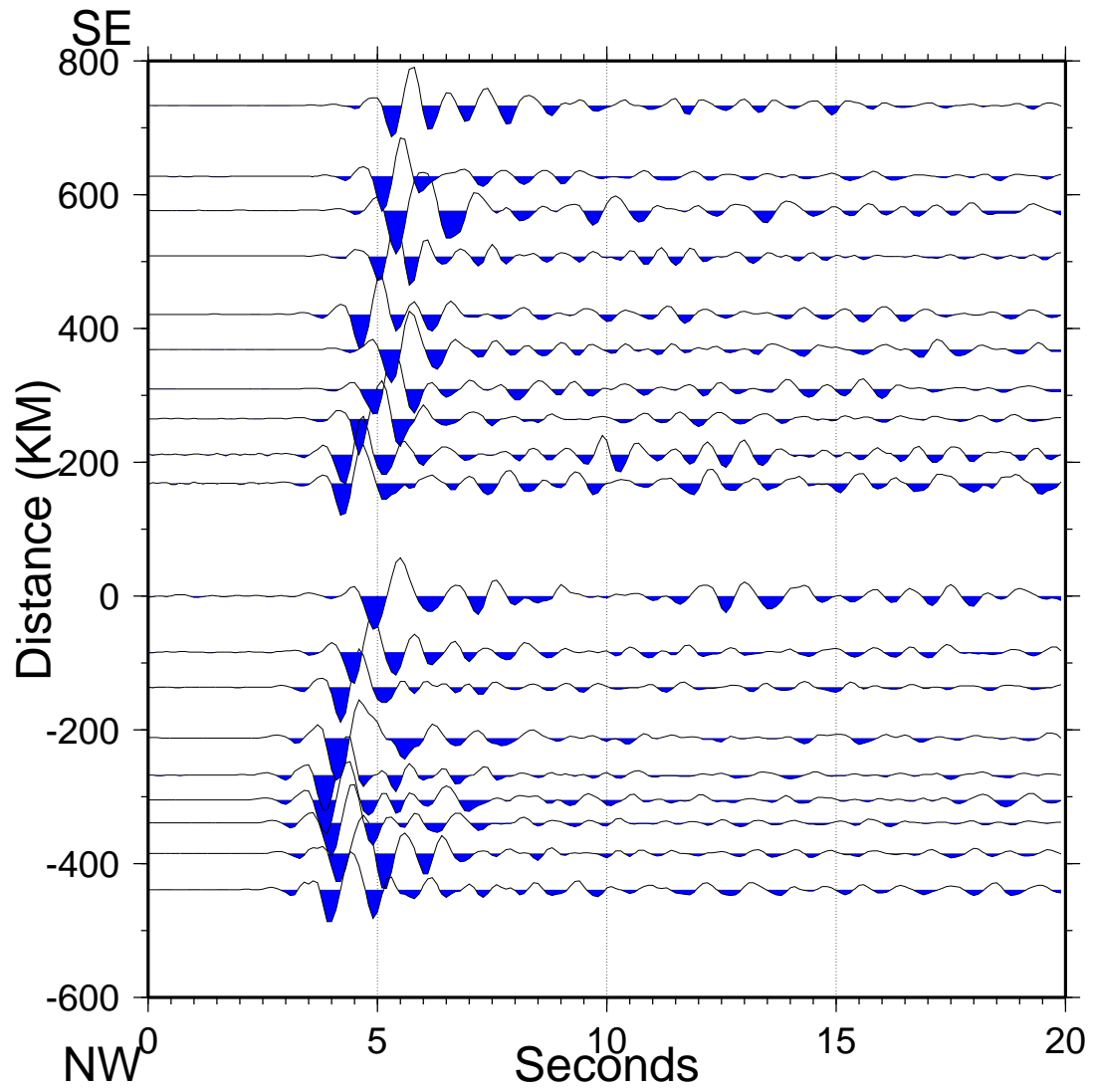


Figure 2.2.1 (B)



**Figure 2.2.2**



**Figure 2.2.3**

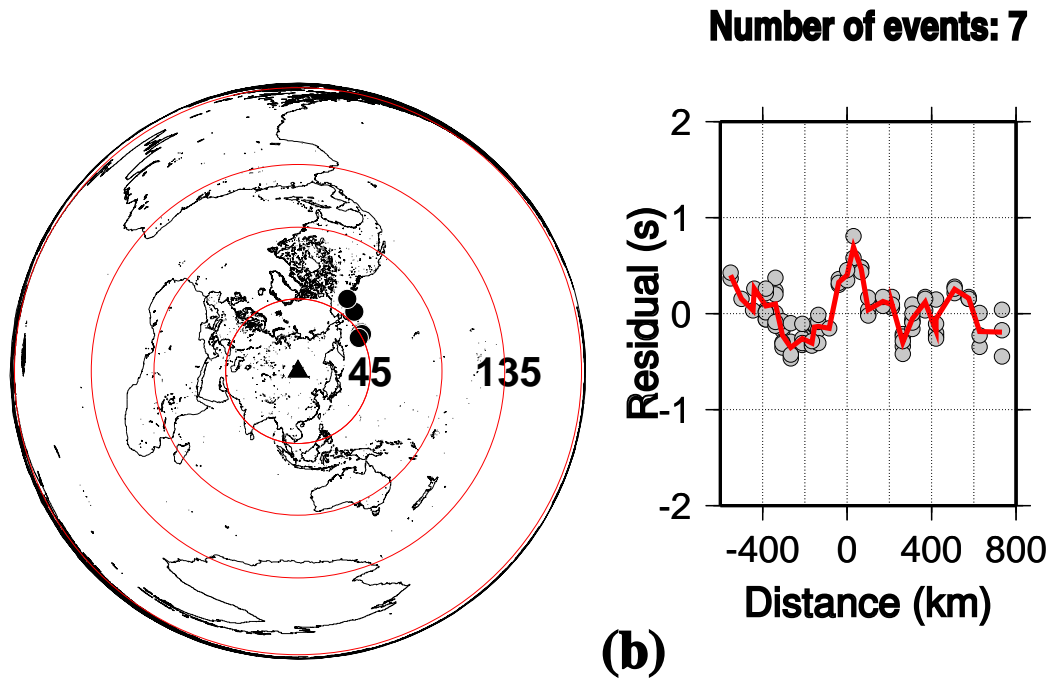
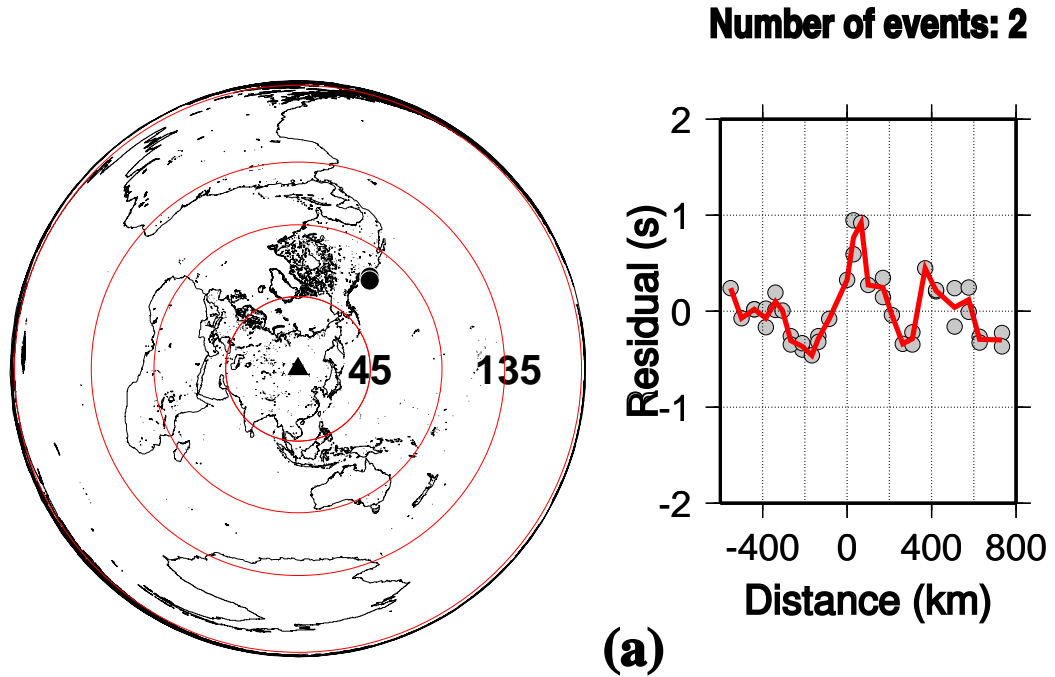


**Figure 2.2.4 (ab)**

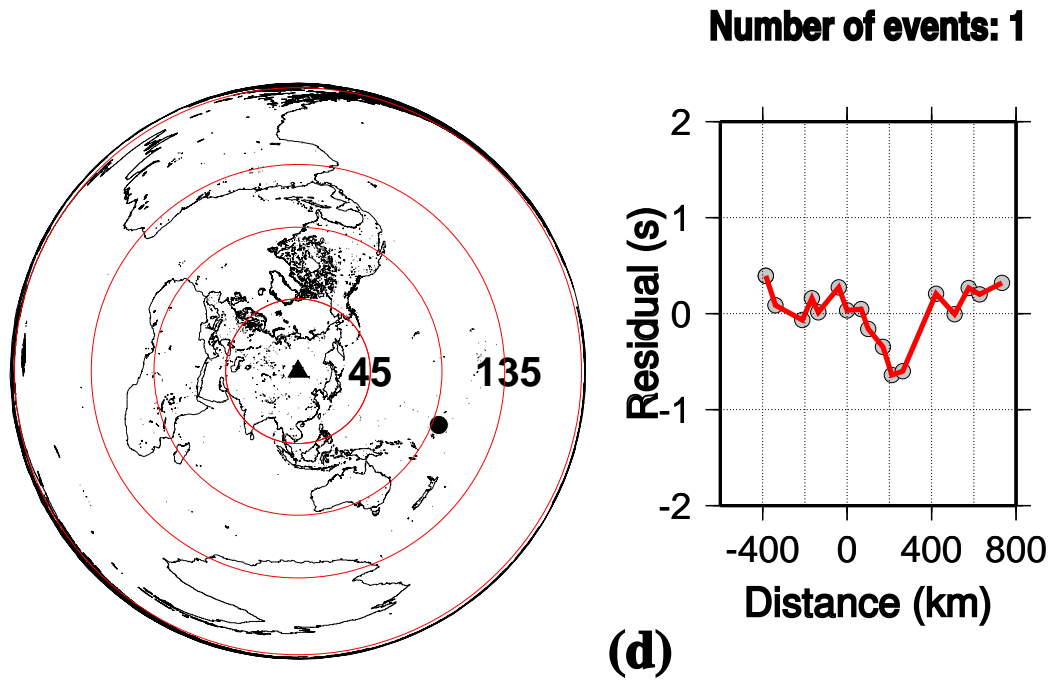
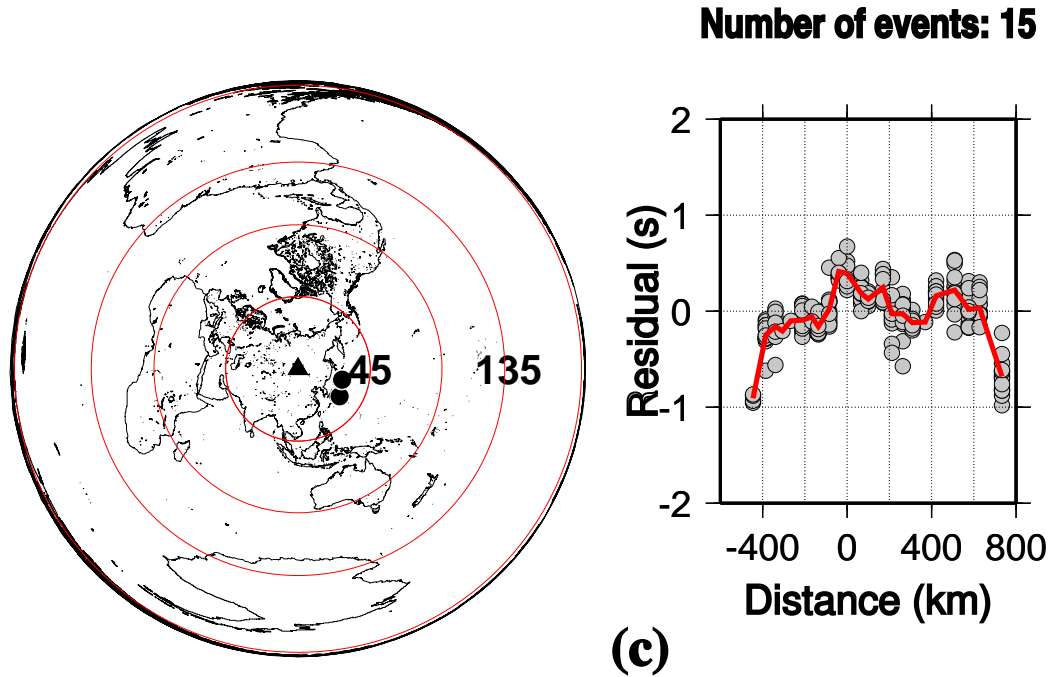
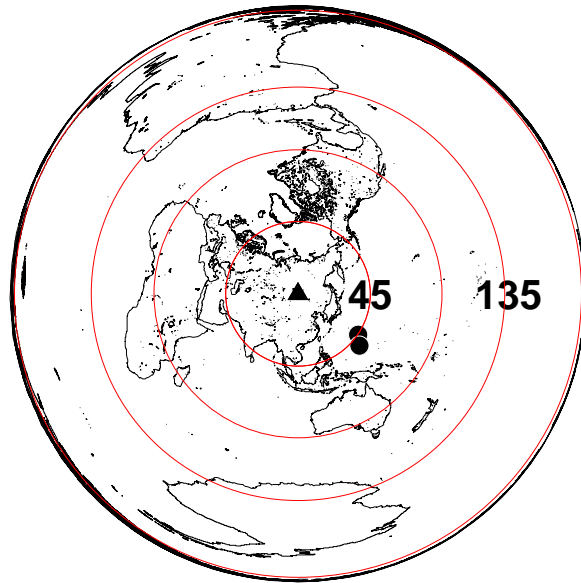
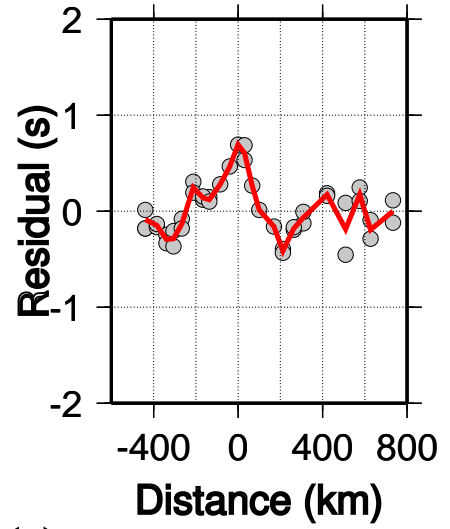


Figure 2.2.4 (cd)

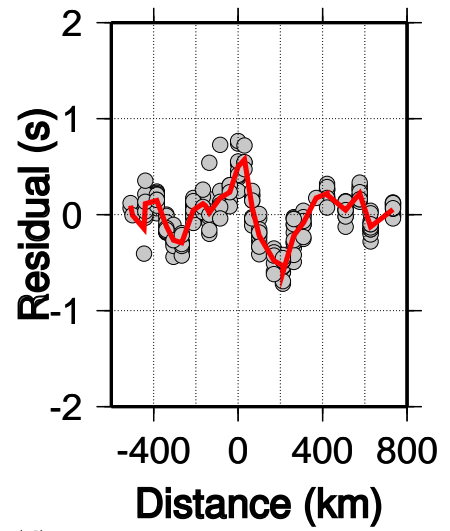
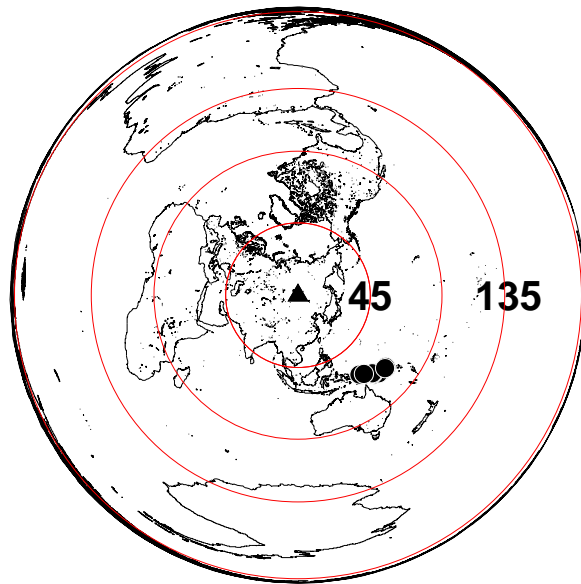


**Number of events: 2**



**(e)**

**Number of events: 13**



**(f)**

**Figure 2.2.4 (ef)**

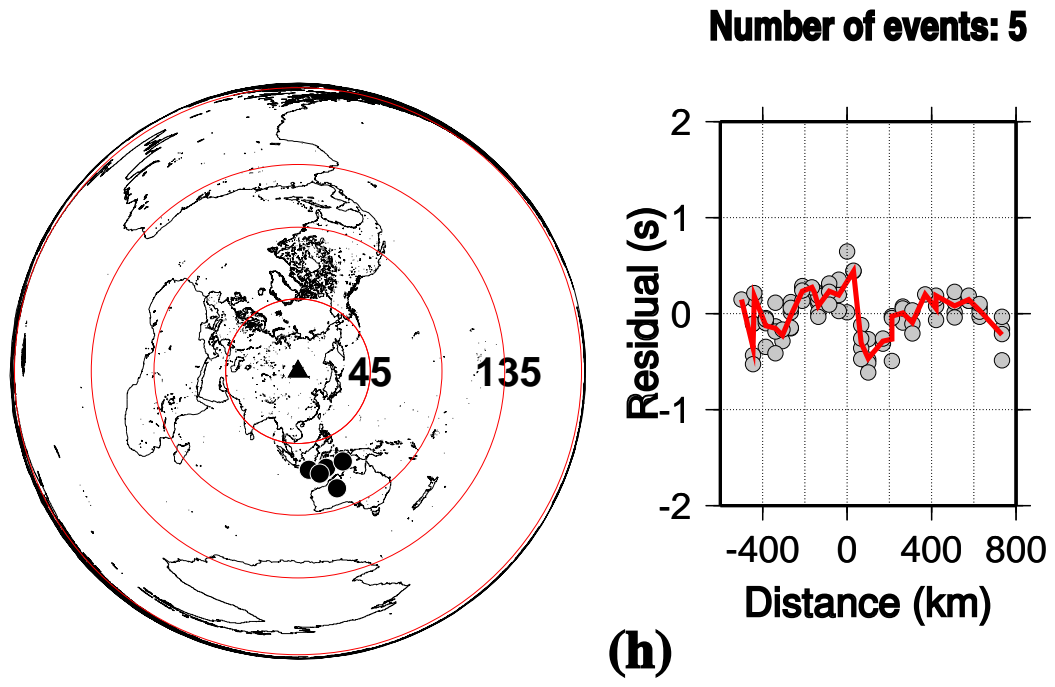
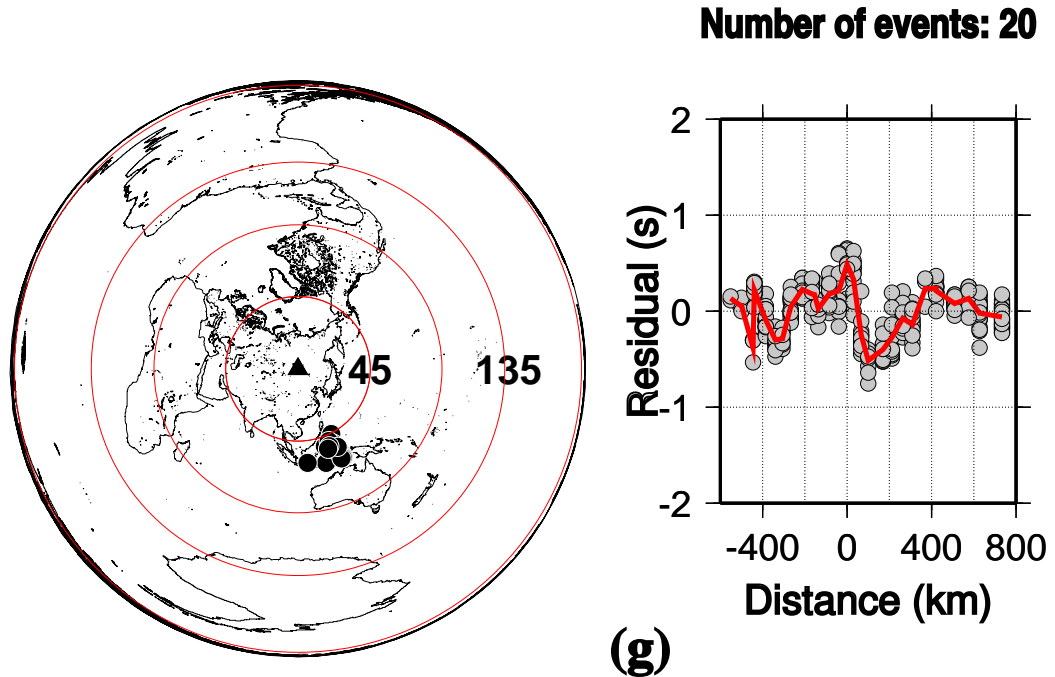
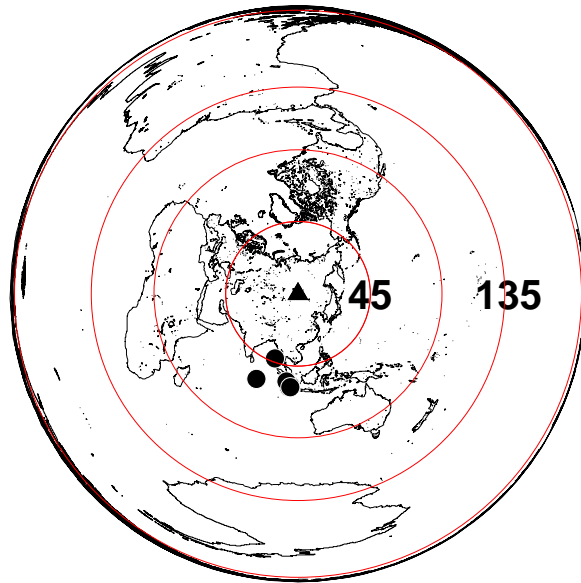
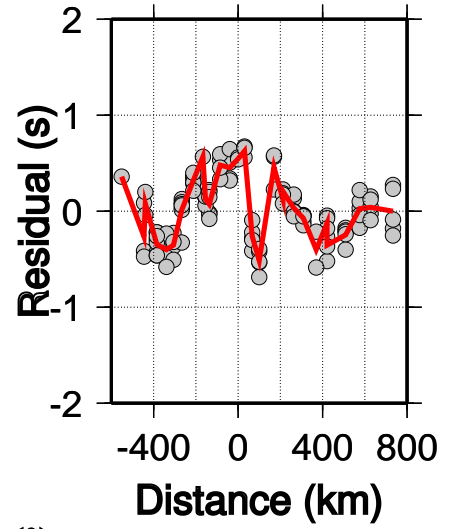


**Figure 2.2.4 (gh)**

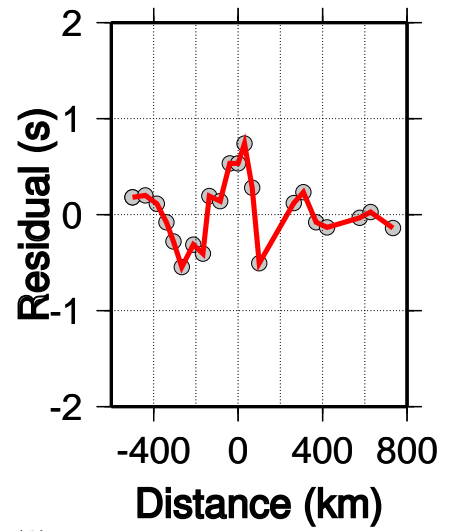
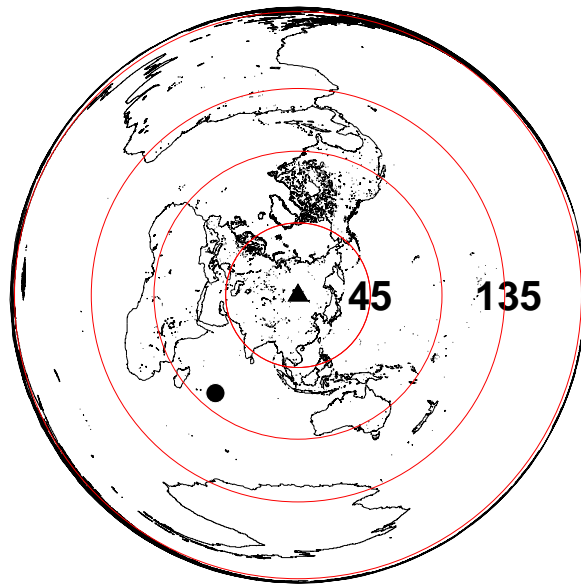


**Number of events: 7**



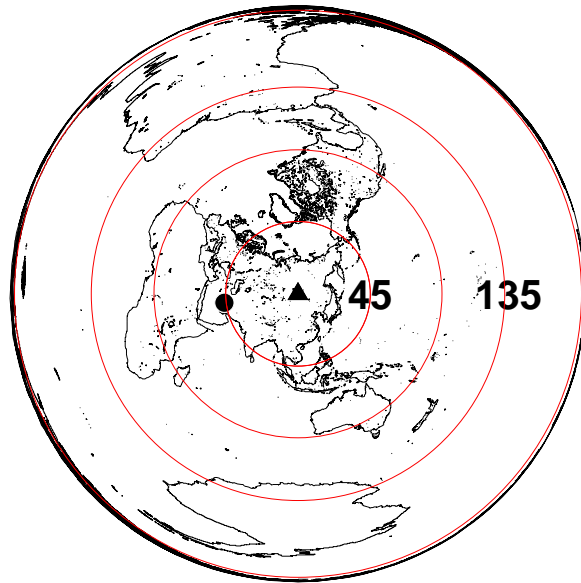
**(i)**

**Number of events: 1**

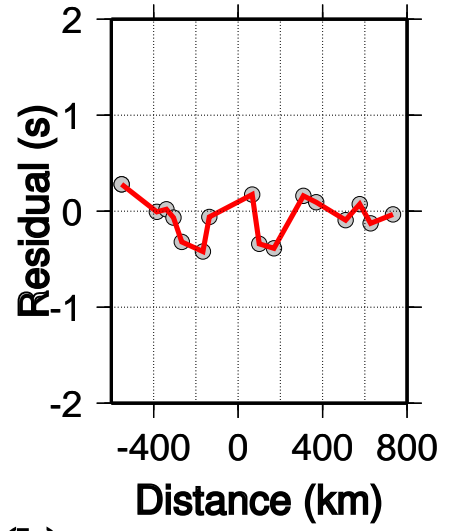


**(j)**

**Figure 2.2.4 (ij)**

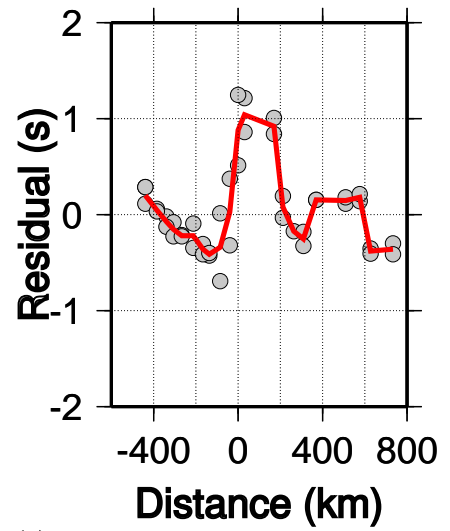
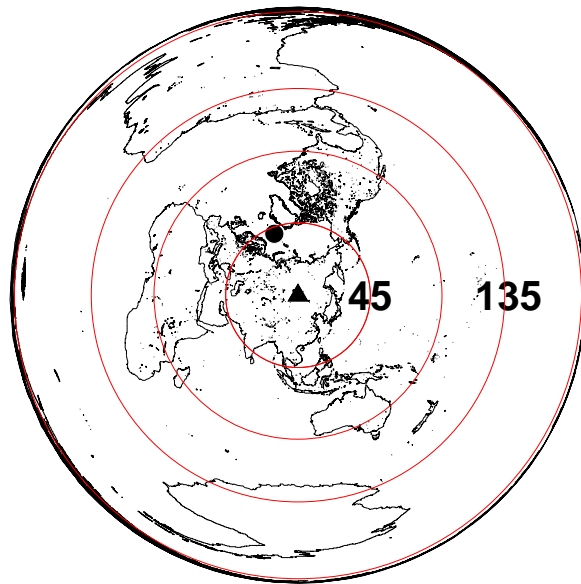


**Number of events: 1**



**(k)**

**Number of events: 2**



**(l)**

**Figure 2.2.4 (kl)**

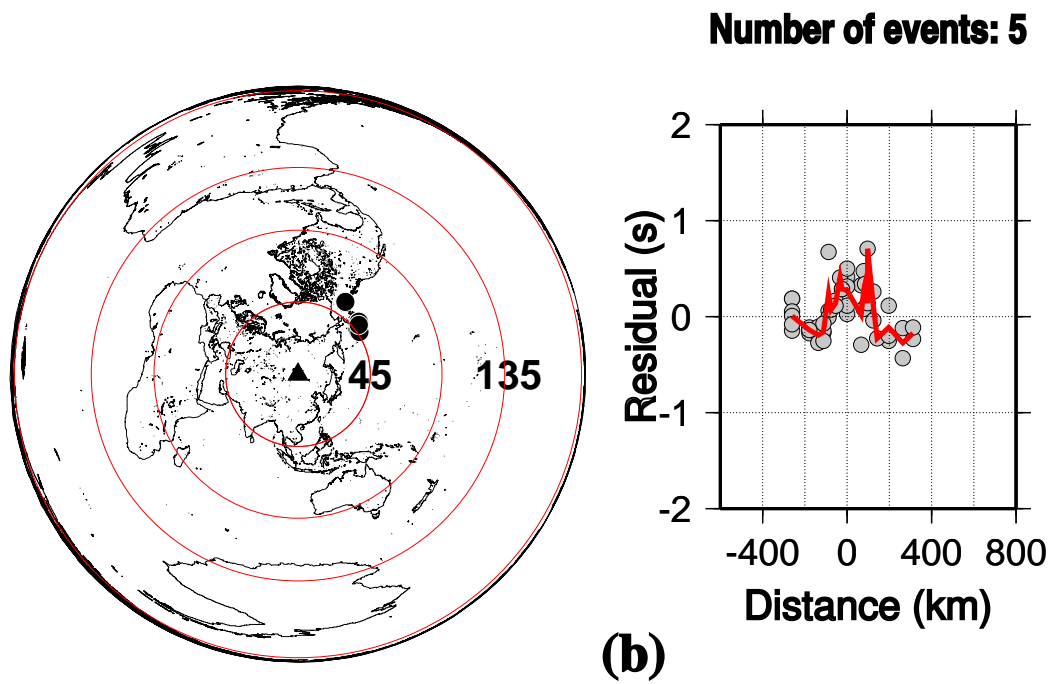
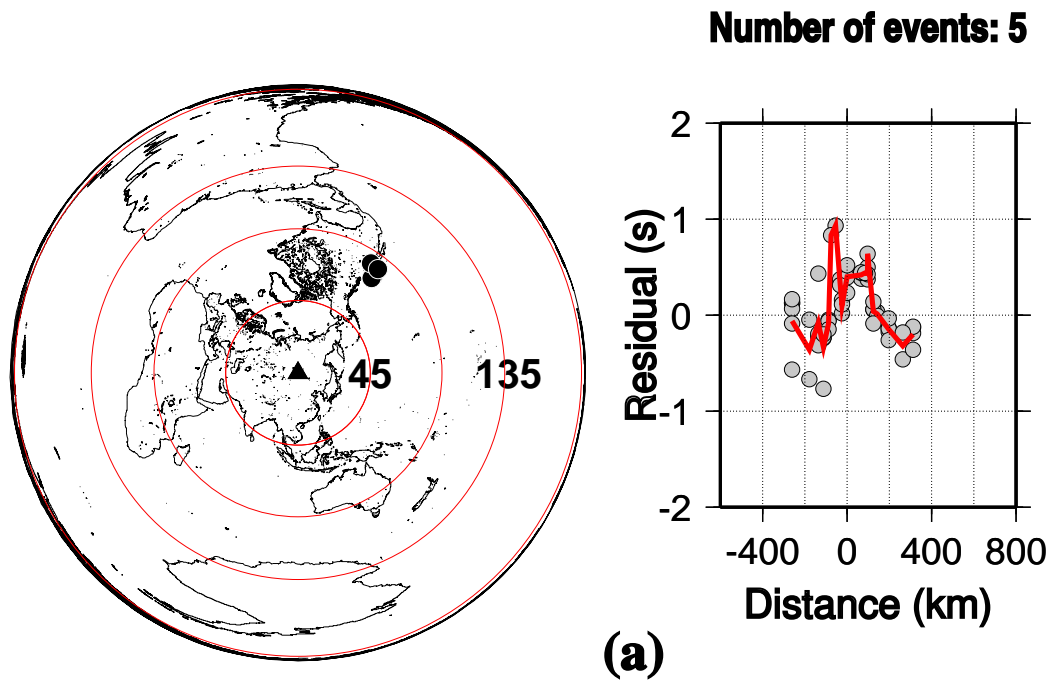


Figure 2.2.5 (ab)

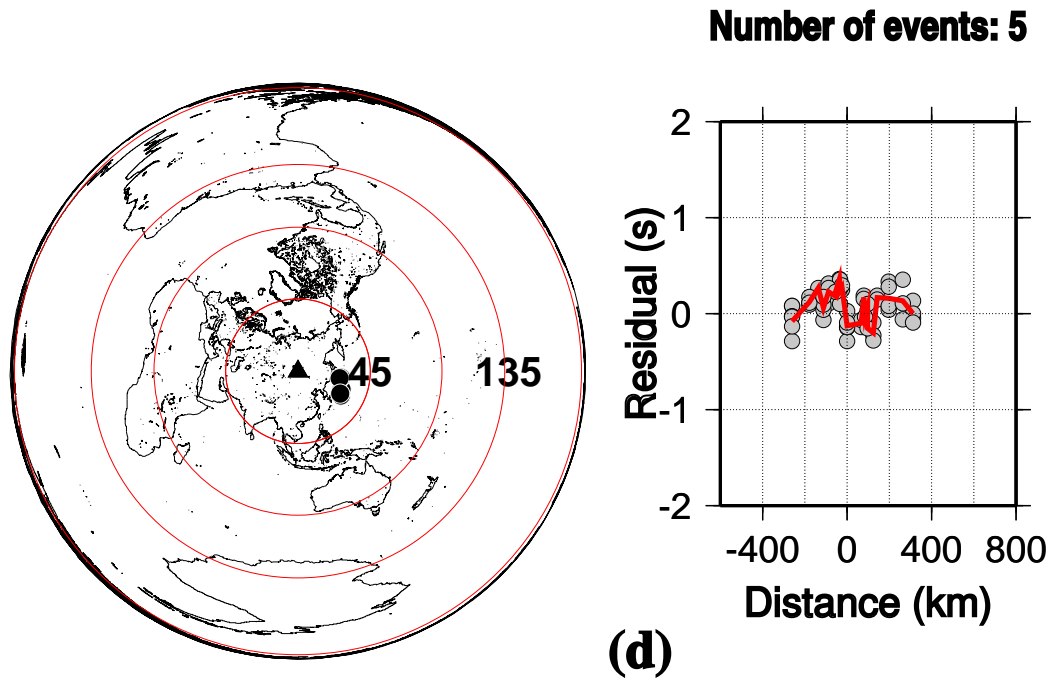
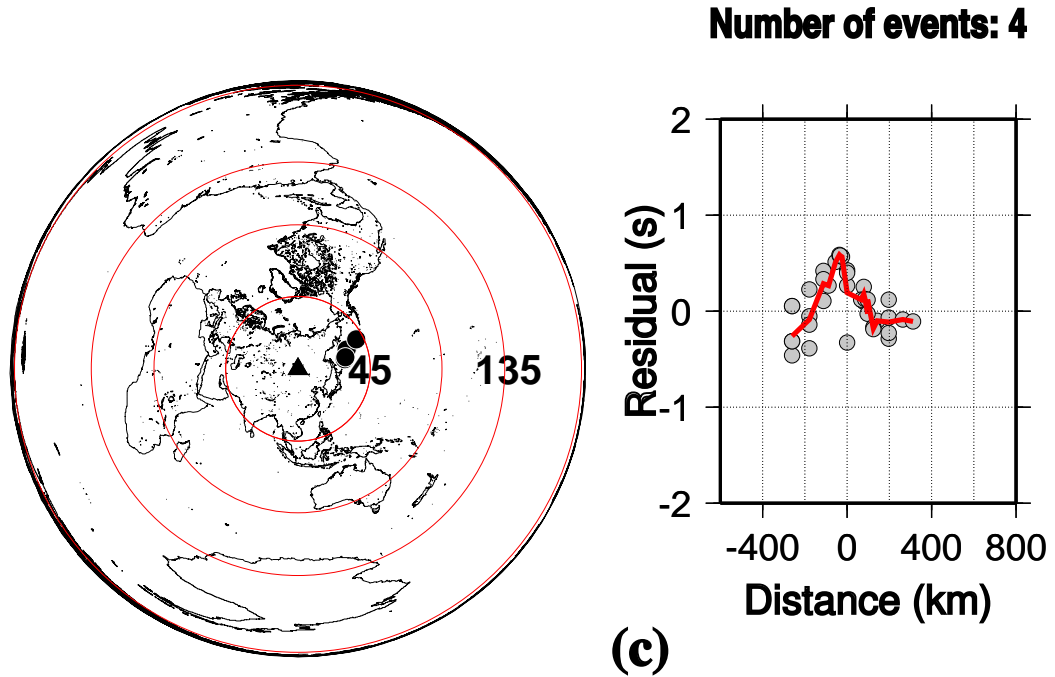
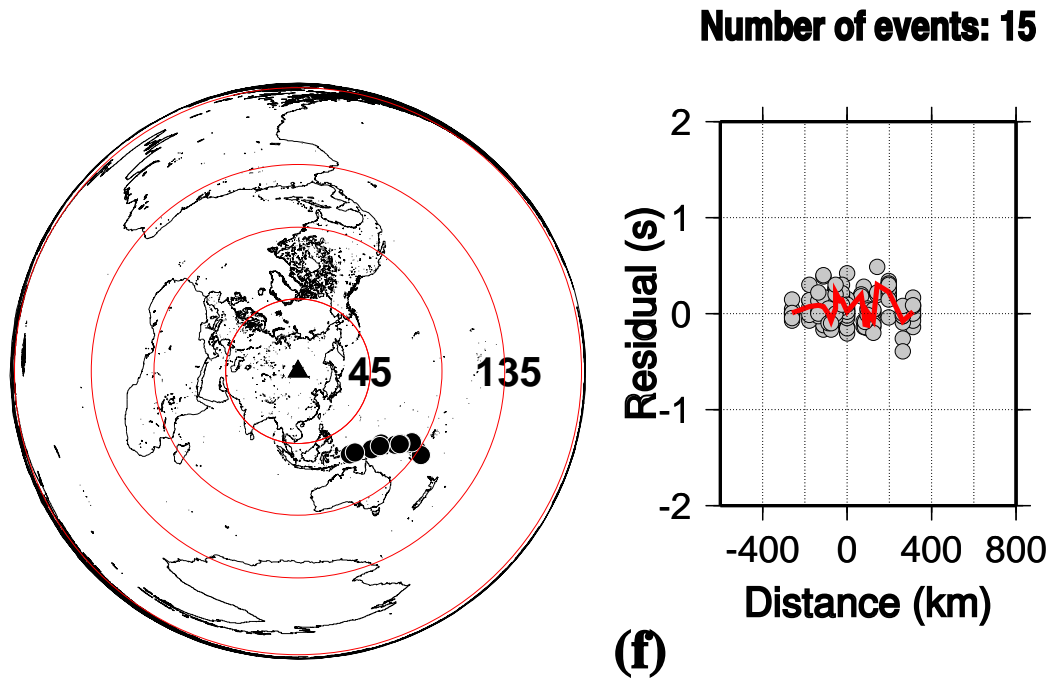
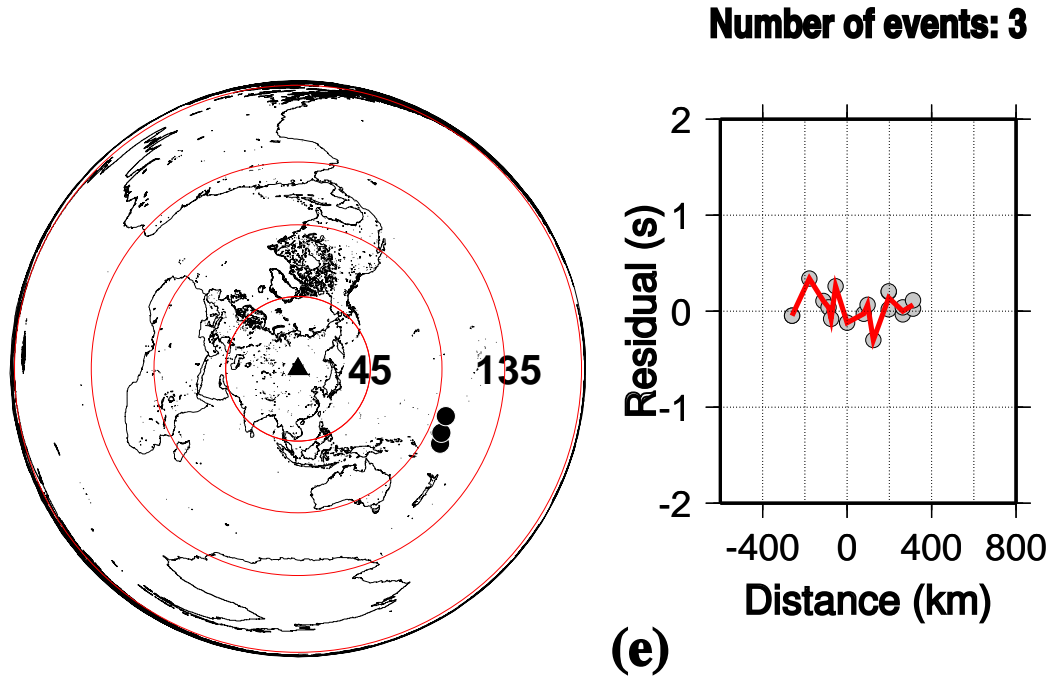


Figure 2.2.5 (cd)



**Figure 2.2.5 (ef)**

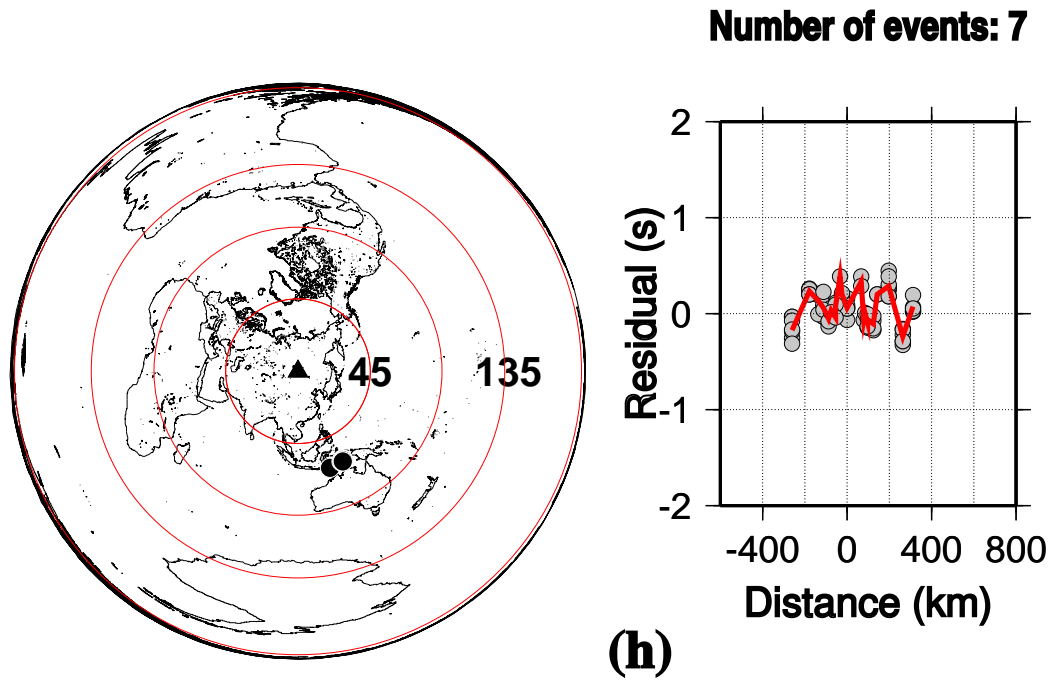
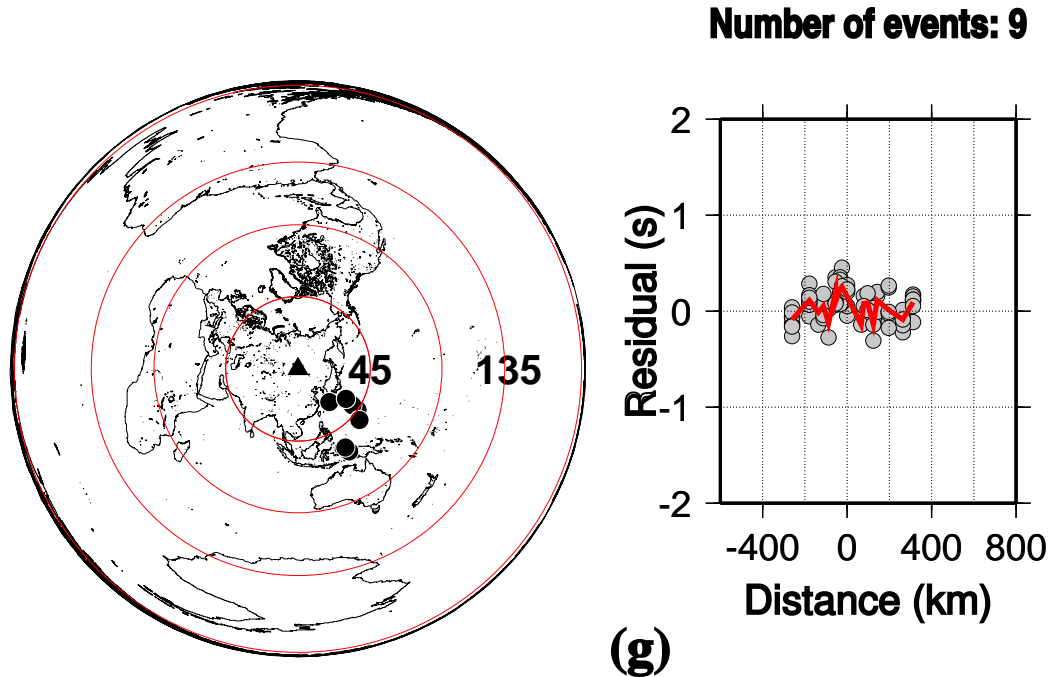
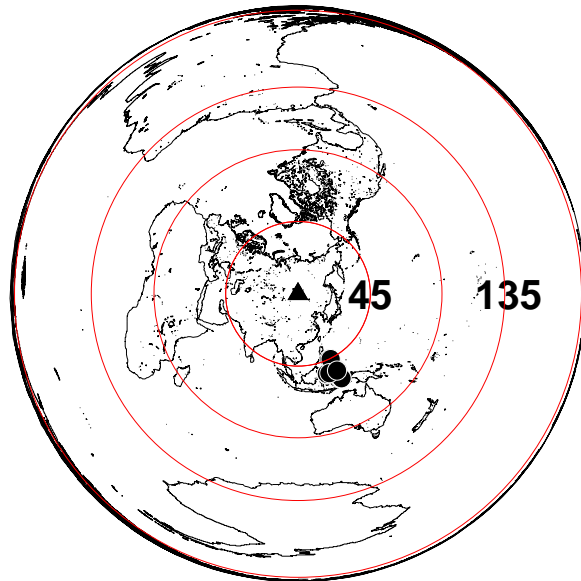
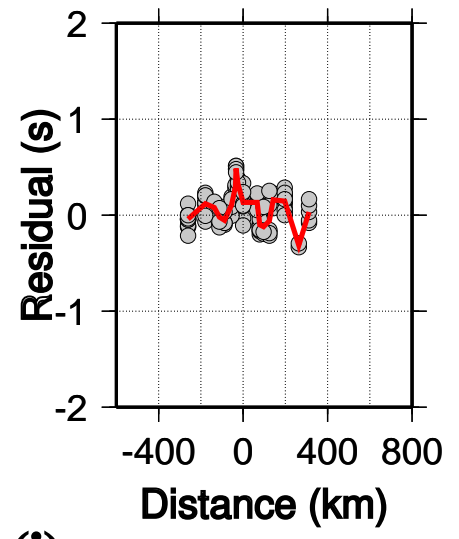


Figure 2.2.5 (gh)

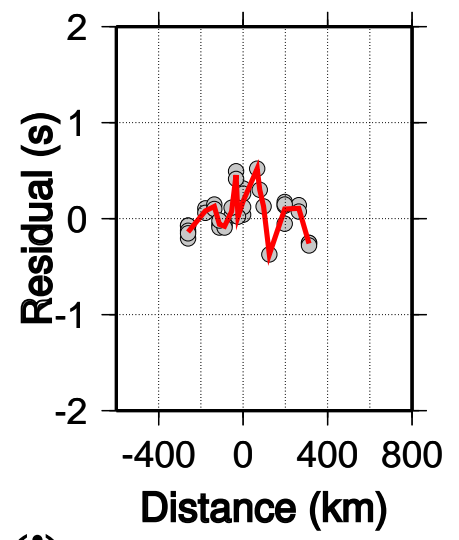
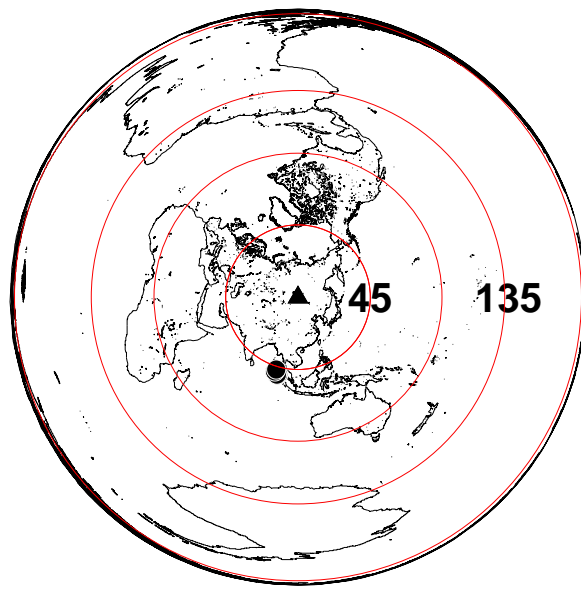


**Number of events: 15**



**(i)**

**Number of events: 4**



**(j)**

**Figure 2.2.5 (ij)**

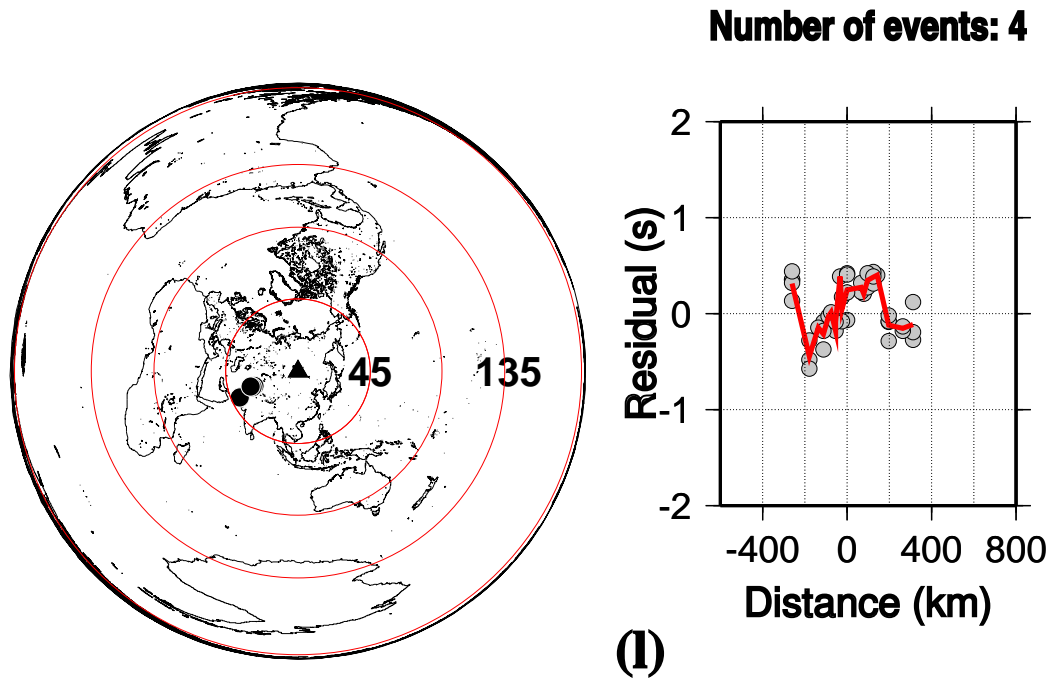
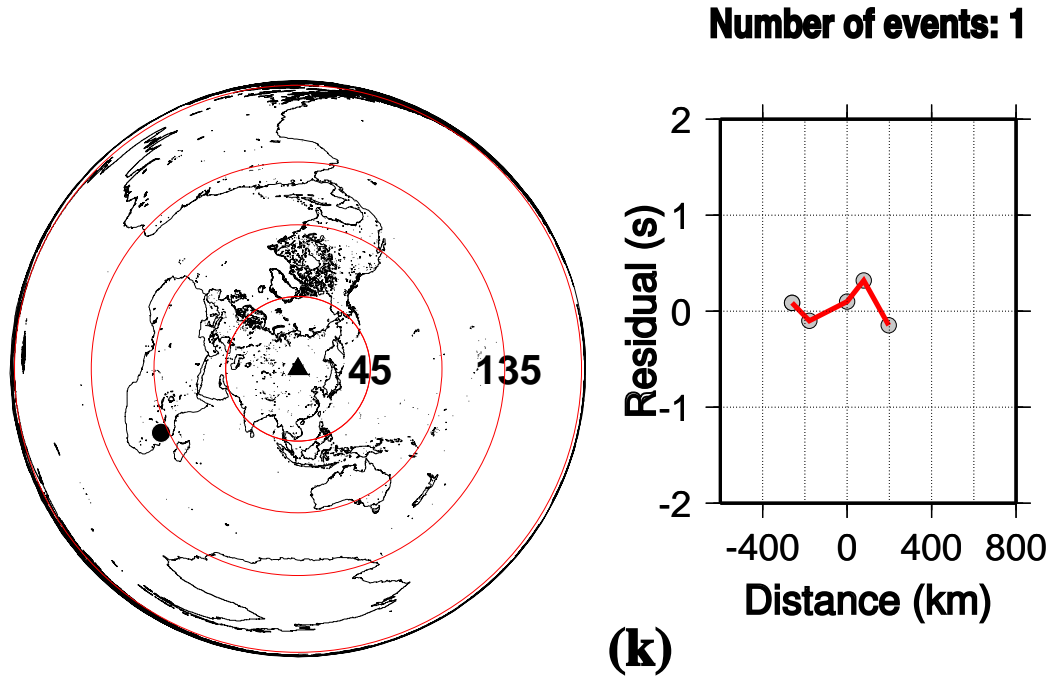


**Figure 2.2.5 (kl)**

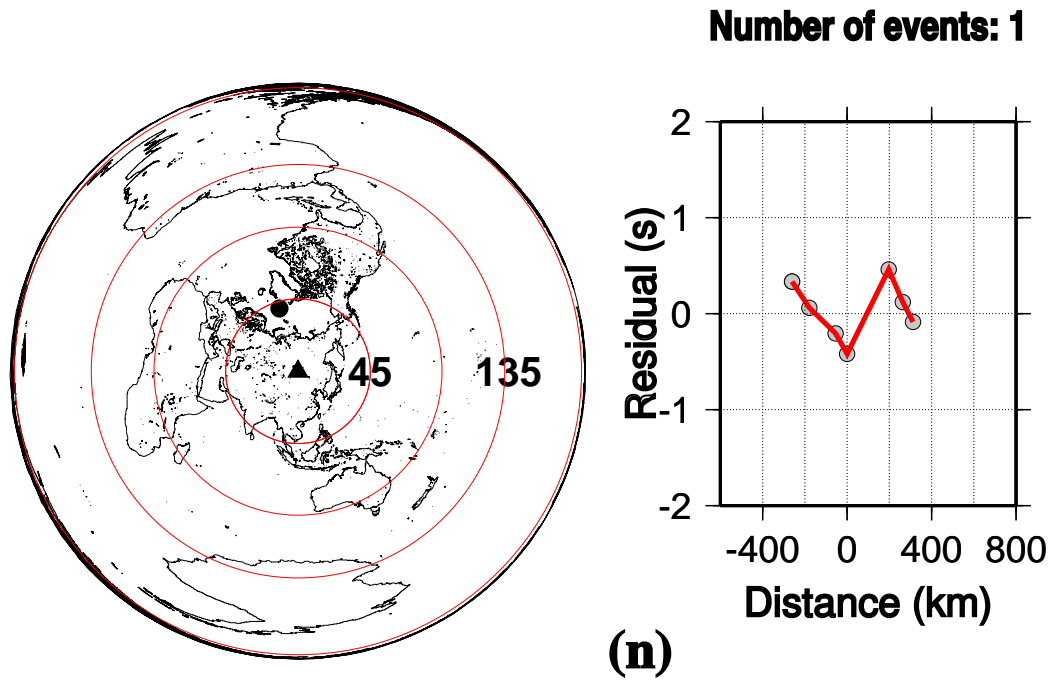
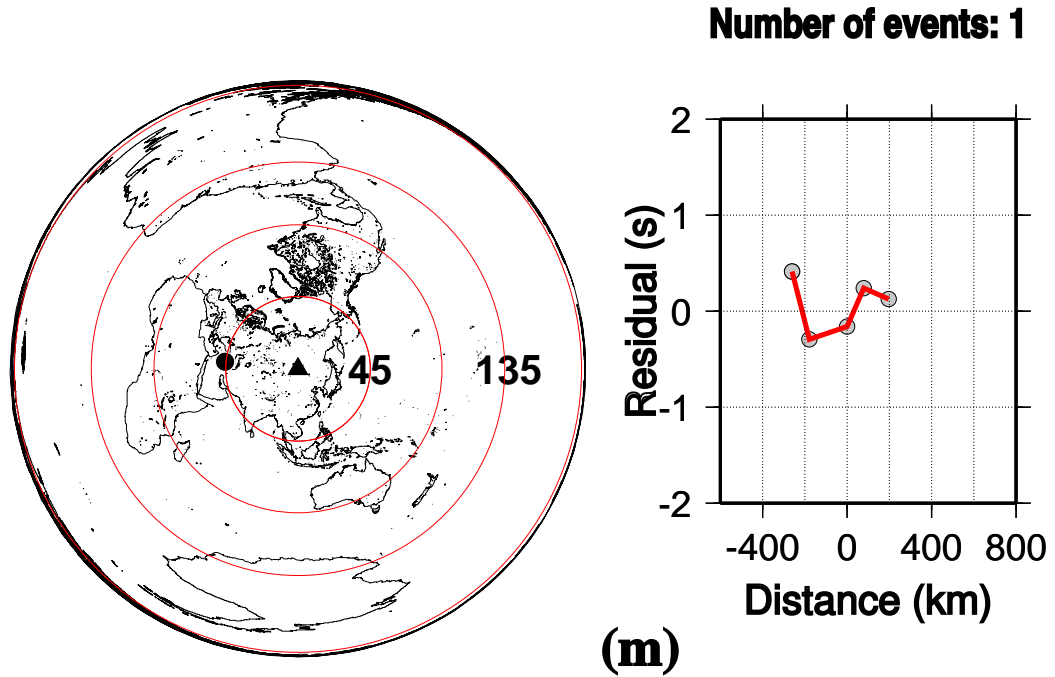


**Figure 2.2.5 (mn)**

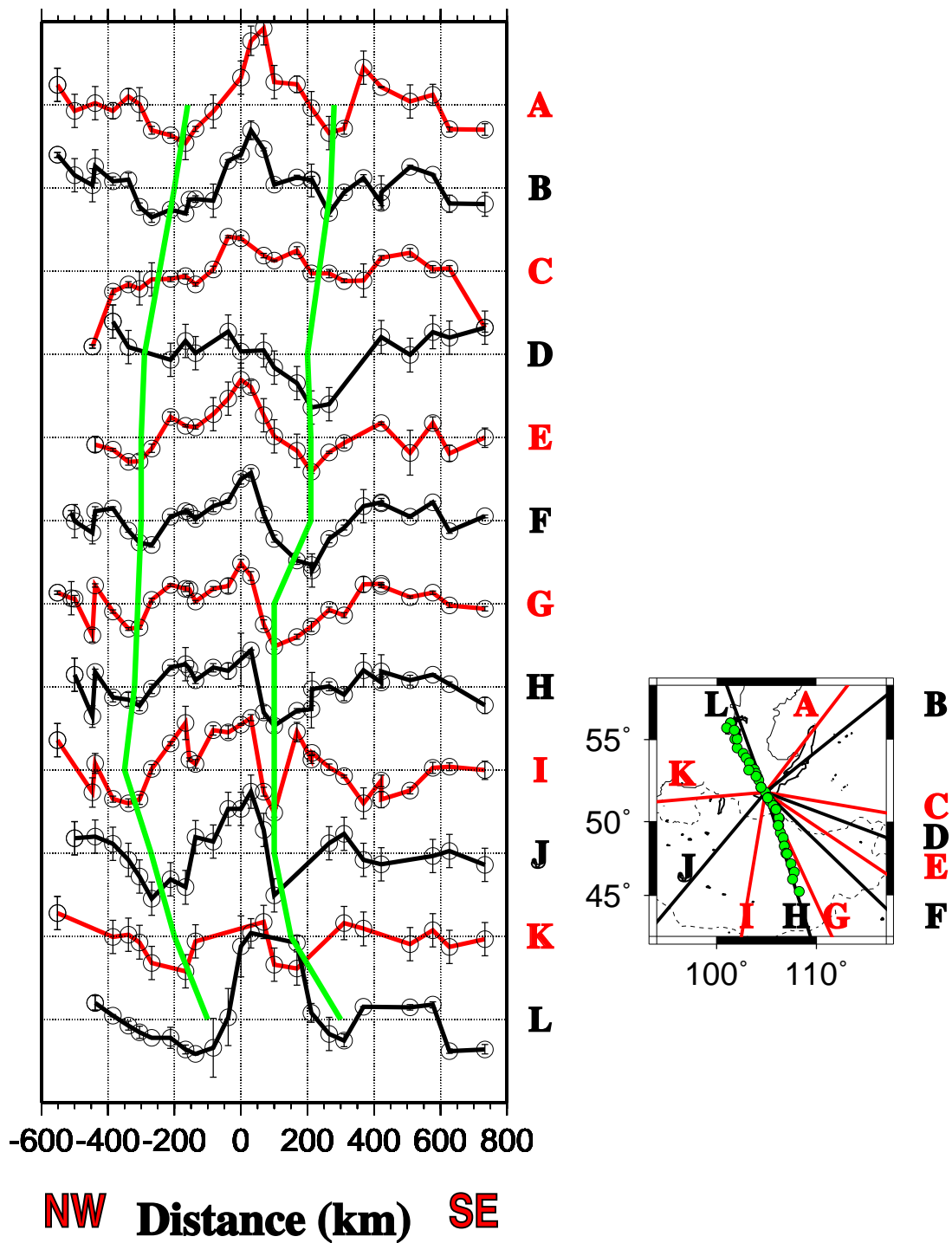


Figure 2.2.6

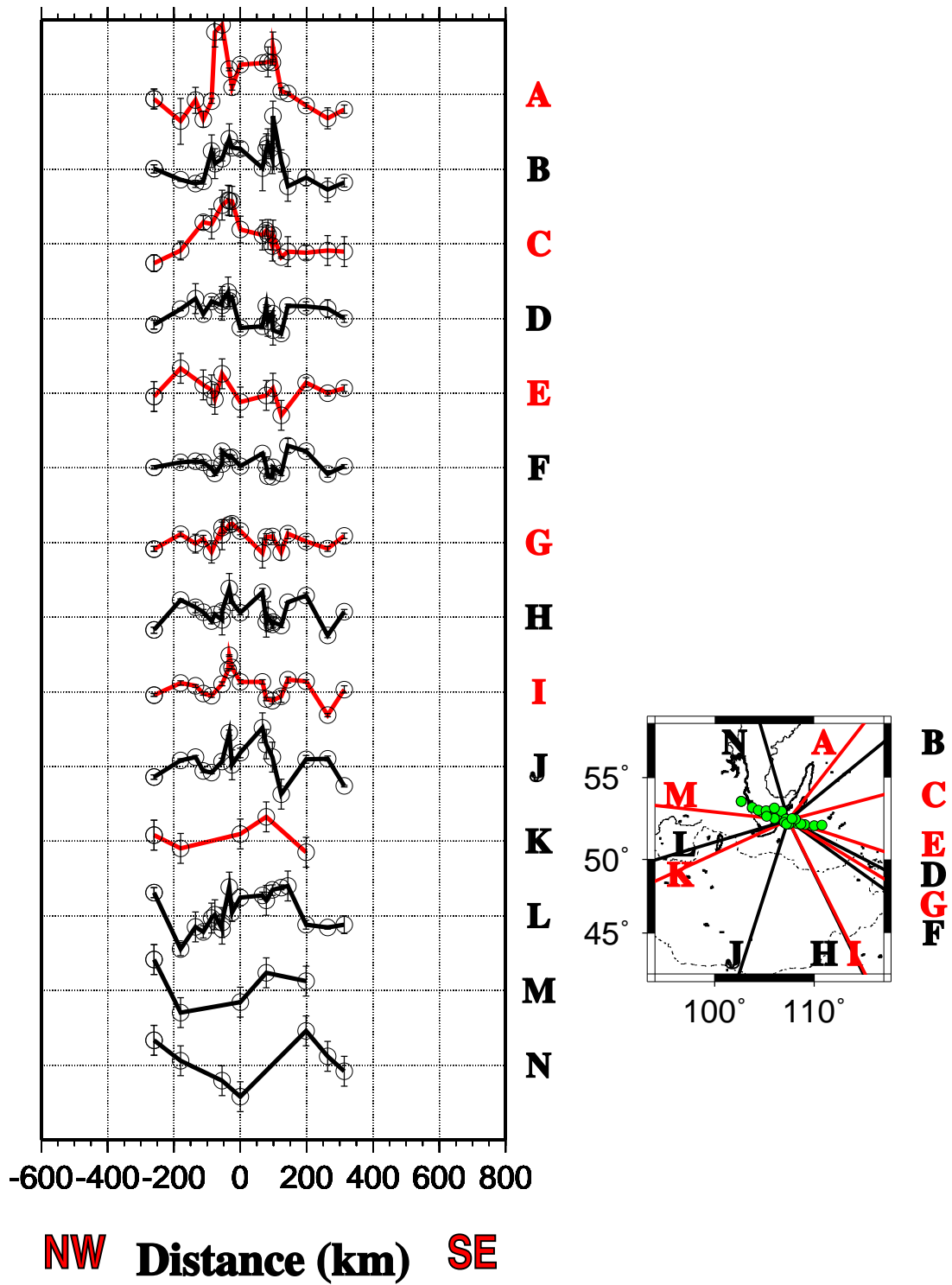


Figure 2.2.7

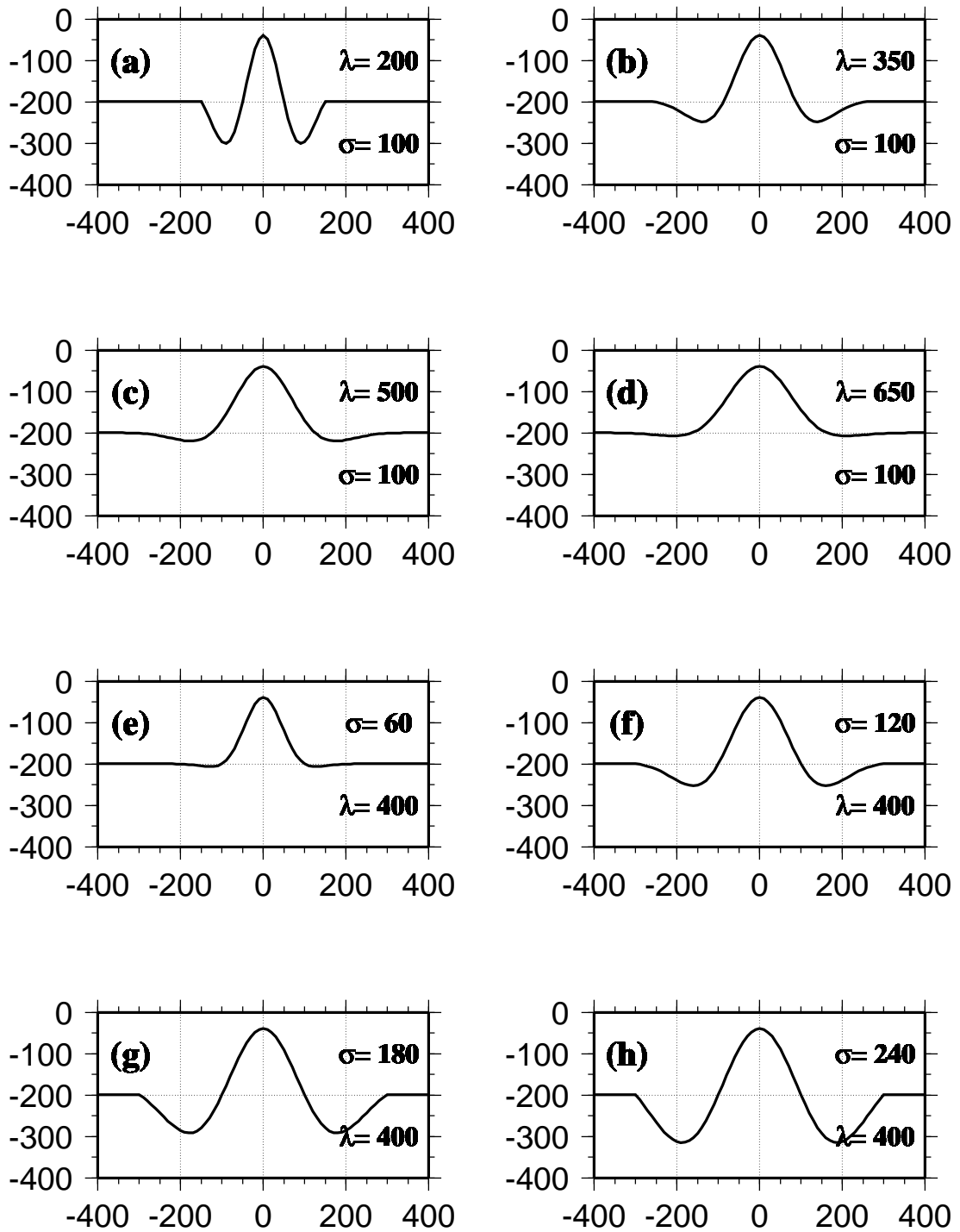


Figure 2.3.1

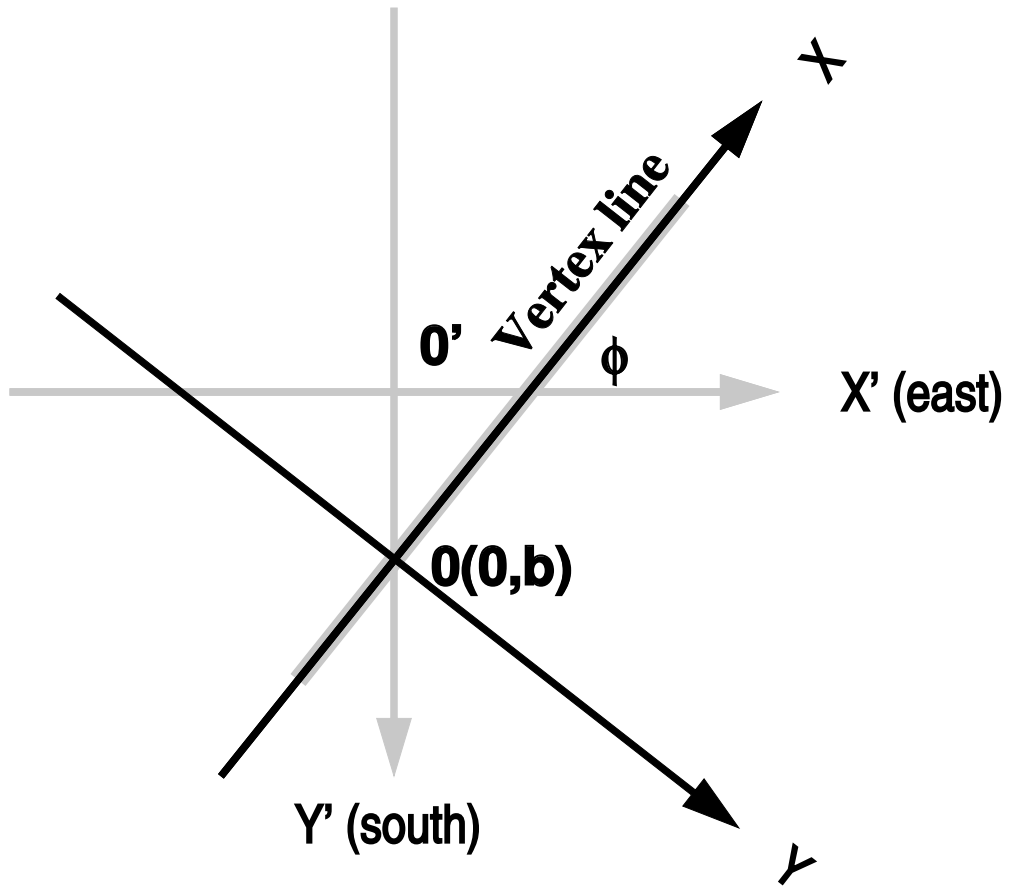
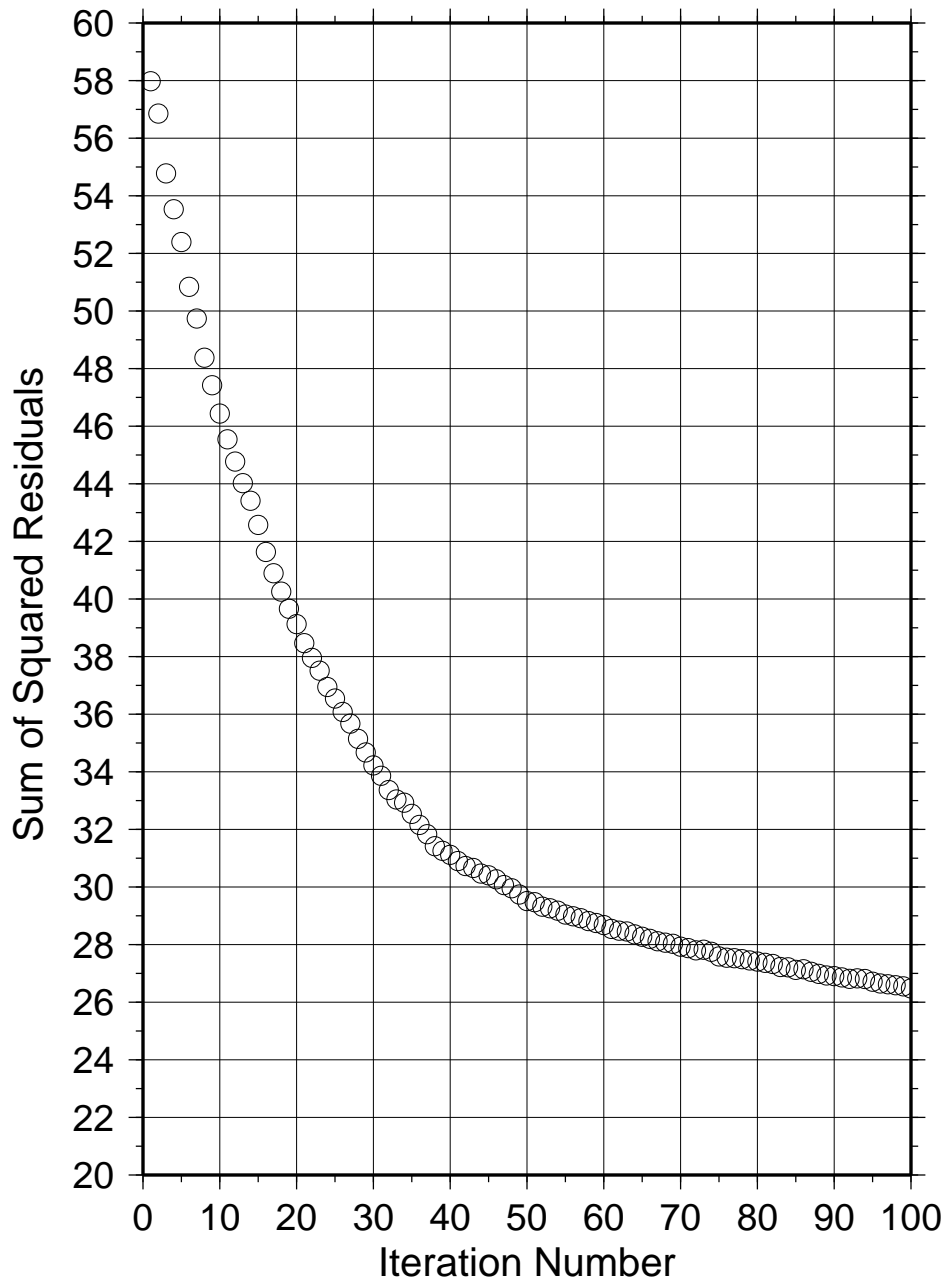


Figure 2.3.2



**Figure 2.5.1**

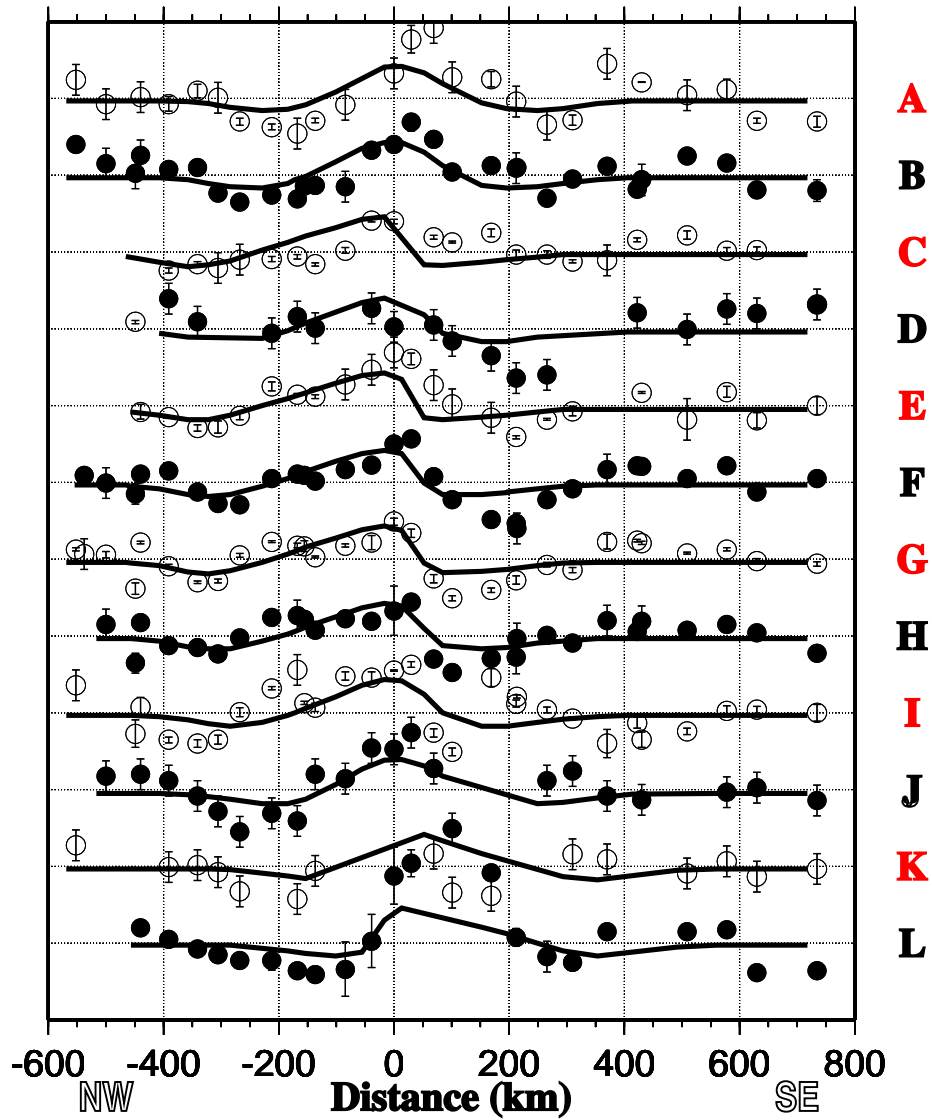
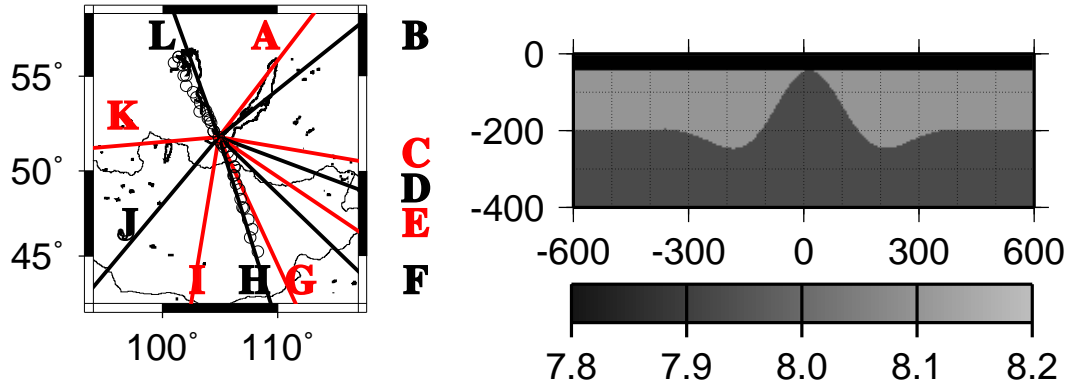


Figure 2.5.2 (a)

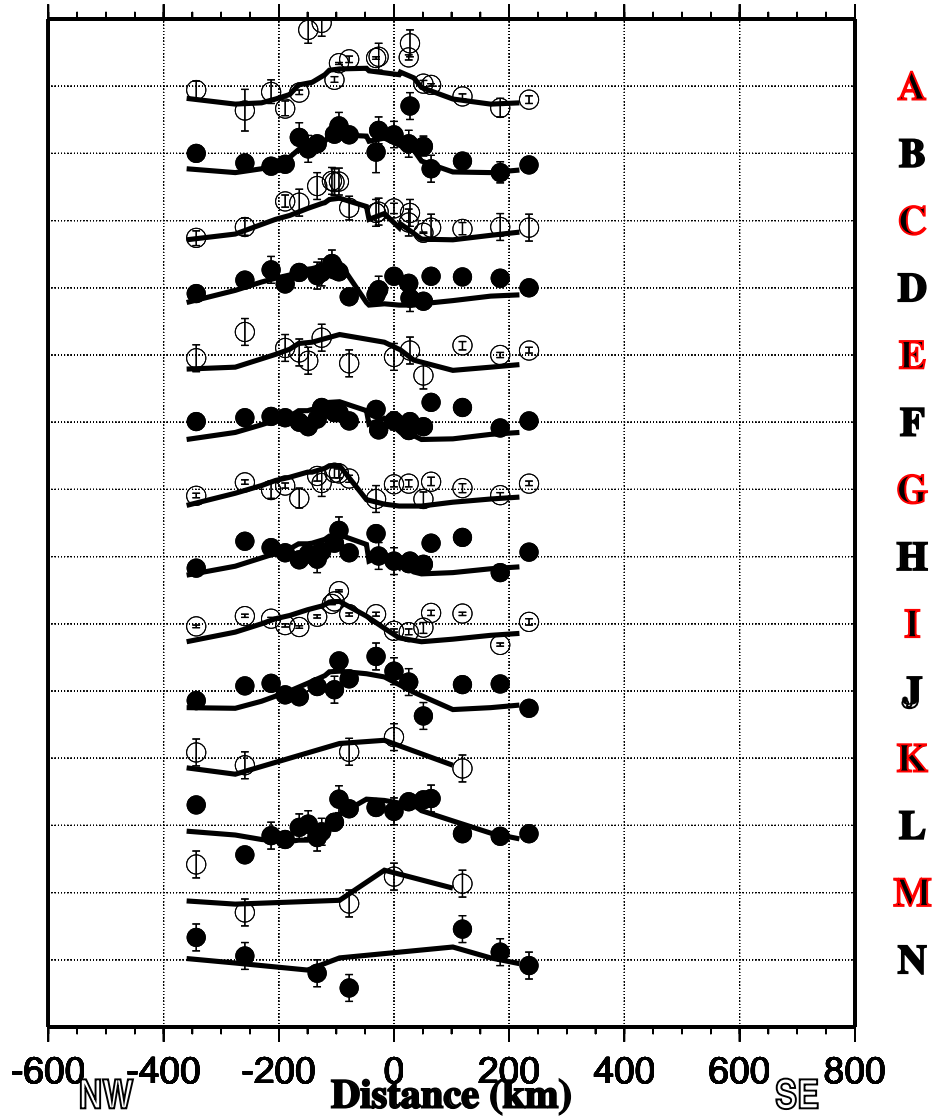
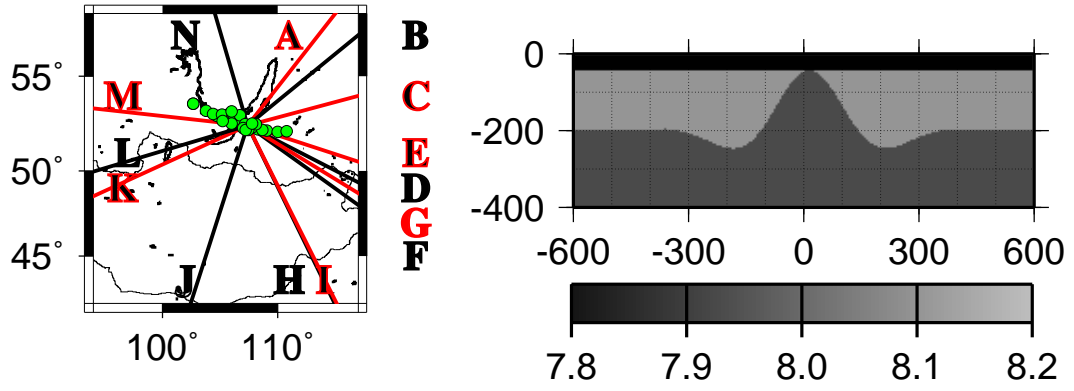


Figure 2.5.2 (b)

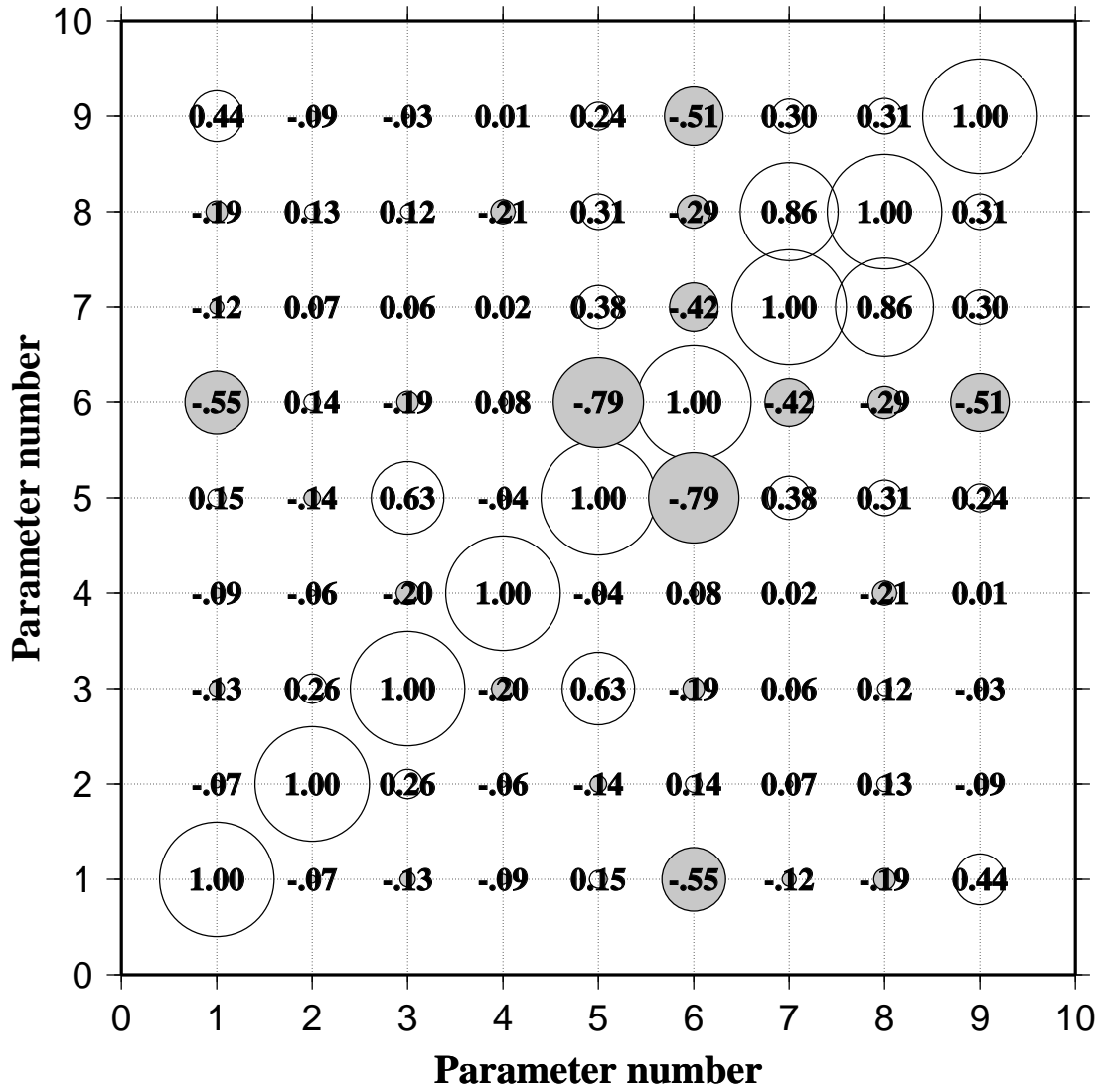
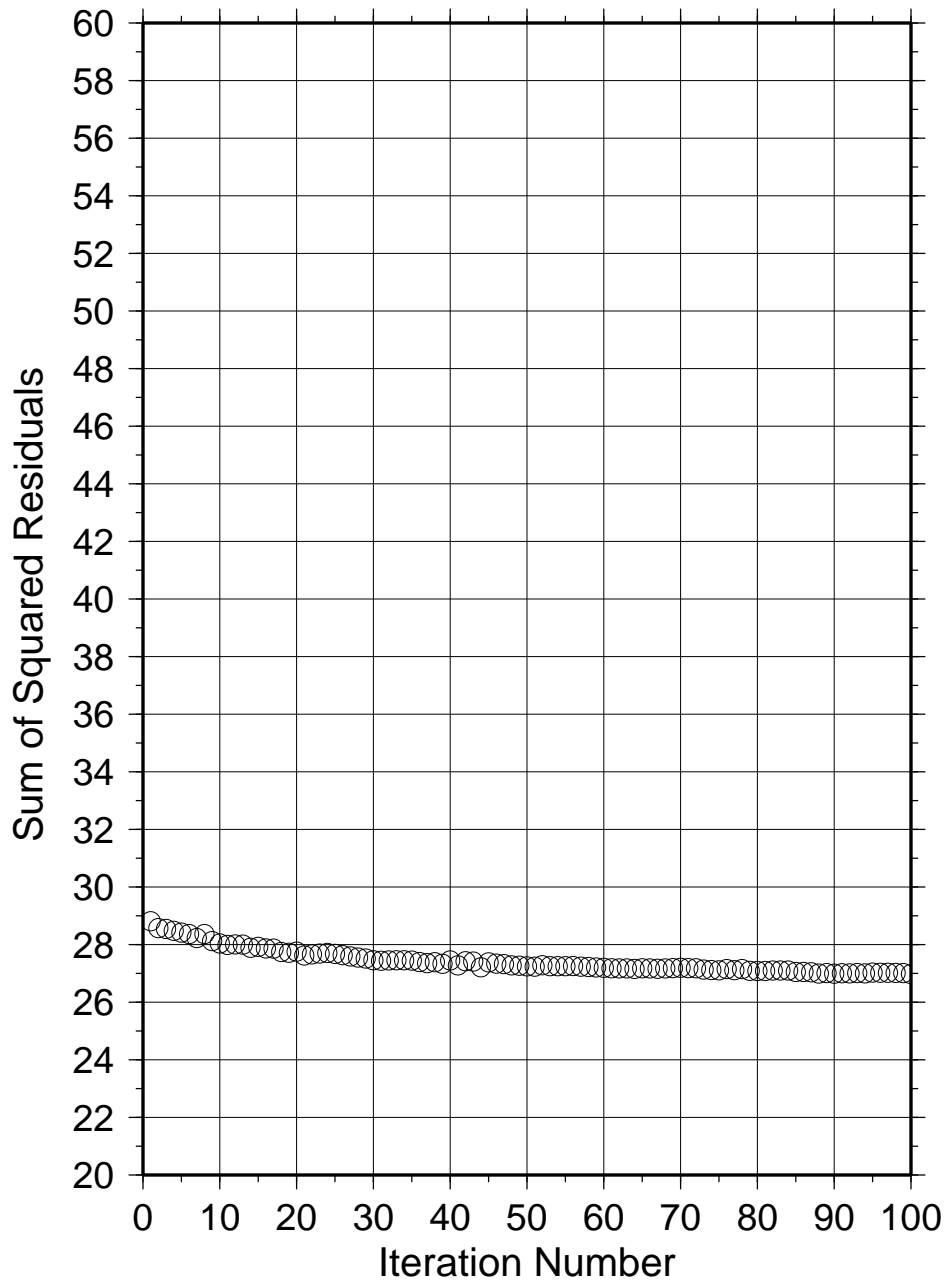


Figure 2.5.3



**Figure 2.5.4**

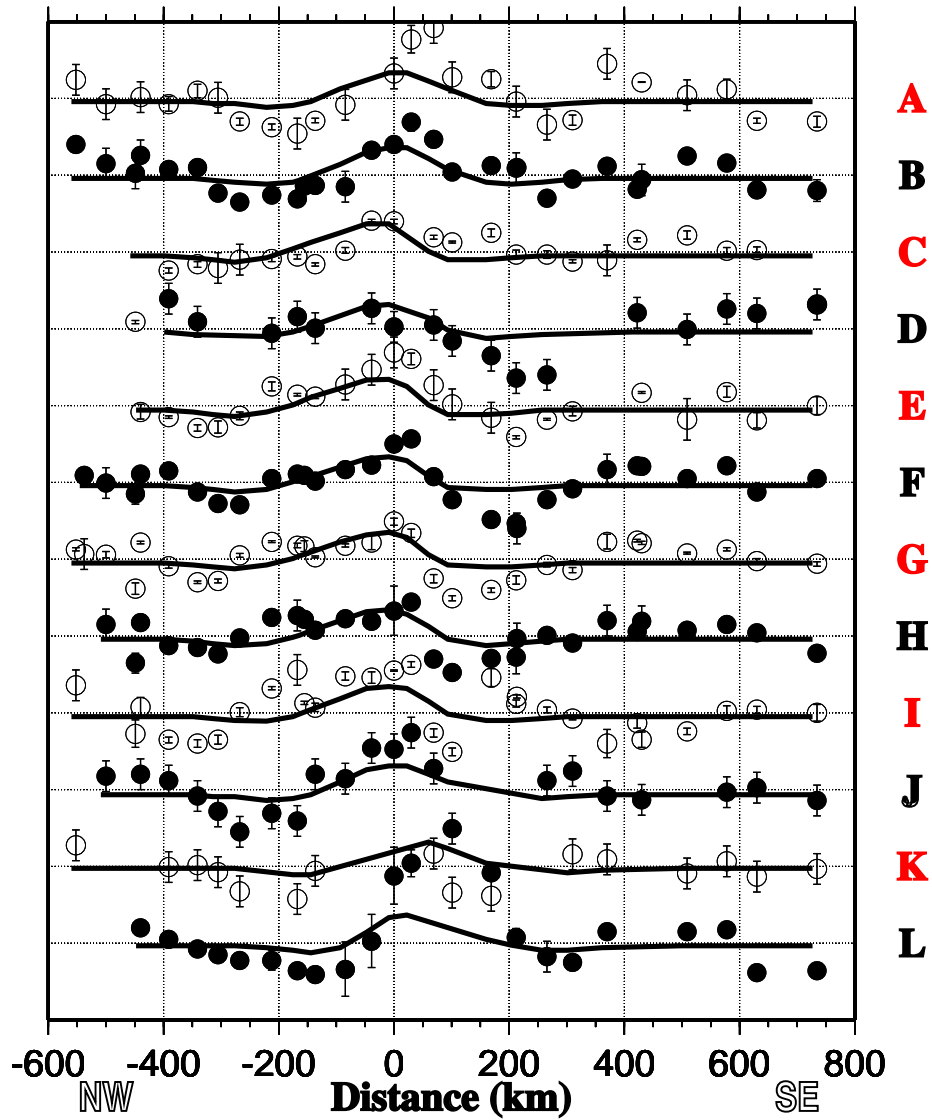
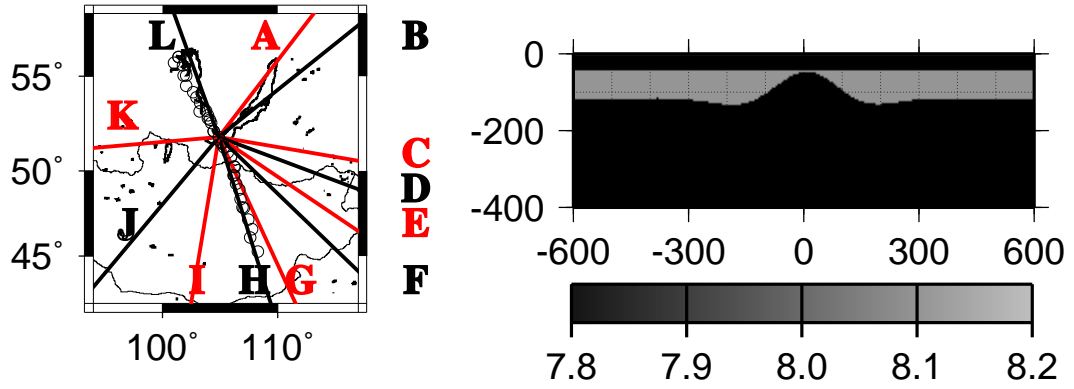


Figure 2.5.5 (a)

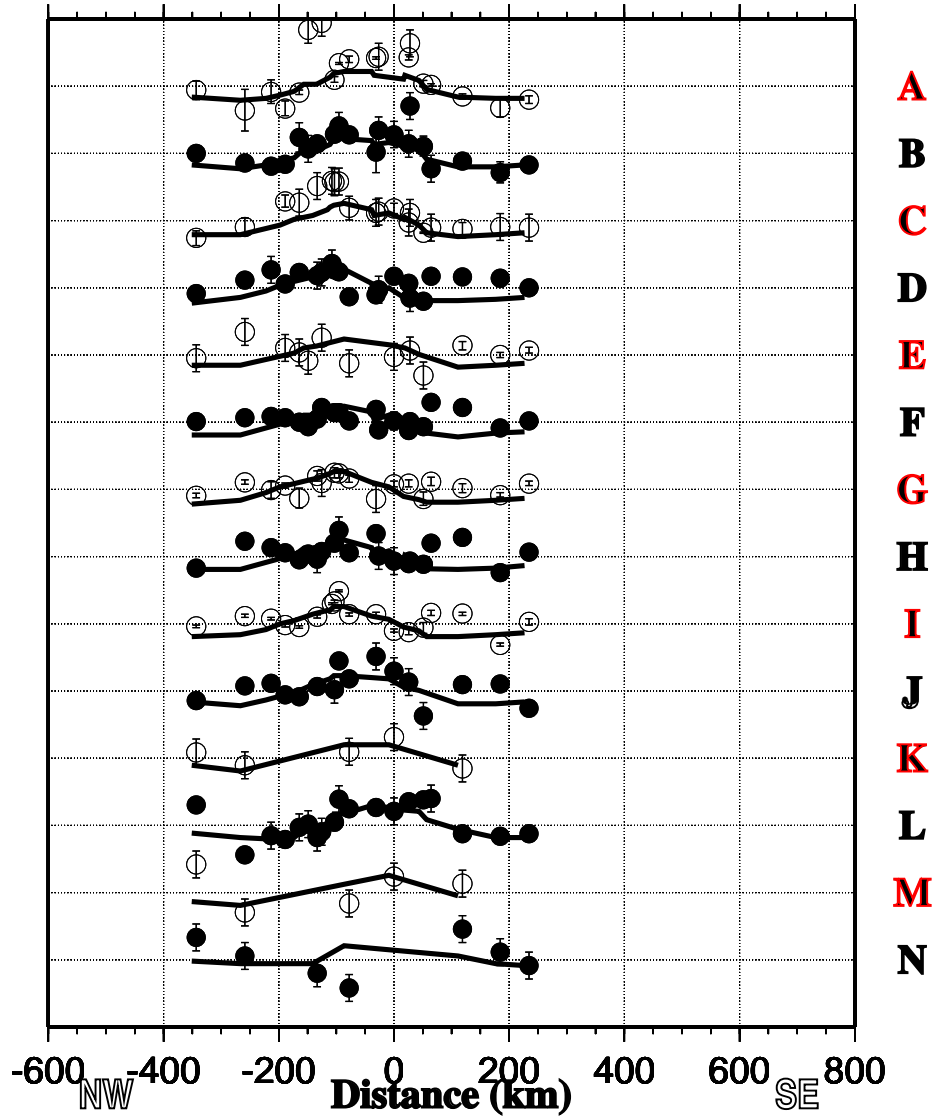
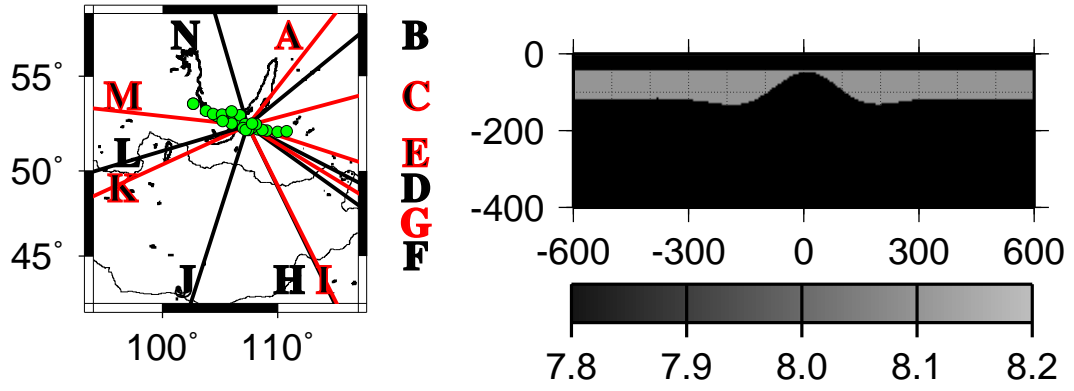


Figure 2.5.5 (b)

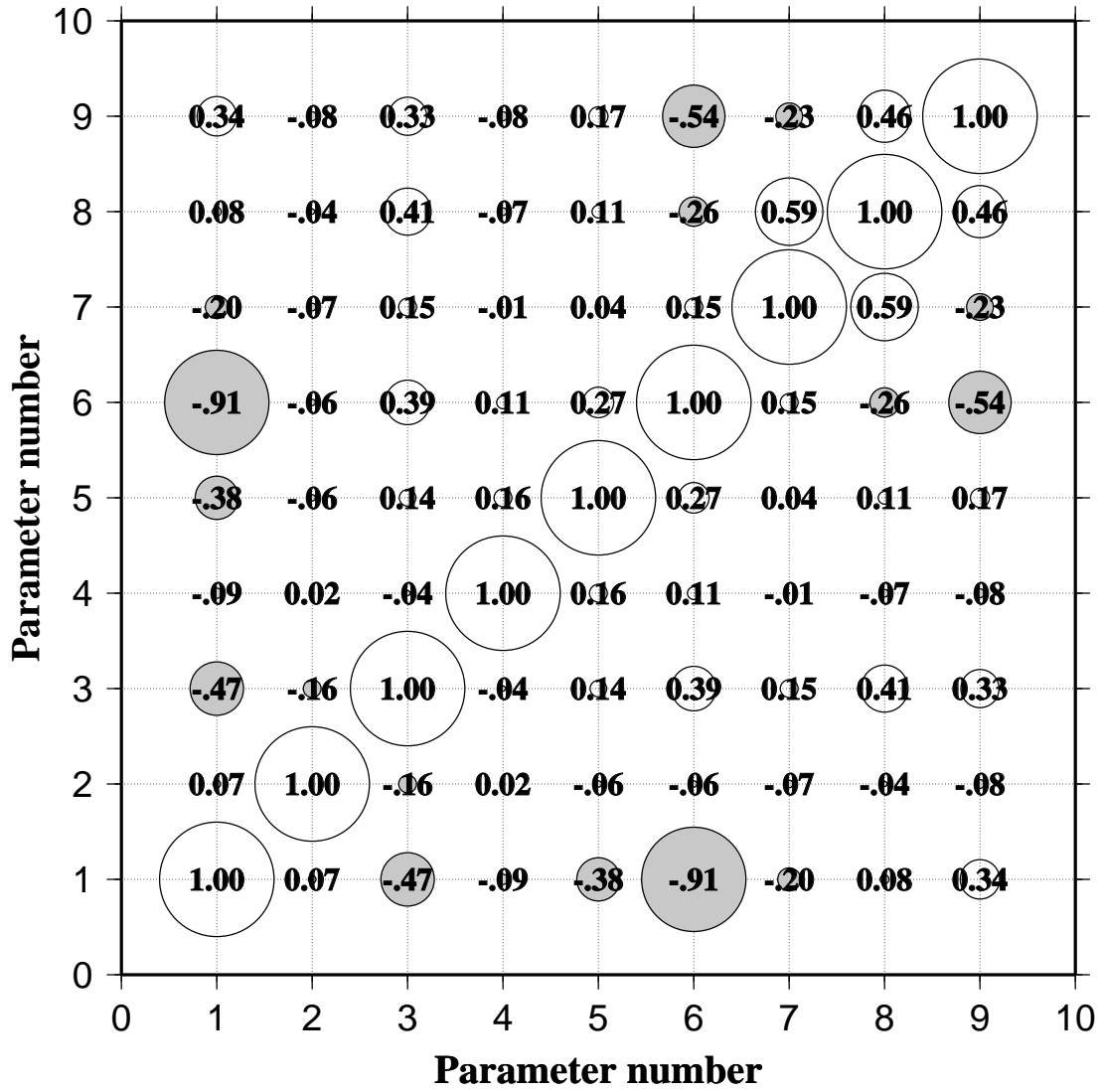
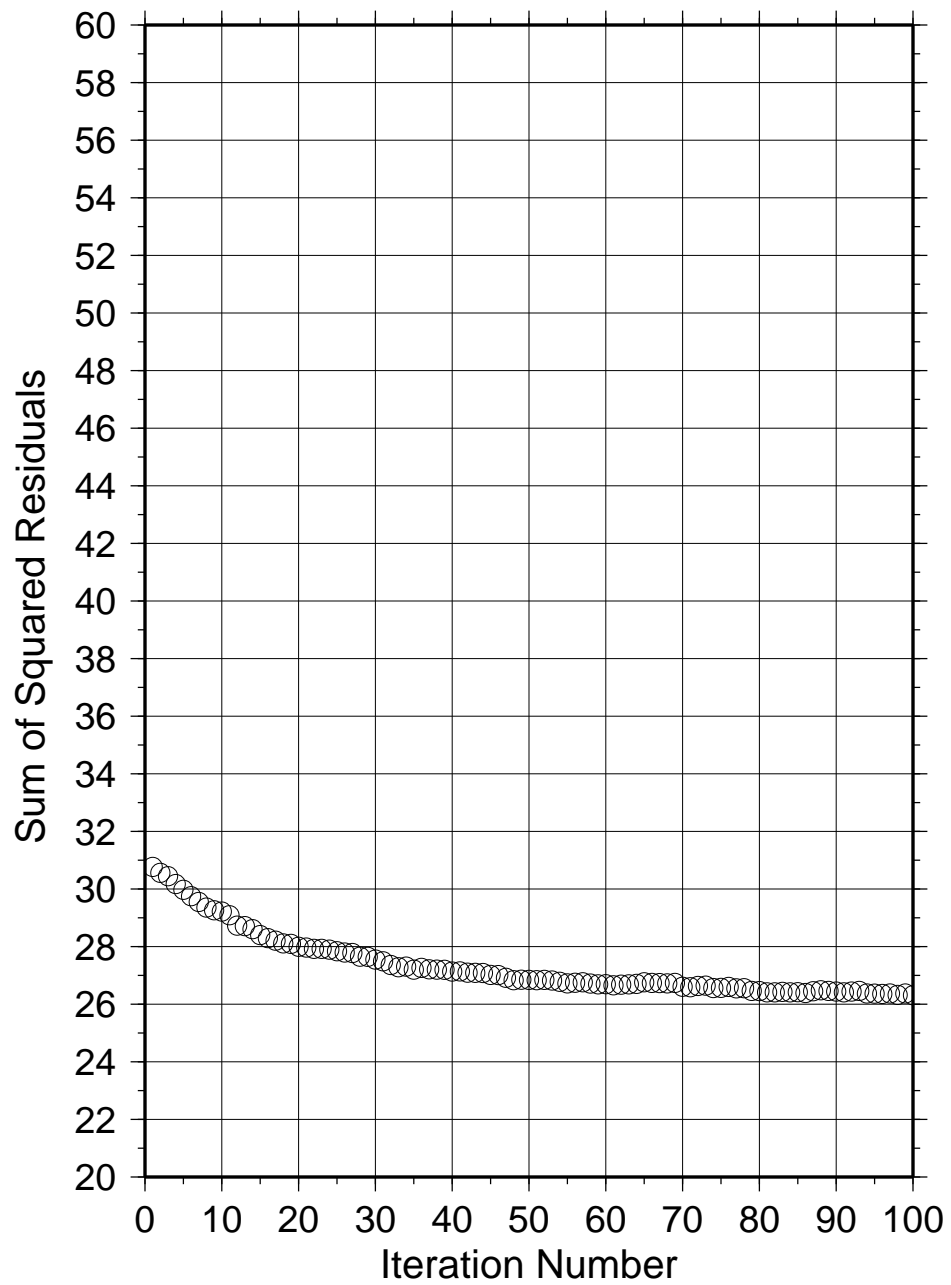


Figure 2.5.6



**Figure 2.5.7**

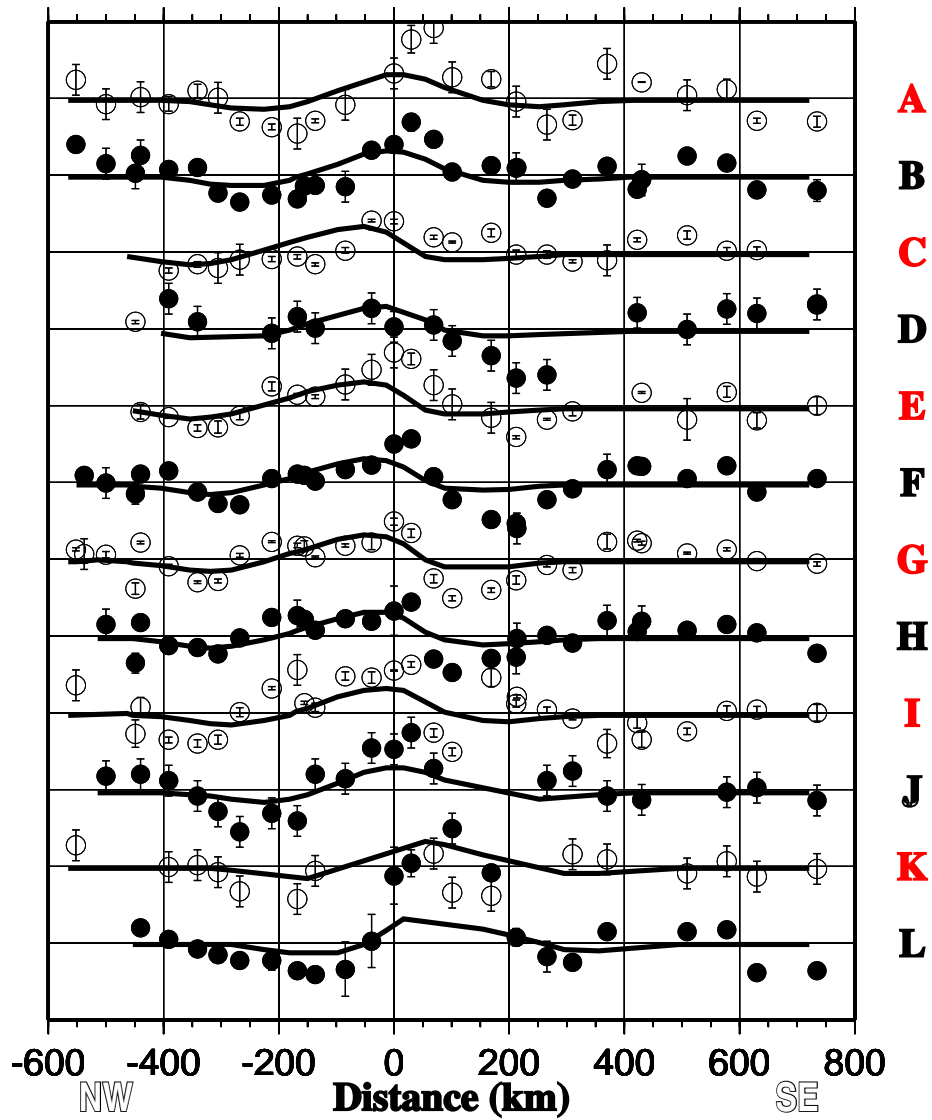
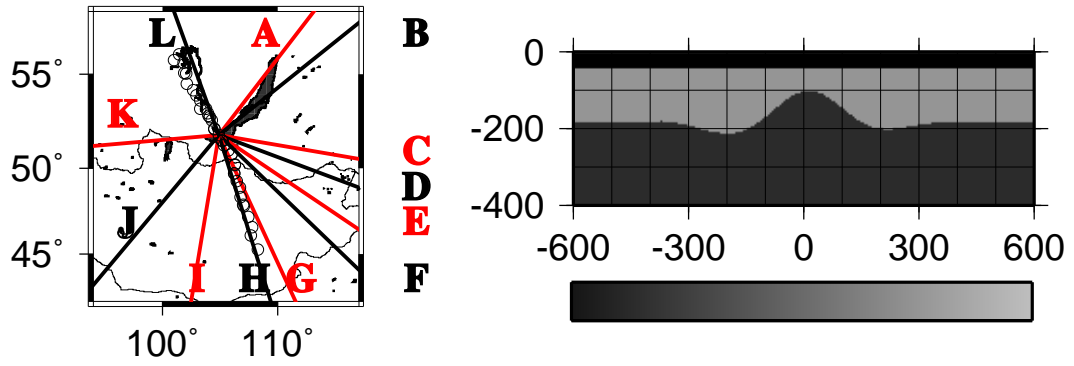


Figure 2.5.8 (a)

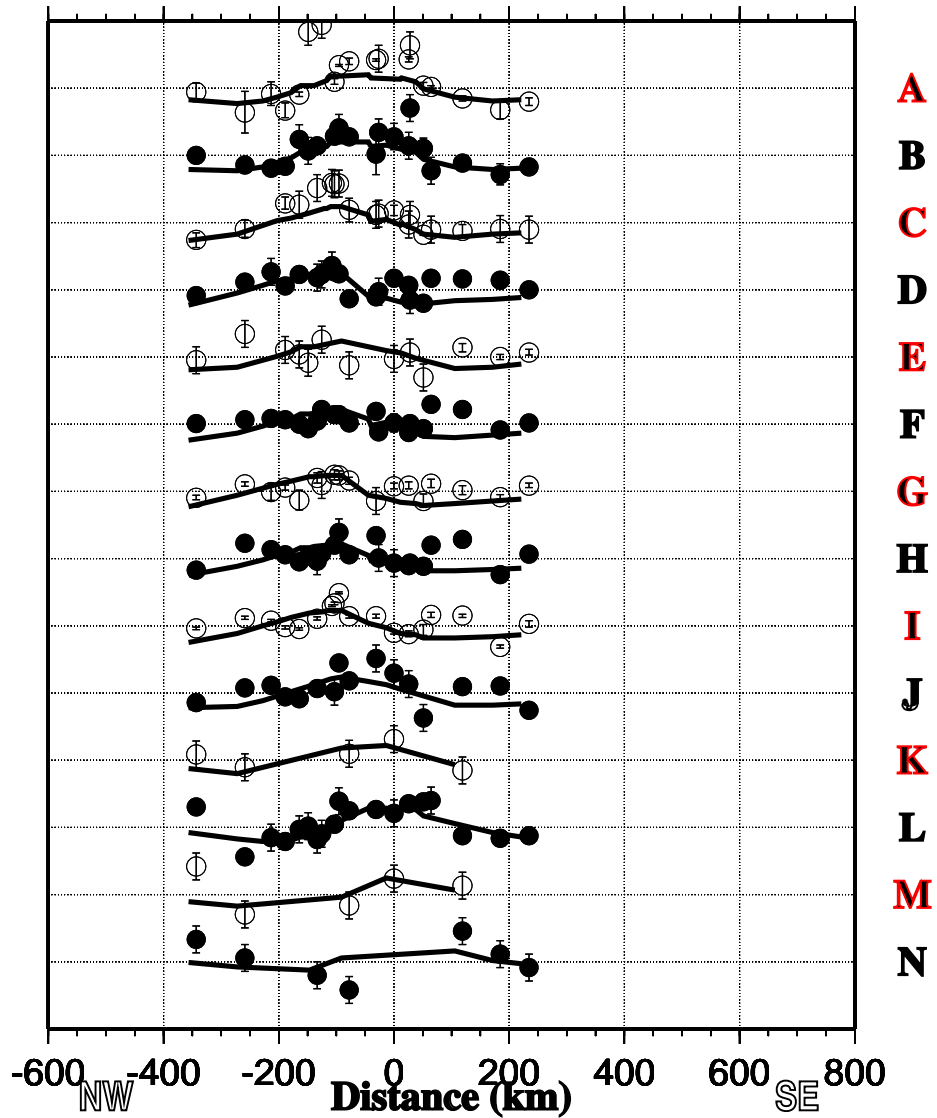
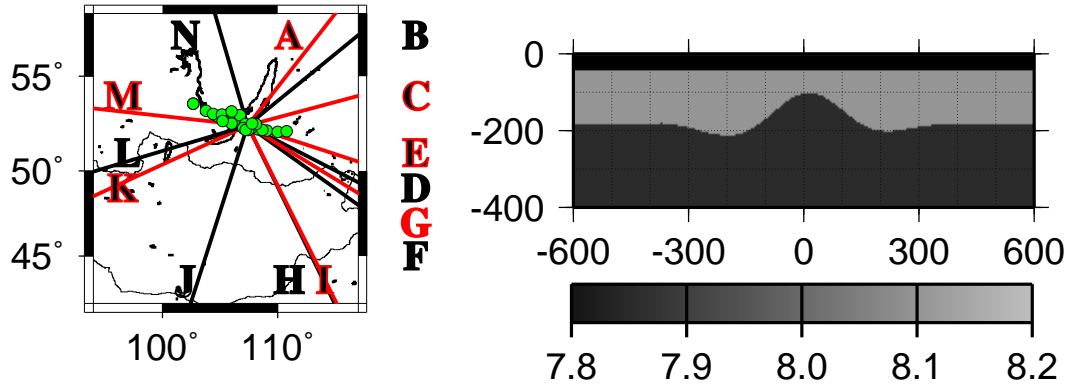


Figure 2.5.8 (b)

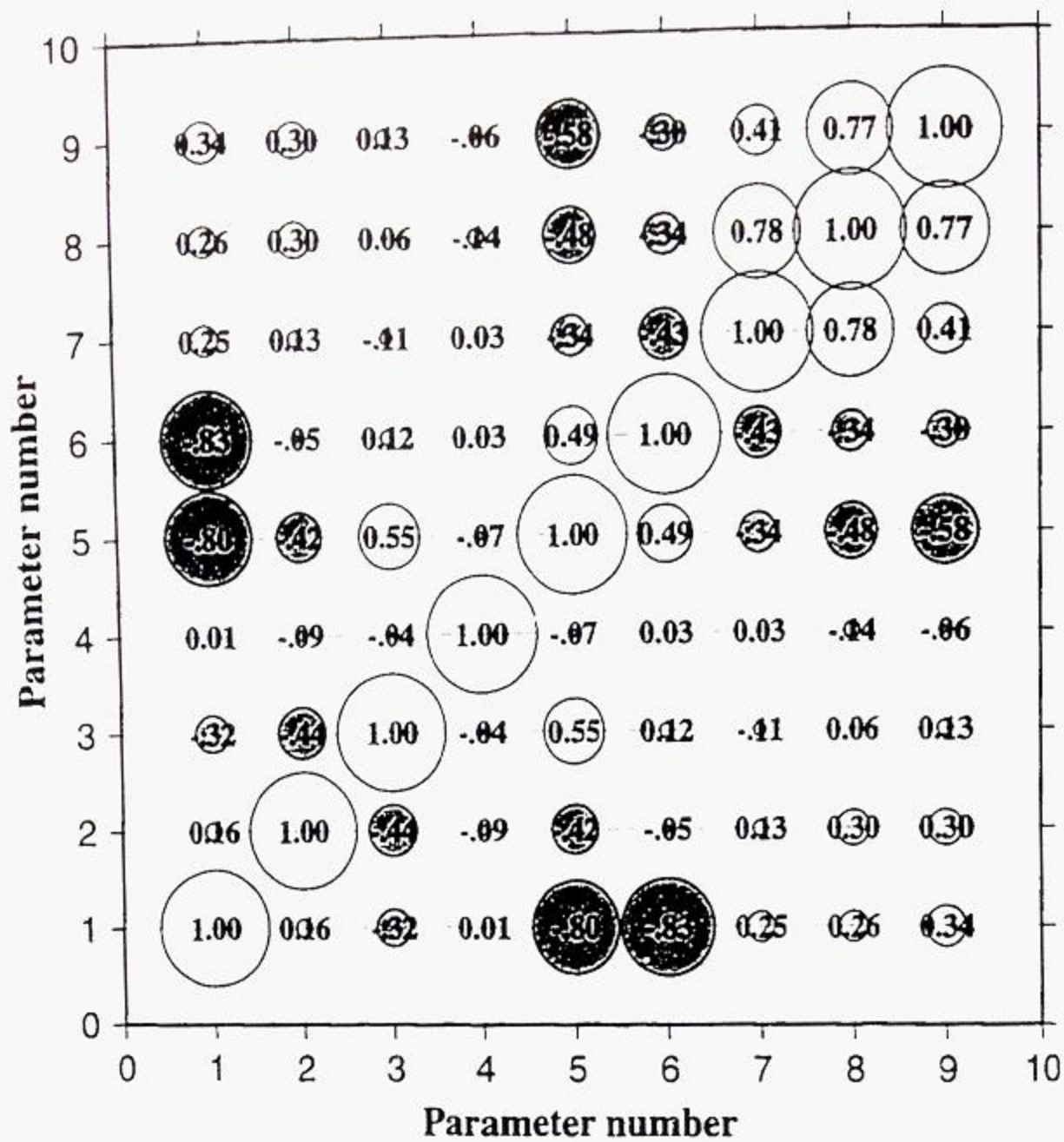
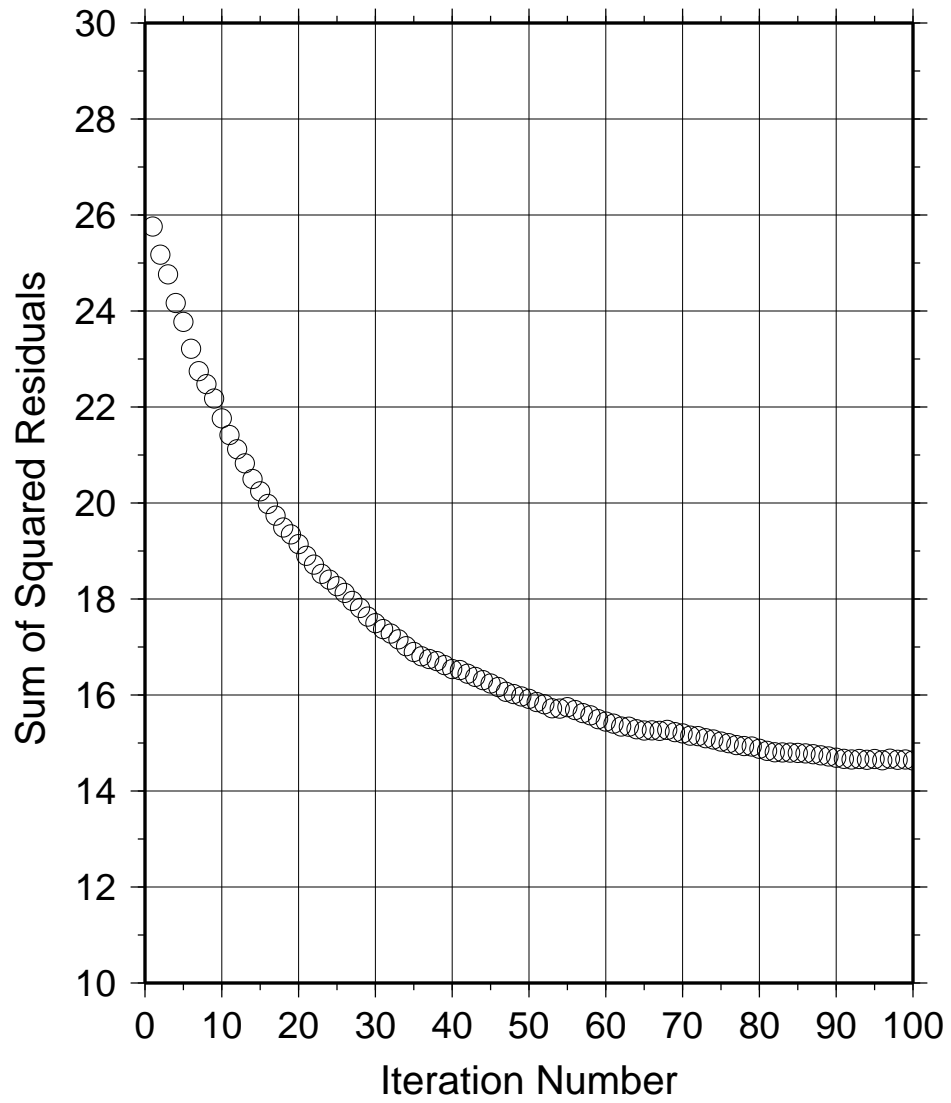


Figure 2.5.9



**Figure 2.5.10**

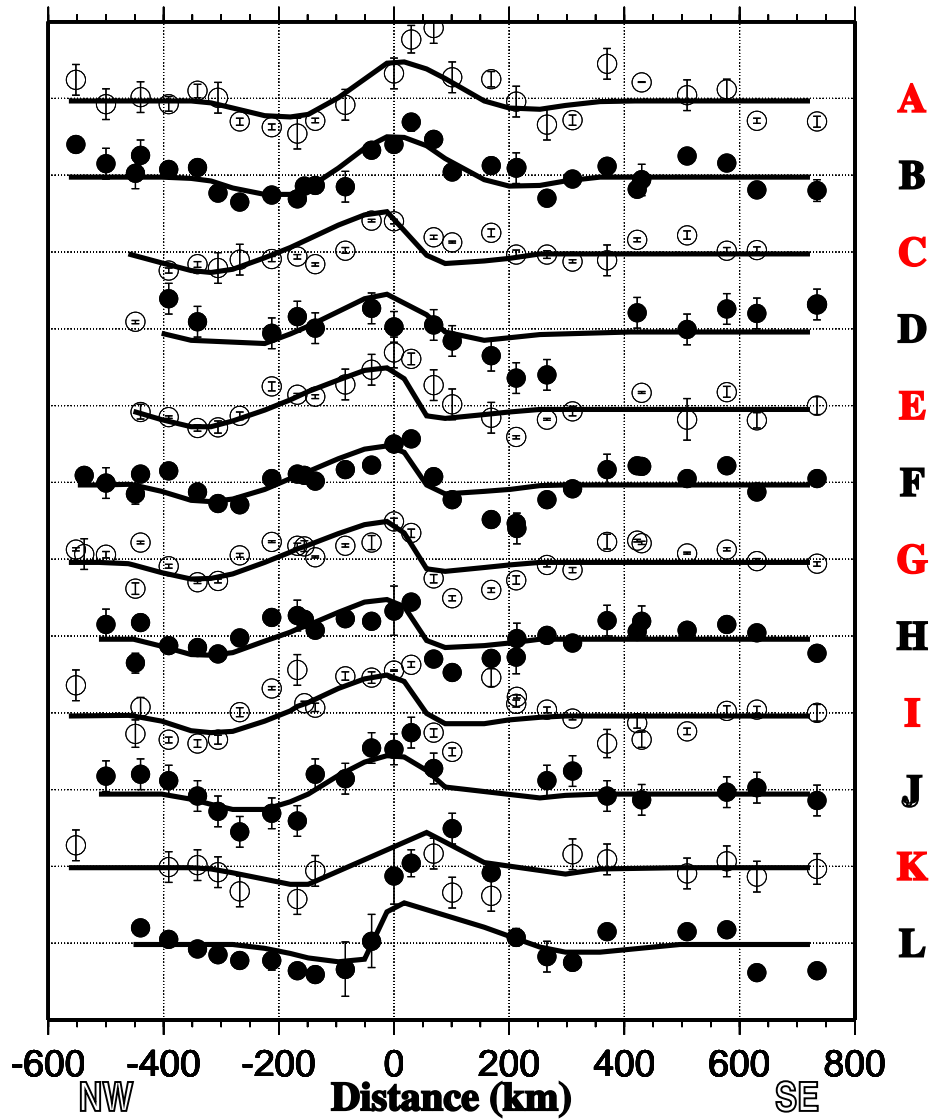
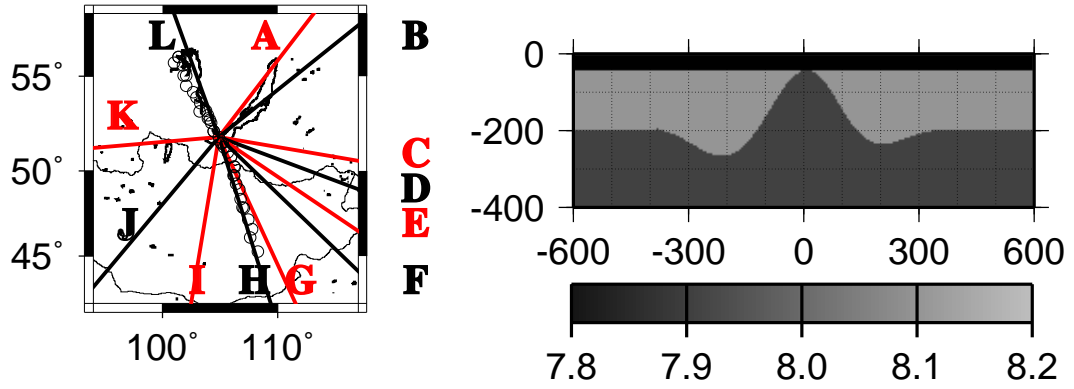


Figure 2.5.11

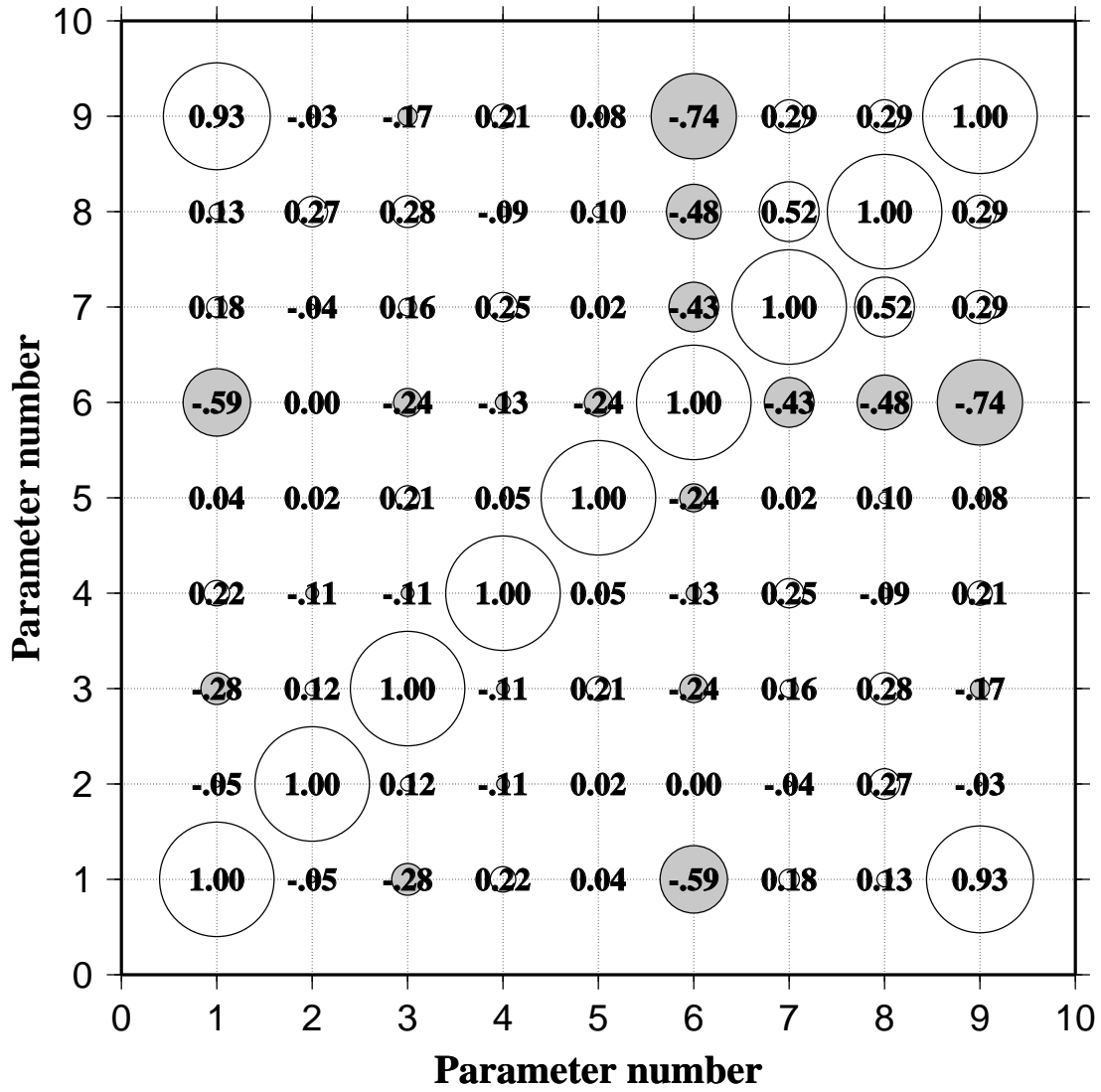


Figure 2.5.12

**Table 2.2.1.** Events used in travel-time studies

Group No.	Origin		Coordinates		Depth, km	Mag.
	Day	Time,UT	Latitude,	Longitude,		
			°N	°E		
92A	217	06:13	43.423	-127.160	10	5.0
92A	261	07:02	44.478	-129.498	10	5.0
92B	176	12:11	51.494	-173.359	33	5.7
92B	177	04:37	51.594	-173.440	33	5.1
92B	180	20:58	51.506	-174.804	33	5.0
92B	232	00:57	50.479	-174.846	33	6.1
92B	256	14:59	57.320	-155.074	56	0.4
92B	261	22:16	60.034	-140.570	0	5.4
92B	265	20:30	51.176	-179.057	33	5.0
92C	200	08:20	39.327	143.301	33	5.4
92C	200	08:36	39.361	143.376	33	6.1
92C	200	10:20	39.389	143.079	32	6.0
92C	200	10:59	39.398	143.255	28	5.5
92C	200	11:48	39.085	143.260	31	5.4
92C	200	13:56	39.466	143.026	21	5.7
92C	200	14:45	39.326	143.279	28	5.0
92C	200	17:27	39.596	143.213	31	5.4
92C	200	18:12	39.121	143.208	31	5.4
92C	200	20:55	39.603	143.288	33	5.6
92C	200	21:18	39.294	143.059	33	5.6
92C	200	21:31	39.278	143.637	28	5.1
92C	200	21:36	30.770	137.268	475	5.5
92C	200	21:45	39.256	143.268	33	5.0
92C	202	19:39	39.227	143.428	24	5.0
92D	200	06:57	-15.807	-177.570	400	5.3
92E	228	21:30	18.494	145.571	193	5.0
92E	246	10:23	12.382	144.138	33	5.4
92F	180	06:52	-5.980	154.383	69	5.1
92F	197	01:16	-5.968	146.662	61	5.1
92F	200	07:57	-6.513	147.867	41	5.7
92F	201	02:40	-6.713	147.541	81	5.4
92F	203	20:01	-3.898	141.388	110	5.0
92F	204	11:46	-5.623	154.187	84	5.0
92F	206	02:09	-7.048	149.946	44	5.7
92F	206	14:26	-7.022	150.005	36	5.3
92F	221	20:38	-5.772	146.921	126	5.4
92F	229	10:23	-5.393	146.659	237	6.0
92F	240	13:25	-5.961	153.625	49	5.1
92F	246	21:27	-3.280	139.850	59	5.1

**Table 2.2.1.** (continued)

Group No.	Origin		Coordinates		Depth, km	Mag.
	Day	Time,UT	Latitude,	Longitude,		
			°N	°E		
92G	194	23:41	3.117	121.996	616	5.6
92G	195	00:10	3.237	121.862	612	5.2
92G	196	07:03	-4.706	125.435	477	5.6
92G	206	20:47	1.634	126.969	79	5.0
92G	210	17:30	-4.441	127.514	299	5.4
92G	213	14:02	10.092	126.288	48	5.3
92G	215	05:50	-0.898	127.590	33	5.8
92G	215	12:03	-7.118	121.724	483	6.2
92G	218	04:53	-5.341	131.086	47	5.0
92G	221	02:50	10.065	126.260	32	5.2
92G	222	19:49	4.016	126.509	68	6.1
92G	224	01:55	-0.110	127.195	40	5.0
92G	232	02:57	-5.777	131.022	109	5.0
92G	234	22:11	5.926	124.201	27	5.0
92G	239	08:25	-5.960	130.477	94	5.1
92G	243	14:42	-6.230	129.861	123	5.1
92G	244	11:14	1.306	128.627	54	5.3
92G	246	05:50	-6.038	112.139	634	5.8
92G	253	15:58	2.760	124.281	284	5.0
92G	268	12:08	1.341	123.444	24	5.0
92H	178	02:36	-8.908	112.577	68	5.1
92H	197	00:17	-22.358	126.564	10	5.1
92H	197	18:04	-8.814	121.479	116	5.7
92H	225	17:29	-6.641	130.501	79	5.5
92H	244	04:39	-11.558	118.281	26	5.5
92I	176	12:27	-5.358	103.015	48	5.3
92I	178	05:15	-5.671	102.432	33	5.0
92I	193	12:53	-4.367	102.897	83	5.2
92I	196	07:42	-2.202	100.871	57	5.2
92I	218	02:09	-5.566	102.863	57	5.5
92I	229	14:49	-3.070	84.960	33	5.7
92I	260	04:23	11.617	93.623	153	5.2
92J	234	09:54	-18.329	65.035	10	5.1
92K	267	21:59	29.823	51.090	33	5.1
92L	253	13:08	76.205	7.241	24	5.7
92L	254	14:54	76.264	7.710	29	5.2
91A	228	22:26	41.697	-125.385	10	5.5
91A	229	19:29	40.235	-124.348	12	6.0
91A	229	22:17	41.821	-125.397	13	6.2
91A	257	19:00	37.226	-116.428	0	5.5

**Table 2.2.1.** (continued)

Group No.	Origin		Coordinates		Depth, km	Mag.
	Day	Time,UT	Latitude,	Longitude,		
			°N	°E		
91A	260	21:10	35.828	-121.323	8	5.2
91B	201	11:48	54.565	-161.654	32	5.8
91B	226	12:53	54.389	-169.296	274	5.7
91B	227	23:27	52.823	-170.789	104	5.3
91B	257	10:25	61.384	-140.005	10	5.0
91B	267	20:05	53.996	-164.297	33	5.0
91C	205	03:10	52.150	162.243	33	5.1
91C	217	11:08	51.675	176.351	33	5.1
91C	262	01:41	48.818	154.870	35	5.6
91C	265	06:32	49.644	156.549	30	5.5
91D	205	09:36	32.229	138.766	245	5.1
91D	218	14:49	35.725	141.044	28	5.9
91D	238	14:59	42.100	144.635	28	5.8
91D	245	03:03	42.292	143.019	65	5.2
91D	246	08:44	33.649	138.778	27	5.9
91E	204	21:16	-24.766	-179.592	467	5.0
91E	241	05:21	-20.710	-177.749	376	5.4
91E	264	15:19	-16.232	-173.004	17	5.8
91F	220	15:26	-4.540	151.900	174	5.1
91F	226	19:15	-13.593	167.607	13	6.1
91F	227	05:21	-18.660	168.868	145	5.0
91F	236	08:03	-14.607	166.869	83	5.3
91F	238	22:52	-14.601	167.274	232	5.0
91F	244	07:18	-3.442	134.569	33	5.0
91F	244	08:22	-22.436	170.257	39	5.1
91F	259	17:47	-5.487	147.055	214	5.1
91F	259	22:19	-13.246	167.139	162	5.4
91F	263	12:24	-5.428	146.448	145	5.1
91F	269	09:14	-9.283	158.620	25	5.2
91F	270	23:01	-3.359	137.625	63	5.5
91F	271	20:26	-5.814	150.959	28	5.8
91F	275	14:32	-10.402	161.363	91	5.4
91F	275	17:49	-10.272	161.064	95	5.2
91G	215	08:33	29.330	129.081	17	5.5
91G	225	22:31	18.896	145.177	603	5.1
91G	228	01:47	22.710	143.189	136	4.9
91G	242	01:29	-3.351	134.441	33	5.4
91G	249	13:14	-0.301	132.775	20	5.1
91G	252	14:30	12.796	143.927	33	5.1
91G	252	15:06	12.678	144.008	30	5.0

**Table 2.2.1.** (continued)

Group No.	Origin		Coordinates		Depth, km	Mag.
	Day	Time,UT	Latitude, °N	Longitude, °E		
91G	271	09:38	27.868	140.820	33	5.2
91G	271	10:48	27.926	140.742	33	5.1
91H	206	12:25	-5.763	130.758	33	5.2
91H	235	20:16	-9.209	123.526	31	5.4
91H	236	11:13	-6.065	130.368	148	5.6
91H	249	11:46	-6.124	130.622	146	5.3
91H	263	14:47	-6.486	129.850	180	5.4
91H	267	05:06	-6.551	130.230	83	5.3
91H	273	12:08	-6.751	130.442	64	5.2
91I	202	22:59	3.008	128.434	34	5.9
91I	204	11:22	5.826	125.983	146	5.6
91I	207	15:04	-2.090	128.055	26	5.2
91I	210	01:50	-2.958	129.415	33	5.2
91I	214	06:27	10.286	125.175	22	5.0
91I	220	04:00	1.294	122.663	45	5.3
91I	220	22:08	1.331	122.643	33	5.1
91I	221	06:28	1.409	122.706	37	5.5
91I	221	23:31	-3.079	129.783	21	5.1
91I	223	14:43	-3.141	130.320	33	5.7
91I	225	20:14	-3.061	130.412	25	5.2
91I	226	17:43	3.159	127.949	123	5.5
91I	235	16:16	9.977	126.120	32	5.2
91I	238	06:39	1.775	124.035	326	4.9
91I	266	15:48	2.354	128.333	135	5.1
91J	204	13:25	3.775	95.932	46	5.8
91J	218	02:17	3.827	95.374	18	6.0
91J	237	05:00	5.649	94.116	44	5.2
91J	238	20:54	6.882	94.609	21	5.8
91K	205	13:54	-18.274	34.856	32	5.2
91L	220	11:12	26.879	65.848	53	5.3
91L	232	08:46	37.646	72.150	135	5.2
91L	251	10:14	36.264	71.324	132	5.0
91L	262	04:58	35.921	69.862	99	5.0
91M	205	09:45	36.520	44.066	25	5.4
91N	244	06:51	78.967	3.604	10	5.2

**Table 2.2.2.** Location of stations used in travel-time studies

Station No.	Coordinates		Elevation, meters
	Latitude,	Longitude,	
	°N	°E	
9101	53.620	102.645	494
9102	53.246	103.767	586
9103	52.984	104.714	567
9104	53.034	105.648	777
9105	52.767	106.345	628
9106	52.464	107.379	1012
9107	52.264	108.273	962
9108	52.207	109.078	885
9109	52.118	110.024	918
9110	52.172	110.785	923
9121	53.089	104.386	635
9122	53.058	105.146	679
9123	52.900	106.040	890
9124	53.062	106.128	863
9125	53.025	106.701	633
9126	52.559	105.977	571
9127	53.203	105.973	817
9128	52.690	105.217	796
9131	52.537	107.180	963
9132	52.370	107.759	776
9133	52.241	108.654	829
9134	52.325	106.986	755
9135	52.245	107.463	751
9136	52.549	108.120	1168
9137	52.246	107.231	713
9138	52.559	107.751	837
9141	51.680	103.644	974
9200	55.965	101.410	501
9201	55.678	100.990	457
9202	55.052	101.850	513
9203	54.516	102.070	495
9204	54.193	102.649	567
9205	53.929	102.934	472
9206	53.649	103.255	471
9207	53.243	103.767	586
9208	52.993	103.927	619
9209	52.778	104.105	476
9210	52.622	104.234	506
9211	52.169	104.469	537
9212	51.847	104.893	469
9213	55.022	102.055	457
9214	52.854	103.966	466
9215	55.560	101.803	457

**Table 2.2.2.** (continued)

Station No.	Coordinates		Elevation, meters
	Latitude,	Longitude,	
	°N	°E	
9216	52.162	104.464	534
9217	53.215	103.246	457
9220	51.550	105.167	1037
9221	51.292	105.339	1251
9222	51.021	105.682	979
9223	50.791	105.970	842
9224	51.526	105.121	1121
9280	50.193	106.254	825
9281	50.242	106.240	815
9282	49.738	106.202	985
9283	49.288	106.412	1059
9284	48.931	106.682	1163
9285	48.383	106.783	1410
9286	47.921	106.954	1629
9287	47.209	107.422	1524
9288	46.635	107.758	1524
9289	46.115	107.619	1429
9290	45.262	108.260	1230
9291	49.747	106.188	994
9292	47.866	107.051	1693

**Table 2.2.3.** Event Group Information

Group	No. of	$\bar{\phi} \pm \sigma_{\bar{\phi}}$	$\bar{\Delta} \pm \sigma_{\bar{\Delta}}$	$\bar{Lat} \pm \sigma_{\bar{Lat}}$	$\bar{Lon} \pm \sigma_{\bar{Lon}}$	$\bar{\theta} \pm \sigma_{\bar{\theta}}$
No.	Events	(Degrees)	(Degrees)	(Degrees)	(Degrees)	(Degrees)
92A	2	37.56± 0.31	74.88± 0.64	43.95± 0.37	-128.33± 0.83	19.95± 0.18
92B	7	51.30± 3.45	49.80± 1.50	53.37± 1.30	-167.31± 4.93	26.56± 0.40
92C	15	99.69± 1.28	28.29± 0.14	38.77± 0.55	142.86± 0.39	31.50± 0.05
92D	1	110.54± 0.00	93.41± 0.00	-15.81± 0.00	-177.57± 0.00	15.60± 0.00
92E	2	124.00± 2.19	46.63± 1.52	15.44± 2.16	144.85± 0.51	27.35± 0.39
92F	13	133.90± 1.10	66.22± 0.80	-5.62± 0.33	147.81± 1.25	22.16± 0.21
92G	20	155.24± 1.15	52.96± 1.18	-0.16± 1.18	125.72± 0.94	25.67± 0.31
92H	5	162.67± 2.92	63.59± 2.45	-11.66± 2.49	121.88± 2.80	22.78± 0.63
92I	7	189.45± 3.27	53.15± 2.13	-2.09± 2.16	98.67± 2.42	25.66± 0.56
92J	1	219.91± 0.00	77.30± 0.00	-18.33± 0.00	65.04± 0.00	19.20± 0.00
92K	1	265.01± 0.00	45.72± 0.00	29.82± 0.00	51.09± 0.00	27.60± 0.00
92L	2	340.05± 0.00	43.92± 0.05	76.23± 0.02	7.48± 0.17	28.20± 0.00
91A	5	37.19± 0.74	78.92± 1.43	39.36± 1.08	-122.58± 1.53	18.84± 0.39
91B	5	48.07± 3.48	49.79± 1.26	55.43± 1.36	-161.21± 4.97	26.58± 0.36
91C	4	70.68± 2.97	33.58± 2.20	50.57± 0.69	162.50± 4.22	30.52± 0.45
91D	5	108.68± 4.13	28.23± 0.71	37.20± 1.89	141.25± 1.04	31.54± 0.18
91E	3	113.57± 2.41	97.71± 0.75	-20.57± 2.01	-176.78± 1.60	15.17± 0.07
91F	15	129.79± 2.11	75.72± 2.53	-10.34± 1.45	157.17± 2.92	19.67± 0.67
91G	9	131.58± 3.43	44.06± 3.34	16.51± 3.81	139.35± 1.82	27.96± 0.84
91H	7	155.04± 1.10	61.67± 0.19	-6.71± 0.40	129.40± 0.91	23.39± 0.05
91I	15	155.49± 0.76	52.90± 1.14	1.74± 1.09	126.80± 0.70	25.70± 0.30
91J	4	196.78± 0.59	48.18± 0.59	5.03± 0.65	95.01± 0.35	26.93± 0.17
91K	1	245.37± 0.00	94.08± 0.00	-18.27± 0.00	34.86± 0.00	15.50± 0.00
91L	4	251.53± 1.29	32.45± 2.24	34.18± 2.13	69.80± 1.21	30.73± 0.44
91M	1	276.32± 0.00	46.44± 0.00	36.52± 0.00	44.07± 0.00	27.40± 0.00
91N	1	343.71± 0.00	41.79± 0.00	78.97± 0.00	3.60± 0.00	28.70± 0.00

# CHAPTER 3

## SKS Splitting Measurements and Interpretation

### 3.1 Introduction

Measurement of anisotropy in seismic velocities is becoming increasingly important in the understanding of the Earth's interior and dynamics. SKS splitting is one of the most effective diagnostics for upper mantle anisotropy, ideal for characterizing anisotropy beneath the receiver [e.g., Kind et al., 1985; Silver and Chan, 1988, 1991; Silver and Kaneshima, 1993; Gao et al., 1994a; Liu et al., 1995].

#### • *The SKS phase and SKS splitting*

Anisotropy of the mantle is readily detected by birefringent effects on SKS phases from earthquakes with epicentral distance greater than  $85^\circ$  [e.g., Kind et al., 1985; Silver and Chan, 1988; 1991; Ansel and Nataf, 1989; Vinnik et al., 1989; Savage et al., 1990; Makeyeva et al., 1990; Gao et al., 1994a]. The SKS phase travels as an S-wave in the crust and mantle, but as a P-wave through the liquid outer core (Figure 3.1.1). At the core-mantle boundary on the receiver side, the direction of particle motion is known, because the SKS phase is converted from the longitudinal P-wave motion. If this shear wave encounters anisotropic material on its path to the receiver, it may split into two different polarizations having different velocities denoted fast and slow (Figure 3.1.1). The difference in arrival time between the fast and slow directions, which can amount to seconds, quantifies the degree of splitting.

#### • *Causes of upper mantle anisotropy*

The causes for shear wave splitting have been discussed in great detail elsewhere [e.g., Karato, 1989; Savage et al., 1990; Babuska and Cara, 1991; Silver and Chan, 1991; Chastel et al., 1993]. It is generally believed that the main cause for

SKS splitting in the mantle is the preferred orientation of crystallographic axes of elastically anisotropic minerals in the upper mantle.

Both olivine and orthopyroxene are important highly anisotropic upper mantle constituents. Mantle peridotites typically contain more than 65% olivine and 20% orthopyroxene [Anderson, 1989]. Since orthopyroxene is not as abundant and anisotropic as olivine and for the sake of simplicity, in the discussion we will assume that the upper mantle beneath the study area is composed of a certain percentage of oriented olivine. The rest is randomly oriented olivine, orthopyroxene, and other mantle minerals.

Figure 3.1.2 shows velocities of P-waves traveling along different directions through an olivine crystal. The fastest direction is along the  $a$ -axis with  $V_a = 9.87$  km/s; along the  $b$  axis the P wave has the slowest velocity with  $V_b = 7.73$  km/s; and along the  $c$ -axis the P-wave has the intermediate velocity with  $V_c = 8.65$  km/s.

Under uniaxial compression, the  $a$ -axis of olivine turns to be perpendicular to the maximum compressional strain direction; under pure shear, it is perpendicular to the shortening direction; and under progressive simple shear, it is aligned in the flow direction [Nicolas and Christensen, 1987; Savage et al., 1990; Silver and Chan, 1991; Chastel et al., 1993].

Figure 3.1.3 shows schematically the preferred orientation of olivine crystallographic axes under upper mantle horizontal and vertical flows beneath a hypothetical continental or oceanic rift. Away from the rift axis, where the dominant flow is horizontal, the  $a$ -axes of olivine-rich aggregates are horizontal and cluster around the flow direction, which is perpendicular to the rift. Both the  $a$ - and  $c$ -axes

concentrate in the horizontal flow plane. The  $b$ - axes are vertical and align perpendicular to the flow plane [Nicolas and Poirier, 1976; Anderson, 1989]. Therefore in areas with dominant horizontal flow, the observed fast SKS polarization direction reflects the preferred orientation of the crystallographic  $a$ - axis of olivine, which is the flow direction, and the slow direction reflects that of the  $c$ - axis.

In the vicinity of the rift axis, vertical flow dominates. The  $a$ - axis of olivine aggregates is vertical and the  $b$ - and  $c$ - axes are horizontal with the  $b$ - axis perpendicular to the flow plane, which is vertical and parallel to the rift axis and the  $c$ - axis is along it (Figure 3.1.3). Therefore in areas with dominant vertical flow, the observed fast SKS polarization direction is parallel to the rift direction and reflects the preferred orientation of the crystallographic  $c$ - axis of olivine; the slow direction is perpendicular to the rift axis and reflects the preferred orientation of the  $b$ - axis.

• *Previous studies*

SKS splitting measurements have accumulated rapidly over the last 10 years. The most extensive studies have been made in central California and Nevada [Savage and Silver, 1993]; in southern California [Liu et al., 1995]; along a profile traversing southern Tibet [McNamara et al., 1994]; in the Tien Shan area [Makeyeva et al., 1992]; along a 1200 km profile traversing southern Siberia, Lake Baikal, and Mongolia [Gao et al., 1994a]; and in southern America traversing the Andes [Russo and Silver, 1994].

Two previous studies have been made in the Rio Grande rift of north America [Sandvol et al., 1992], and in the East Africa rift [Gao et al., 1994c]. Given their relevance to the present study, the major results are reviewed in detail here. Figure

3.1.4 shows SKS splitting measurements at 6 stations in the Rio Grande rift [Sandvol et al., 1992]. The stations are within or very close to the rift valley. The size of the dots is proportional to the splitting time which ranges from 0.9 to 1.5 seconds. The orientation of the bars represents the polarization direction of the fast SKS phase (hereafter referred to as the 'fast direction'). The fast directions are parallel or sub-parallel to the rift axis. No measurements are available on the flanks of the rift zone. West of the rift, in California and Nevada, the dominant fast direction is east-west [Savage and Silver, 1993; Liu et al.; 1995].

Gao and others [1994c] measured SKS splitting in data from 14 stations located in the East Africa rift (Figure 3.1.5). Their results show that the fast directions are dominantly NS, i.e., parallel or sub-parallel to the rift axis. Most of the stations were within or very close to the rift valley. The results from these two major continental rifts will be compared with the results of this study, and will be explained using a small-scale mantle convection model in Chapter 5.

## 3.2 Method

### • *Formulation*

The splitting parameters are the polarization of the fast split shear wave  $\phi$  (measured clockwise from the North) and the travel time difference between the fast and slow shear waves  $\delta t$ . We apply the following procedure for the determination of these parameters. The procedure is obtained directly from the geometric relations of the split fast and slow components and the radial and transverse components. The same result can also be deduced based on the principle of "minimum transverse energy" of Bowman and Ando [1987] [e.g., Silver and Chan, 1991].

Assume that in a spherical isotropic Earth, the radially polarized teleseismic SKS phase is  $S(t)$ . When it encounters a homogeneous anisotropic layer with horizontal symmetrical axes,  $S(t)$  splits into two orthogonal components with the same waveform but travel at different speeds. The fast and slow components (i.e.  $S_f(t)$  and  $S_s(t)$ ) can be expressed as [Babuska and Cara, 1991]

$$S_f(t) = S(t) \cos(\theta) \quad (3.2.1)$$

$$S_s(t) = -S(t - \delta t) \sin(\theta) \quad (3.2.2)$$

where  $\theta$  is the angle between the radial and fast components (Figure 3.2.1), and  $\delta t$  is the time delay of the slow component. Multiplying by  $\sin(\theta)$  on both sides of (3.2.1) and  $\cos(\theta)$  on both sides of (3.2.2) and replacing  $(t - \delta t)$  by  $t$  in (3.2.2), we have

$$S_f(t) \sin(\theta) + S_s(t + \delta t) \cos(\theta) = 0 \quad (3.2.3)$$

Select a portion of seismograms containing the SKS arrivals which start at data point  $m_1$  and end at  $m_2$ . For a trial pair of  $\delta t$  and  $\theta$ , define an error function

$$E(\delta t, \theta) = \sum_{i=m_1}^{m_2} [S_f(i) \sin(\theta) + S_s(i + n\delta t) \cos(\theta)]^2 \quad (3.2.4)$$

where  $n$  is the number of samples per second. Obviously the minimum of  $E(\delta t, \theta)$  corresponds to the optimal pair of  $\delta t$  and  $\theta$ . The trial fast and slow components can be obtained from rotating the north-south and east-west components according to the trial fast direction  $\phi$ , which is the angle clockwise from the north to the trial fast direction,

$$S_f(i) = S_n(i) \cos(\phi) + S_e(i) \sin(\phi) \quad (3.2.5)$$

$$S_s(i) = -S_n(i) \sin(\phi) + S_e(i) \cos(\phi) \quad (3.2.6)$$

Where  $S_n$  and  $S_e$  are the NS and EW components, respectively, of a three- component seismic station.

Before arriving at the anisotropic layer, the near- vertical- incident SKS phase vibrates along the direction of the great circle connecting receiver and the source; after entering an anisotropic layer, it splits into two components with time separation  $\delta t$  and vibrates in two orthogonal directions, i.e. the fast direction ( $\phi$ ) and the slow direction ( $90^\circ + \phi$ ). The amplitudes of the two components are determined by equations (3.2.1) and (3.2.2) and the waveform of the two components is the same, except for a lag of  $\delta t$ . It is obvious from equations (3.2.1) and (3.2.2) that by advancing the slow component  $\delta t$  seconds, and by dividing  $S_f(t)$  and  $S_s(t)$  by  $\cos(\theta)$  and  $\sin(\theta)$ , respectively, the corrected particle motion pattern is a tilted straight line with slope  $45^\circ$ .

• *Accuracy and resolution tests*

If the minimum value of  $E(\delta t, \theta)$ , i.e.,  $E_{min}(\delta t, \theta)$  can be regarded as a  $\chi^2$  distribution with  $n$  degrees of freedom, then the  $(1 - \alpha)\%$  confidence region can be found using [Silver and Chan, 1991; Jenkins and Watts, 1968; Bates and Watts, 1988]

$$\frac{E}{E_{min}} \leq 1 + \frac{2}{n - 2} f_{2, n-2}(1 - \alpha) \quad (3.2.7)$$

where  $f$  is the inverse of the  $F$  probability distribution, and  $n$  is the number of degrees of freedom.

Since not all the points in a seismogram are independent data points, the actual degrees of freedom  $n$  is usually much less than  $m - 2$ , where  $m$  is the number of data points in a seismogram. Silver and Chan [1991] provided a method for the

estimation of the degrees of freedom  $n$  for band-limited signals such as seismograms. They concluded that for intermediate period sensors  $n$  approximately equals to the length of the seismogram window used in seconds. For instance, if the SKS window is 20 seconds, which is a typical value used in our measurements, then the 95% confidence region is confined by the contour line with the value  $E = 1.3 * E_{min}$ .

We use synthetic seismograms with added noise to test the accuracy and resolution of the measurements for waves with different waveform and noise level. We construct synthetic seismograms by using a given pair of parameters  $(\theta_0, \delta t_0)$ . Note that for modeling in this section we assume that the radial direction aligns with the north direction, i.e., we assume that the back azimuth is  $180^\circ$ . Therefore  $\phi = \theta$  (Figure 3.2.1).

A certain level of Gaussian noise is added to the synthetic seismograms before searching for the optimal parameter pair. The bias between the given parameters and the optimal parameters is related to both the waveform of the signal and the noise level, as will be shown below.

Assume that  $S(t)$ , the radially polarized teleseismic SKS phase in equation (3.2.1), is a decaying sine wave, i.e.,

$$S(t) = \exp[-c * (t - t_1)] \sin[2\pi * f * (t - t_1)] \quad (3.2.8)$$

where  $c$  is the decay factor,  $t_1$  is the arrival time of the shear wave, and  $f$  is the frequency.

The fast and slow components are constructed using Equations 3.2.1 and 3.2.2 by using a given pair of parameters  $(\theta_0, \delta t_0)$ , and by adding a certain amount of Gaussian noise. The magnitude of the noise is controlled by a prescribed signal-to-noise ratio (s2n).

The synthetic fast and slow components are used in searching for the optimal parameters according to Equation 3.2.4.

Two types of waves with different peak frequencies are considered. The first type is formed by using  $f = 0.4$  Hz, where  $f$  is the frequency of the sine wave in Equation 3.2.8, and for the second type  $f = 0.1$  Hz. Most of the SKS phases that are used in the study have central frequencies approximately ranging from 0.2 to 0.6 Hz.

Figure 3.2.2 shows the radially polarized SKS phase ( $S(t)$  in Equation 3.2.1) and contour maps of  $E(\delta t, \theta)$  (the error function defined in Equation 3.2.4) for different given pairs of parameters  $(\theta_0, \delta t_0)$ , and different noise levels (s2n) for  $f = 0.4$  Hz.  $\theta_0$  is taken as  $1^\circ, n * 15^\circ$ , and  $89^\circ$  where  $n = 1, \dots, 5$  and  $\delta t_0$  is taken as 1.5 seconds. When the signal is noise-free, the calculated and given parameters are exactly the same, as shown in Figure 3.2.2A. As the noise level increases, the difference between the given and calculated parameters increases, especially for the  $\theta_0$  near-zero and near- $90^\circ$  cases (e.g., Figure 3.2.2C). Two minima are observed on the contour maps, one of them corresponds to the given parameters, and the other is located at  $\theta_0 + 90^\circ$ . The minimum corresponding to the given parameters is always smaller than the other minimum.

The second type of waves are formed using  $f = 0.1$  Hz. The results are shown in Figure 3.2.3. By using the same decay factor and the lower frequency than in the case of  $f = 0.4$  cause the waveform to be less periodic, and as a result there is only one persistent minimum corresponding to the given parameters on the contour maps. Compared with the higher frequency case, the minima on the contour maps are broader and therefore the resolution of the results is lower.

The measurement with the highest quality is made when all of the following conditions are satisfied: 1). the seismograms are noise-free; 2). the angle between the fast direction and the radial direction, i.e.,  $\theta$  equals  $45^\circ$ ; 3). the waveform has high frequency and is non-periodic.

When the difference between the radial and fast directions is near  $0^\circ$  or  $90^\circ$ , the anisotropy effect cannot be observed and the measurements are null. Three non-distinguishable possibilities can be obtained from such a case: 1) the upper mantle beneath the station is isotropic; 2) the upper mantle beneath the station is anisotropic with an unknown splitting time and a fast direction parallel to the radial direction; 3) the upper mantle beneath the station is anisotropic with an unknown splitting time and a fast direction perpendicular to the radial direction.

• *Determination of the maximum depth of the anisotropic layer*

The incidence of the SKS phase is nearly vertical; therefore it is impossible to determine the depth of the source of anisotropy from the observed splittings.

We introduce a Fresnel integral approach to model the anisotropic SKS phases aiming to determine the maximum depth of the anisotropic layer. The approach assumes that the transition of observed anisotropy is caused by the interference of waves from two half planes at the same depth with different fast directions (Figure 3.2.4).

For a monochromatic plane wave with circular frequency  $\omega$  the signal recorded at each point  $(X, Y)$  on the receiver plane can be expressed as [e.g. Lipson and Lipson, 1981]

$$\Gamma(X, Y, t; \omega) = A \int_{-\infty}^{+\infty} \int_{-\infty}^{+\infty} \phi f(x, y) \exp[i(ks - \omega t)] dx dy, \quad (3.2.9)$$

where  $A$  is the amplitude of the incident wave,  $k = \omega/c$  is the wavenumber,  $s$  is the distance between a secondary source at  $(x, y)$  and the receiver at  $(X, Y)$  hence  $s = (s_0^2 + x'^2 + y'^2)^{1/2}$  where  $s_0$  is the perpendicular distance between the receiver and source planes,  $x' = x - X, y' = y - Y$ ;  $\phi$  is a constant and  $f(x, y)$  is the transparency function which is the ratio of the transmitted amplitude to the incident amplitude [Sun and McMechan, 1989]. For our purpose,  $f(x, y) \equiv 1$ .

By taking the Taylor expansion with respect to  $s$  and omitting the higher orders equation 3.2.9 can be written as [Sun and McMechan, 1989]

$$\Gamma(X, Y, t; \omega) = A \exp[i(k s_0 - \omega t)] \int_{-\infty}^{+\infty} \int_{-\infty}^{+\infty} \phi f(x, y) \exp\left[\frac{ik}{2s_0}(x'^2 + y'^2)\right] dx dy, \quad (3.2.10)$$

Following Sun and McMechan [1989]  $\phi$  can be determined as

$$\phi = -ik/2\pi s_0 \quad (3.2.11)$$

by using the constraint that  $|\Gamma| = A$  when  $f(x, y) = 1$  and the geometrical relations

$$\int_0^{\infty} \cos kx^2 dx = \int_0^{\infty} \sin kx^2 dx = \frac{1}{2} \left(\frac{\pi}{2k}\right)^{1/2}. \quad (3.2.12)$$

The Y-axis separates two regions with different splitting parameters:  $(\phi_1, \delta t_1)$  when  $x < 0$  and  $(\phi_2, \delta t_2)$  when  $x > 0$ . The receivers are all along the X-axis. After some algebra, the monochromatic wave recorded at point  $(X, 0)$  can be expressed as  $\Gamma(X, t; \omega) =$

$$\sum_{m=1}^4 \vec{A}_m \exp[i(k s_0 - \omega(t + \delta t_m))](1 - i) \frac{k}{\pi s_0} \int_0^X \exp\left(\frac{ik}{2s_0} x'^2\right) dx. \quad (3.2.13)$$

where  $m$  equals 1 through 4, representing the fast and slow components for regions 1 and 2, respectively. For the two fast components,  $\delta t = 0$ , i.e.,  $\delta t_1 = \delta t_3 = 0$ ;  $A_m$

is the amplitude of the  $m$ th component and can be obtained from equations 3.2.1 and 3.2.2 for a given incident isotropic SKS arrival. The two synthetic horizontal components are computed by projecting the resulting  $\Gamma(X, t; \omega)$  onto the North and East directions, respectively.

The above method is only applicable to monochromatic waves. To model real seismograms we first decompose a wavelet into amplitudes and the phase angles of a series of monochromatic waves by using Fourier transforms; then we integrate equation 3.2.13 over all constituent waves to obtain synthetic seismograms, which are used to calculate splitting parameters.

Due to the interference of waves from the two regions the resulting fast directions are different from the values computed from ray theory, especially when the distance from the station to the boundary is less than the radius of the first Fresnel zone.

We determine the splitting parameters using synthetic seismograms along a profile across a boundary of anisotropy. The depth of the anisotropic layer is varied from 50 to 500km; the corresponding transitions in splitting directions range from 50 to 100 km. The results show that a sharp transition in anisotropy at depth gives rise to an extended transition zone in observed splitting directions at the surface. Thus although SKS splitting can occur at any depth beneath the core-mantel boundary and the surface, observations of rapid spatial variation place limits on its maximum depth which depends on the width of the transition zone (see Figure 3.2.5).

### 3.3 Data

Figure 3.3.1 shows stations used in the study of SKS splitting. Station locations can be found in Table 3.3.1. The entire study area is divided into 4 areas

which approximately correspond to the major tectonic provinces of the area. Areas A and B belong to the Baikal rift zone with area A including the NE rift valleys and area B the central and southern rift valleys. Area C is the Siberian platform and area D the Mongolian fold belt. The stations within an area are numbered from the North to South, e.g., the northern-most station in area A is A01 and the southern-most one is A11.

The 63 stations used in this study belong to two seismic networks. The thirty-five stations named 92xx in Table 3.3.1 were digital seismographs that were installed and operated during the summer of 1992, by a field team from UCLA, U. Wisconsin, and the Institute of Earth's Crust, Irkutsk. The other stations with alphabetical names such as 'boda' in Table 3.3.1 belong to the Russian Baikal Analog Seismograph Network operated by IEC since 1980. The analog seismograms were scanned at CalTech and digitized at UCLA using the NXSCAN software package [Humphrey and Helmberger, 1993].

• *Digital data*

The digital data, i.e., data recorded in the summer of 1992, were selected using the following procedure:

1) *selection of possible events.* According to the ISC bulletin, between day 165, 1992 and day 273, 1992, sixty events with  $mb \geq 5.3$  occurred within the distance range  $80 - 140^\circ$  from the middle of our profile. All the horizontal traces of these events were labeled with the SKS theoretical arrival time according to the IASPEI 1991 Earth model [Kennet and Engdahl, 1991].

2) *selection of SKS events.* All the traces from the 60 events were inspected visually and those showing observable arrivals on at least one station within 10

seconds after the SKS arrival time were identified. Nine events suitable for SKS studies were selected.

3) *selection of SKS traces.* All the traces from the 9 SKS events were inspected visually. Only those showing observable SKS arrivals were selected. The reasons that some stations have less measurements than others are a). poor performance; b). high noise level; c). installed at a later time or pulled out at an earlier time; d). rejected due to other reasons (see next paragraph).

4) *rejection of SKS traces.* A selected SKS trace was rejected if it suffered from one or more of the following problems: a). *Interference of S.* When the station-event distance is less than  $87^\circ$ , S waves arrive less than 10 seconds after SKS; b). *Interference by another event.* Since the studied area is one of the most seismically active regions within a continent, a lot of local events occurred during the period. We rejected the SKS traces contaminated by those events; c). *Bad or tilted channels.* During each station service, we programed the recorders to input a 12 volt step pulse into the 3 sensors and recorded the response. If one of the 3 sensors was significantly tilted, the amplitude of the response would be smaller than that of the other two, and the frequency response would also be different. If the tilted sensor was a horizontal one, the data would not be suitable for SKS splitting study.

After the above selecting-rejecting procedure, a total of 97 measurements from 28 digital stations were made.

• *Analog data*

The analog data, i.e., data recorded by the Russian seismic network, were selected using the following procedure:

1) *Selection of possible events.* According to the ISC bulletin, between day 1, 1980 and day 366, 1992, thirty-three events with  $mb \geq 6.4$  occurred within the distance range  $85^\circ - 130^\circ$  from at least one station in the network. Records from two more events, which occurred during the 1992 experiments were also selected. All the traces were scanned into TIFF format.

2) *Selection of SKS events.* All the traces from the 35 events were inspected visually and those showing observable SKS arrivals on at least one station within 10 seconds after the SKS arrival time were identified. Twenty-two events suitable for SKS studies were selected. The horizontal traces from the events with observable and digitizable SKS phases were digitized and labeled with the SKS theoretical arrival time according to the IASPEI 1991 Earth model [Kennet and Engdahl, 1991].

After the above selection procedure, a total of 74 measurements from 35 analog stations were made.

The locations of the 31 events used in the study are shown in Figure 3.3.2. Event information is listed in Table 3.3.2.

### 3.4 Measurements

The results consist of two groups of measurements, the previously published measurements at 28 sites by Gao et al. [1994a], and the new measurements at 35 sites made in this study that will be described in this section. The number in the brackets following the four-letter station name is the station number. Station locations can be found in Table 3.3.1.

**•arsh (B09):** There are two measurements for this station (event No. 14 and 27 in Table 3.3.2). Both events have back azimuths of about  $108^\circ$ . Transverse SKS is

observable on both events but not as strong as the radial components, indicating the existence of splitting. The final result for this station is taken as the weighted mean of the two measurements.

•**boda (A01)**: There are two measurements for this station (event No. 14 and 27). One event has back azimuths of  $115^\circ$ , and the other has  $93^\circ$ . Transverse SKS is observable on both events but is not as strong as the radial components, indicating the existence of splitting. The final result for this station is taken as the weighted mean of the two measurements.

•**char (A02)**: There are 5 measurements for this station (event No. 1, 9, 14, 17, 27). All the events are in a narrow back azimuthal band of  $119^\circ$ - $125^\circ$ . Three of the 5 measurements are null or nearly null, implying that the fast direction is either near  $120^\circ$  or  $30^\circ$ , or no splitting. As indicated by synthetic tests of the resolution power of the method, in such a situation a high signal-to-noise ratio record is needed to determine which of the three possibilities is right. Fortunately both event 1 and 9 satisfy this criterion. The final result for this station is taken as the weighted mean from event 1 and 9.

•**chit (D02)**: Nine events (event No. 3, 6, 7, 9, 10, 14, 17, 18, 27) have observable SKS signals and are used in the measurement. The back azimuths range from  $113^\circ$  to  $128^\circ$ . Transverse SKS are not clearly observable on all the events. Therefore the final result for this station is null, i.e., either has no splitting, or has splitting with fast direction about  $120^\circ$  or  $30^\circ$  with unknown splitting time. A minimum of one event from another azimuth is needed to determine the result.

•**hapc (D06)**: Transverse SKS phases on all the three events (event No. 14, 17, 27) have comparable or even greater amplitude than radial SKS phases. The back

azimuths range from  $114^\circ$  to  $117^\circ$ . The resulting fast directions are  $70 \pm 13^\circ$ ,  $73 \pm 10^\circ$ , and  $68 \pm 17^\circ$ , and the splitting times are  $0.6 \pm 0.2s$ ,  $0.7 \pm 0.2s$ , and  $0.6 \pm 0.3s$ , respectively for the three events. Figure 3.4.1.D06 shows seismograms, particle motion patterns and the contour maps of the error function for the 3 events. The reason for the high resolution is that the difference between the actual fast direction and the direction of the coming ray is close to  $45^\circ$  or  $135^\circ$ . The final result for this station is taken as the weighted mean from the 3 events.

•**irku (C11)**: The two events (event No. 3 and 14) display weak transverse SKS energy, implying that both measurements are null. The back azimuths are  $121^\circ$  and  $108^\circ$ . Therefore the final result for this station is null, i.e., either has no splitting, or has splitting with fast direction about  $115^\circ$  or  $25^\circ$  with unknown splitting time. The Result is consistent with Gao et al. [1994a] for a nearby station about 20 km south of this station (station C12).

•**kala (A08)**: One event (event No. 14) is available for this station. The signal-to-noise ratio is high ( $> 10$ ) and the transverse component is clearly observable (Figure 3.4.1.A08).

•**kovo (A07)**: One event (event No. 27) is available for this station. Both the transverse and radial components are strong and the result is well resolved.

•**kumo (A09)**: One event (event No. 17) is available for this station. Both the transverse and radial components are strong and the result is well resolved.

•**mond (B12)**: Five events are used (event No. 1, 6, 14, 17, 27). The back azimuths range from  $106^\circ$  to  $112^\circ$ . The fast directions from the first 4 events are between  $122^\circ - 132^\circ$ , and the last event (No. 27) has two nearly equal minima at

125° and 34° with the latter being the smallest. The final result for this station is the weighted mean from the first 4 events.

●**nely (A03)**: Three events (event No. 14, 17, 27) have observable SKS signals and are used in the measurement. The back azimuths range from 117° to 120°. Transverse SKS are not clearly observable on all the events. Therefore the final result for this station is null, i.e., either has no splitting, or has splitting with fast direction about 119° or 29° with unknown splitting time. A minimum of one event from another azimuth is needed to determine the result.

●**nizh (B01)**: Transverse SKS phases on all the five events (event No. 1, 9, 14, 17, 27) have comparable amplitude to the radial SKS phases. The back azimuths range from 112° to 118°. The resulting fast directions are consistent with each other, ranging from 33° to 56°. The final result for this station is the weighted mean from the 5 events.

●**ongu (B05)**: Two events (event No. 14, and 27) have observable SKS signals and are used in the measurement. The back azimuths are 110° and 113°. Transverse SKS are not clearly observable on all the events, indicating that the final result for this station is null, i.e., either has no splitting, or has splitting with fast direction about 111° or 21° with unknown splitting time.

●**orli (B08)**: This is the most intriguing station. The signals from four of the five events (event No. 1, 9, 14, 17, 27) are excellent and the parameters are well resolved but are inconsistent with each other (Figure 3.4.1.B08). The three events (14, 17, and 27) which occurred after the year 1988 and have back azimuths  $< 110^\circ$  have consistent results for  $\phi$  ( $145 \pm 10^\circ$ ,  $138 \pm 7^\circ$ ,  $138 \pm 9^\circ$ ) and  $\delta t$  ( $0.9 \pm 0.3s$ ,  $1.1 \pm 0.3s$ ,  $1.0 \pm 0.3s$ ). Event No. 1 which occurred in 1980 and has a back azimuth of  $110.0^\circ$  gives

well resolved results of  $\phi = 70 \pm 9^\circ$ ,  $\delta t = 0.8 \pm 0.2s$ . Transverse SKS phase on event No. 9, which occurred in 1986 and has almost identical back azimuth as event No. 1, is weak and the result is nearly null, implying that the fast direction could be  $110^\circ$  or  $20^\circ$ . The inconsistency might indicate the existence of two rather than one anisotropic layer, which may result in quick changes in  $\phi$  with a small change of back azimuth. A detailed discussion of this subject can be found in Silver and Savage [1993]. An application of their method can be found in Liu et al., [1995]. To resolve the anisotropy parameters for the possible two layers, more measurements and broader azimuthal coverage are required. The other possibility might be that at some moment between 1986 day 146 and 1989 day 070, a modification (or a correction) of the recording conditions was performed. Under such an assumption the results from the last 3 events which occurred after the assumed modification, are more reliable.

The final results for this station consist of two different estimates. The first one is from event 1, and the second one is the weighted mean of event 14, 17, and 27. The null measurement from event 9 is mentioned here but is excluded in the final result.

●**ozer (A05)**: One event (event No. 27) is available for this station. Both the transverse and radial components are strong and the result is well resolved.

●**sbai (B02)**: One event (event No. 14) is available for this station. The amplitude of the transverse component is about 1/3 of that of the radial component. Both components are strong compared with the noise.

●**solo (B04)**: One event (event No. 1) is available for this station. The radial SKS phase is strong but the transverse component is hardly observable. Therefore the

final result for this station is null, i.e., either has no splitting, or has splitting with fast direction about  $116^\circ$  or  $26^\circ$  with unknown splitting time.

•**suvo (B06)**: Three events (event No. 9, 14, and 17) are available for this station. The back azimuths are between  $112^\circ$  and  $119^\circ$ . Clearly observable transverse SKS phases on event No. 9 and 17 indicate anisotropy. The fast directions from event No. 9 and 14 are  $16 \pm 7^\circ$  and  $14 \pm 9^\circ$ ; from event 17 it is  $82 \pm 35^\circ$ . The final results for this station consist of two different estimates. The first is the weighted mean of event 9 and 14, and the second is from event 17.

•**tala (B13)**: All the six events (event No. 6, 9, 10, 14, 17, 27) used for this station show clearly observable transverse SKS energy, although not as strong as the radial components (Figure 3.4.1.B13). The resulting fast directions are consistent with each other, ranging from  $119^\circ$  to  $130^\circ$ . The final result for this station is the weighted mean of all the 6 events.

•**tonn (A06)**: One event (event No. 31) is available for this station. Both the transverse and radial components are strong and the result is well resolved.

•**tsip (A11)**: One event (event No. 3) is available for this station. Both the transverse and radial components are strong and the result is well resolved.

•**tupi (D01)**: The two events (Event No. 8 and 17) available for this station have different back azimuths relative to the station. If only the second event were available, the result would be a typical null measurement (Figure 3.4.1.D01). However, the availability of event 8, which is approximately from the West, gives a resolved measurement.

•**turi (A04)**: One event (event No. 27) is available for this station. Both the transverse and radial components are strong and the result is well resolved.

•**tyrg (B07)**: Among the 5 events (event No. 1, 9, 10, 17, 31) used by this station, four events give consistent results with  $39^\circ \leq \phi \leq 49^\circ$  and  $0.7s \leq \delta t \leq 1.1s$ . Event No. 9 has a back azimuth of  $116^\circ$  and gives a fast direction of  $107^\circ$ , a mere  $9^\circ$  difference between the radial direction and the fast direction. Therefore the result from event No. 9 is nearly null and is excluded in the averaging (Figure 3.4.1.B07).

•**uaki (A10)**: Three events (event No. 9, 14, 27) are used. The back azimuths range from  $115^\circ$  to  $121^\circ$ . Transverse SKS are observable but are relatively weak compared with the radial components, indicating minimal splitting. Therefore the final result for this station is nearly null, i.e., either has no splitting, or has splitting with fast direction about  $120^\circ$  or  $30^\circ$  with unknown splitting time.

•**ulun (B03)**: One event (event No. 27) is available for this station. Both the transverse and radial components are strong and the result is well resolved.

•**zaka (B25)**: Among the three events (event No. 14, 17, and 27) two of them gives similar results ( $\phi = 52 \pm 15^\circ, \delta t = 0.8 \pm 0.4s$  for event No. 17), and ( $\phi = 73 \pm 10^\circ, \delta t = 0.9 \pm 0.3s$  for event No. 27). Event 14 gives well defined but different results ( $\phi = 127 \pm 12^\circ, \delta t = 1.7 \pm 0.5s$ ). Our data set cannot generate a consistent result.

The final results for this station consist of two different estimates. The first is from event 14, and the second is the weighted mean of event 17 and 27.

•**9233 (B14)**: One event (event No. 27) is available for this station. Both the transverse and radial components are strong and the result is well resolved.

•**9235 (B17)**: The two events (event No. 25 and 27) show strong transverse and radial signals. The results from them are similar. The final result is the weighted mean from the two events.

•**9237 (B24)**: The two events (event No. 25 and 27) show strong transverse and radial signals. The results from them are similar. The final result is the weighted mean from the two events.

•**9250 (B11)**: The SKS signal from the only event (event No. 27) available for this station is noisy and the transverse component is hardly observable. Therefore the final result for this station is probably null, i.e., either has no splitting, or has splitting with fast direction about  $112^\circ$  or  $22^\circ$  with unknown splitting time.

•**9270 (B16)**: The SKS signal from the only event (event No. 27) available for this station is noisy and the transverse component is hardly observable. Therefore the final result for this station is probably null, i.e., either has no splitting, or has splitting with fast direction about  $114^\circ$  or  $24^\circ$  with unknown splitting time.

•**9271 (B20)**: The SKS signal from the only event (event No. 27) available for this station is noisy and the transverse component is hardly observable. Therefore the final result for this station is probably null, i.e., either has no splitting, or has splitting with fast direction about  $111^\circ$  or  $21^\circ$  with unknown splitting time.

•**9272 (B19)**: The two events (event No. 25 and 27) show strong transverse and radial signals. The results from them are similar with ( $\phi = 144 \pm 10^\circ$ ,  $\delta t = 1.2 \pm 0.3s$  for event No. 25, and ( $\phi = 138 \pm 10^\circ$ ,  $\delta t = 1.0 \pm 0.3s$  for event No. 27). The final result is the weighted mean from the two events.

### 3.5 Results

The final results of SKS splitting measurements (Figure 3.4.2, Table 3.3.1) are obtained by weighted averaging according to the 95% confidence interval of each individual measurement. Figure 3.4.2B plots well-defined measurements. The

splitting ranges from 0.3 to 2.1 seconds which is consistent with a layer of 30 to 210 km thick characterized by 4% anisotropy.

- *Area A*

In the middle part of this area, the fast directions are approximately E-W (e.g. A02, A04-07), except for station A09. The station on the northern boundary (A01) and the station on the southern boundary (A11) has a NW-SE fast direction.

- *Area B*

Most of the stations with null measurements and dual- measurements are within this area. Five stations (B01-02, B07, B17, and B24) near the rift axis show fast directions of about NE, which is parallel to the surface expression of the rift and the strike of the two dimensional low velocity structure revealed in Chapters 2 and 4. Rift-parallel fast directions have been observed along the axes of the Rio Grande and the Kenya rifts. More detailed comparison and explanation will be presented in Chapter five. Most of the rest of the stations show fast directions perpendicular to the rift axis. The rapid change of the fast directions on station B17 and B18, which are 30 km apart, may indicate that the source of anisotropy in the area is shallow, at a maximum depth of 50 km, as revealed by the Fresnel zone forward modelling (Figure 3.2.5).

- *Area C*

The fast direction is dominantly NW-SE which is perpendicular to the rift axis.

- *Area D*

In the northern part of this area the fast directions are dominantly perpendicular to the rift axis, while at the transition to the fold belt in northern Mongolia,

the fast direction changes to nearly E-W, i.e. parallel to the faulting and fold axis. The transition takes place between stations D07 and D09, over a distance of about 90 km. Using the result of Fresnel zone forward modeling described in section 3.2.2 (Figure 3.2.5), the maximum depth of the source of the anisotropy near this transition is about 350 km, which is in the asthenosphere or the lithosphere. If the anisotropy contrast lies significantly deeper than this, the Fresnel zone is broader and the transition in the fast directions would spread out over a longer distance than observed. For instance, if the depth is 1000 km, the length of the transition zone would be 200 km.

### **3.6 Tectonic implications**

As mentioned in section 3.1, it is generally believed that the main cause for SKS splitting in the mantle is the preferred orientation in the upper mantle of crystallographic axes of elastically anisotropic minerals such as olivine. Under uniaxial compression, the  $a$ -axis of olivine turns to be perpendicular to the maximum compressional strain direction; under pure shear, it is perpendicular to the shortening direction; and under progressive simple shear, it is aligned in the flow direction. The alignment can be caused by recent or present-day flow in the asthenosphere [Vinnik et al., 1989; 1992], or by fossil anisotropy which was caused by past tectonic events and was maintained in the lithosphere [Silver and Chan, 1989; 1991].

Mobility of olivine crystals at temperatures above 900°C is high and therefore the survival of fossil anisotropy is very unlikely at about 150 km and deeper beneath Precambrian platforms such as the Siberian Craton [Vinnik et al., 1992]. Beneath present-day continental rifts such as the BRZ, the 900°C isotherm is thought to

upward to a depth of about 50 km [Zorin and Osokina, 1984]. The thickness of the layer cooler than 900°C ('rigid layer') is about 50 km in the vicinity of the BRZ.

Away from the BRZ the 150 km rigid layer is enough to generate the observed 1 s splitting. However, near the rift axis (in area B), the thickness of the rigid layer is too small to generate the observed splitting, if all the anisotropy is fossil anisotropy. Therefore at least part and probably most of the observed splitting must originate in the asthenosphere. Our observations (Figure 3.4.2) reveal that the dominant fast directions beneath the Siberian platform, the BRZ, and the northern part of the Mongolia fold belt are all NW-SE. If the anisotropy observed in area C and D (Figure 3.4.2) are fossil anisotropies, their fast directions are accidentally the same as the present-day anisotropy observed in area B. If we assume that the fossil and present-day fast directions are random, then the probability of the two having similar ( $\pm 20^\circ$ ) values is about 1/9. Because the Siberian platform and the Mongolian fold belt may have experienced different tectonic deformation and as a result the probability for all the three different tectonic regions having the same fossil anisotropy is even smaller. Therefore the observed anisotropy is unlikely to be fossil anisotropy.

Another fact arguing against the fossil anisotropy theory is the transition of fast directions from NW-SE to EW in northern Mongolia. The transition takes place in the same tectonic unit and does not correspond to any major geologic discontinuity on the surface. The fossil anisotropy within a tectonic unit is expected to be the same.

In the NE part of the BRZ (area A), the observations also favor recently generated anisotropy. Inside the E-W left-lateral shear zone which traverses the

central part of the area along approximately  $56.5^{\circ}\text{N}$  (see Figure 5.3.2 in Chapter 5), the fast directions are parallel or sub-parallel to the shear direction, similar to the results obtained along the northern California part of the San Andreas fault [Savage and Silver, 1993]. The shearing is a result of the opening of the main part of the BRZ. Outside the shear zone the fast directions become approximately perpendicular to the rift axis.

The fast direction for the southern part of the profile is roughly E-W. This may have been generated in a layer of mantle deformed by the collision of India and Asia. It could also reflect fossil anisotropy. However, this fast direction is consistent with the dominant direction found across the Tibetan Plateau [McNamara et al., 1994]. Both the Tibetan and the Mongolian Plateaus have been deformed by Cenozoic deformation related to the collision. The observed fast directions in both regions may have the same origin, i.e., the recent continental collision.

The major features of the SKS splitting observations, as well as the P-wave travel time residuals described in Chapter two, are explained by a small-scale mantle convection model described in Chapter five.

## FIGURE CAPTIONS

Figure 3.1.1: Schematic diagram showing a ray path of the SKS phase. The source is on the left and the receiver on the right side. Before entering the Core, the orientation of the S-wave is determined by the focal mechanism, source side anisotropy and other factors; at the CMB, the S-wave converts to P-wave and travels through the liquid outer Core; at the CMB on the receiver side, the P-wave converts to radially polarized S-wave. When this linear S-wave encounters a zone of anisotropy, it splits into two orthogonal components with different speeds, which combined forms an elliptically polarized wave.

Figure 3.1.2: Diagram showing velocities of P-waves traveling along different crystallographic axes of an olivine crystal. The fastest direction is along the  $a$ -axis with  $V_a = 9.87$  km/s; along the  $b$ -axis the P wave has the slowest velocity with  $V_b = 7.73$  km/s; and along the  $c$ -axis the P-wave has the intermediate velocity with  $V_c = 8.65$  km/s.

Figure 3.1.3: Schematic diagram showing the preferred orientation of olivine crystallographic axes under upper mantle horizontal and vertical flows beneath a continental or oceanic rift.

Figure 3.1.4: SKS splitting measurements at 6 stations in the Rio Grande rift [Sandvol et al., 1992]. The orientation of the bars drawn through each dot gives the fast polarization direction; the size of the dots is proportional to the splitting time. Also shown are topography and major rivers in the area.

Figure 3.1.5: SKS splitting measurements at 14 stations in the East African rift [Gao et al., 1994c].

Figure 3.2.1: Diagram showing geometric relations between the un-split SKS ( $S(t)$ ), the fast component ( $S_f(t)$ ), and the slow component ( $S_s(t)$ ).

Figure 3.2.2: Diagrams showing the radially polarized SKS phase and contour maps of the error function for different parameters ( $\theta_0, \delta t_0$ ), and different noise levels (s2n) for  $f = 0.4$  Hz. For all the contour maps  $\delta t_0 = 1.5$  sec and the  $\theta$ 's used are labeled on the right side of the maps. Each page is for a different s2n, which is indicated in the icon on the lower-left corner of each page.

Figure 3.2.3: Same as Figure 3.2.2 but for  $f = 0.1$  Hz.

Figure 3.2.4: Modeling the maximum depth of anisotropy contrast from length of transition zone at surface.

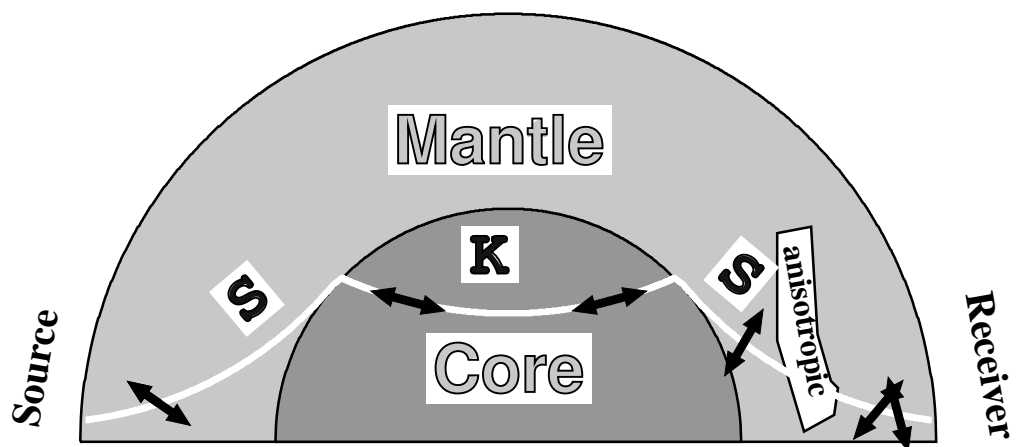
Figure 3.2.5: Fast directions calculated using synthetic seismograms along 10 profiles across an anisotropy boundary, which is at zero distance. Each profile is for an anisotropy boundary at different depth, which ranges from 50 to 500 km.

Figure 3.3.1: A Mercator projection map showing locations of stations used in the study of SKS splitting.

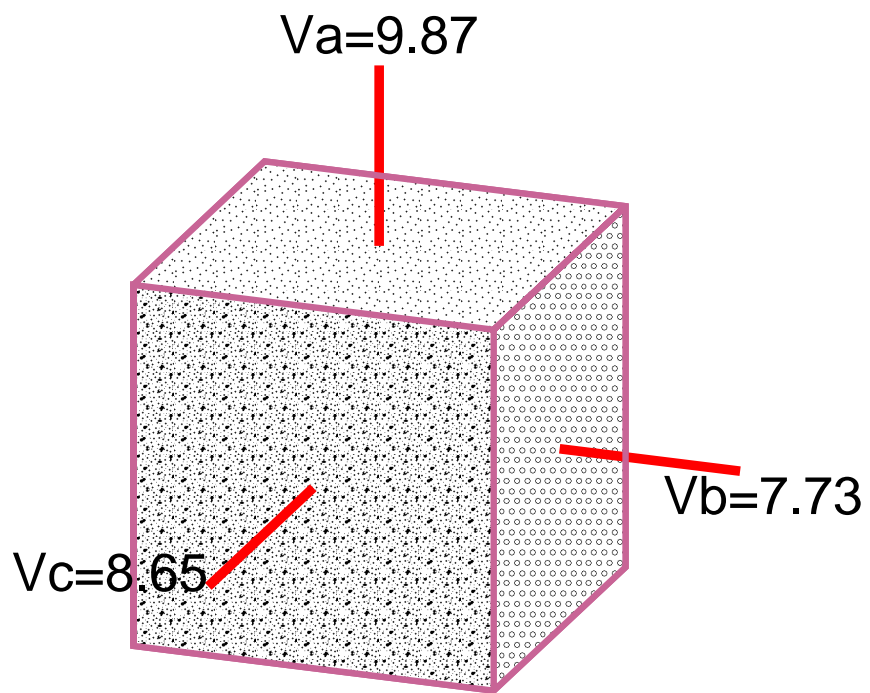
Figure 3.3.2: An azimuthal equidistant projection map showing epicenters of events used in the study of SKS splitting. The center of the map is station B15 (9224), which is on the southern shore of the Lake. The three circles represent  $45^\circ, 90^\circ$ , and  $135^\circ$  epicentral distances.

Figure 3.4.1: Diagrams showing (A) original seismograms of radial and transverse components and (B) their particle motion pattern, (C) corrected seismograms of radial and transverse components and (D) their particle motion pattern, and the contour map of the error function (E). The seismograms in (C) were corrected from those shown in (A) using the optimal parameter pair indicated by a dot on (E). Station and event names, back azimuth (BAZ) and distance (DIST) of the event relative to the station, as well as the optimal parameters and their errors are indicated on the lower-right part of each page. The 95% confidence region is confined by a thick contour line, which is 1.3 times the minimum value of the error function.

Figure 3.4.2: Maps showing the region with the stations of the seismic array extending from the Siberian platform across the Baikal rift zone into Mongolia. The diagram on the top is a two-times enlargement of the rectangle in the lower diagram. Figure A shows all the measurements, including well defined single measurements, dual- measurements, and null measurements; Figure B shows only well-defined single measurements. Stations with well-defined measurements are represented by single circles with size proportional to the splitting. The line drawn through each circle gives the fast polarization direction. Those with 2 inconsistent results are plotted as double circles. Stations represented by squares are null measurements on which anisotropy effect cannot be clearly observed. Filled circles are previously measured [Gao et al., 1994a].



**Figure 3.1.1**



**Figure 3.1.2**

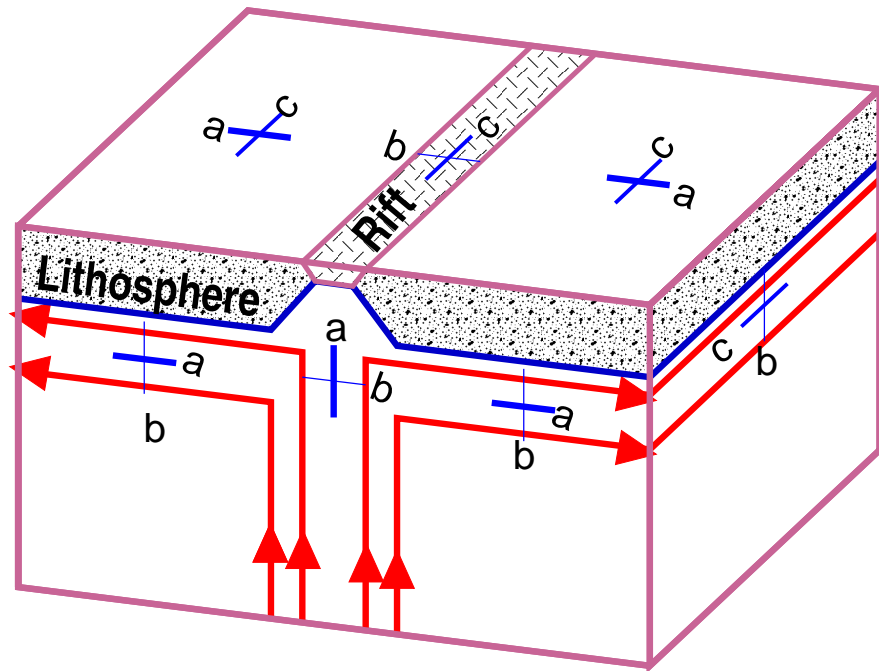


**Figure 3.1.3**

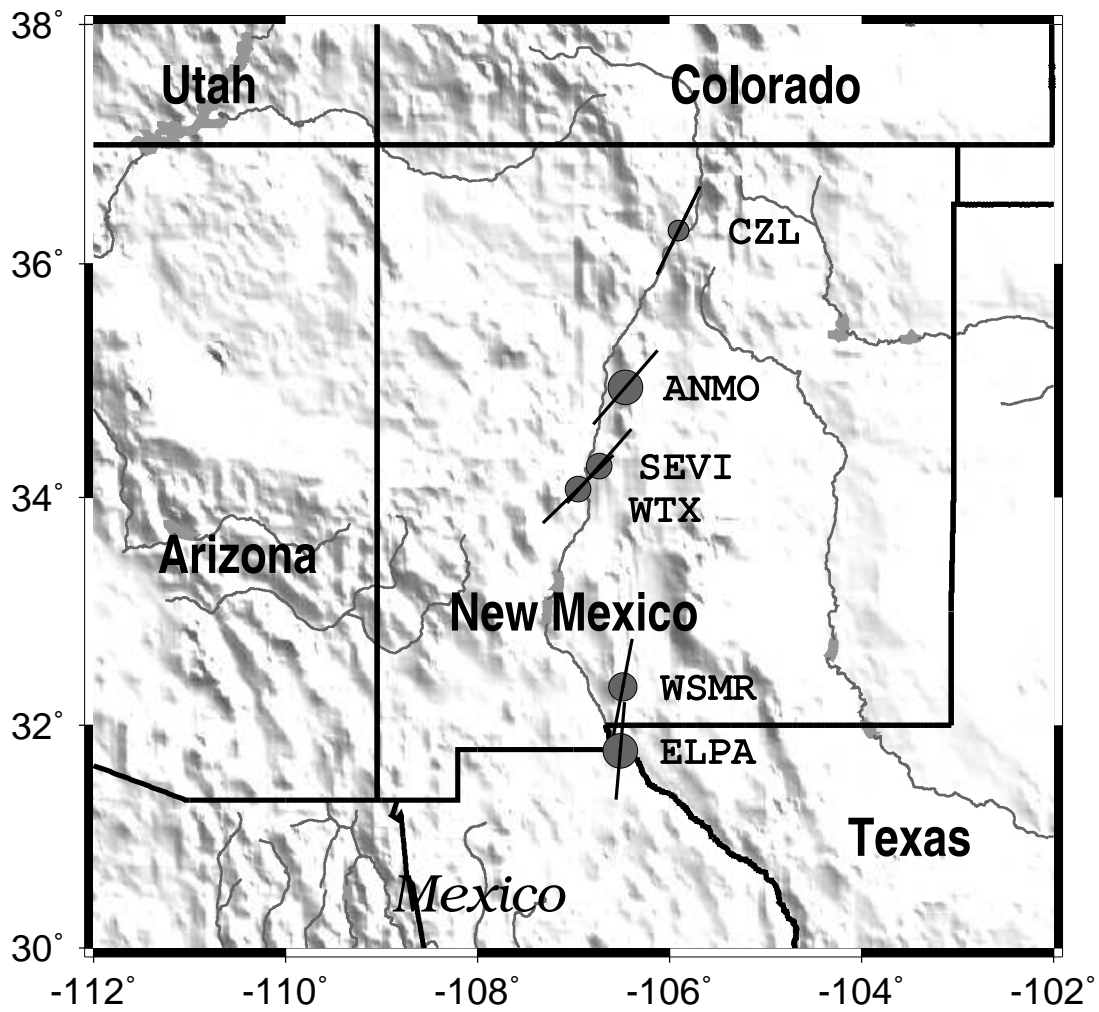


**Figure 3.1.4**

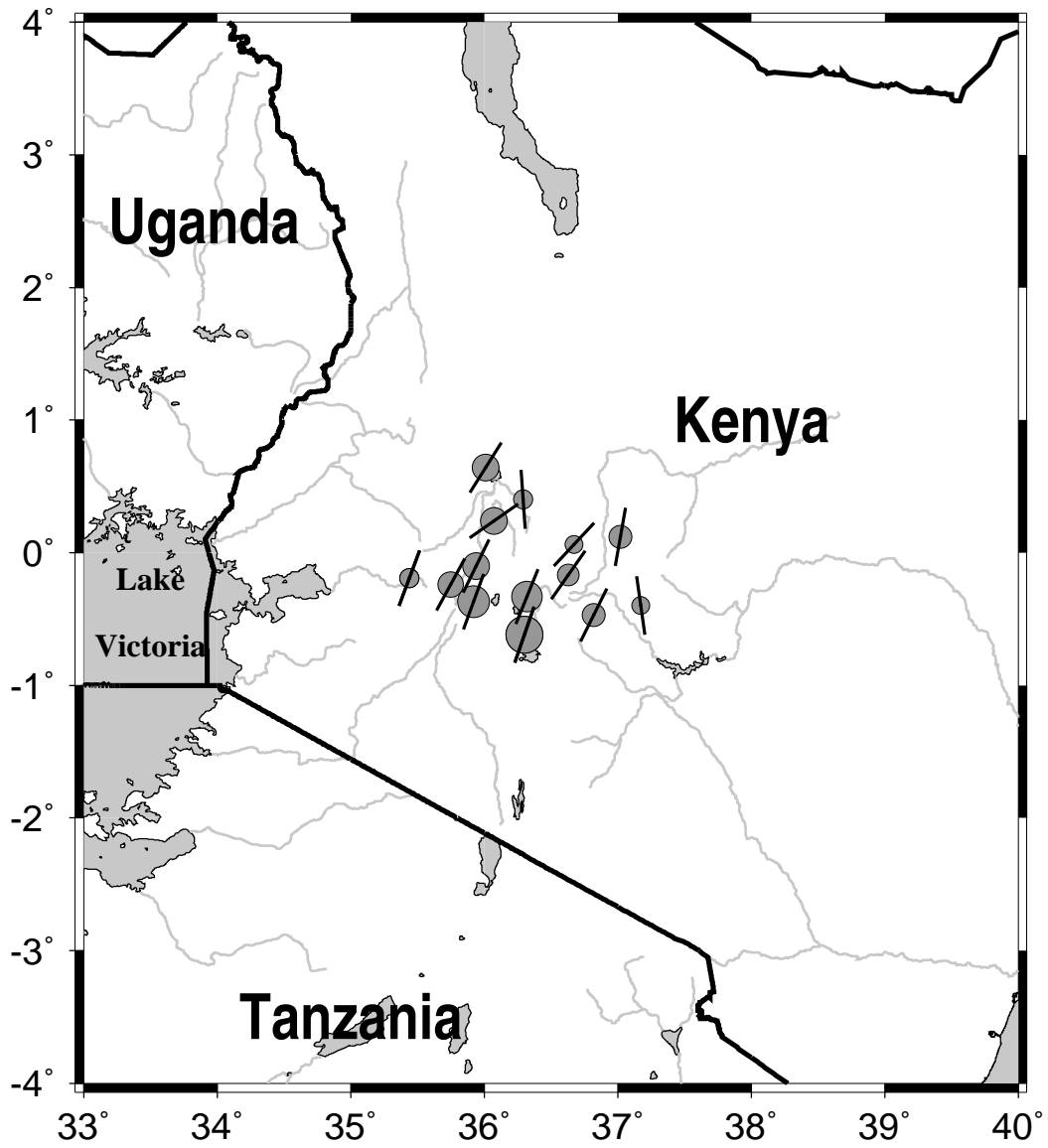


**Figure 3.1.5**

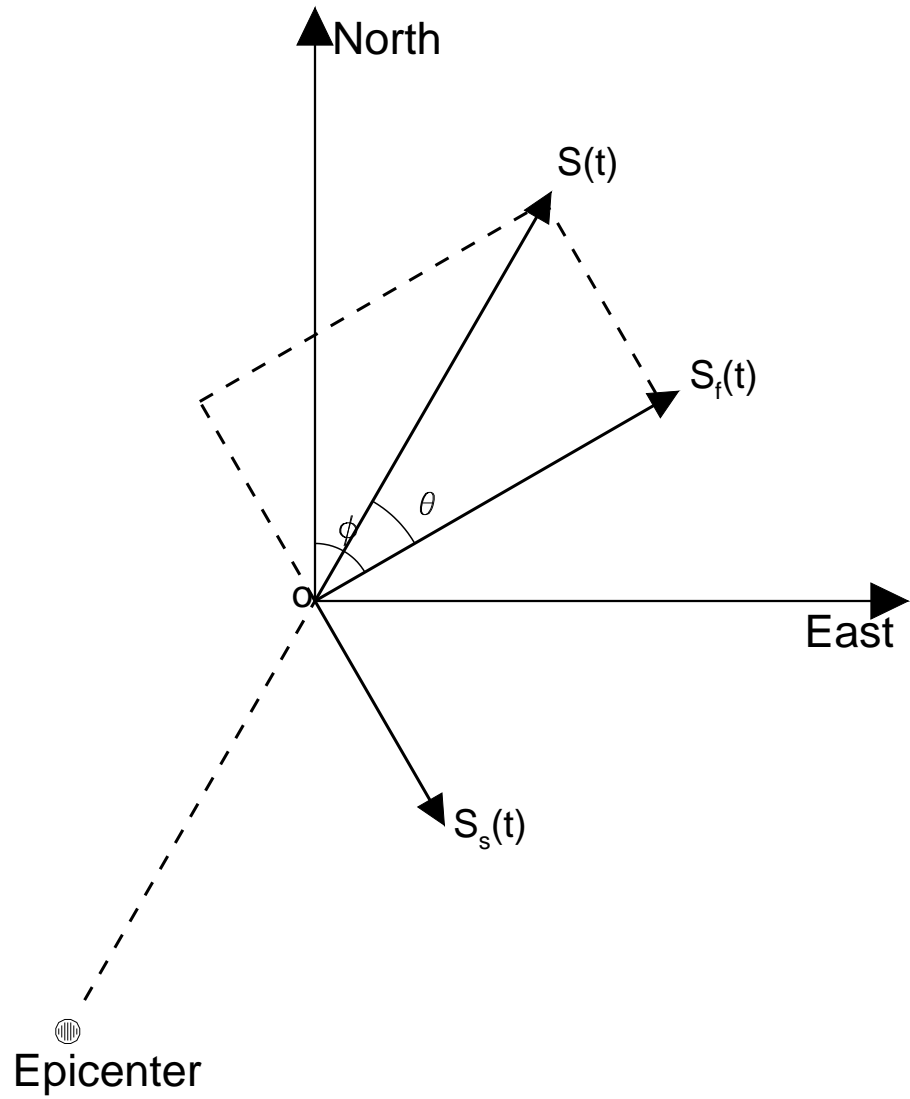


Figure 3.2.1

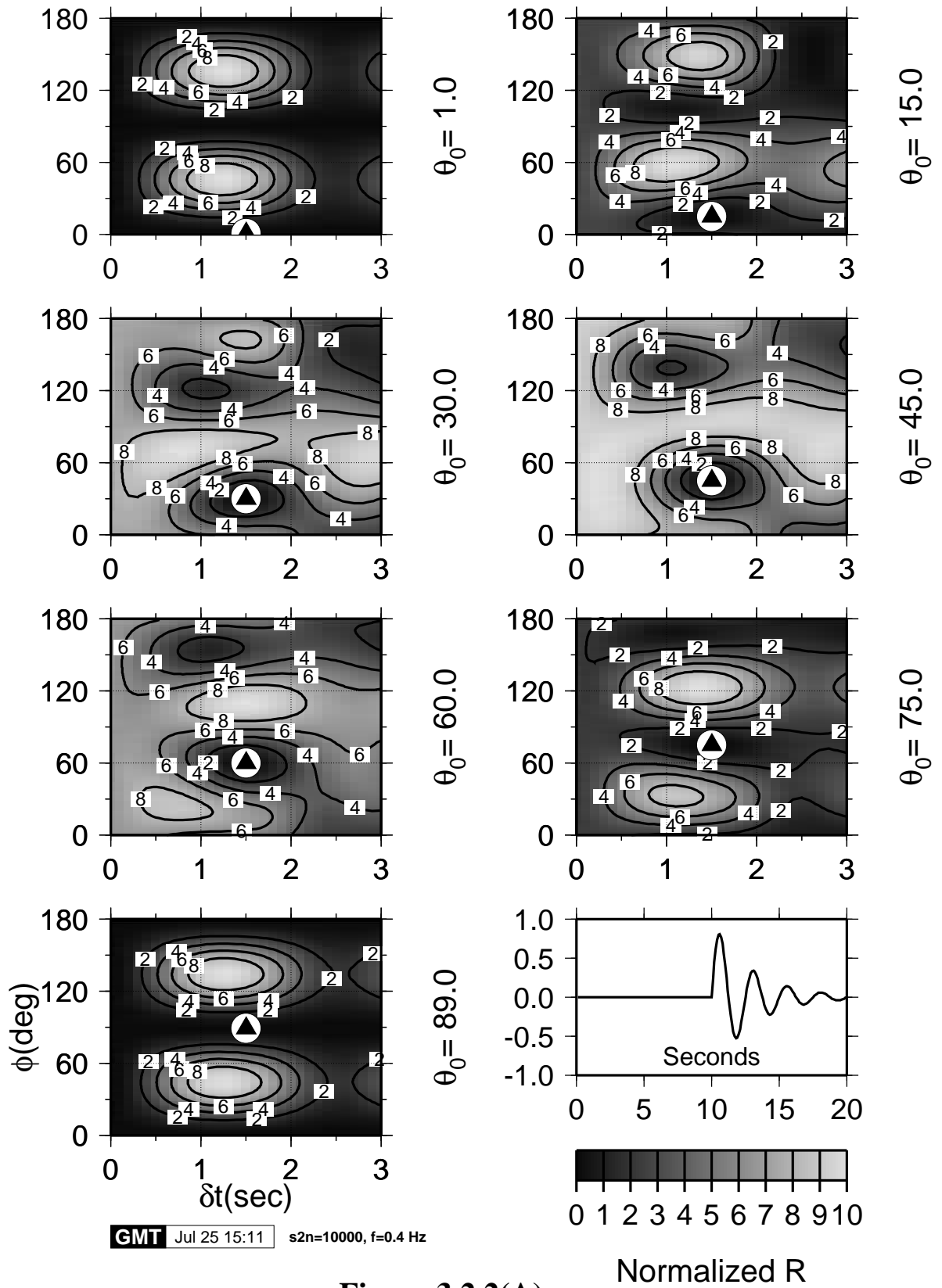


Figure 3.2.2(A)

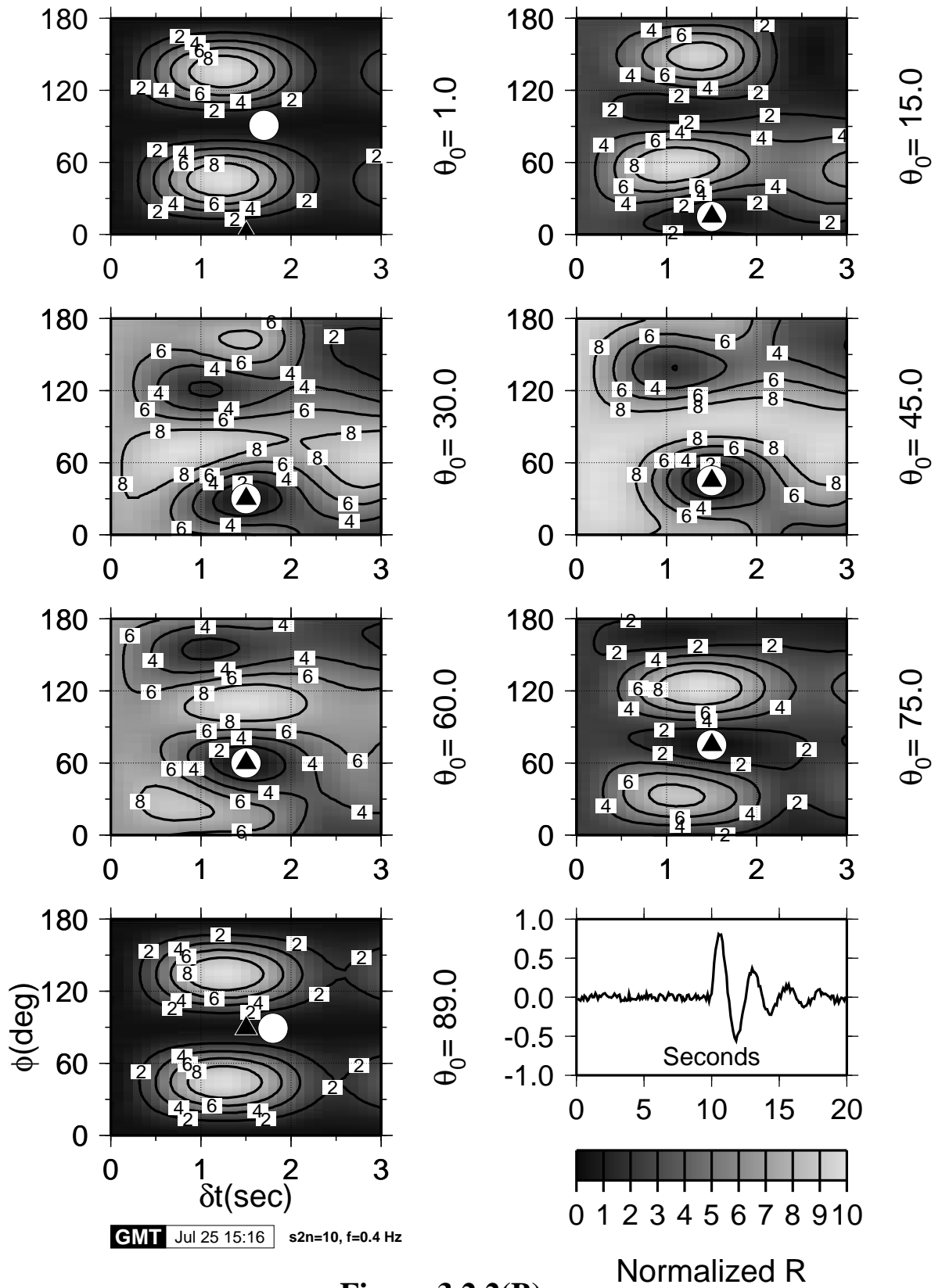


Figure 3.2.2(B)

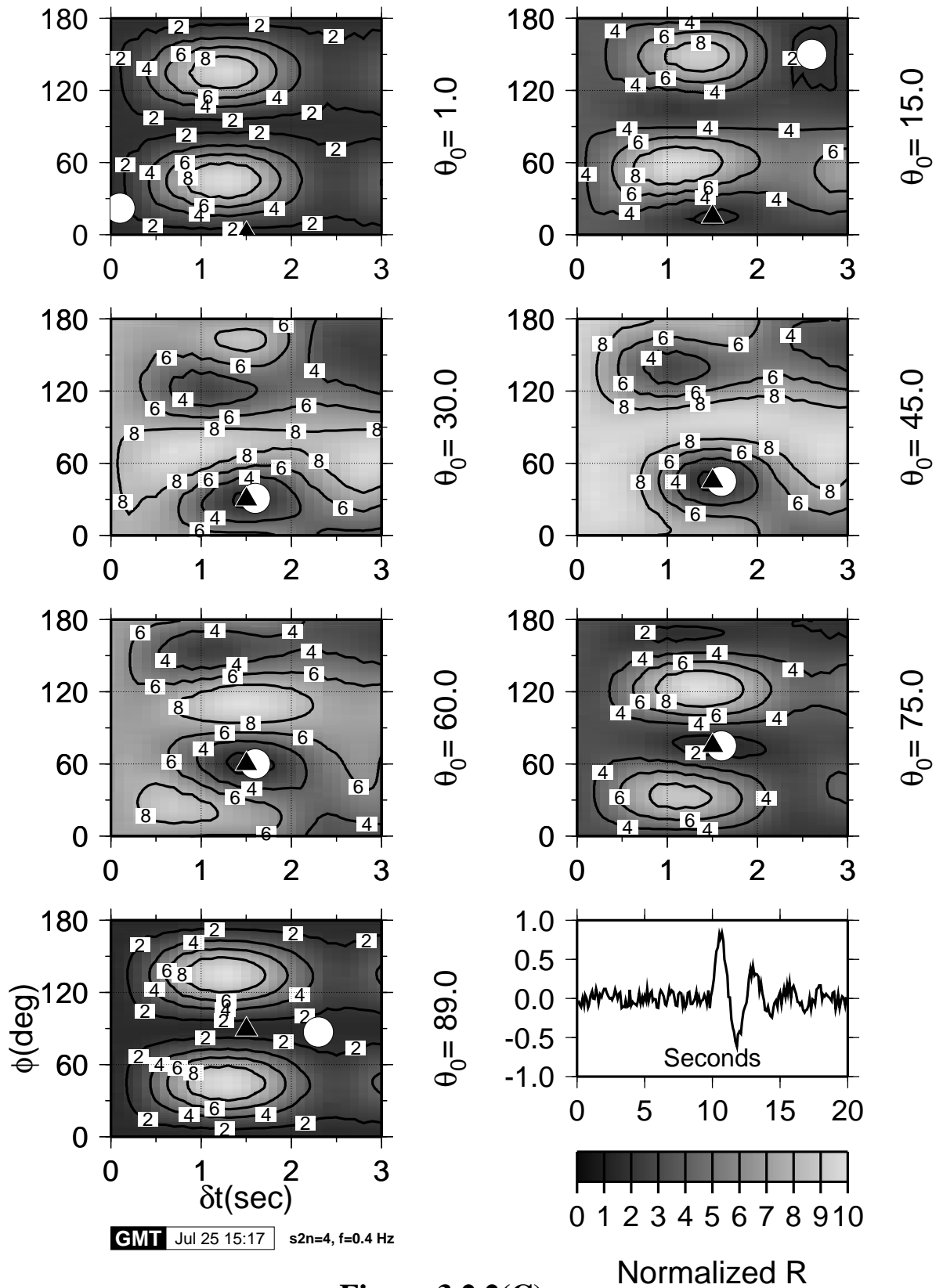


Figure 3.2.2(C)

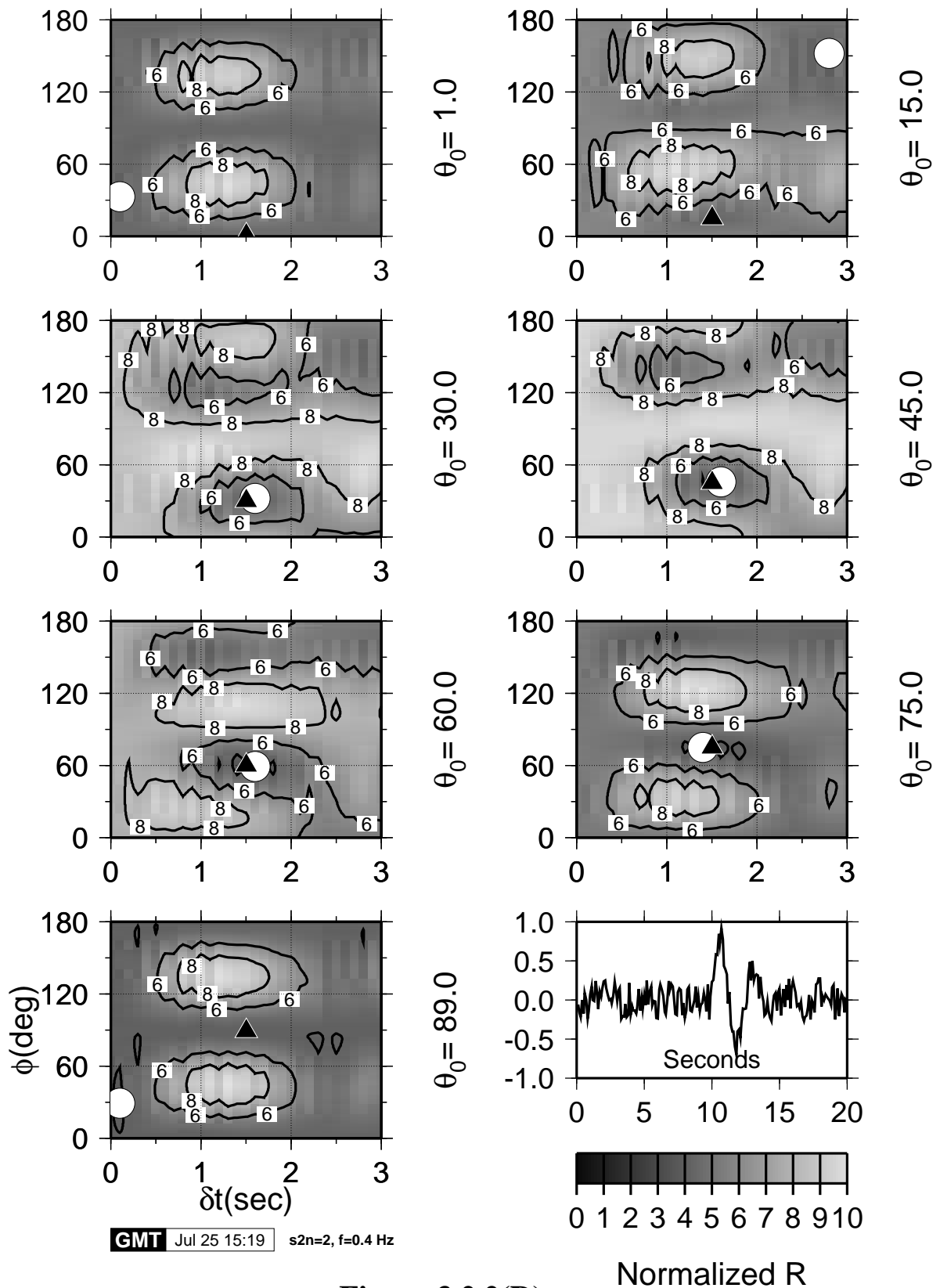


Figure 3.2.2(D)

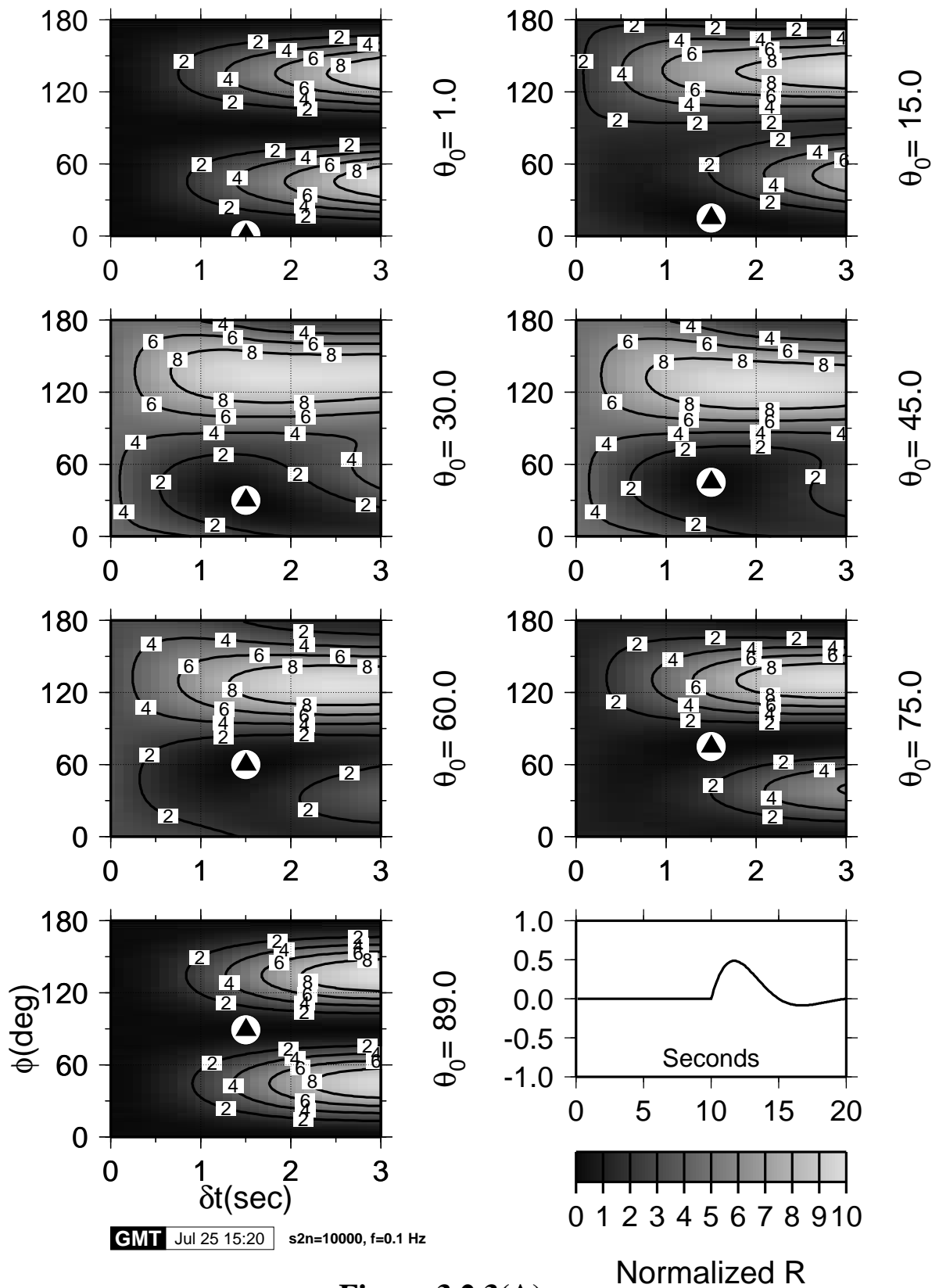


Figure 3.2.3(A)

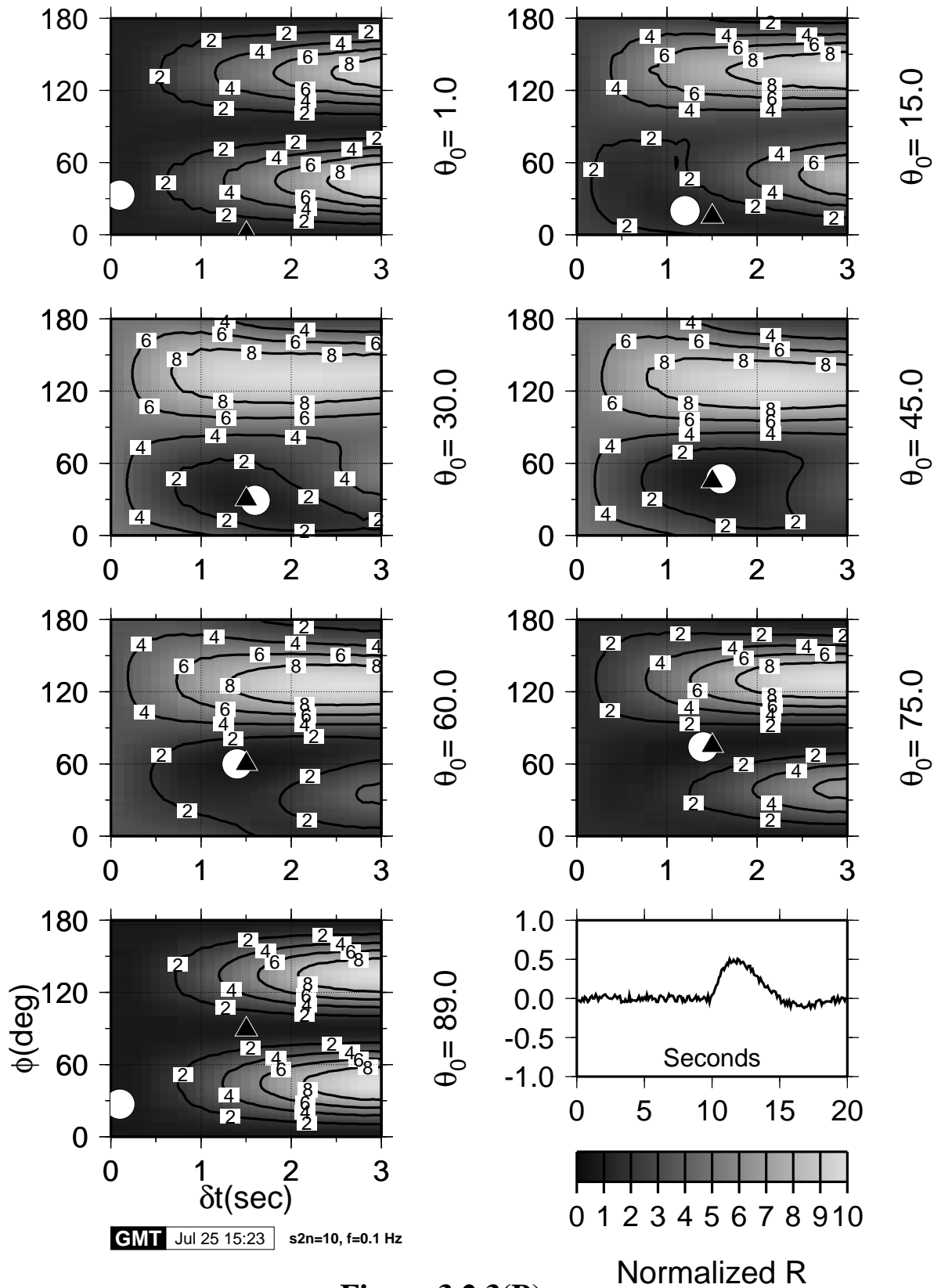


Figure 3.2.3(B)

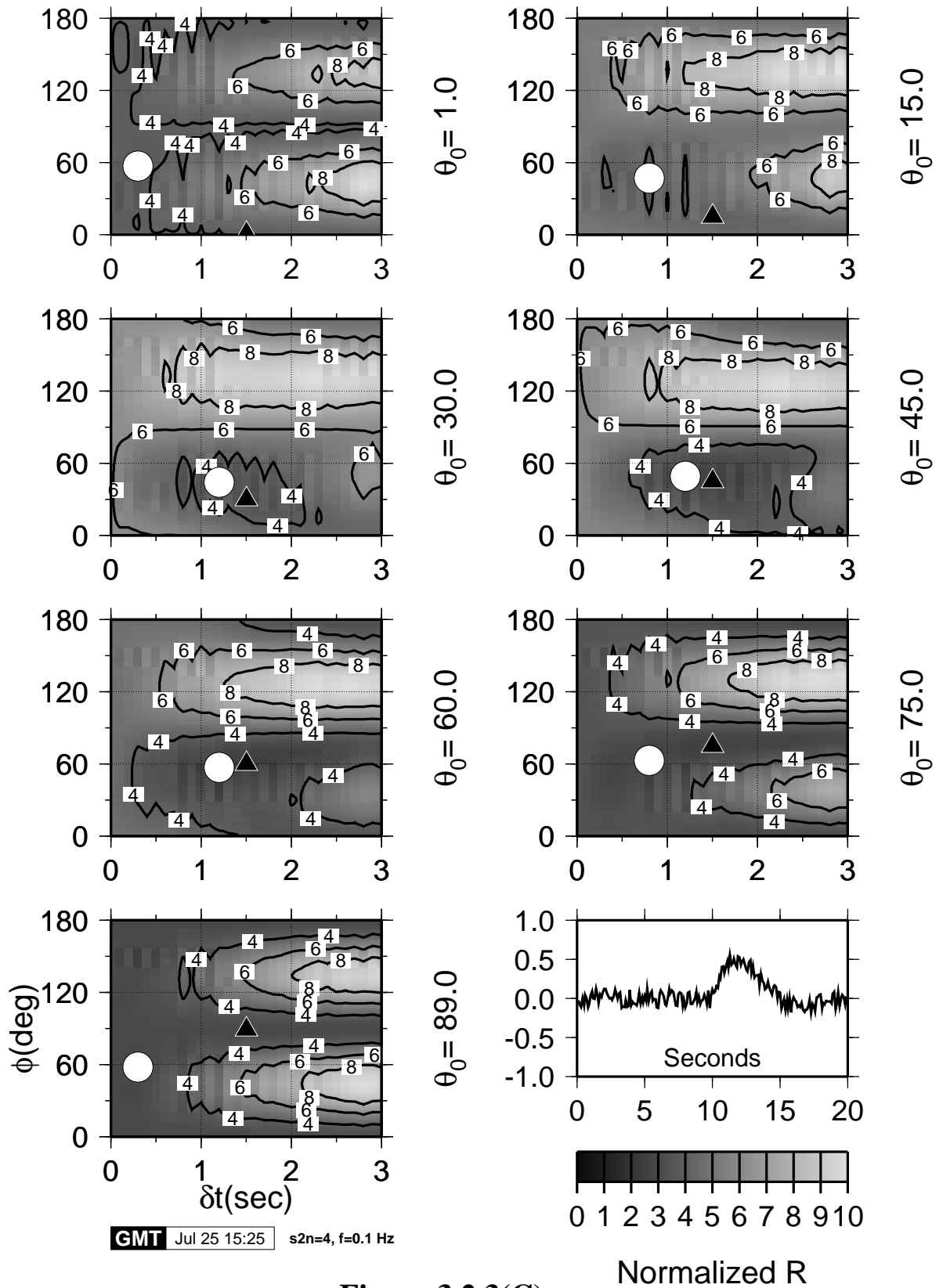


Figure 3.2.3(C)

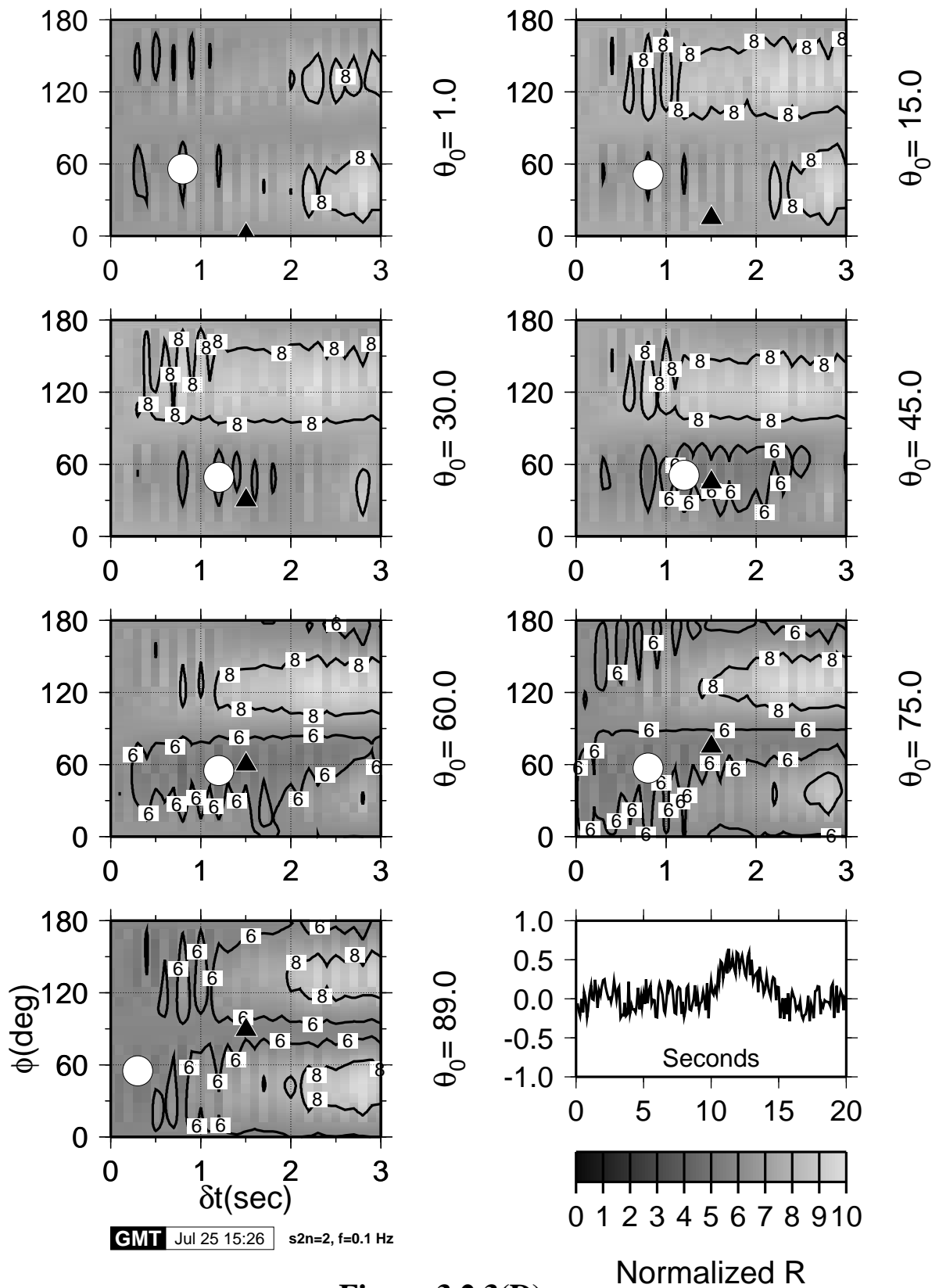


Figure 3.2.3(D)

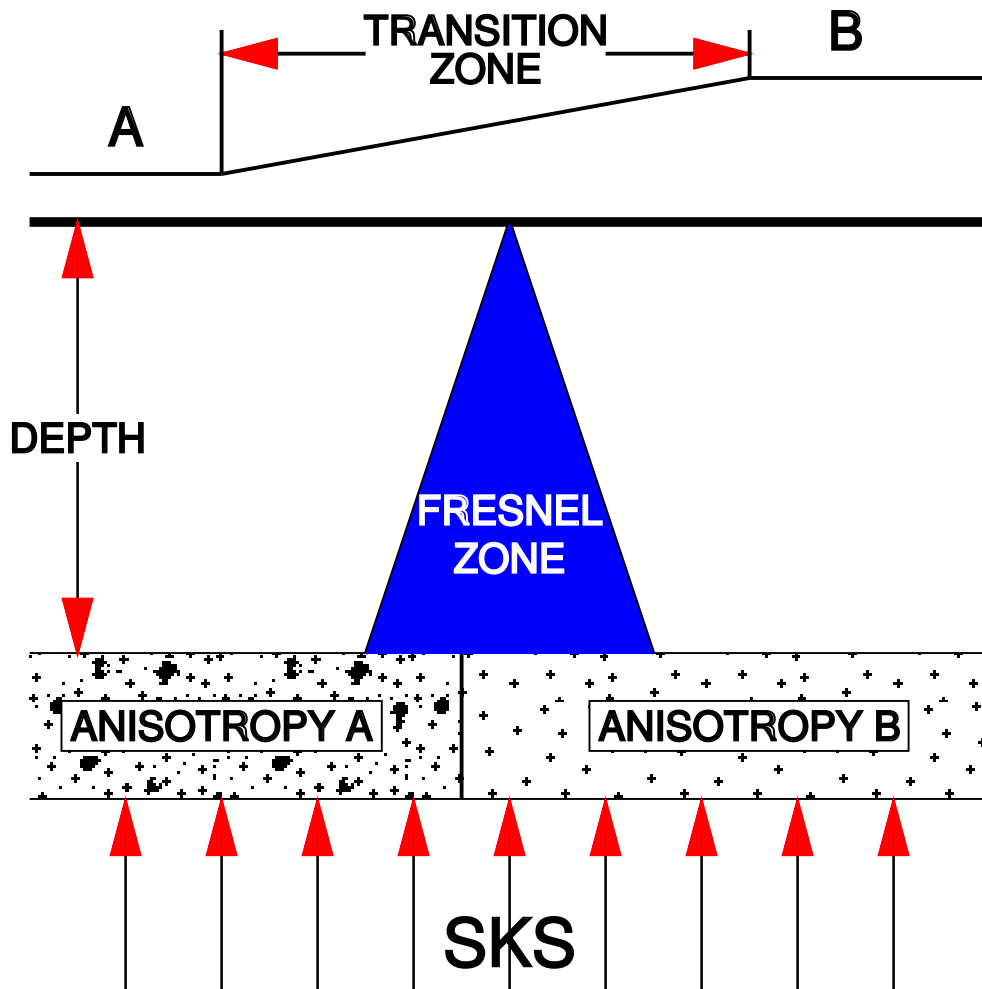
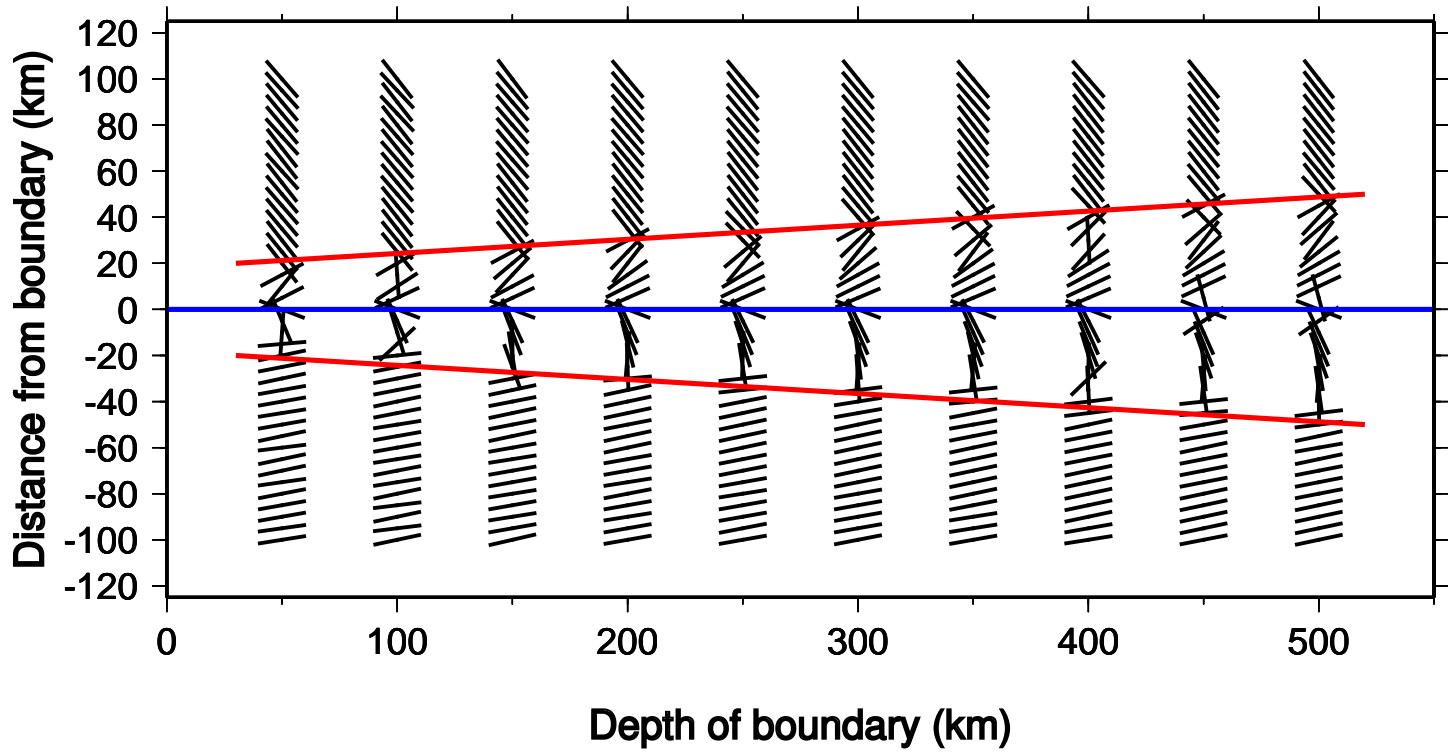
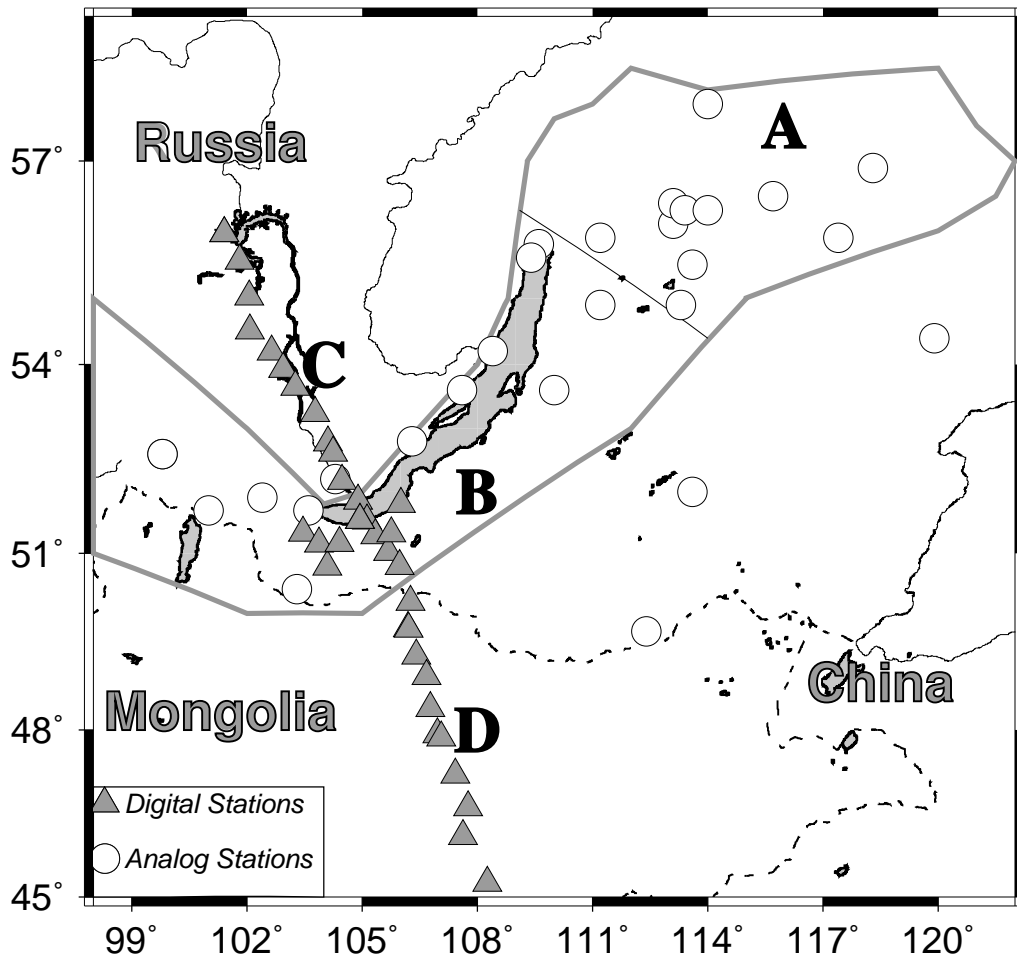


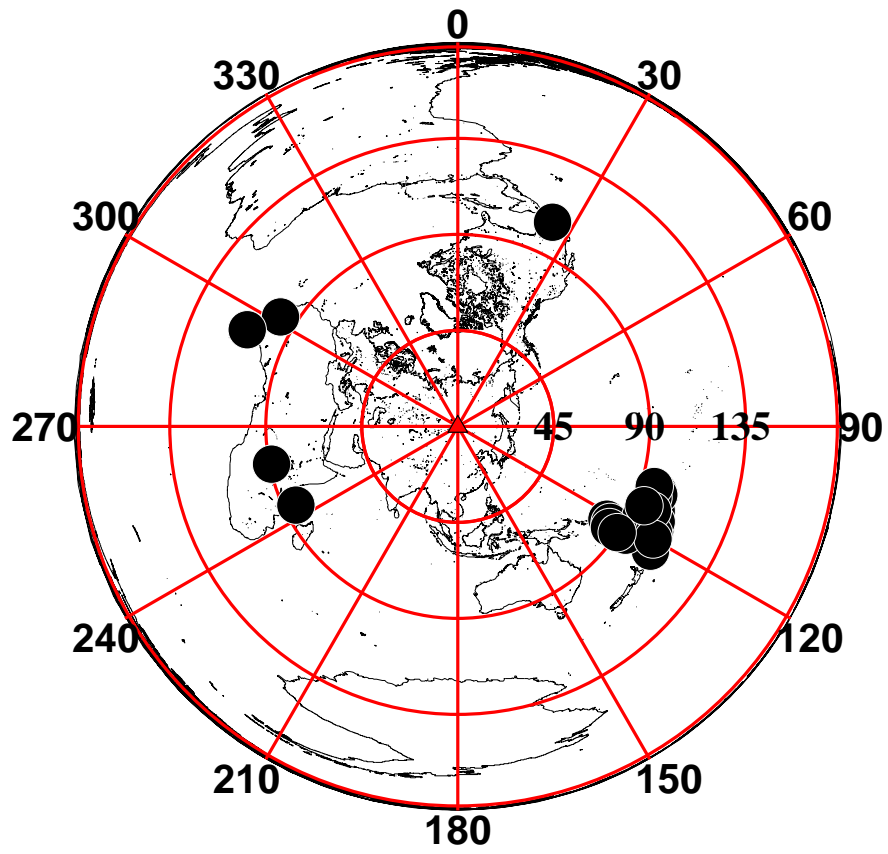
Figure 3.2.4

Figure 3.2.5

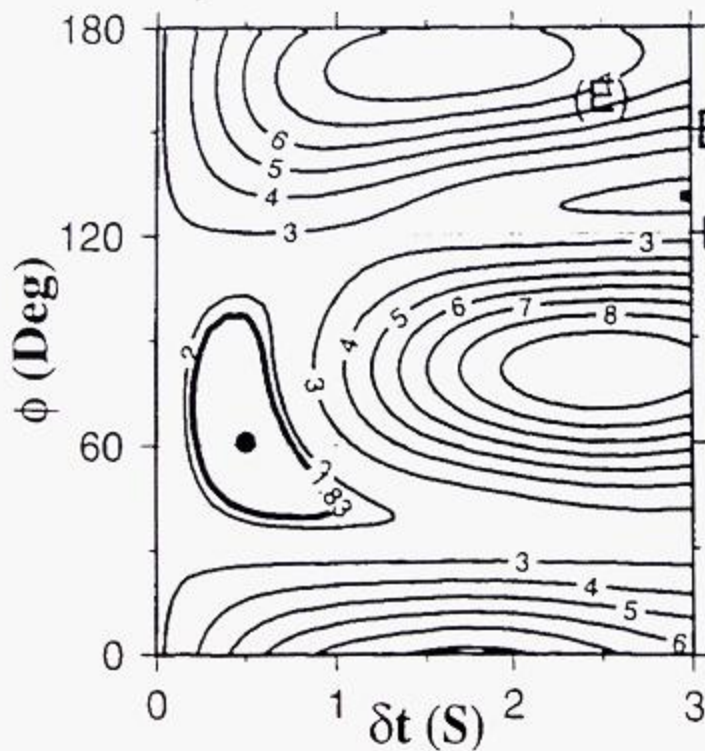
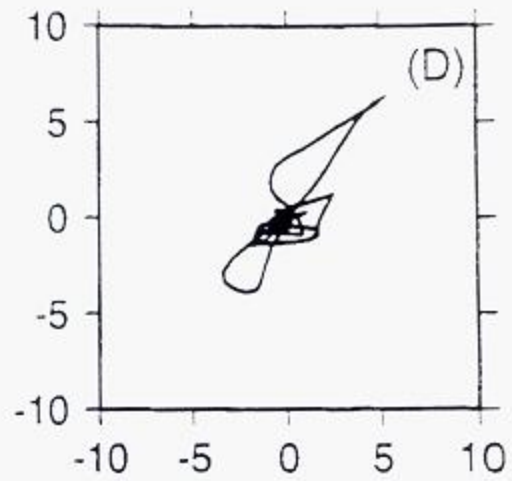
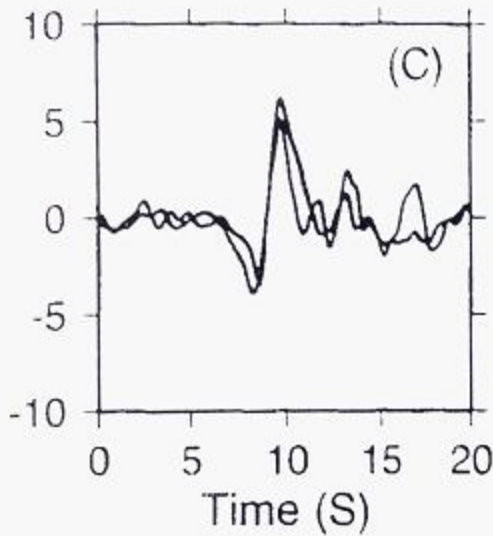
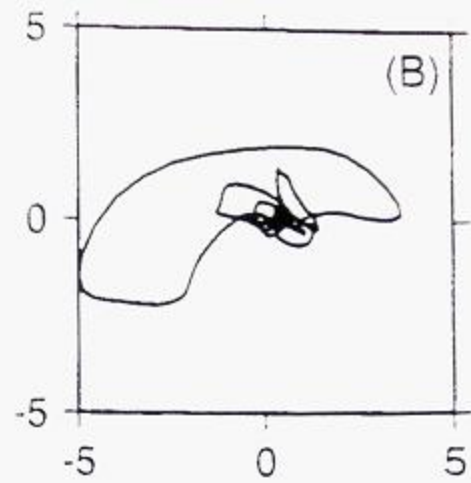
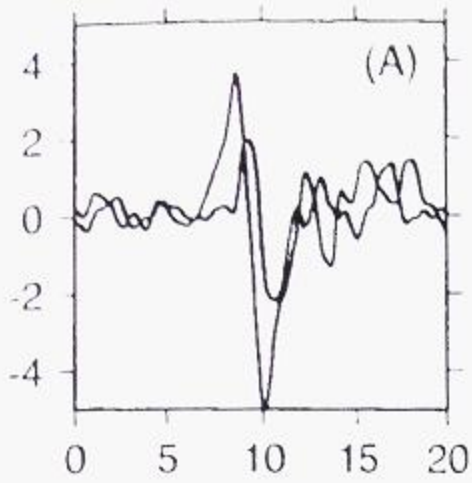




**Figure 3.3.1**

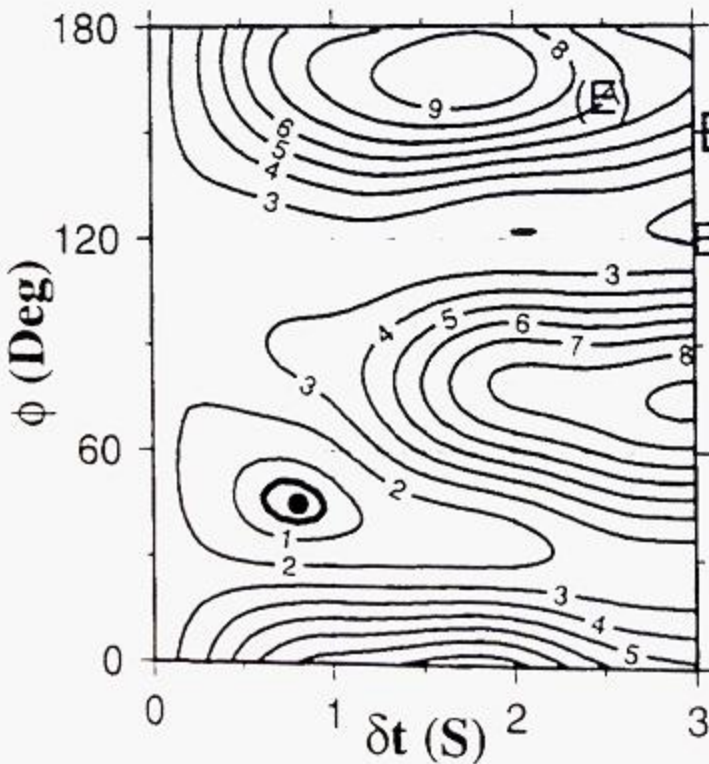
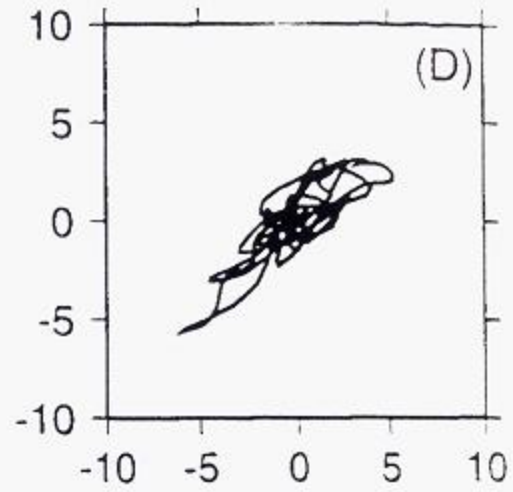
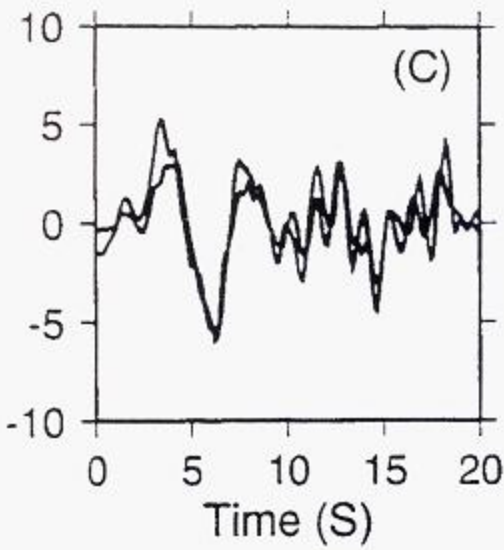
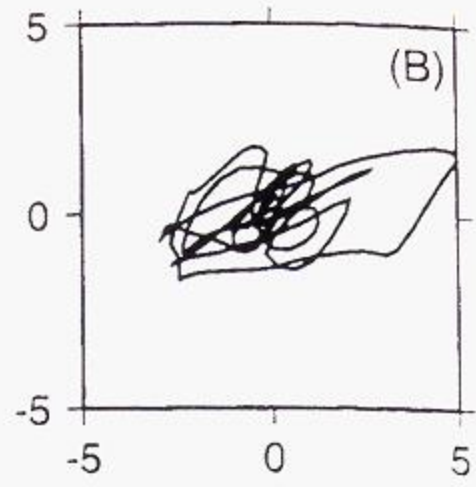
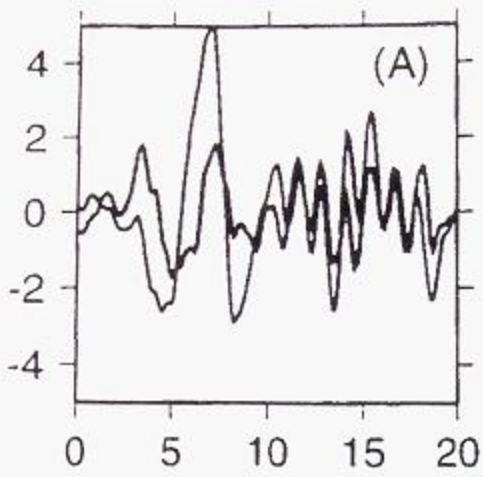


**Figure 3.3.2**



Station: kala (A08)  
 EQ890700505 (No.14)  
 BAZ= 117.9 °, Dist= 92.8 °  
 $\phi = 61.0^\circ$ ,  $\delta t = 0.5$  s  
 $\sigma_\phi = 35.0^\circ$ ,  $\sigma_{\delta t} = 0.3$  s

Figure 3.4.1.A08



Station: tyrg (B07)

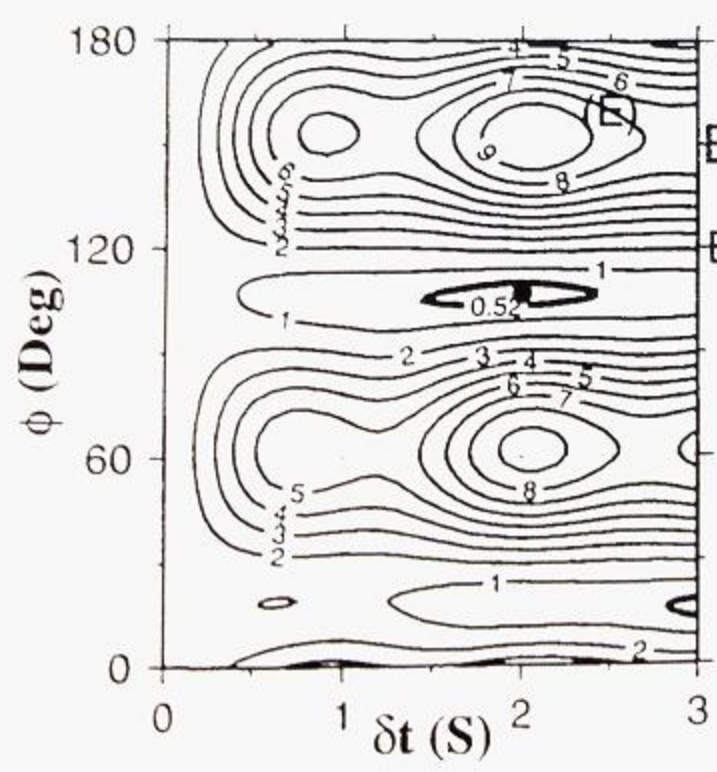
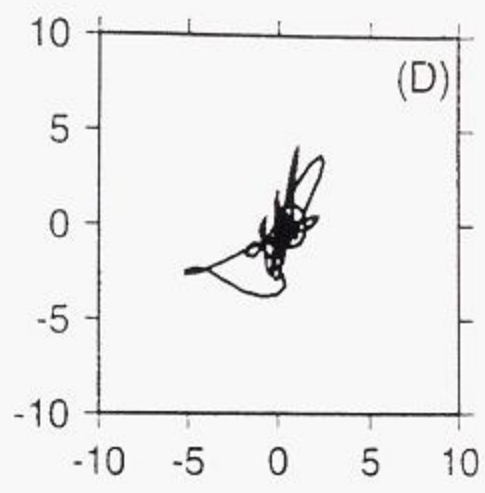
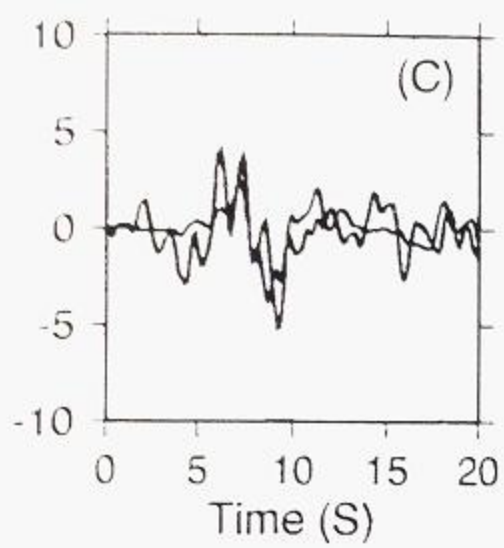
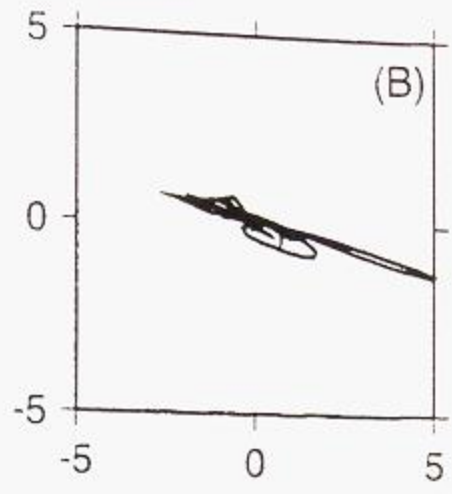
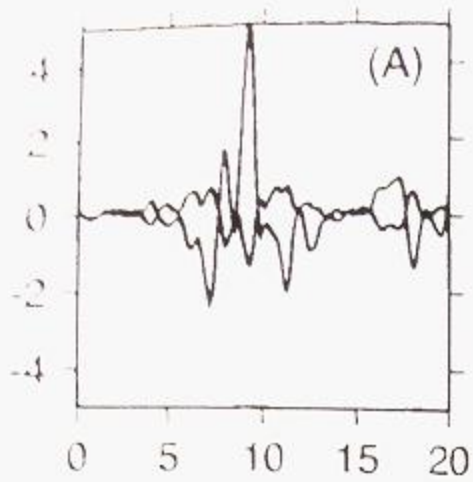
EQ801041804 (No.01)

BAZ= 114.8 °, Dist= 100.6 °

$\phi = 45.0^\circ$ ,  $\delta t = 0.8$  s

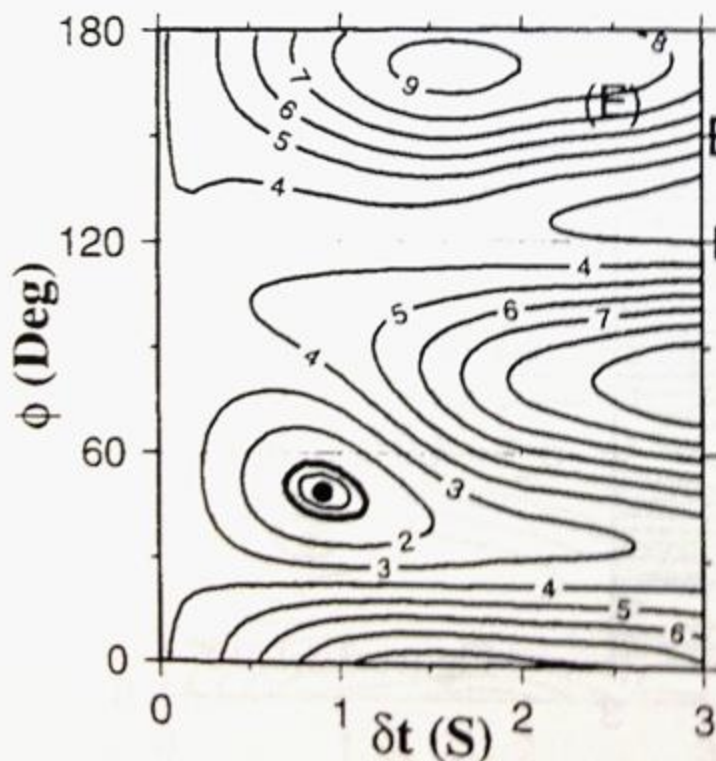
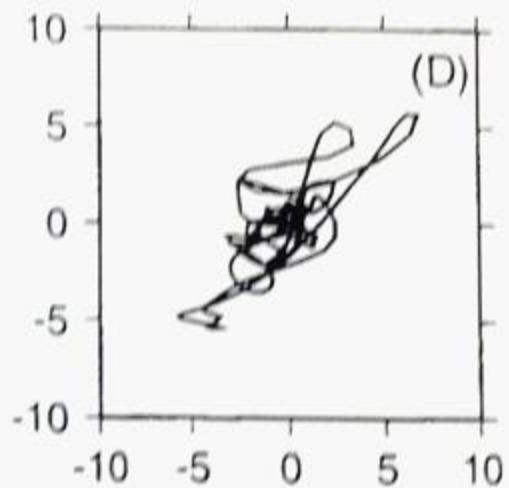
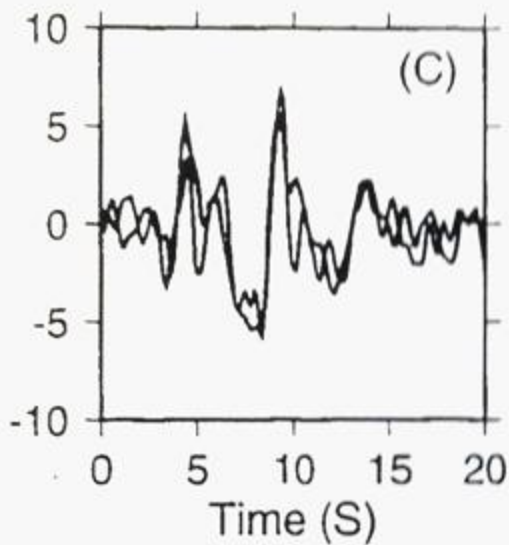
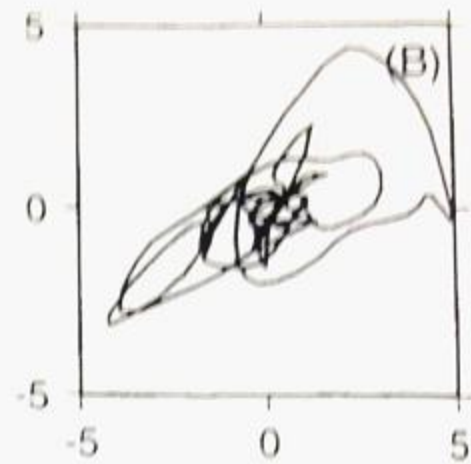
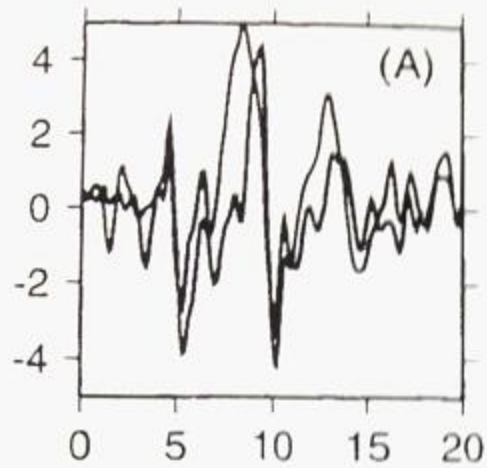
$\sigma_\phi = 6.0^\circ$ ,  $\sigma_{\delta t} = 0.2$  s

Figure 3.4.1.B07



Station: tyrg (B07)  
 EQ861461906 (No.09)  
 BAZ= 115.7 °, Dist= 95.8 °  
 $\phi = 107.0^\circ$ ,  $\delta t = 2.0$  s  
 $\sigma_\phi = 4.0^\circ$ ,  $\sigma_{\delta t} = 0.5$  s

Figure 3.4.1.B07



Station: tyrg (B07)

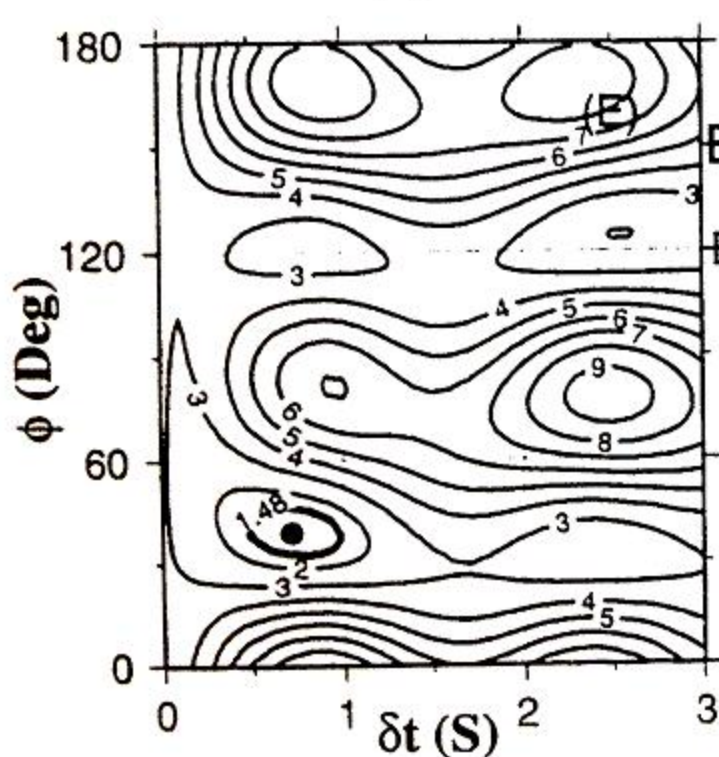
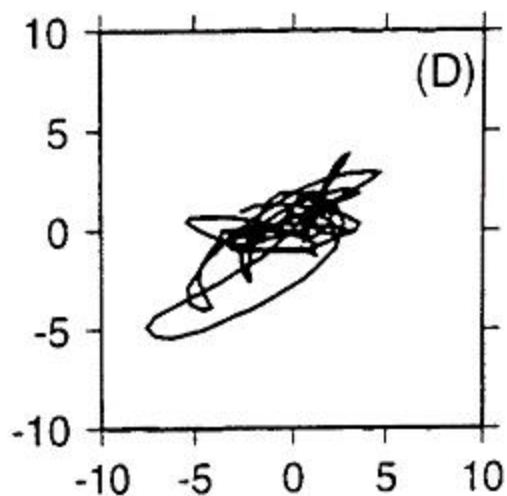
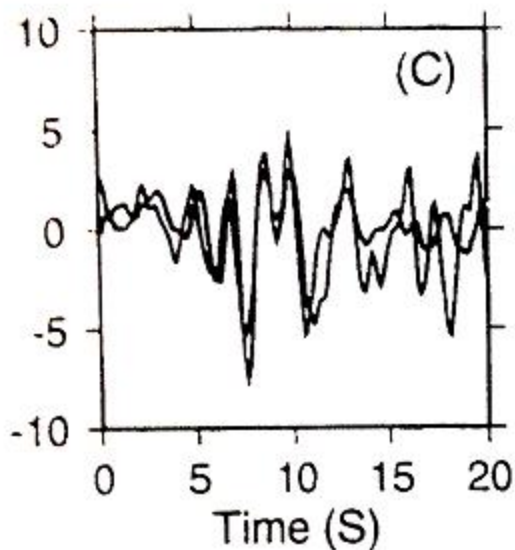
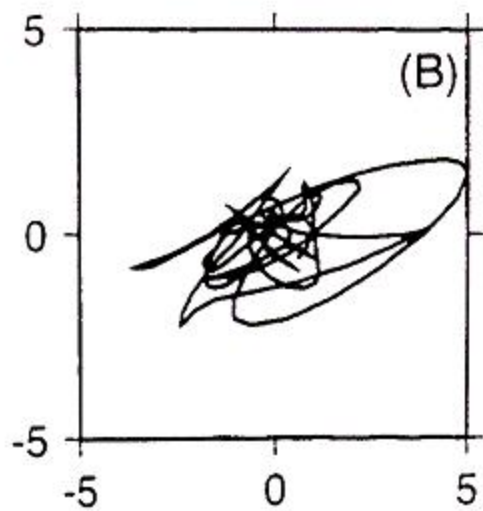
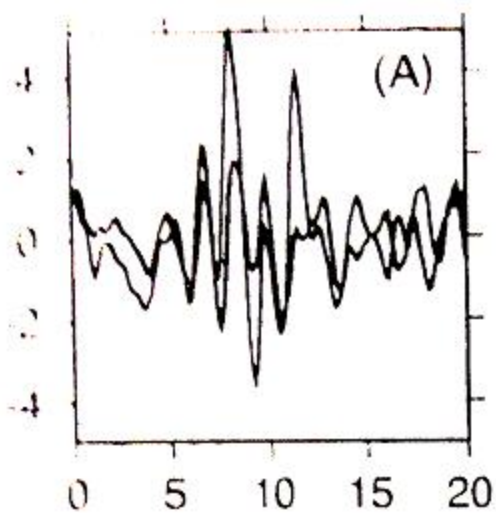
EQ863030128 (No.10)

BAZ= 113.2 °, Dist= 99.6 °

$\phi = 49.0^\circ$ ,  $\delta t = 0.9$  s

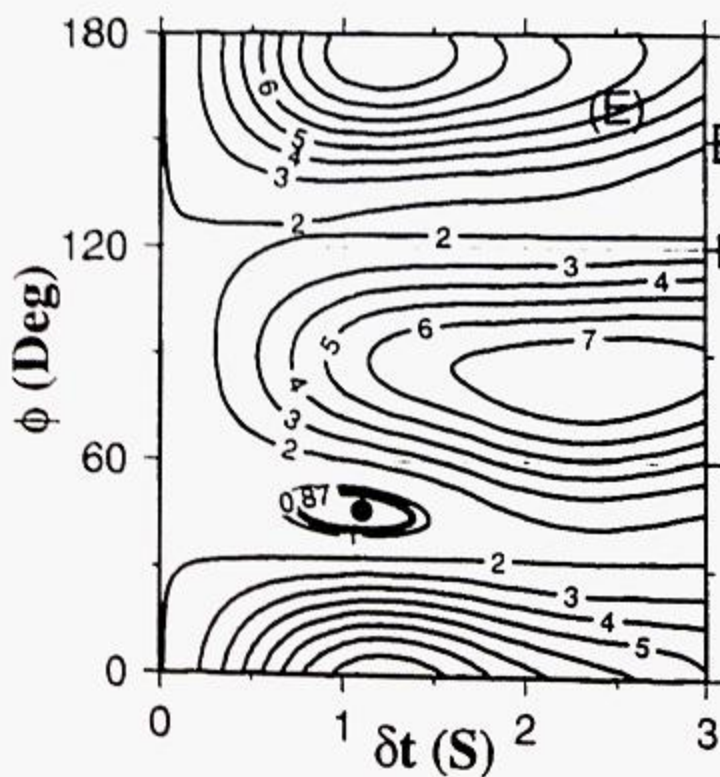
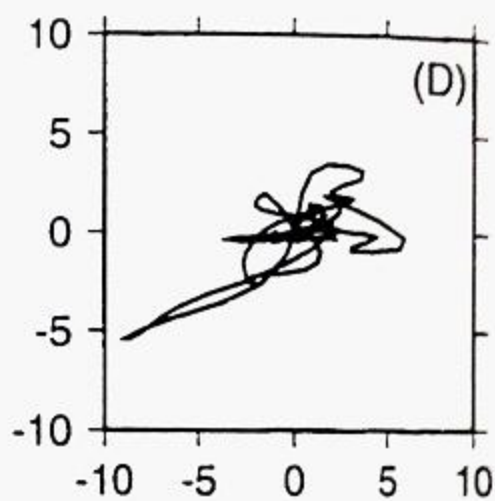
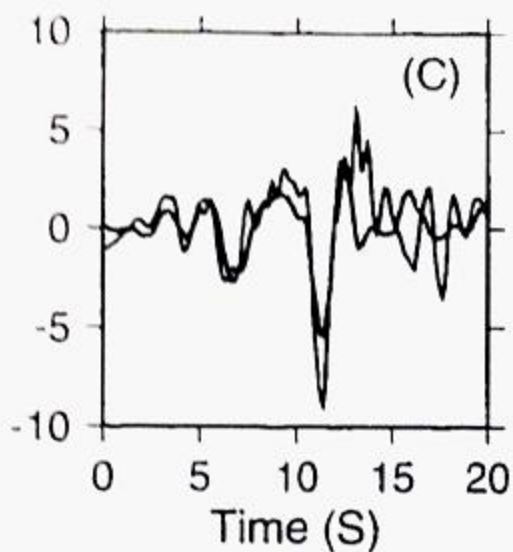
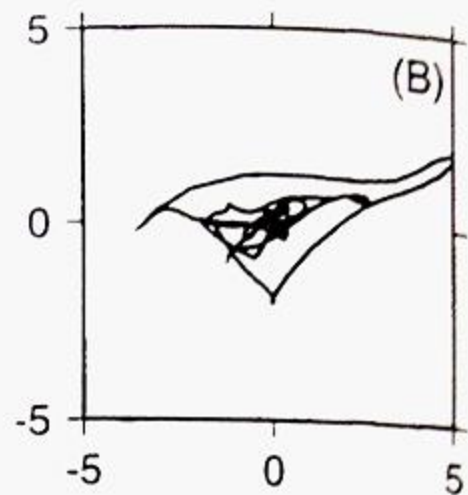
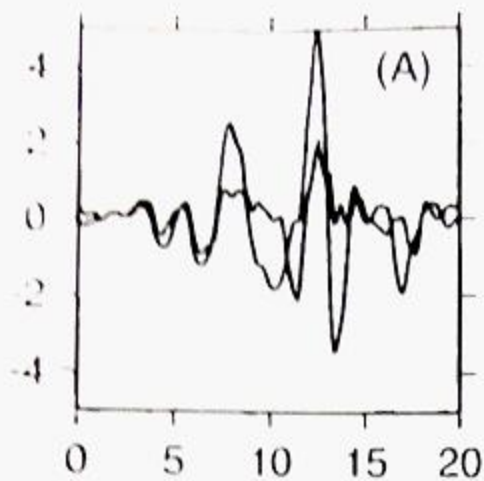
$\sigma_\phi = 8.0^\circ$ ,  $\sigma_{\delta t} = 0.2$  s

Figure 3.4.1.B07



Station: tyrg (B07)  
 EQ901742138 (No.17)  
 BAZ= 113.0 °, Dist= 99.5 °  
 $\phi = 39.0^\circ$ ,  $\delta t = 0.7$  s  
 $\sigma_\phi = 7.0^\circ$ ,  $\sigma_{\delta t} = 0.3$  s

Figure 3.4.1.B07



Station: tyrg (B07)

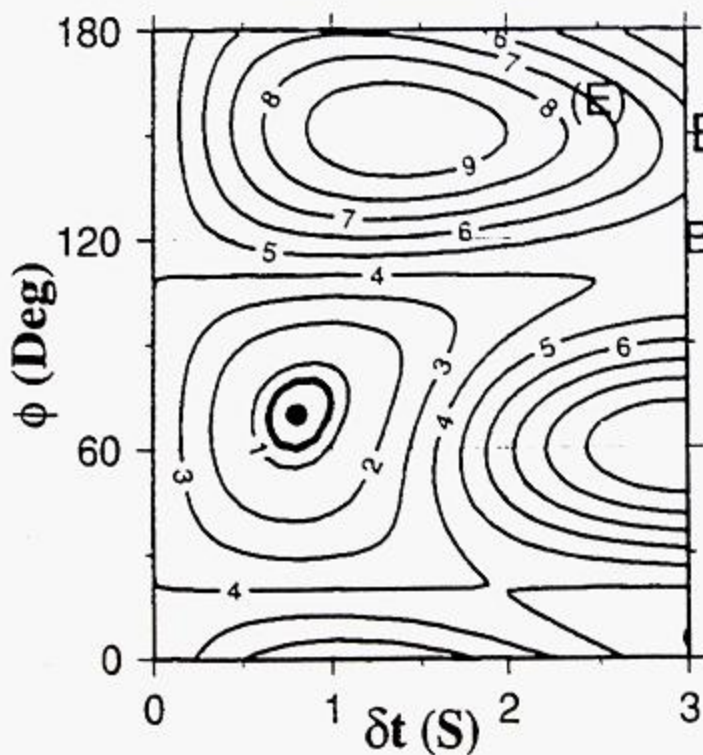
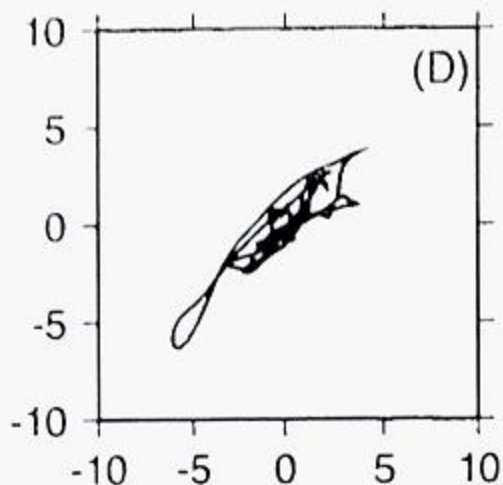
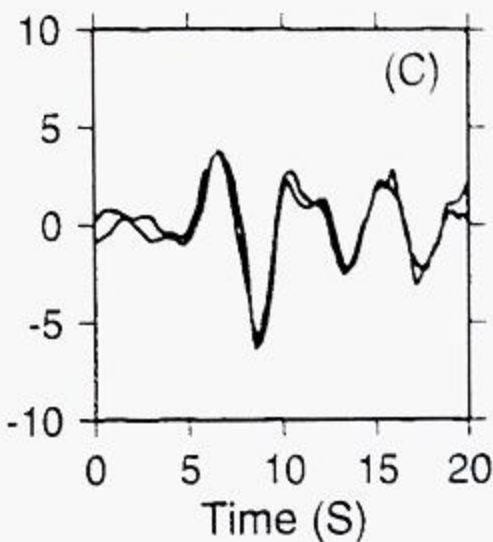
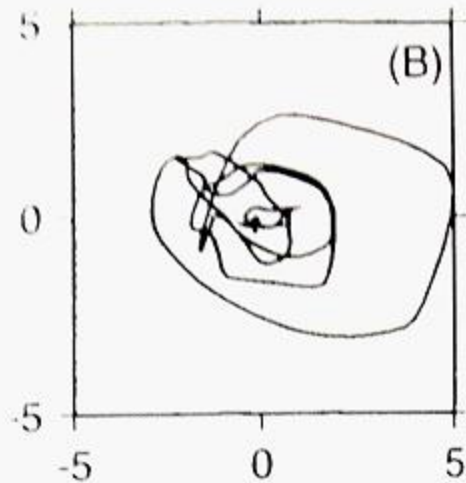
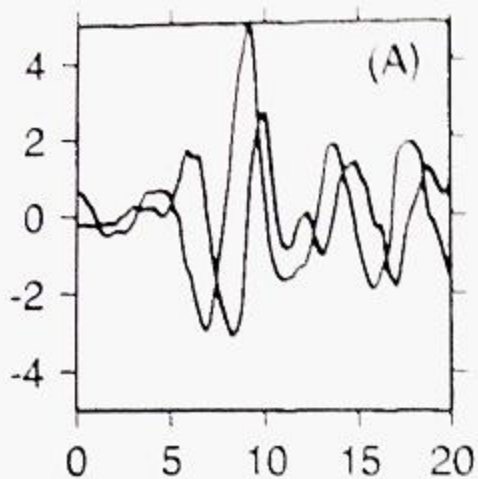
EQ922851924 (No.31)

BAZ= 123.0 °, Dist= 89.8 °

$\phi = 46.0^\circ$ ,  $\delta t = 1.1$  s

$\sigma_\phi = 6.0^\circ$ ,  $\sigma_{\delta t} = 0.4$  s

Figure 3.4.1.B07



Station: orli (B08)

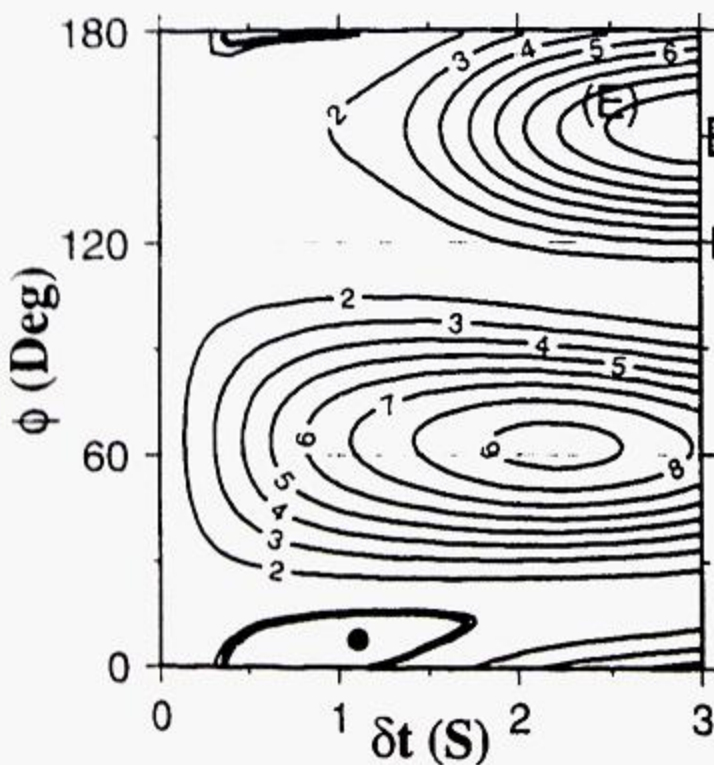
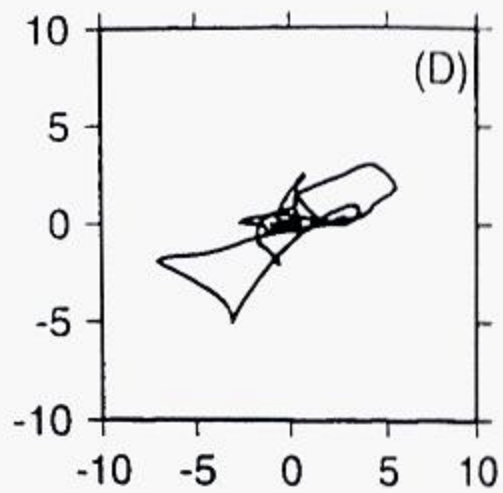
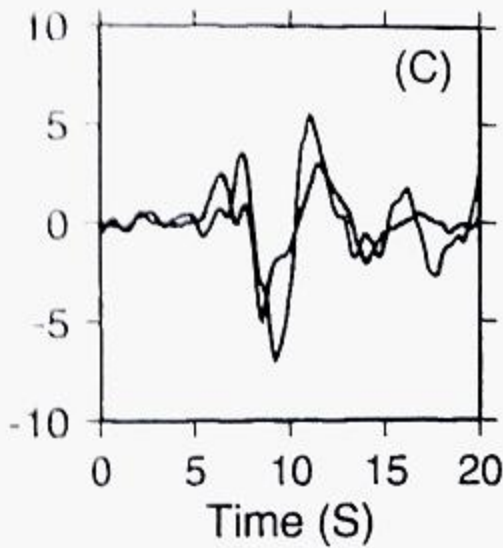
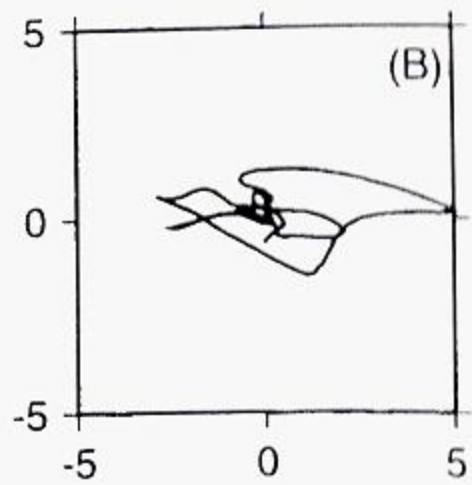
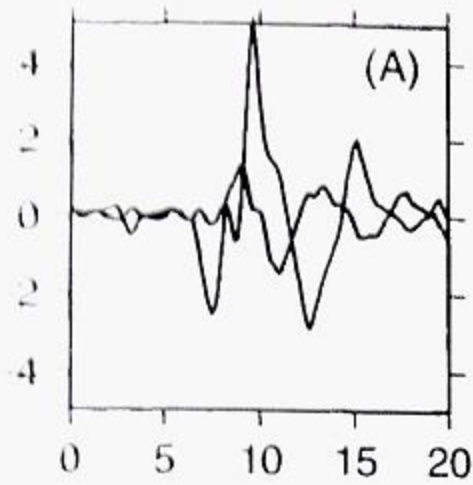
EQ801041804 (No.01)

BAZ= 110.0 °, Dist= 104.2 °

$\phi = 70.0^\circ$ ,  $\delta t = 0.8$  s

$\sigma_\phi = 10.0^\circ$ ,  $\sigma_{\delta t} = 0.2$  s

**Figure 3.4.1.B08**



Station: orli (B08)

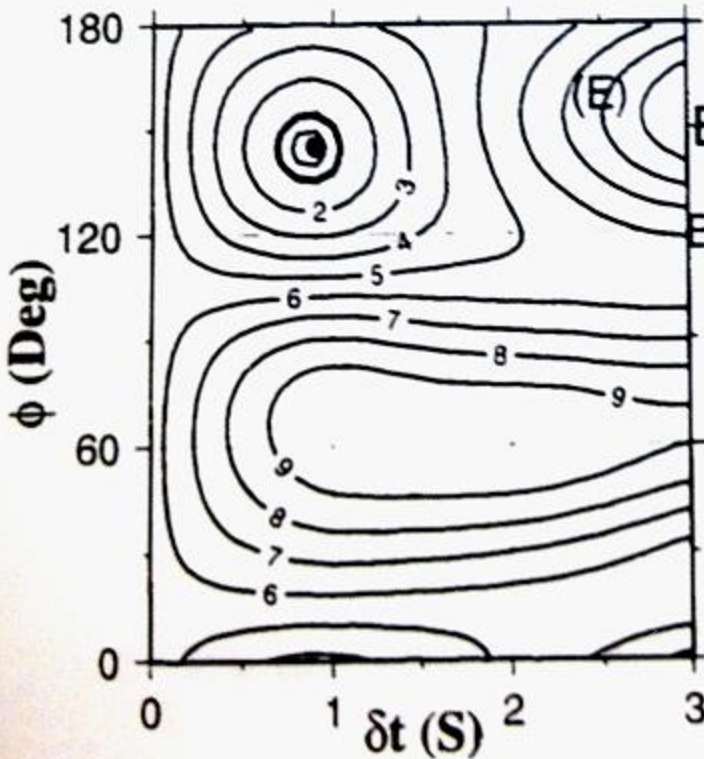
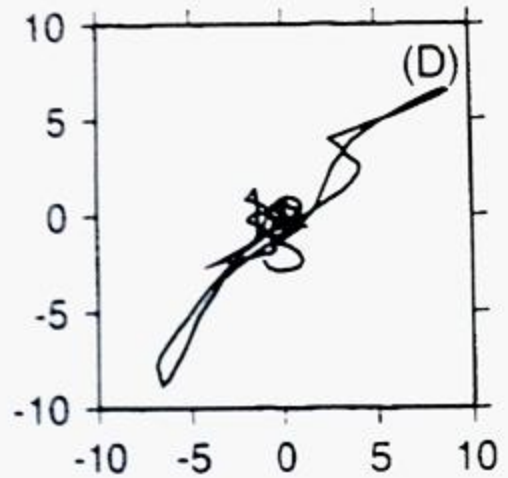
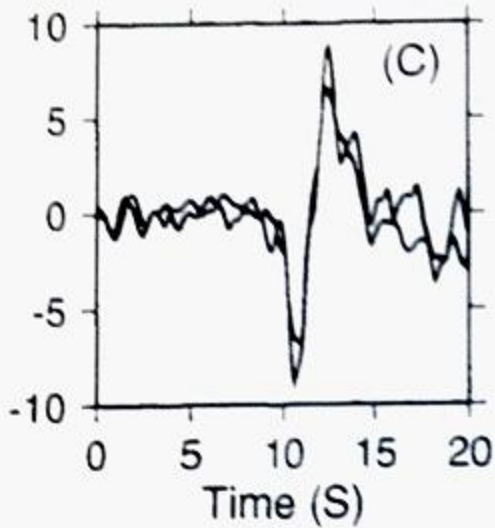
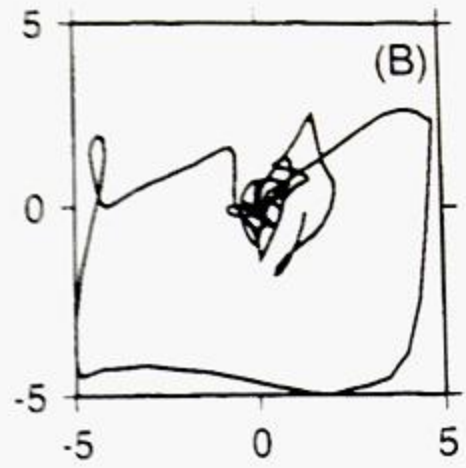
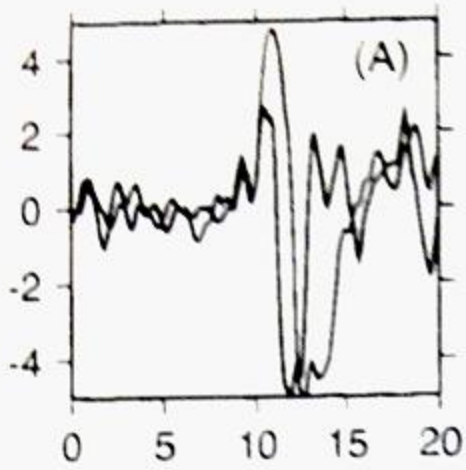
EQ861461906 (No.09)

BAZ= 110.8 °, Dist= 99.4 °

$\phi = 8.0^\circ$ ,  $\delta t = 1.1$  s

$\sigma_\phi = 7.0^\circ$ ,  $\sigma_{\delta t} = 0.7$  s

Figure 3.4.1.B08



Station: orli (B08)

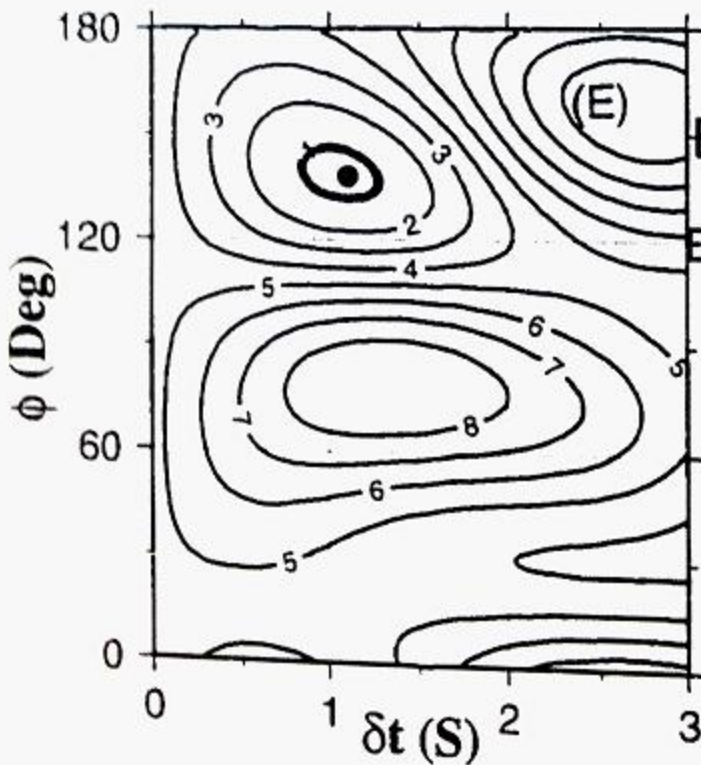
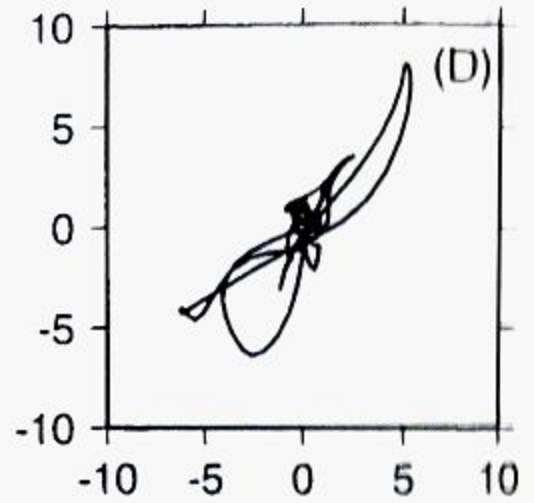
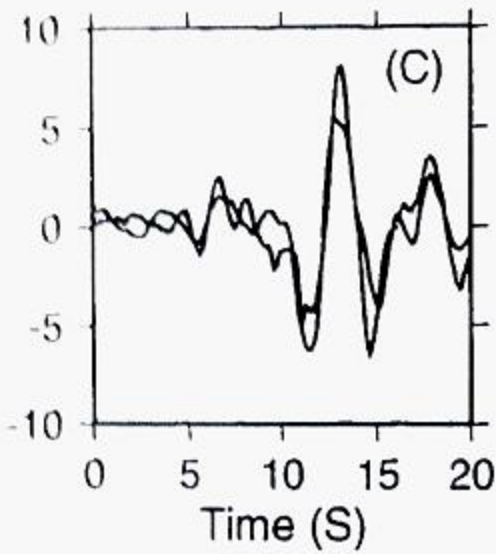
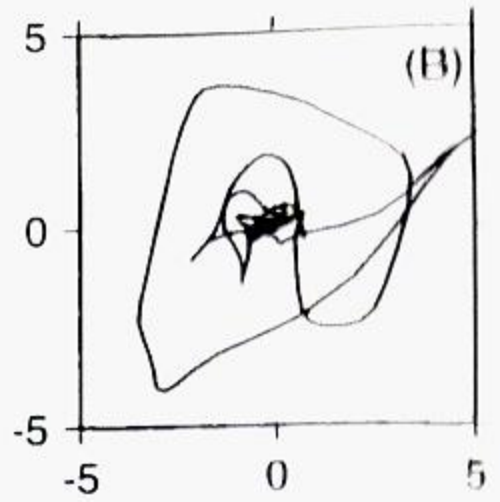
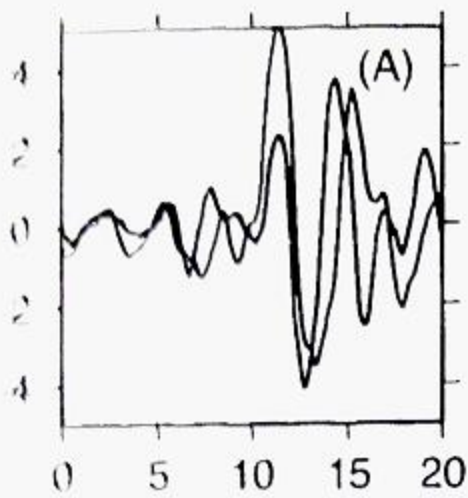
EQ890700505 (No.14)

BAZ= 104.5 °, Dist= 101.2 °

$\phi = 145.0^\circ$ ,  $\delta t = 0.9$  s

$\sigma_\phi = 10.0^\circ$ ,  $\sigma_{\delta t} = 0.3$  s

Figure 3.4.1.B08



Station: orli (B08)

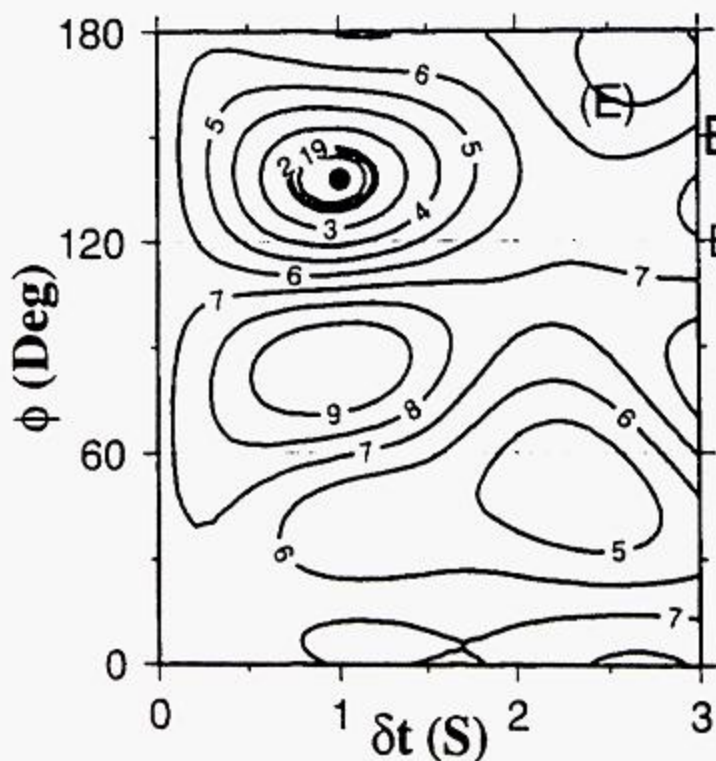
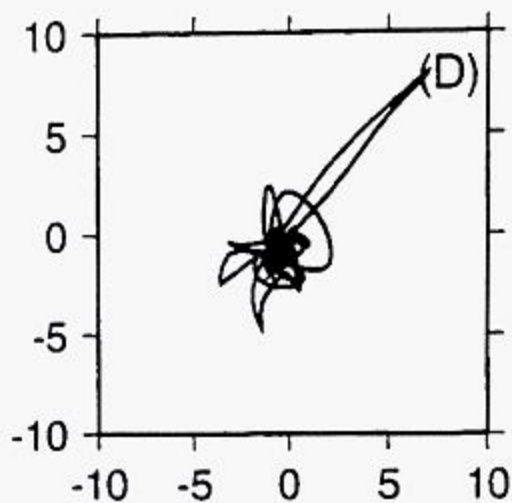
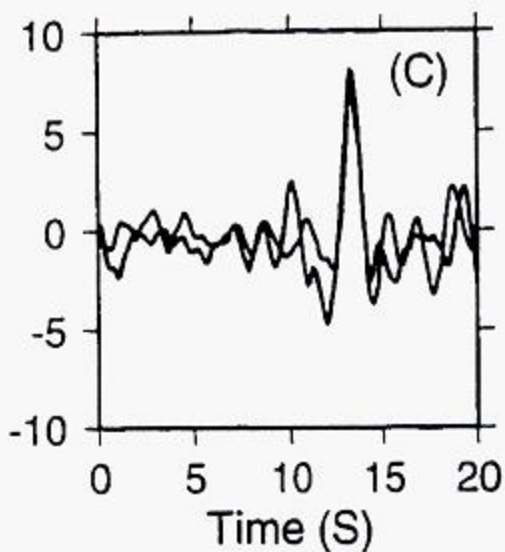
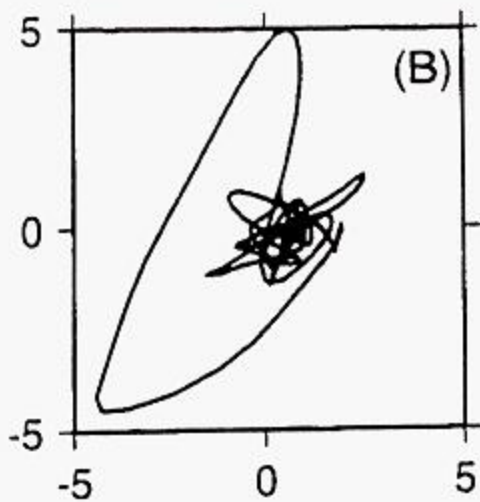
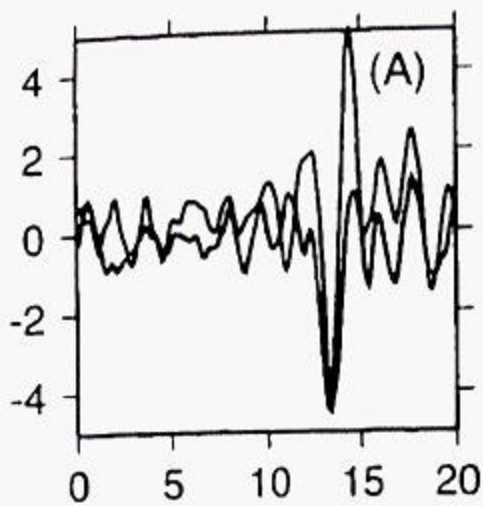
EQ901742138 (No.17)

BAZ= 108.2 °, Dist= 103.2 °

$\phi = 138.0^\circ$ ,  $\delta t = 1.1$  s

$\sigma_\phi = 7.0^\circ$ ,  $\sigma_{\delta t} = 0.3$  s

Figure 3.4.1.B08



Station: orli (B08)

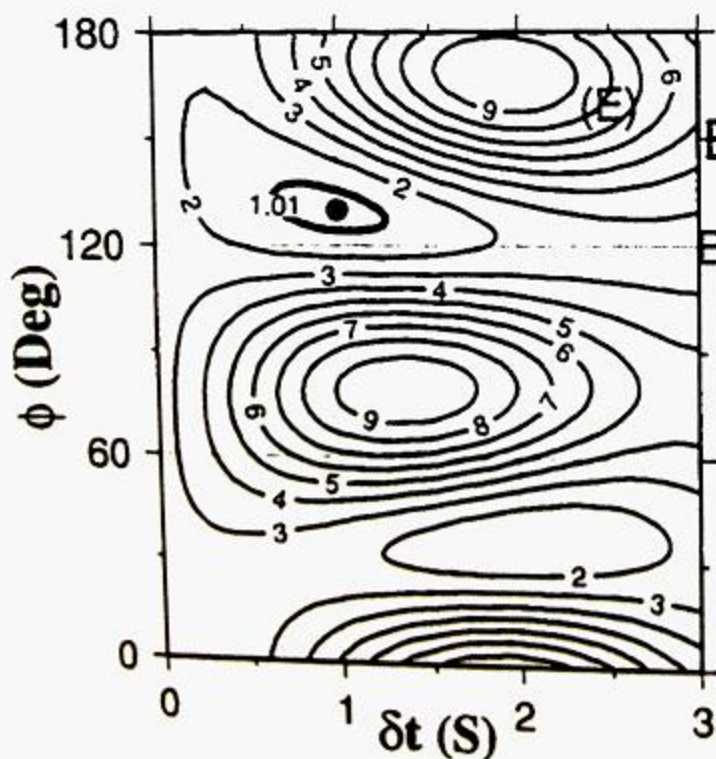
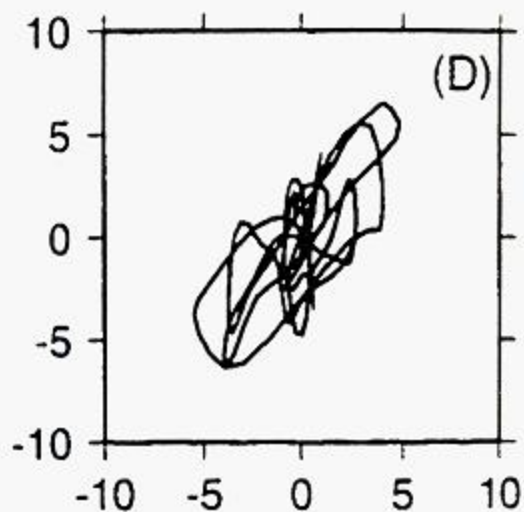
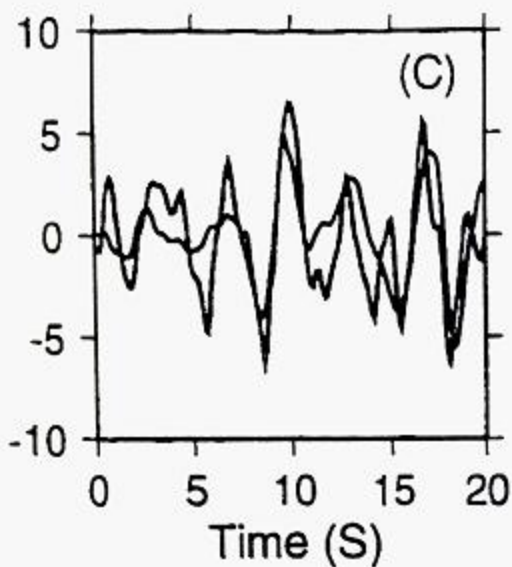
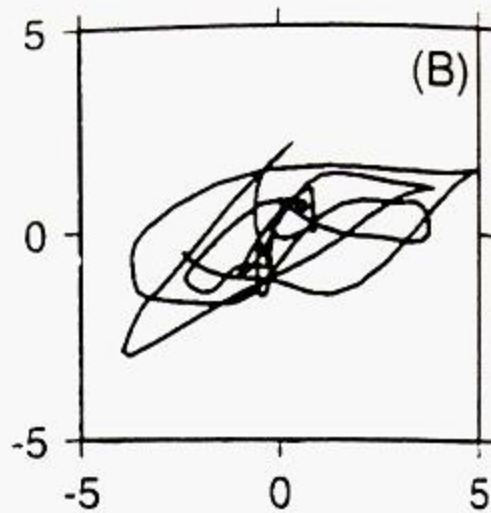
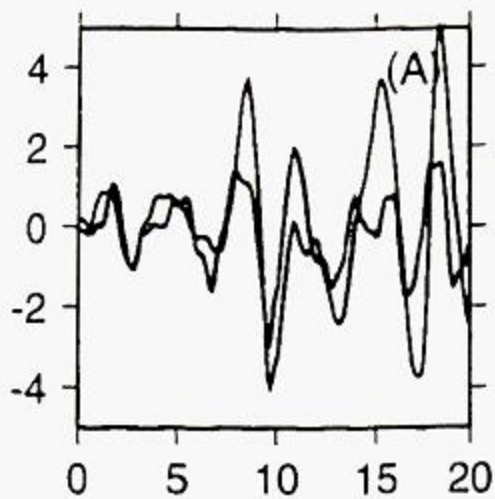
EQ922432009 (No.27)

BAZ= 107.5 °, Dist= 98.8 °

$\phi = 138.0^\circ$ ,  $\delta t = 1.0$  s

$\sigma_\phi = 9.0^\circ$ ,  $\sigma_{\delta t} = 0.3$  s

**Figure 3.4.1.B08**



Station: tala (B13)

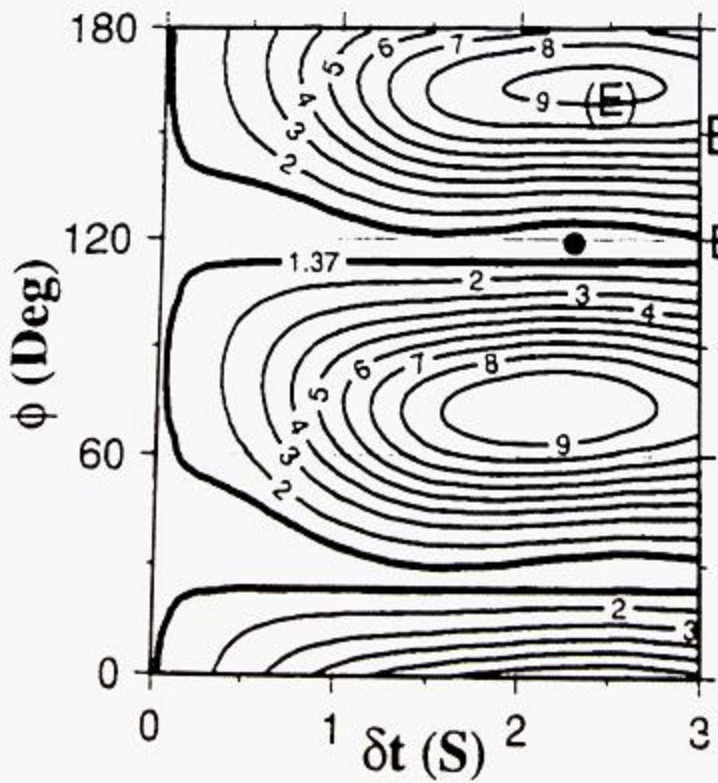
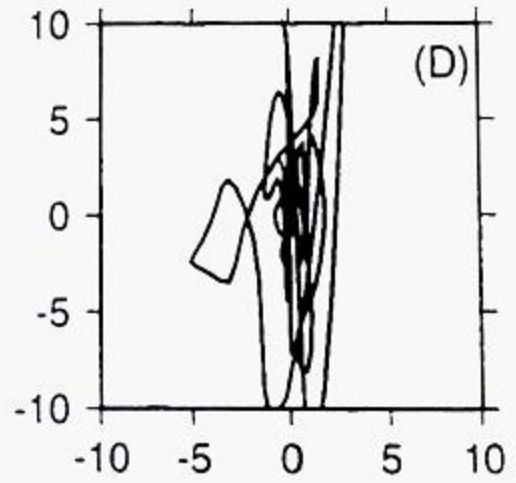
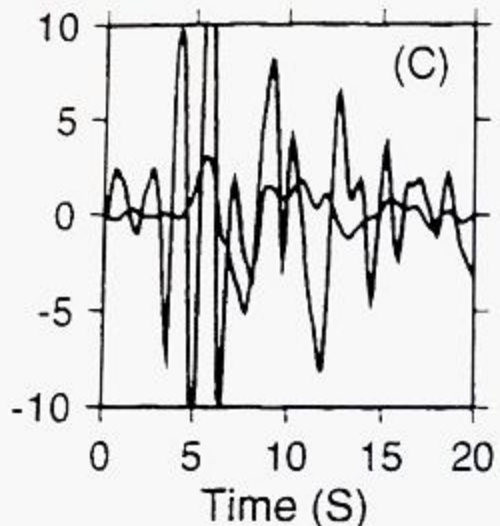
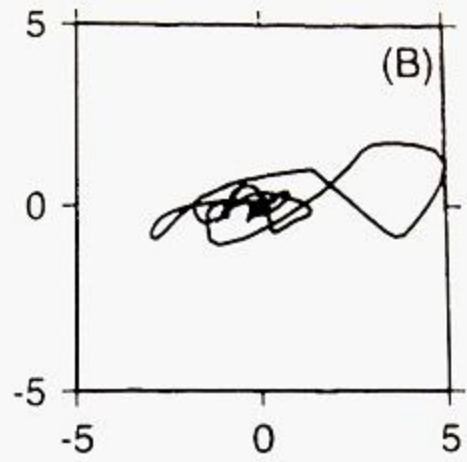
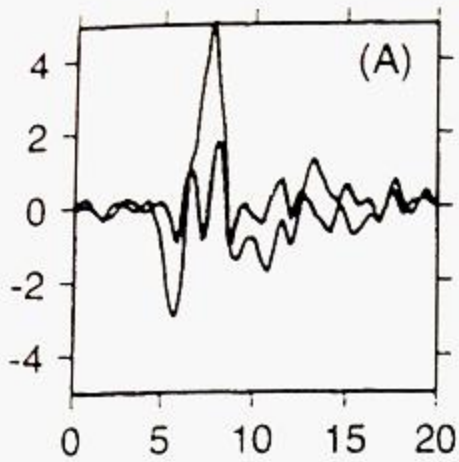
EQ842720003 (No.06)

BAZ= 113.5 °, Dist= 104.3 °

$\phi = 130.0^\circ$ ,  $\delta t = 1.0$  s

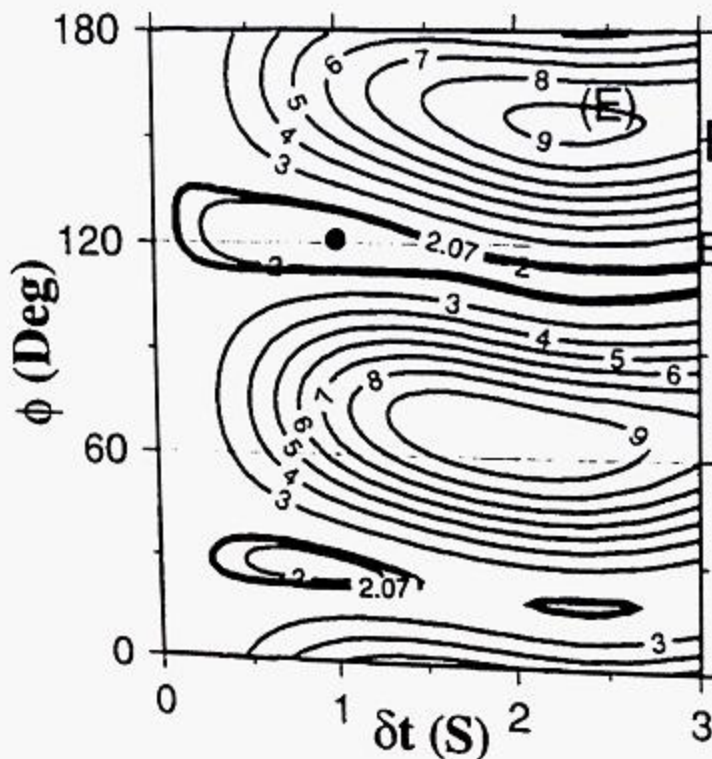
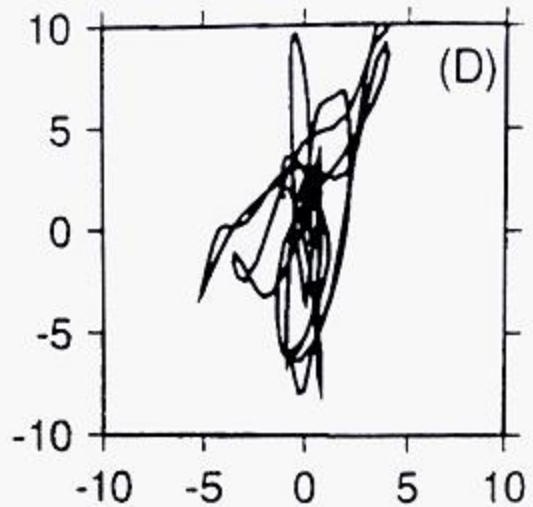
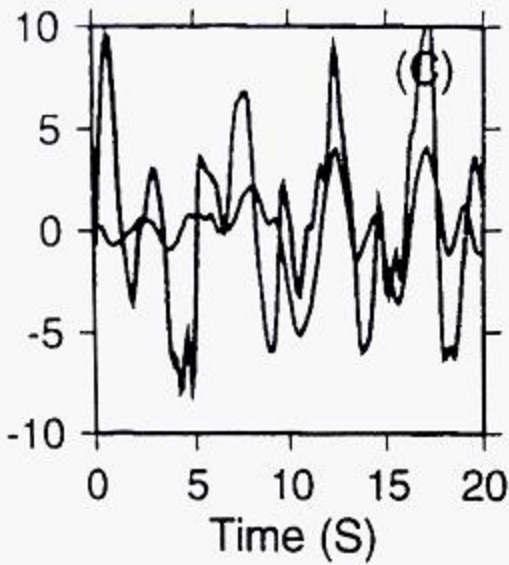
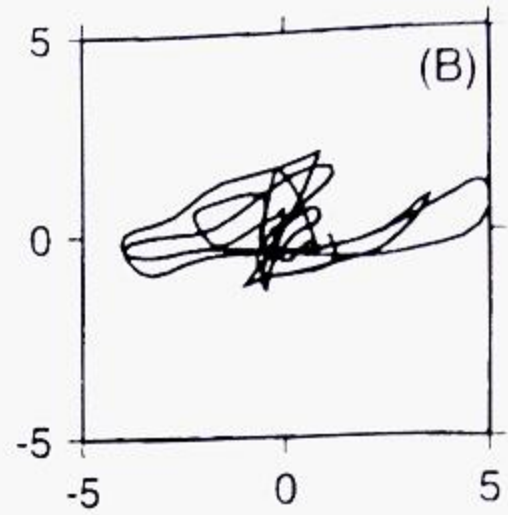
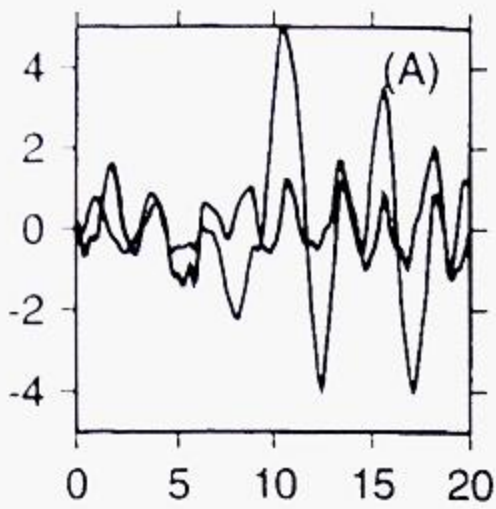
$\sigma_\phi = 6.0^\circ$ ,  $\sigma_{\delta t} = 0.4$  s

**Figure 3.4.1.B13**



Station: tala (B13)  
 EQ861461906 (No.09)  
 BAZ= 113.8 °, Dist= 96.9 °  
 $\phi = 119.0$  °,  $\delta t = 2.3$  s  
 $\sigma_{\phi} = 96.0$  °,  $\sigma_{\delta t} = 3.1$  s

Figure 3.4.1.B13



Station: tala (B13)

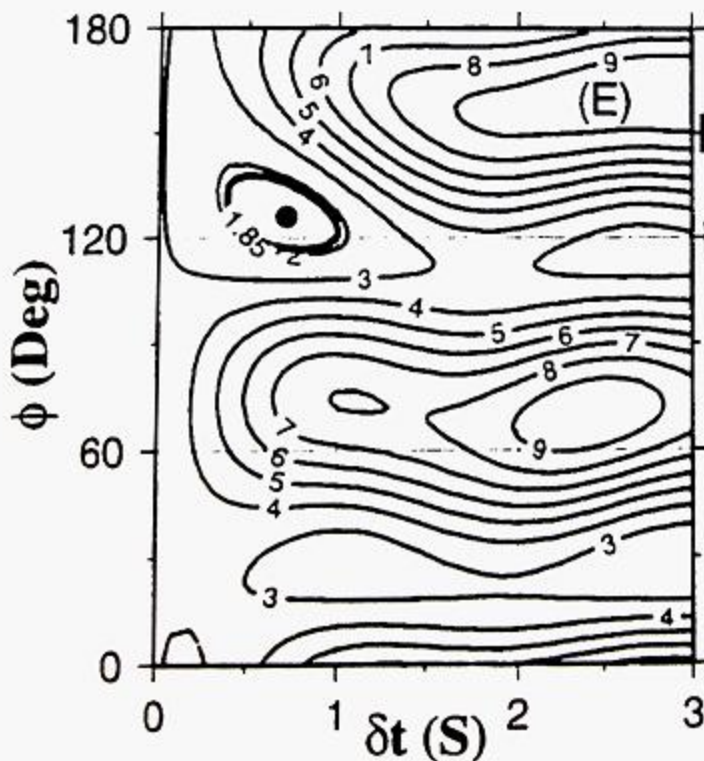
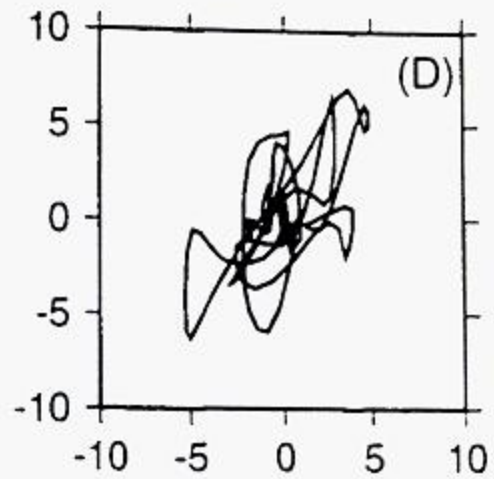
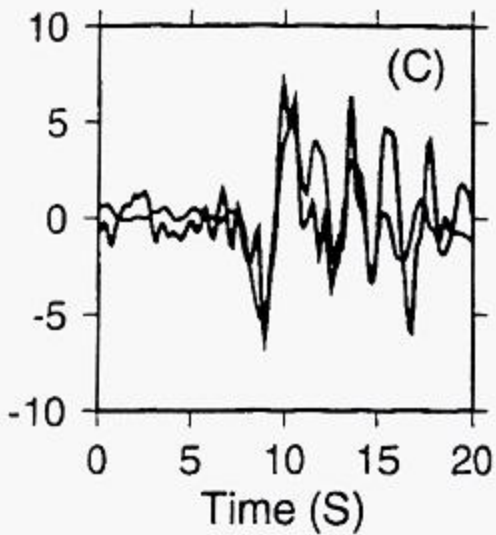
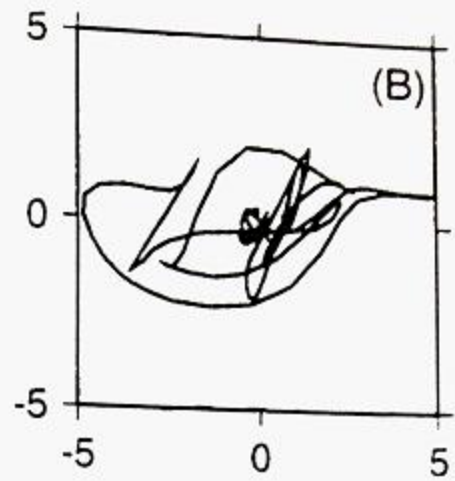
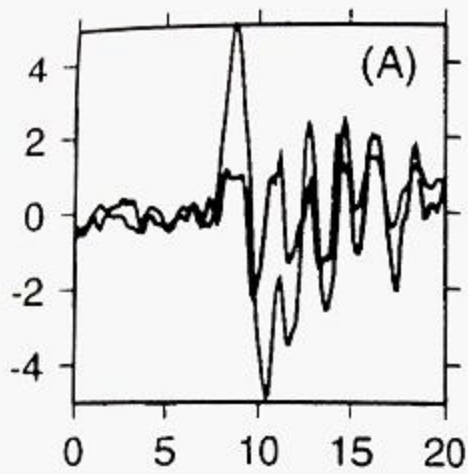
EQ863030128 (No.10)

BAZ= 111.4 °, Dist= 100.7 °

$\phi = 121.0^\circ$ ,  $\delta t = 1.0$  s

$\sigma_\phi = 100.0^\circ$ ,  $\sigma_{\delta t} = 0.9$  s

Figure 3.4.1.B13



Station: taly (B13)

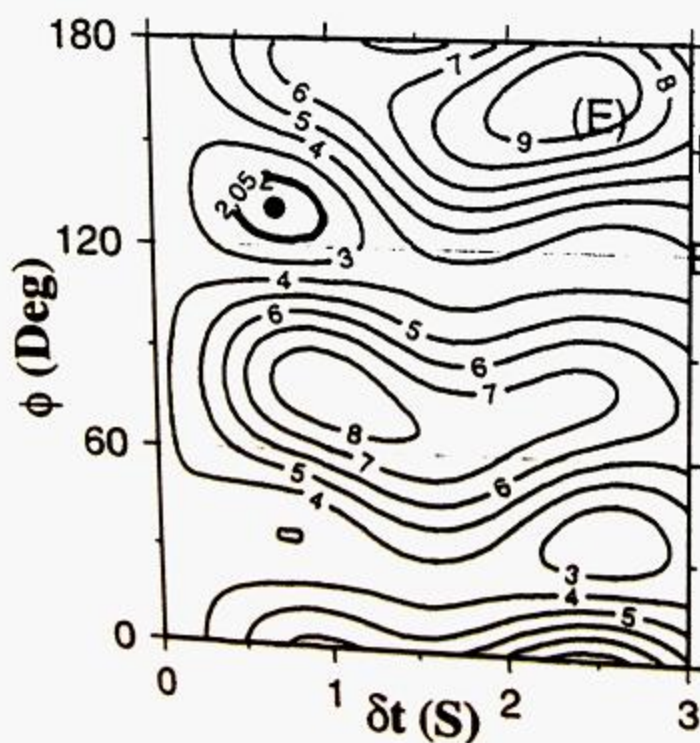
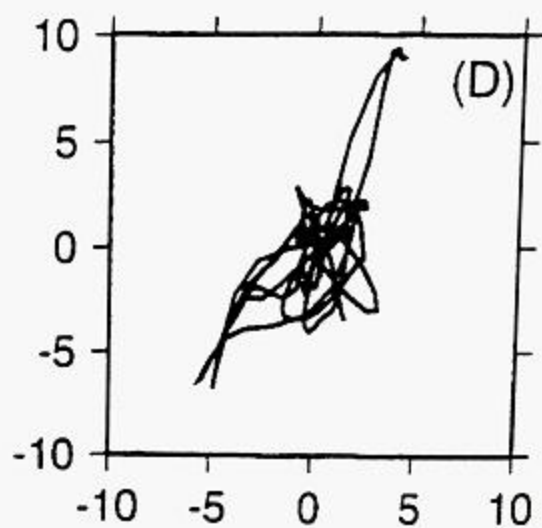
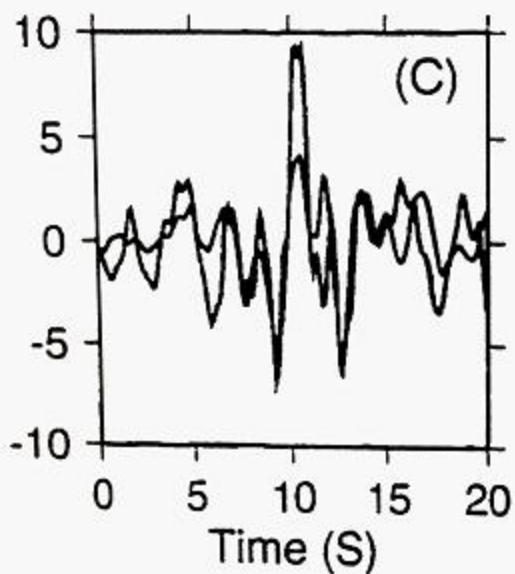
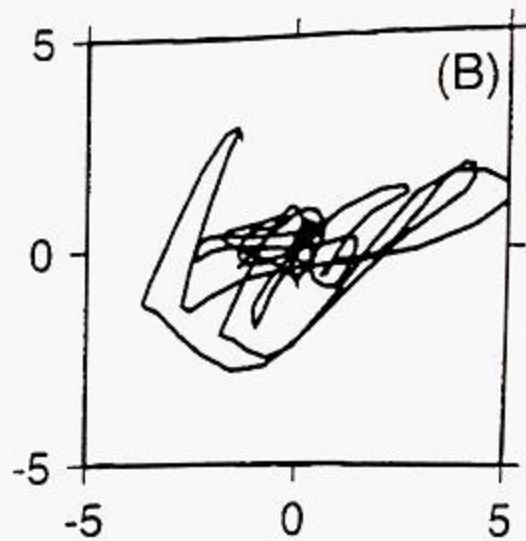
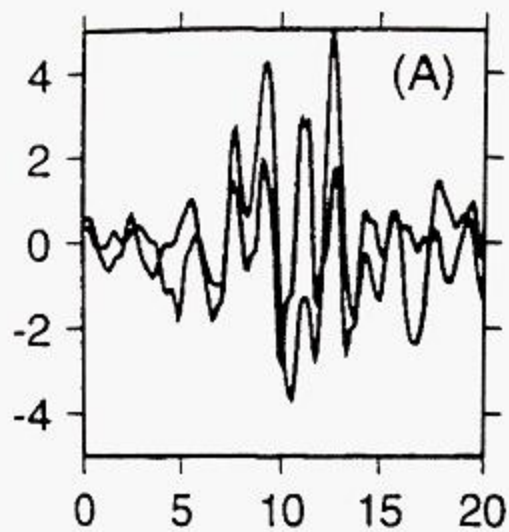
EQ890700505 (No.14)

BAZ= 107.5 °, Dist= 98.7 °

$\phi = 126.0$  °,  $\delta t = 0.7$  s

$\sigma_{\phi} = 10.0$  °,  $\sigma_{\delta t} = 0.3$  s

Figure 3.4.1.B13



Station: tala (B13)

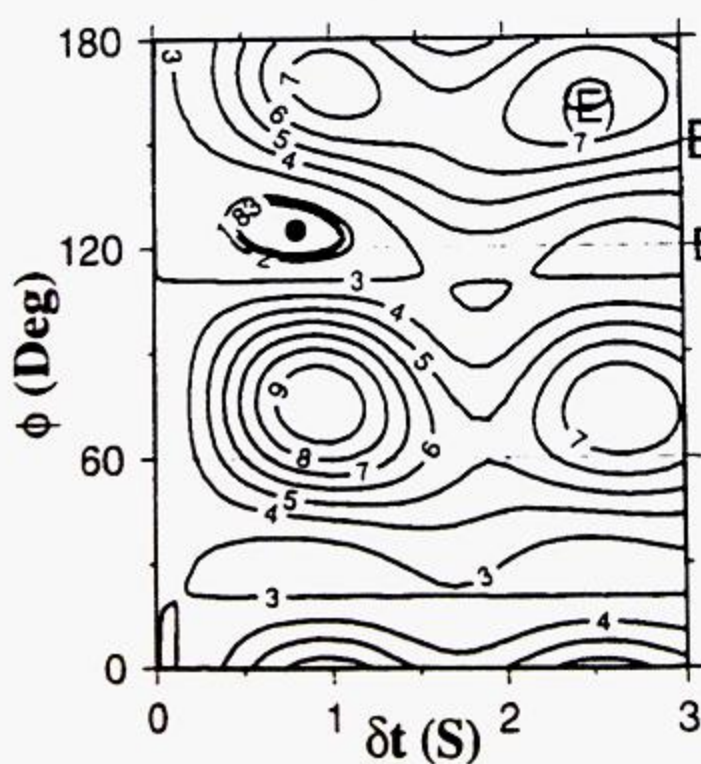
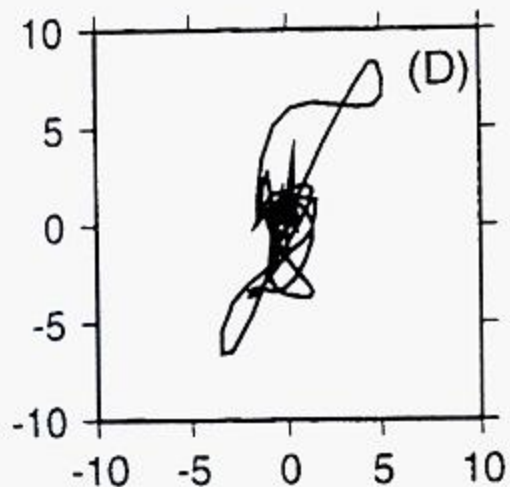
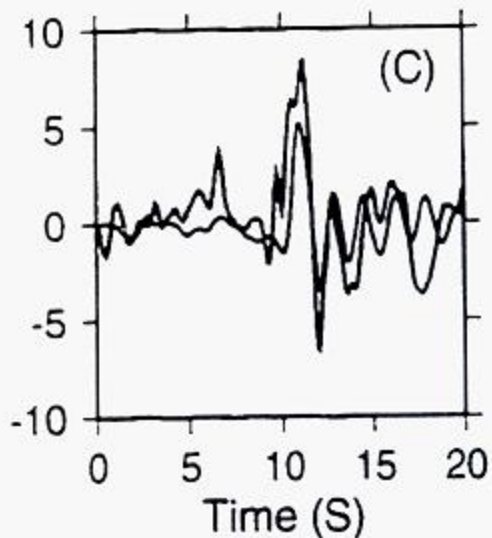
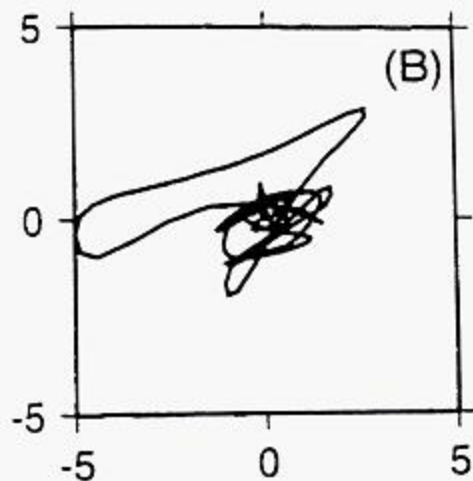
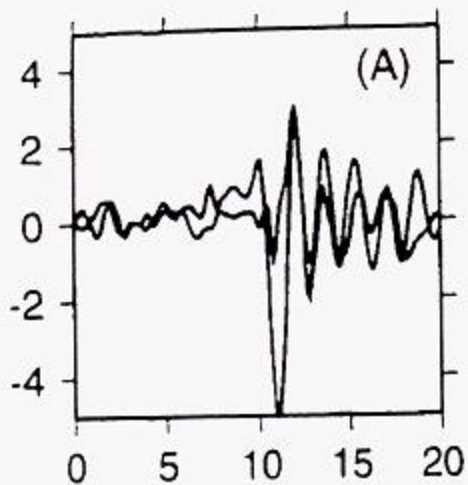
EQ901742138 (No.17)

BAZ= 111.2 °, Dist= 100.6 °

$\phi = 131.0^\circ$ ,  $\delta t = 0.7$  s

$\sigma_\phi = 10.0^\circ$ ,  $\sigma_{\delta t} = 0.3$  s

Figure 3.4.1.B13



Station: tala (B13)

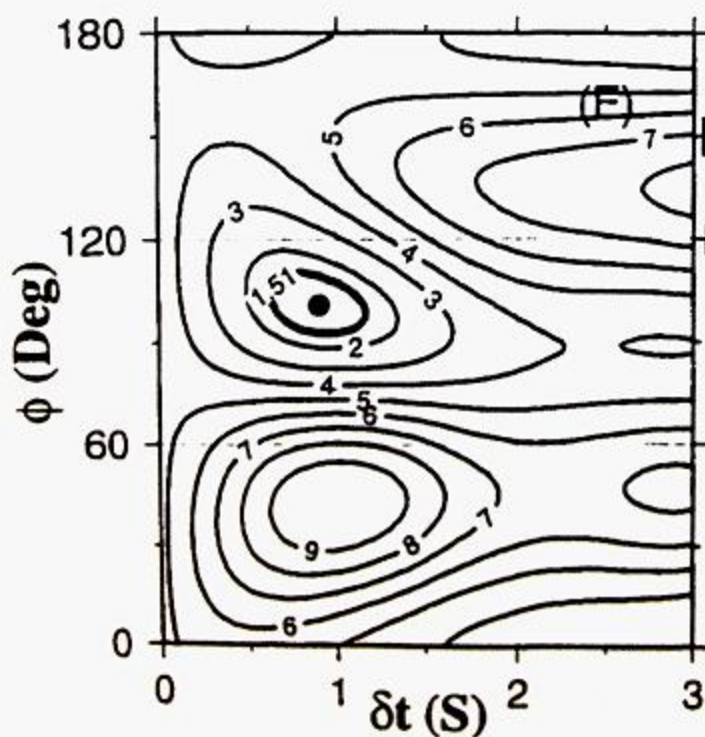
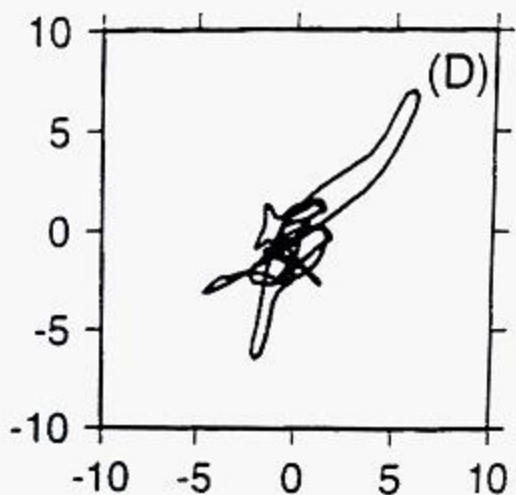
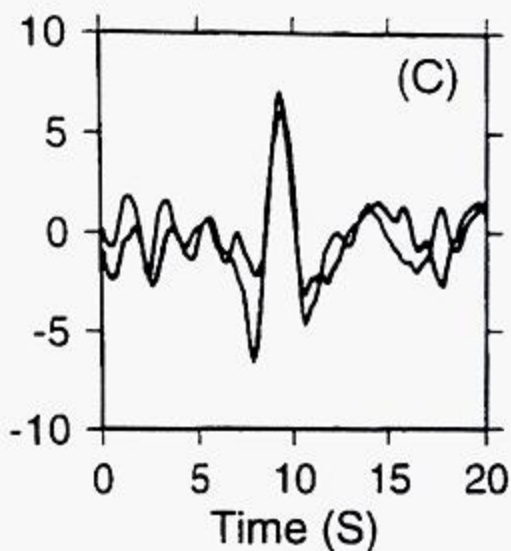
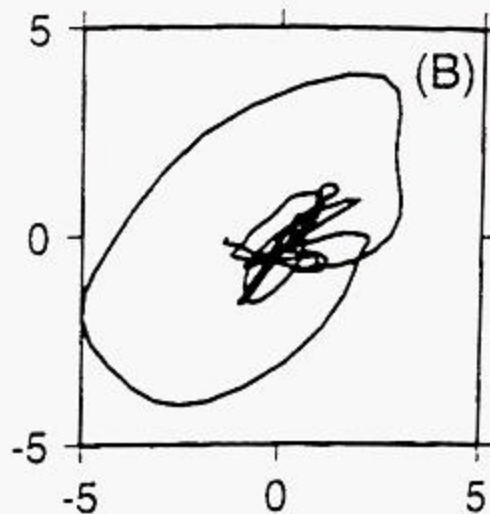
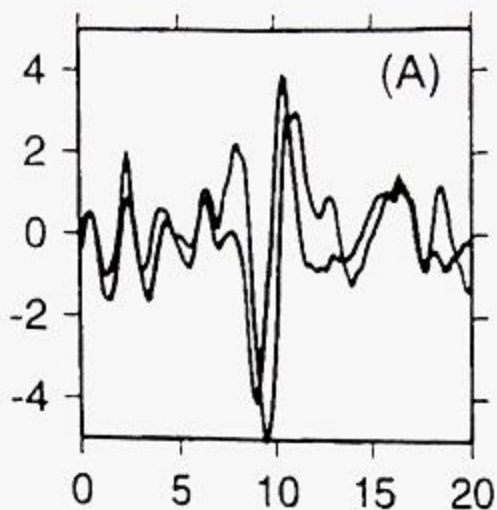
EQ922432009 (No.27)

BAZ= 110.5 °, Dist= 96.3 °

$\phi = 125.0^\circ$ ,  $\delta t = 0.8$  s

$\sigma_\phi = 8.0^\circ$ ,  $\sigma_{\delta t} = 0.4$  s

Figure 3.4.1.B13



Station: tupi (D01)

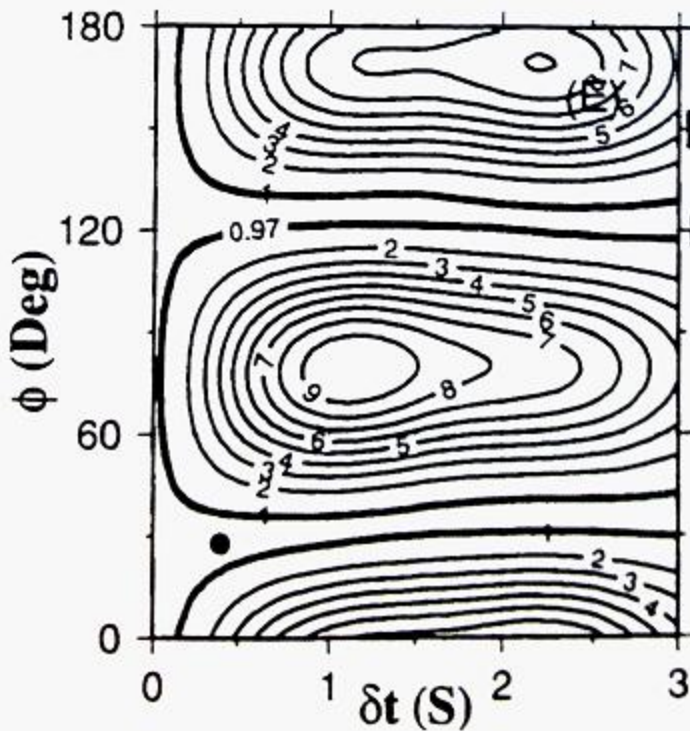
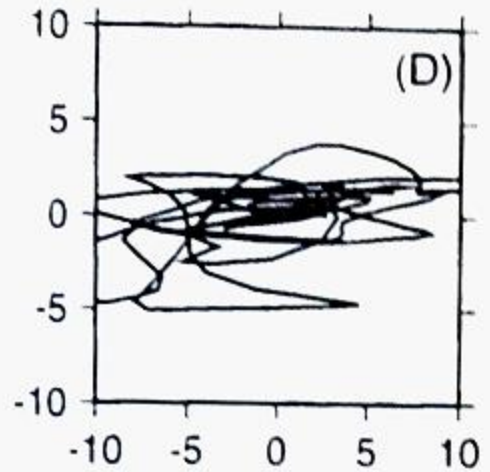
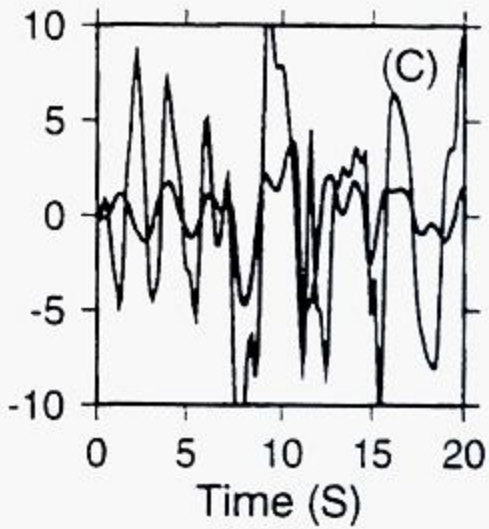
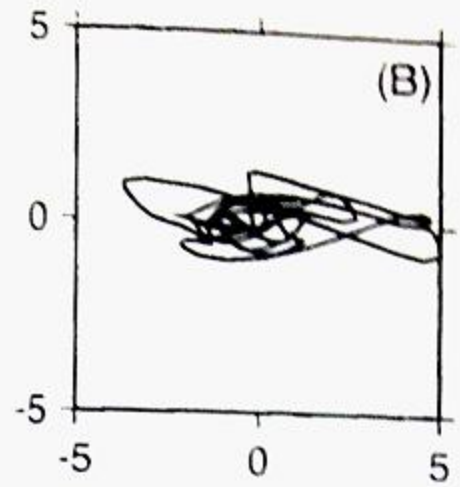
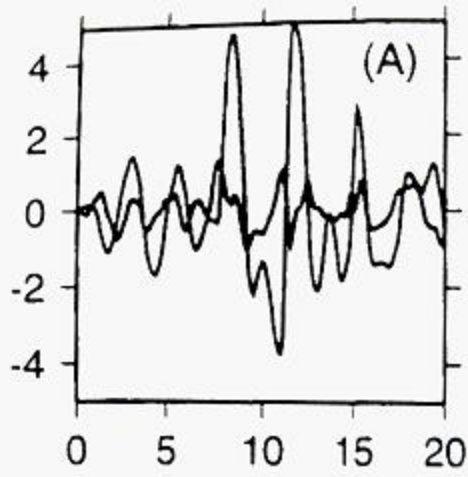
EQ851341811 (No.08)

BAZ= 254.6 °, Dist= 91.9 °

$\phi = 101.0^\circ$ ,  $\delta t = 0.9$  s

$\sigma_\phi = 8.0^\circ$ ,  $\sigma_{\delta t} = 0.3$  s

**Figure 3.4.1.D01**



Station: tupi (D01)

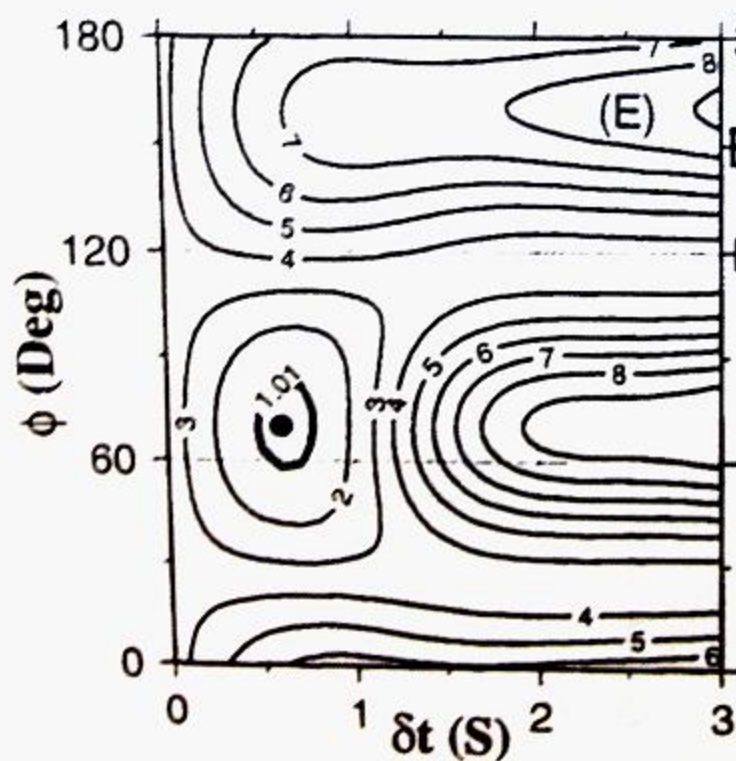
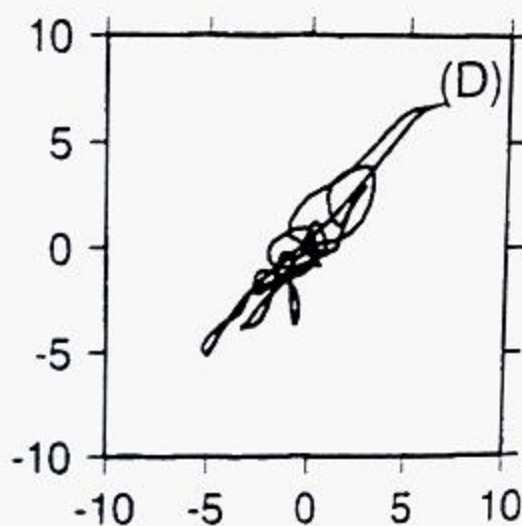
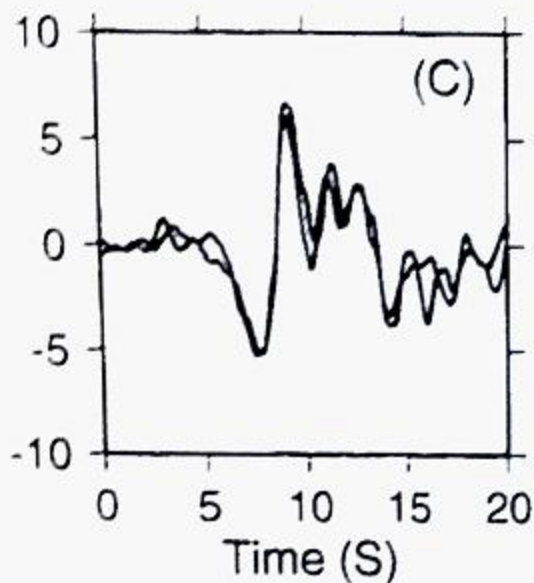
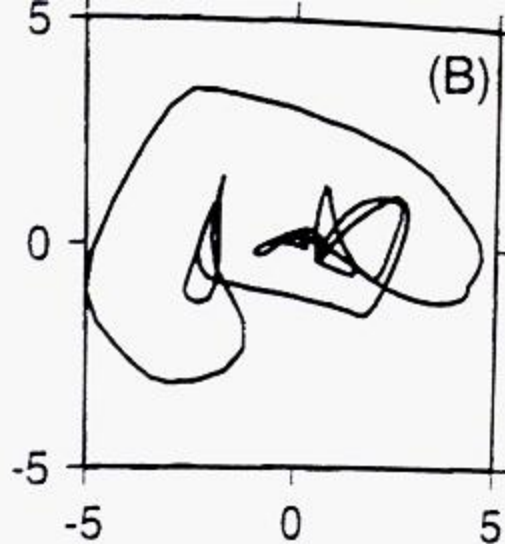
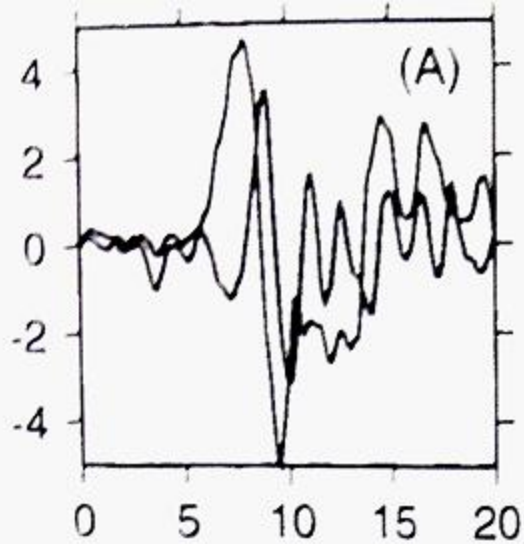
EQ901742138 (No.17)

BAZ= 123.4 °, Dist= 93.1 °

$\phi = 28.0^\circ$ ,  $\delta t = 0.4$  s

$\sigma_\phi = 104.0^\circ$ ,  $\sigma_{\delta t} = 0.6$  s

Figure 3.4.1.D01



Station: hapc (D06)

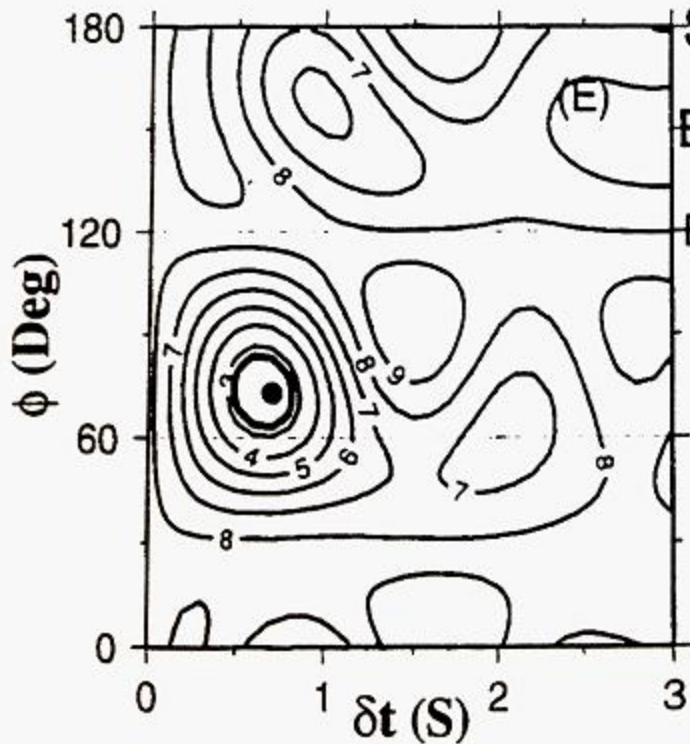
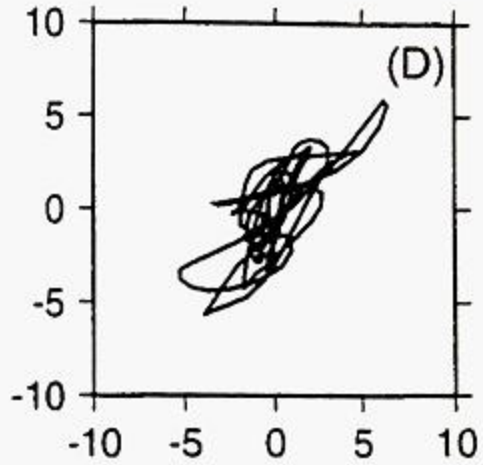
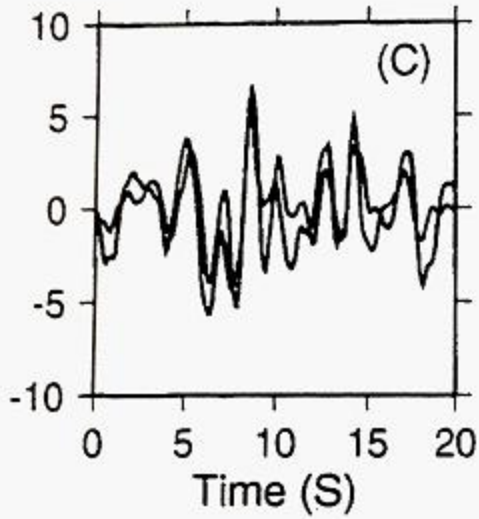
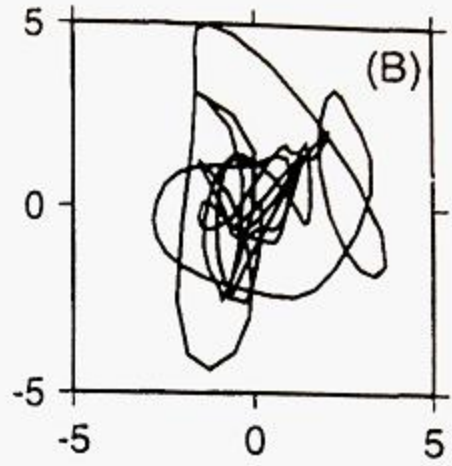
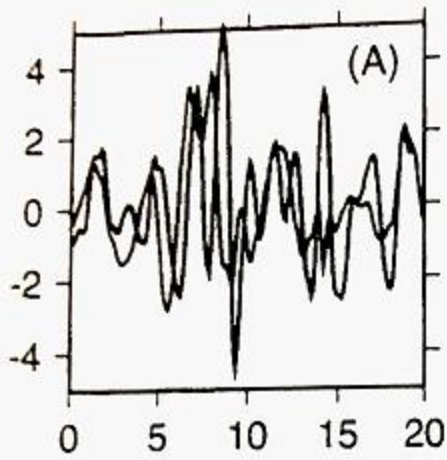
EQ890700505 (No.14)

BAZ= 114.3 °, Dist= 92.8 °

$\phi = 70.0$  °,  $\delta t = 0.6$  s

$\sigma_{\phi} = 13.0$  °,  $\sigma_{\delta t} = 0.2$  s

**Figure 3.4.1.D06**



Station: hapc (D06)

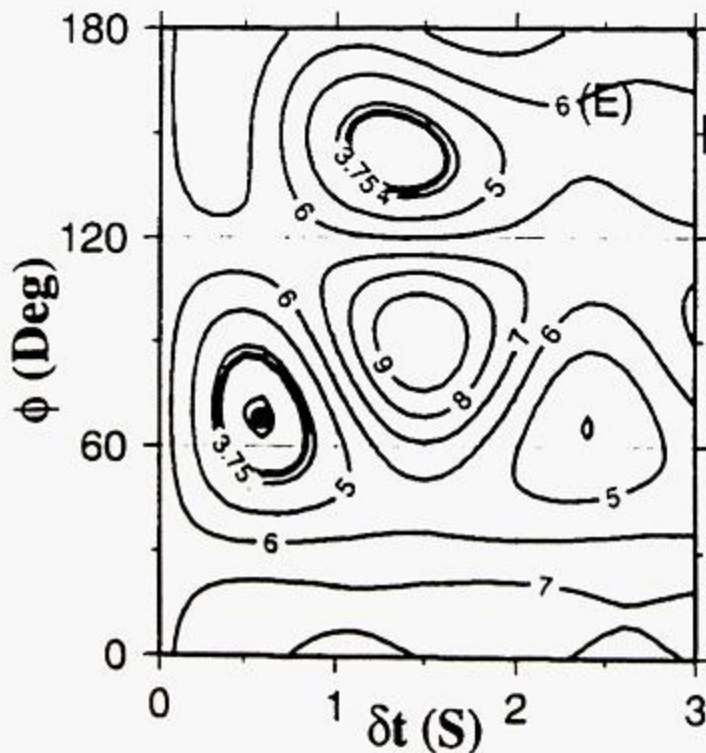
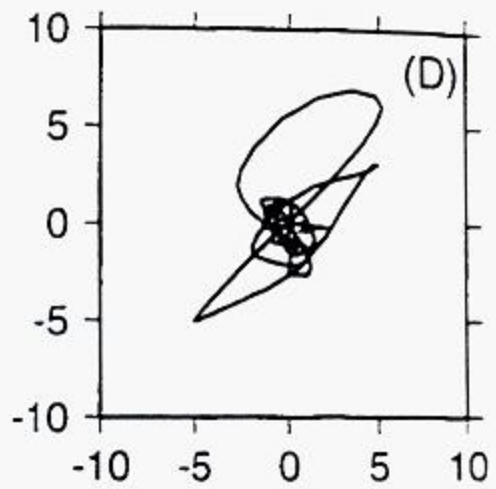
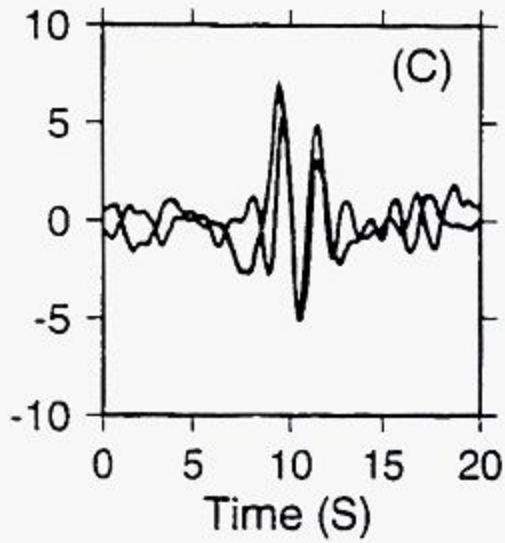
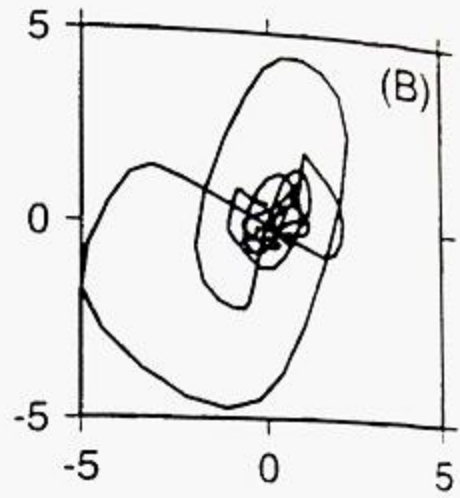
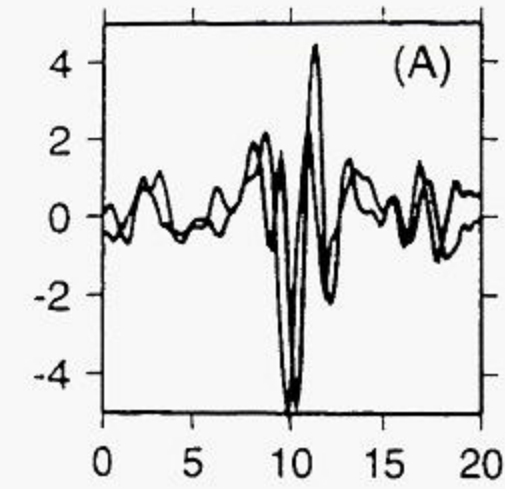
EQ901742138 (No.17)

BAZ= 117.9 °, Dist= 94.7 °

$\phi = 73.0^\circ$ ,  $\delta t = 0.7$  s

$\sigma_\phi = 10.0^\circ$ ,  $\sigma_{\delta t} = 0.3$  s

Figure 3.4.1.D06



Station: hapc (D06)

EQ922432009 (No.27)

BAZ= 117.3 °, Dist= 90.4 °

$\phi = 68.0^\circ$ ,  $\delta t = 0.6$  s

$\sigma_\phi = 17.0^\circ$ ,  $\sigma_{\delta t} = 0.3$  s

**Figure 3.4.1.D06**

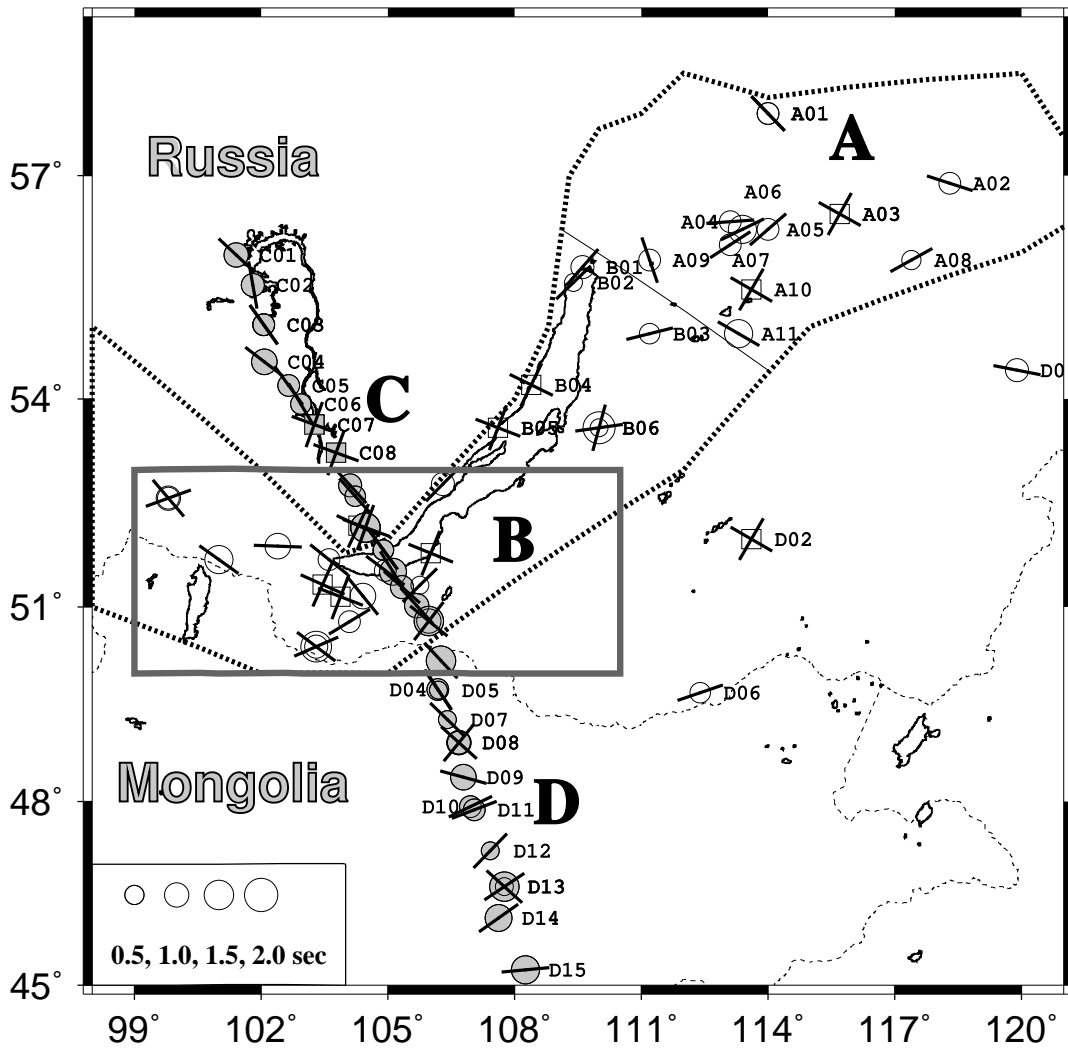
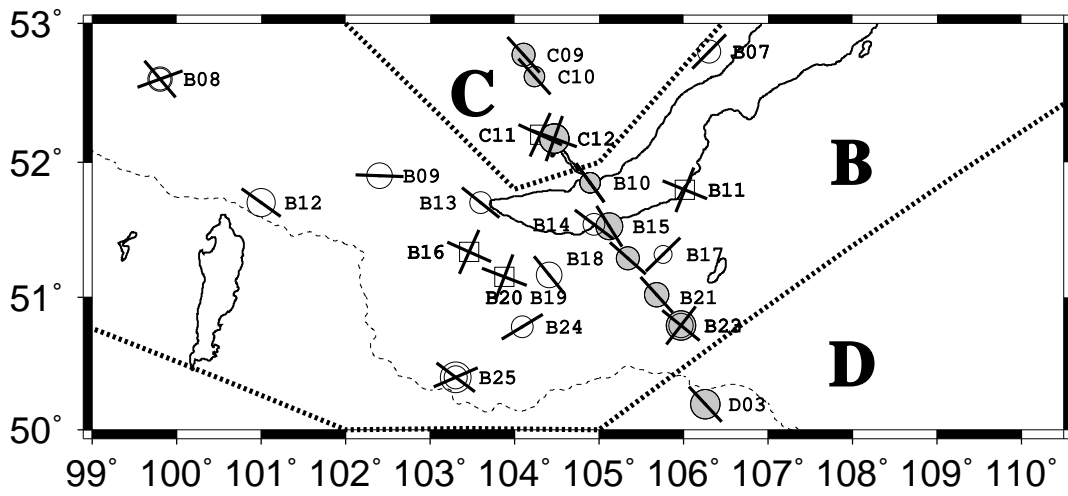


Figure 3.4.2 (A)

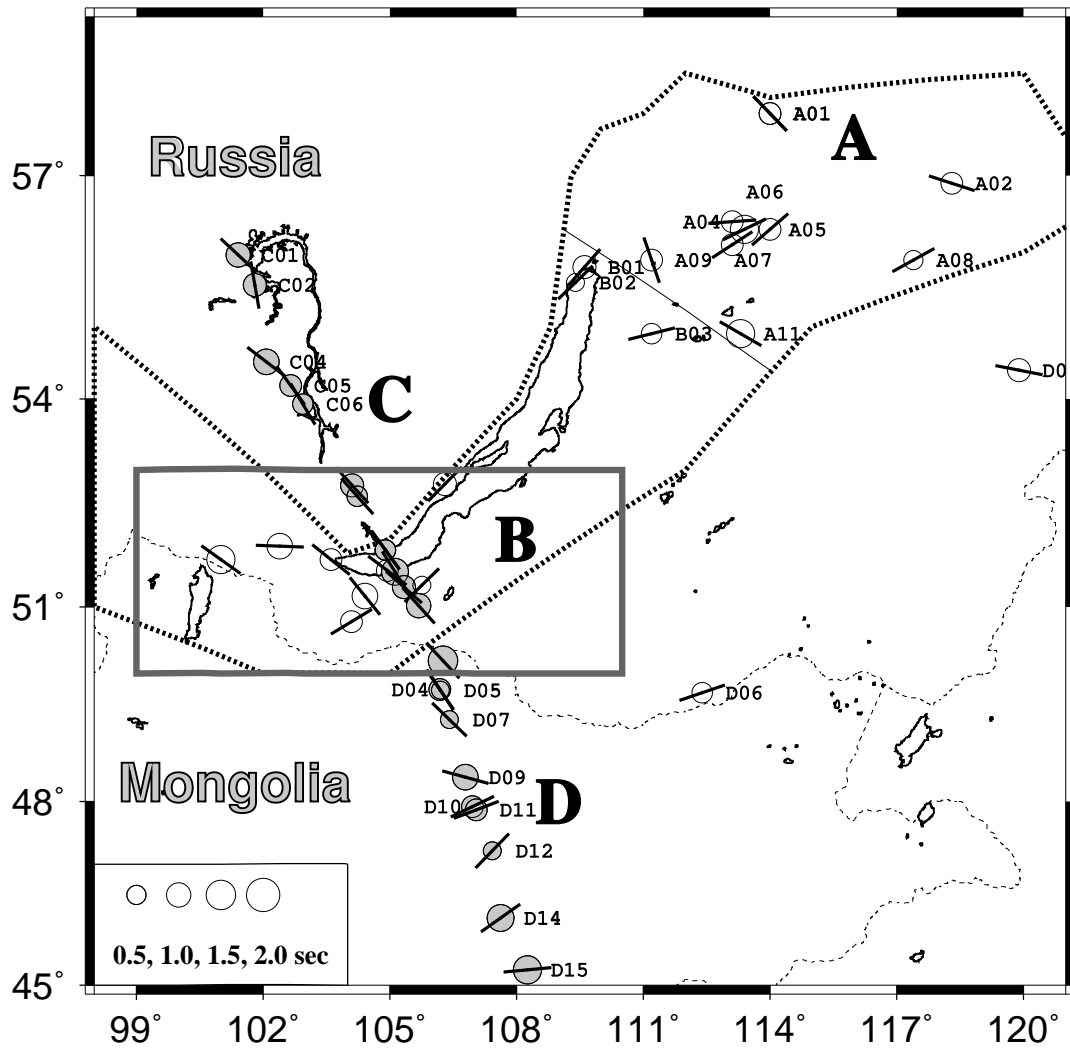
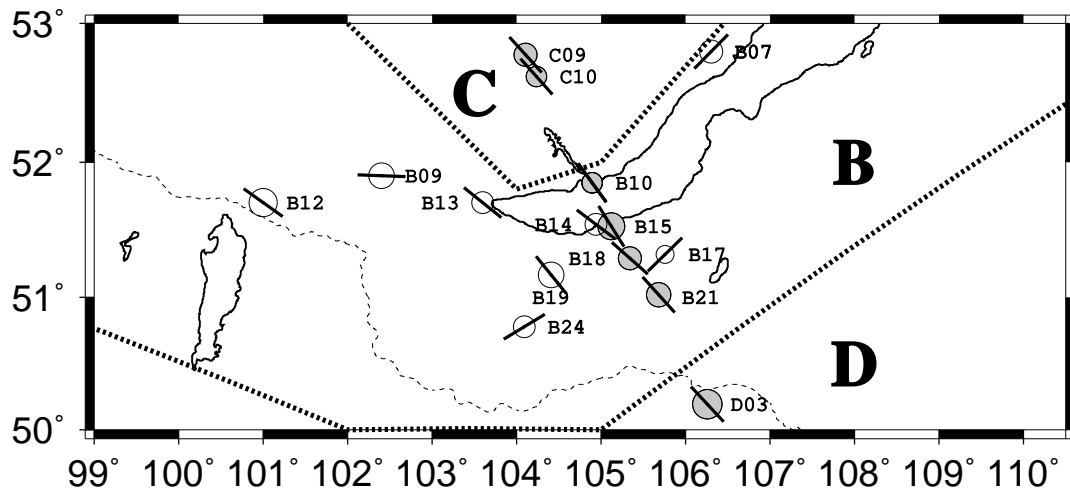


Figure 3.4.2 (B)

**Table 3.3.1.** SKS splitting measurement results

Station No.	Station Name	Coordinates		Fast direction( $^{\circ}$ )	Splitting time(sec)	number of events
		Latitude( $^{\circ}$ )	Longitude( $^{\circ}$ )			
A01	boda	57.800	114.000	136.0 $\pm$ 13.0	0.70 $\pm$ 0.50	2
A02	char	56.900	118.300	107.9 $\pm$ 6.0	0.82 $\pm$ 0.24	2
A03	nely	56.500	115.700	29.0 $\pm$ —	—	0
A03	nely	56.500	115.700	119.0 $\pm$ —	—	3
A04	turi	56.400	113.100	86.0 $\pm$ 24.0	0.80 $\pm$ 0.50	1
A05	ozer	56.300	114.000	49.0 $\pm$ 7.0	0.70 $\pm$ 0.30	1
A06	tonn	56.300	113.400	64.0 $\pm$ 8.0	1.40 $\pm$ 0.30	1
A07	kovo	56.100	113.100	57.0 $\pm$ 9.0	0.80 $\pm$ 0.30	1
A08	kala	55.900	117.400	61.0 $\pm$ 35.0	0.50 $\pm$ 0.30	1
A09	kumo	55.900	111.200	161.0 $\pm$ 24.0	0.70 $\pm$ 0.50	1
A10	uaki	55.500	113.600	30.0 $\pm$ —	—	0
A10	uaki	55.500	113.600	120.0 $\pm$ —	—	3
A11	tsip	54.900	113.300	120.0 $\pm$ 6.0	1.40 $\pm$ 0.90	1
B01	nizh	55.800	109.600	41.3 $\pm$ 3.2	0.84 $\pm$ 0.19	5
B02	sbai	55.600	109.400	46.0 $\pm$ 50.0	0.30 $\pm$ 0.20	1
B03	ulun	54.900	111.200	76.0 $\pm$ 20.0	0.60 $\pm$ 0.30	1
B04	solo	54.200	108.400	26.0 $\pm$ —	—	0
B04	solo	54.200	108.400	116.0 $\pm$ —	—	1
B05	ongu	53.600	107.600	21.0 $\pm$ —	—	0
B05	ongu	53.600	107.600	111.0 $\pm$ —	—	2
B06	suvo	53.600	110.000	15.2 $\pm$ 5.5	1.80 $\pm$ 0.64	2
B06	suvo	53.600	110.000	82.0 $\pm$ 35.0	0.40 $\pm$ 0.30	1
B07	tyrg	52.800	106.300	44.6 $\pm$ 3.3	0.85 $\pm$ 0.12	4
B08	orli	52.600	99.800	70.0 $\pm$ 10.0	0.80 $\pm$ 0.20	1
B08	orli	52.600	99.800	139.6 $\pm$ 4.8	1.00 $\pm$ 0.17	3
B09	arsh	51.900	102.400	92.1 $\pm$ 11.9	1.18 $\pm$ 0.50	2
B10	9212	51.847	104.893	144.0 $\pm$ 19.0	0.60 $\pm$ 0.40	1
B11	9250	51.799	106.015	22.0 $\pm$ —	—	0
B11	9250	51.799	106.015	112.0 $\pm$ —	—	1
B12	mond	51.700	101.000	125.5 $\pm$ 2.9	1.48 $\pm$ 0.20	4
B13	tala	51.700	103.600	128.7 $\pm$ 4.3	0.82 $\pm$ 0.20	6
B14	9233	51.541	104.942	127.0 $\pm$ 10.0	0.70 $\pm$ 0.30	1
B15	9224	51.526	105.121	148.0 $\pm$ 17.0	1.30 $\pm$ 0.30	1
B16	9270	51.336	103.458	24.0 $\pm$ —	—	0
B16	9270	51.336	103.458	114.0 $\pm$ —	—	1
B17	9235	51.320	105.761	45.7 $\pm$ 8.7	0.39 $\pm$ 0.17	2
B18	9221	51.292	105.339	131.5 $\pm$ 6.3	0.91 $\pm$ 0.25	3
B19	9272	51.167	104.407	141.0 $\pm$ 7.1	1.10 $\pm$ 0.21	2
B20	9271	51.153	103.877	21.0 $\pm$ —	—	0
B20	9271	51.153	103.877	111.0 $\pm$ —	—	1
B21	9222	51.021	105.682	137.9 $\pm$ 6.2	1.09 $\pm$ 0.14	3
B22	9223	50.791	105.970	37.6 $\pm$ 3.8	1.00 $\pm$ 0.21	2
B23	9223	50.791	105.970	129.0 $\pm$ 7.0	1.60 $\pm$ 0.41	2

**Table 3.3.1.** (continued)

Station No.	Station Name	Coordinates		Fast direction( $^{\circ}$ )	Splitting time(sec)	number of events
		Latitude( $^{\circ}$ )	Longitude( $^{\circ}$ )			
B24	9237	50.780	104.089	58.8 $\pm$ 5.5	0.83 $\pm$ 0.17	2
B25	zaka	50.400	103.300	127.0 $\pm$ 12.0	1.70 $\pm$ 0.50	1
B25	zaka	50.400	103.300	66.5 $\pm$ 8.3	0.86 $\pm$ 0.24	2
C01	9200	55.965	101.410	133.0 $\pm$ 7.0	1.00 $\pm$ 0.50	1
C02	9215	55.560	101.803	170.0 $\pm$ 13.0	0.90 $\pm$ 0.40	1
C03	9213	55.022	102.055	144.8 $\pm$ 3.5	0.82 $\pm$ 0.07	5
C03	9213	55.022	102.055	144.8 $\pm$ 3.5	0.82 $\pm$ 0.07	5
C04	9203	54.516	102.070	127.5 $\pm$ 3.7	1.18 $\pm$ 0.12	9
C05	9204	54.193	102.649	143.8 $\pm$ 2.6	0.72 $\pm$ 0.09	7
C06	9205	53.929	102.934	149.2 $\pm$ 8.9	0.58 $\pm$ 0.15	3
C07	9206	53.649	103.255	20.0 $\pm$ —	—	0
C07	9206	53.649	103.255	110.0 $\pm$ —	—	5
C08	9207	53.243	103.767	20.0 $\pm$ —	—	0
C08	9207	53.243	103.767	110.0 $\pm$ —	—	2
C09	9209	52.778	104.105	137.7 $\pm$ 4.8	0.90 $\pm$ 0.16	3
C10	9210	52.622	104.234	138.2 $\pm$ 7.4	0.60 $\pm$ 0.13	6
C11	irku	52.200	104.300	25.0 $\pm$ —	—	0
C11	irku	52.200	104.300	115.0 $\pm$ —	—	2
C12	9211	52.169	104.469	20.0 $\pm$ —	—	0
C12	9211	52.169	104.469	110.0 $\pm$ —	—	4
D01	tupi	54.400	119.900	101.0 $\pm$ 8.0	0.90 $\pm$ 0.30	1
D02	chit	52.000	113.600	30.0 $\pm$ —	—	0
D02	chit	52.000	113.600	120.0 $\pm$ —	—	9
D03	9280	50.193	106.254	137.0 $\pm$ 16.0	1.50 $\pm$ 0.40	1
D04	9291	49.747	106.188	145.3 $\pm$ 16.0	0.78 $\pm$ 0.14	4
D05	9282	49.738	106.202	147.2 $\pm$ 23.5	0.34 $\pm$ 0.30	2
D06	hapc	49.700	112.400	71.2 $\pm$ 7.2	0.62 $\pm$ 0.15	3
D07	9283	49.288	106.412	134.1 $\pm$ 9.0	0.37 $\pm$ 0.16	4
D08	9284	48.931	106.682	39.1 $\pm$ 10.9	1.04 $\pm$ 0.39	2
D08	9284	48.931	106.682	132.0 $\pm$ 9.9	0.84 $\pm$ 0.57	2
D09	9285	48.383	106.783	105.2 $\pm$ 5.9	1.13 $\pm$ 0.26	4
D10	9286	47.921	106.954	64.4 $\pm$ 4.5	0.75 $\pm$ 0.14	3
D11	9292	47.866	107.051	69.2 $\pm$ 6.2	0.70 $\pm$ 0.13	3
D12	9287	47.209	107.422	44.2 $\pm$ 6.7	0.32 $\pm$ 0.08	4
D13	9288	46.635	107.758	56.2 $\pm$ 9.6	0.40 $\pm$ 0.14	2
D13	9288	46.635	107.758	132.2 $\pm$ 3.1	1.50 $\pm$ 0.19	3
D14	9289	46.115	107.619	54.7 $\pm$ 21.8	1.28 $\pm$ 0.32	3
D15	9290	45.262	108.260	84.7 $\pm$ 34.4	1.42 $\pm$ 0.62	5

**Table 3.3.2.** Events used in SKS splitting studies

Event No.	Origin			Coordinates		Depth, km	Mag.	Back- Az(°)	Distance (°)
	Year	Day	Time,UT	Latitude,	Longitude,				
				°N	°E				
1	1980	104	18:04	-23.466	-177.297	79	6.0	114.12	100.71
2	1980	298	14:53	18.211	-98.240	72	6.0	23.29	107.61
3	1981	187	03:08	-22.293	171.742	33	6.0	121.58	93.72
4	1982	153	12:37	-18.083	-172.492	33	6.0	107.16	99.33
5	1983	356	04:11	11.866	-13.529	11	6.0	299.91	97.68
6	1984	272	00:03	-25.849	-175.911	21	6.0	114.63	103.35
7	1984	289	10:21	-15.860	-173.643	128	6.0	106.63	96.92
8	1985	134	18:11	-10.562	41.424	10	6.0	242.75	82.53
9	1986	146	19:06	-20.190	178.860	538	6.0	114.96	95.95
10	1986	303	01:28	-21.702	-176.616	188	6.0	112.51	99.72
11	1987	279	04:19	-17.940	-172.225	16	6.0	106.87	99.38
12	1988	282	04:46	-18.771	-172.415	35	6.0	107.54	99.91
13	1988	284	18:20	-28.644	-177.553	27	6.0	117.61	104.59
14	1989	070	05:05	-17.766	-174.761	230	6.0	108.67	97.74
15	1990	004	05:32	-15.397	-172.850	53	6.0	105.74	97.03
16	1990	050	06:48	-15.465	166.385	12	6.0	121.96	85.26
17	1990	174	21:38	-21.568	-176.483	180	6.0	112.33	99.70
18	1991	305	16:23	-30.255	-177.981	21	6.0	118.96	105.60
19	1992	177	06:30	-28.063	-176.735	18	6.1	116.65	104.60
20	1992	178	03:18	-33.682	-179.076	33	5.6	121.97	107.65
21	1992	193	10:44	-22.284	-178.507	381	6.2	114.27	99.09
22	1992	217	06:58	-21.584	-177.322	278	5.7	112.96	99.22
23	1992	217	21:08	-12.023	166.496	109	5.9	119.97	82.46
24	1992	238	08:24	-20.620	-175.151	67	5.5	110.75	99.73
25	1992	241	17:15	-22.154	-179.620	597	5.4	115.02	98.36
26	1992	241	18:18	-0.996	-13.557	10	6.0	292.53	108.25
27	1992	243	20:09	-17.738	-178.775	573	5.0	111.69	95.36
28	1992	254	10:43	-22.518	-175.052	39	5.5	111.87	101.26
29	1992	255	03:57	-6.091	26.680	10	6.0	257.19	87.58
30	1992	259	21:04	-14.122	167.263	196	6.1	120.51	84.61
31	1992	285	19:24	-19.276	168.913	157	6.0	122.06	89.75

# CHAPTER 4

## Interpretation of Teleseismic Quasi\_P wave Travel Time Residuals by Assuming an Anisotropic Upper Mantle

### 4.1 Introduction

In Chapter 2 we interpreted the observed teleseismic P-wave travel time residuals by assuming an *isotropic* upper mantle. However, SKS splitting studies described in Chapter 3 indicated that the upper mantle of the study area is anisotropic. The source of anisotropy might be horizontal flow associated with the rift. If we assume that the horizontal flow originates from beneath the rift axis, similar to what happens beneath the mid-ocean ridges, there must be a vertical flow in the vicinity of the rift zone. This vertical flow aligns upper mantle anisotropic minerals such as olivines and orthopyroxenes which are major constituents of the upper mantle, and causes vertical anisotropy. A vertically *anisotropic* upper mantle is used in this chapter for the interpretation of the travel time data.

The model described in this chapter is mainly motivated by the two valleys observed in most of the travel time residual curves. The two downwarps on the lithosphere/asthenosphere boundary at each side of the rift (Figure 2.5.2) have not been observed by previous studies such as Deep Seismic Sounding, gravity and magnetotelluric investigations, and heatflow modeling. Unless the existence of the downwarps is confirmed by some independent approach, the explanation that the valleys are caused by anisotropy is more consistent with previous results, because it does not include a lithospheric downwarp.

Strictly speaking, in anisotropic media, the term P- wave is no longer valid, since the polarization direction no longer aligns with the direction of propagation. The term 'quasi-P' is usually used for the P-wave-like phase [Anderson, 1989]. For the sake of simplicity, we will still use the term 'P-wave' throughout this chapter wherever the term 'quasi-P-wave' is meant. In weakly anisotropic media, the directions of polarization of the quasi-P waves remain close to the direction of propagation [Babuska and Cara, 1991].

Both olivine and orthopyroxene are important highly anisotropic upper mantle constituents. Mantle peridotites typically contain more than 65% olivine and 20% orthopyroxene [Anderson, 1989]. Under plastic flow the orthopyroxene axis with the medium velocity aligns with the flow direction, and the axis with high velocity is perpendicular to the flow plane [Christensen and Lundquist, 1982]. Since orthopyroxene is not as abundant and anisotropic as olivine and for the sake of simplicity, in the discussion we will assume that the upper mantle beneath the study area is composed of a certain percentage of oriented olivine. The rest is randomly oriented olivine, orthopyroxene, and other mantle minerals. Under the assumption of transverse isotropy that we are going to use in this chapter, orthopyroxene has near zero anisotropy.

Anisotropy of the upper mantle most likely originates from preferred orientation of olivine crystals (Figure 3.1.3). Studies to date indicate that the  $a$ - axes of olivine-rich aggregates cluster around the flow direction, the  $a$ - and  $c$ - axes concentrate in the flow plane while the  $b$ - axes align perpendicular to the flow plane [Anderson 1989; Nicolas et al., 1973; Nicolas and Poirier, 1976]. For vertical flow, because the the  $a$ - axis of olivine, along which the P-wave has the highest velocity,

is vertical, the averaged P-wave velocity in the horizontal plane is lower than the vertical P-wave velocity [Anderson, 1989]. On the horizontal plane, since the  $b$ -axes are perpendicular to the flow plane and the  $c$ -axes are in it, the anisotropy is weak with the fast direction for P-wave being in the flow plane (Figure 3.1.3).

If all the three axes are preferredly oriented, the medium is analogous to orthorhombic crystals, which require 9 elastic constants to describe fully [Christensen and Crosson, 1968] and cannot be well resolved by our data set. In this chapter we will use the transverse isotropy assumption. Transversely isotropic materials are characterized by an axis of symmetry normal to which all longitudinal or compressional waves travel at the same velocity [Christensen and Crosson, 1968]. Five independent elastic constants are sufficient to completely describe a transversely isotropic elastic medium. The transversely isotropic medium that we consider in this chapter is formed by an oriented  $a$ -axis, which is vertical, and randomly oriented  $b$ - and  $c$ -axes in the girdle normal to the  $a$ -axis. This form of anisotropy has been observed in many ultramafic rocks and been used extensively for the interpretation of P-wave azimuthal velocity variations [e.g., Fuchs, 1984; Christensen and Crosson, 1968]. A transversely isotropic solid exhibits the same symmetry as a hexagonal crystal [Anderson, 1989; Babuska and Cara, 1991].

Most of the previous studies on P-wave anisotropy have been made under the assumption of horizontal  $a$ -axis alignment caused by horizontal flow [e.g., Hess, 1964; Bamford, 1977]. One of the few studies analogous to ours was made by Blackman et al. [1993] in the Mid-Atlantic Ridge area. Instead of expected later teleseismic P-wave arrivals, they observed early arrivals with the minimum value approximately at the middle of the ridge and interpreted the observation as

the result of vertical-flow-induced anisotropy. Since our data set (Figures 2.3.6 and 2.3.7) exhibits later arrivals around the Baikal rift axis and early arrivals at about 200 km from it, a more complicated model is needed for the interpretation. In this chapter we interpret the travel time residual patterns as combinations of thermal and anisotropic effects caused by vertical flow beneath the Baikal rift zone.

## 4.2. Model construction

Figure 4.2.1 shows the velocity model and theoretical travel time residuals computed for vertically incident rays. The model is composed of an anisotropic low velocity upwarp and a flat asthenospheric layer of anisotropy. The anisotropic region is transversely isotropic with vertical axis of symmetry. A ray with vertical incidence has the highest velocity and a ray with horizontal incidence has the lowest velocity. The anisotropy in both the upwarp and the flat asthenospheric layer is inhomogeneous, with the highest value at zero distance and decays exponentially with increasing distance from the center, as shown in the diagram on the bottom of Figure 4.2.1.

The top diagram of Figure 4.2.1 shows travel time residuals in three cases: when the flat asthenospheric layer of anisotropy is absent, the residual curve consists of positive values with the peak at the center; when the upwarp is absent, the residual curve consists of negative values with the minimum value at the center; for the combined travel time residual curve there are two valleys at  $\pm 150$  km from the center and a reduced peak at the center. The one-peak-and-two-valley feature, as well as the magnitudes of the peak and the valleys are in good agreement with the observed data (Figures 2.2.6 and 2.2.7).

The model was created using 12 parameters, which are described in detail below. The task of this chapter is to improve this model by adjusting the parameters using observed travel time residual data.

According to the laboratory measurements of Verma [1960], the compressional wave velocities for propagation parallel to the 3 crystallographic axes of olivine are  $v_a = 9.87$  km/s,  $v_b = 7.73$  km/s,  $v_c = 8.65$  km/s (Figure 3.1.2). Therefore the maximum anisotropy is

$$\alpha_{max} = \frac{2(v_a - v_b)}{v_a + v_b} = 24.32\%. \quad (4.2.1)$$

If a transversely isotropic medium is composed of 100% olivine crystals with 100% alignment, the maximum velocity is  $v_{max} = v_a = 9.87$  km/s, and the minimum velocity is  $v_{min} = (v_b + v_c)/2 = 8.17$  km/s. Therefore the maximum anisotropy becomes

$$\alpha_{max} = \frac{2(v_{max} - v_{min})}{v_{max} + v_{min}} = 17.22\%. \quad (4.2.2)$$

For non-vertical incidence, the incidence-angle-dependence of velocity in anisotropic media with weak anisotropy ( $< 10\%$ ) can be calculated using the result of Backus [1965] and its modified forms. One of the most frequently used forms for transversely isotropic media is [Bamford, 1977; Crampin and Bamford, 1977; Fuchs, 1984; Anderson, 1989]

$$V_p^2(\theta) - V_0^2 = c_1 \cos(2\theta) + c_2 \cos(4\theta), \quad (4.2.3)$$

where  $V_0$  is the mean velocity,  $\theta$  is the angle between the symmetry axis and the ray direction,  $c_1$  and  $c_2$  are combinations of four elastic constants,  $c_1 = (c_{11} - c_{22})/2$ ;  $c_2 = (c_{11} + c_{22})/8 - c_{12}/4 - c_{66}/2$  [Anderson, 1989].

If the mantle is convecting beneath the rift, it is reasonable to assume that the anisotropy reaches its maximum beneath the rift axis and decreases with increased distance from it,  $c_1$  and  $c_2$  above are considered to be a Gaussian function of distance from the rift axis with the forms (under the coordinate systems of Figure 2.3.2)

$$c_1(y) = c_{10} \exp(-0.5y^2/\sigma^2) \quad (4.2.4)$$

and

$$c_2(y) = c_{20} \exp(-0.5y^2/\sigma^2), \quad (4.2.5)$$

where  $\sigma$  is the standard deviation of the Gaussian function. To include possible asymmetric decay of the anisotropies, an independent  $\sigma$  is used for  $y < 0$  and  $y > 0$ .

The structure is two dimensional with the strike along  $+X$  direction (Figure 2.3.2). The surface of the upwarp is described using a parabola of the form

$$z(y) = a_1 + \lambda y^2, \quad (4.2.6)$$

where  $a_1$  is the depth of the peak of the upwarp, and  $\lambda$  is the coefficient of the parabola. To include possible asymmetric shape of the upwarp, an independent  $\lambda$  is used for  $y < 0$  and  $y > 0$ .

Similar to Chapter two, the strike and location of the vertex line of the two-dimensional structure will also be treated as unknown parameters.

In summary, there are totally twelve unknown parameters to be solved, they are:

1.  $a_1$ : depth of the upwarp;
2.  $\lambda_1$ : coefficient of the left parabola;

3.  $\lambda_2$ : coefficient of the right parabola;
4.  $\gamma$ : asthenospheric-lithospheric mean velocity contrast;
5.  $c_{10}$ : magnitudes of anisotropy parameter 1;
6.  $c_{20}$ : magnitudes of anisotropy parameter 2;
7.  $\sigma_1$ : standard deviation of the left Gaussian function;
8.  $\sigma_2$ : standard deviation of the right Gaussian function;
9.  $\phi_0$ : strike of the structure measured anti-clockwise from the East;
10.  $b$ : location of the vertex line of the 2D structure (see Figure 2.3.2);
11.  $h_1$ : thickness of the flat asthenospheric anisotropy layer.
12.  $h_0$ : depth of the base of the upwarp.

Figure 4.2.2 shows some examples of the function  $f(\theta) = c_1 \cos(2\theta) + c_2 \cos(4\theta)$  for some combinations of  $c_1$  and  $c_2$ , which are parameters of the medium. The curves were calculated for all the possible angles of incidence ( $0^\circ - 45^\circ$ ). The dashed lines are the  $c_1$  term, the dotted lines are the  $c_2$  term, and the solid lines are the sum of the two terms.

The anisotropy  $\alpha$  shown on the top of each diagram in Figure 4.2.2 was calculated using

$$\begin{aligned} \alpha &= 2 \frac{V_p(\theta = 0) - V_p(\theta = 90)}{V_p(\theta = 0) + V_p(\theta = 90)} \\ &= 2 \frac{\sqrt{V_0^2 + c_1 + c_2} - \sqrt{V_0^2 - c_1 + c_2}}{\sqrt{V_0^2 + c_1 + c_2} + \sqrt{V_0^2 - c_1 + c_2}} \end{aligned} \quad (4.2.7),$$

where  $V_p(\theta)$  is defined in Equation 4.2.3,  $V_0$  is taken as 8.0 km/s.

Some of the dominant features of the curves in Figure 4.2.2 are:

- 1). For the same  $c_2$ , a larger  $c_1$  corresponds to a larger anisotropy ( $\alpha$ ) and a stronger  $\theta$  (angle of incidence) dependence of velocity ( $V_p(\theta)$  in Equation 4.2.3).

2). For the same  $c_1$ , a larger  $c_2$  corresponds to a smaller anisotropy ( $\alpha$ ) and a stronger  $\theta$  (angle of incidence) dependence of velocity ( $V_p(\theta)$  in Equation 4.2.3).

3). When  $c_1$  is small and  $c_2 < 0$ , the maximum velocity does not correspond to vertical incidence (e.g. the upper-left plot of Figure 4.2.2c).

For a transversely isotropic olivine aggregate with  $a$ - axes all aligned and  $b$ -,  $c$ - axes random, Crampin and Bamford [1977] found  $c_1 = 15.11, c_2 = 3.342$ . Crosson [1972] fitted the Quartet and Flora data of  $P_n$  velocity variations observed by Raitt et al. [1969] in the oceanic upper mantle off Southern California to obtain  $c_1 = 1.882, c_2 = 0.358$ . Bamford [1977] obtains  $c_1 = 4.658, c_2 = -0.229$  using  $P_n$  velocity data from Western Germany. Although these values were obtained for azimuthal variation of P-wave velocity in the horizontal plane, they give an approximate range of the values that we might expect to get.

### 4.3. Method of computation

In an anisotropic medium the velocity at a point for a specific ray is a function of arrival azimuth and angle of incidence. Under the assumption of transverse isotropy with vertical axis of symmetry used in this chapter, the velocity is only dependent on the angle of incidence. The following steps are taken for the construction of the velocity model and computation of travel times for a given teleseismic event.

1. Divide the  $YOZ$  plane (see coordinate systems in Figure 2.3.2) into small rectangular cells of the size  $dy$  by  $dz$ .

2. Assign each cell a velocity using Equations 4.2.3 through 4.2.6.

3. Separate the ray path into small segments of the length  $ds$  and find the coordinates of the mid-point for each segment according to the arrival azimuth and angle of incidence of the ray.

4. Find the cell for each mid-point. The velocity for each segment of the ray is then determined. The time needed for the ray to travel through the entire medium is the sum of travel times over all the cells.

5. To get travel time residuals relative to the Siberian craton, the computed travel time for a station on the craton is subtracted from the computed travel time of each station.

Obviously, the smaller the cell size and the segment length, the more accurate the calculated travel time residuals will be. In practice, we use  $dy = dz = 5$  km,  $ds = 2$  km in this study. Some empirical tests using small  $dy, dz$  and  $ds$  under different possible velocity structures show that the maximum error for a station between this set of values and the more accurate sets is less than 0.05 seconds, which is less than half of the typical errors of the data set.

#### **4.4. Nonlinear Bayesian inversion: results**

In order to find a starting model for which the computed theoretical travel time residuals approximately match the observed ones, some empirical tests were performed using different combinations of the 12 parameters described in section 4.2.

One of these tests is shown in Figures 4.2.1 and 4.4.1. The one-peak-and-two-valley feature and the movement of the locations of the valleys observed in the data are reproduced well. The magnitudes of the peaks and the valleys are also approximately matched.

The starting parameters and their standard deviations are chosen based on previous studies and our data set described in section 2.3, as well as some forward modelling.

One of the most important previous studies is the Deep Seismic Sounding conducted along some thousands of km long profiles in the area. Figure 4.4.2 shows an averaged velocity section of the upper mantle beneath the Siberian craton [Egorkin et al., 1984]. The sudden velocity change from 8.75 to 8.35 km/s at 200 km depth implies that the averaged lithospheric thickness of the Siberian Craton is 200 km. The sudden increase of velocity at the depth of 425 km (from 9.4 to 10 km/s) may correspond to the olivine spinel transition. The velocities above 425 km were better resolved than those below this depth.

The starting parameters and their standard deviations are chosen according to previous results, as well as some forward modelling.

$a_1$ , the depth of the peak of the asthenospheric upwarp, is chosen as  $50 \pm 10$  km based on some of the previous studies [e.g. Logatchev and Zorin, 1992; Gao et al., 1994b] and the results from in Chapter 2.

$\lambda_1$  and  $\lambda_2$ , the coefficients of the left and right parabola, are set to be  $0.01 \pm 0.001$ . This choice results in an upwarp with a width of 250 km extending 200 km deep, which is close to some of the previous results.

$\gamma$ , the velocity contrast between the lithosphere and the upwarped asthenosphere, is chosen as  $6 \pm 0.3\%$ .

$c_{10}$  and  $c_{20}$ , magnitudes of anisotropy parameters, are chosen as  $2 \pm 0.2$  and  $0 \pm 0.2$  respectively. The maximum anisotropy calculated using these values is about 6%. Empirical tests of the function  $f(\theta) = c_1 \cos(2\theta) + c_2 \cos(4\theta)$  in section

4.2 indicate that a positive  $c_2$  tends to enlarge the difference of the magnitude of travel time residuals for different angles of incidence, which is not a clear feature on our data set. Therefore,  $c_2$  must be near zero or even a negative number.

$\sigma_1$  and  $\sigma_2$ , the standard deviation of the left and right Gaussian function describing the decay of  $c_1$  and  $c_2$  (Equations. 4.2.4 and 4.2.5) respectively, are chosen as 200 km with standard deviation 40 km. Empirical tests indicate that small  $\sigma_1$  and  $\sigma_2$  reduce the magnitudes of or eliminate the two valleys on the travel time residual curves; large  $\sigma_1$  and  $\sigma_2$  result in valleys with unrealistic depths.

$\phi_0$ , the orientation of the two-dimensional structure measured anti-clockwise from the East, is set to be  $50 \pm 10^\circ$ , which is approximately the orientation of the surface expression of the rift.

$b$ , the offset of the vertex line (Figure 2.3.2), is set to be  $0 \pm 10$  km.

$h_1$ , thickness of the flat asthenospheric layer of vertical anisotropy, is set to be  $200 \pm 5$  km; and  $h_0$ , the depth of the base of the upwarp (i.e. the thickness of the normal lithosphere) is set to be  $200 \pm 10$  km. The bottom of the asthenosphere may correspond to a change from olivine-rich mantle to olivine-poor mantle [Anderson, 1989]. We therefore initially put the low limit of the anisotropic layer ( $h_0 + h_1$ ) at 400 km, approximately at the bottom of the asthenosphere (Figure 4.4.2).

The result of the inversion is obtained after 100 iterations. Figure 4.4.3 shows the sum of squared residuals (SSR) at each iteration. After 100 iterations, the SSR dropped from 60 to 26. No significant decreasing of SSR is observed after the 50th iteration, implying that 100 iterations are (more than) enough. The inversion took about 6 hours on a SUN Sparc 5 workstation. The errors of the parameters are

calculated from the diagonal elements of the covariance matrix defined in Equation 2.4.25. The resulting parameters are:

1.  $a_1 = 45 \pm 15$  km
2.  $\lambda_1 = 0.00877 \pm 0.00065$  km<sup>-1</sup>
3.  $\lambda_2 = 0.01363 \pm 0.00070$  km<sup>-1</sup>
4.  $\gamma = 2.53 \pm 0.09\%$
5.  $c_1 = 1.573 \pm 0.053$  km<sup>2</sup>/s<sup>2</sup>
6.  $c_2 = -0.692 \pm 0.052$  km<sup>2</sup>/s<sup>2</sup>
7.  $\sigma_1 = 350 \pm 125$  km
8.  $\sigma_2 = 170 \pm 40$  km
9.  $\phi_0 = 51.8^\circ \pm 0.8^\circ$
10.  $b = 33 \pm 20$  km
11.  $h_1 = 170 \pm 20$  km
12.  $h_0 = 230 \pm 30$  km

The resulting velocity model is shown on Figure 4.4.4 for rays with 28° incident angle. The fitted and original data are shown in Figure 4.4.5.

The results indicate that the low velocity upwarp starts at a depth of 230 km and reaches 45 km deep. The velocity inside the upwarp is 2.5% lower than the outside velocity at the same depth. At the bottom the upwarp is about 260 km wide.

The strike of the structure is 52° measured anti-clockwise from the East and the vertex line of the 2D structure is 33 km south of the origin of coordinate system  $X'O'Y'$  (Figure 2.3.2), which is at the southern shore of the 30 km wide Lake. The inversion indicates that the vertex line of the 2D structure is approximately parallel

to the axis of the surficial appearance of the rift, but shifts about 25 km to the southeast.

The estimated vertical anisotropy at the top of the flat asthenospheric layer of anisotropy computed using Equation 4.2.7 is shown in Figure 4.4.6. The maximum vertical anisotropy is 2.8%. An asymmetric shape of the anisotropy curve is revealed. At the same distance from the rift axis the NW side, i.e. beneath the Siberian platform the asthenosphere is more anisotropic than on the SE side. Both the observed rift-perpendicular horizontal anisotropy described in Chapter 3 using the SKS phase and the vertical anisotropy revealed in this chapter may originate from the same upper mantle flow system. It is reasonable to say that a greater vertical anisotropy is the result of stronger vertical flow, which in turn results in a stronger and therefore a far-reaching horizontal flow perpendicular to the rift axis. This asymmetry in the flow may explain our observations that on the Siberian platform the rift-perpendicular fast SKS direction reaches at least 600 km from the rift, and on the Mongolia fold belt side it changes direction at a distance about 300 km from the rift.

Figure 4.4.7 shows the cross correlation coefficients between the parameters. While most of the parameters are highly independent, some parameter pairs have large coefficients. A significant positive correlation between  $\gamma$  and  $c_1$  ( $C_{4-5} = 0.36$ ) indicates that increasing the velocity contrast in the upwarp has similar effects on the fitting as increasing the degree of vertical anisotropy. On the other hand, a significant negative correlation between  $\gamma$  and  $h_0$  ( $C_{4-12} = -0.68$ ) indicates that increasing the velocity contrast in the upwarp has similar effects on the fitting as reducing the height of the upwarp.

The trace of the matrix describing the resolution provided by observed data is (Equation 2.4.26)

$$R_a = 8.8,$$

and the trace of the matrix describing the resolution provided by prior data is (Equation 2.4.27)

$$R_b = 3.2,$$

implying that the observed data contributed to about 73% to the solution of the parameters and the rest is contributed by the prior data.

## FIGURE CAPTIONS

Figure 4.2.1: Velocity model (mid-diagram), theoretical travel time residuals computed for vertically incident rays (top), and vertical anisotropy across the profile (bottom). The model is composed of an anisotropic low velocity upwarp and a flat asthenospheric layer of anisotropy. The anisotropic media are transversely isotropic with vertical axis of symmetry. The travel time residuals are computed for the case 1) when the flat asthenospheric layer of anisotropy is absent (dashed line); 2) when the upwarp is absent (dotted line); and 3) when both are present (solid line).

Figure 4.2.2: Examples of  $f(\theta) = c_1 \cos(2\theta) + c_2 \cos(4\theta)$  for some combinations of  $c_1$  and  $c_2$ , which are property parameters of the medium. The curves were calculated in all the possible angle of incidence in the range ( $0^\circ - 45^\circ$ ). The dashed lines are the  $c_1$  term, the dotted lines are the  $c_2$  term, and the solid lines are the sum of the two terms.  $\alpha$  is the vertical anisotropy.

Figure 4.4.1: Same as Figure 4.2.1 but for non-vertical incidence. For different angles of incidence the velocity inside the anisotropic media is different, as indicated by the difference in the brightness of the imaging. For instance, the velocity inside the anisotropic parts is higher for  $\theta = 10^\circ$  (figure A) than than for  $\theta = 30^\circ$  (figure C).

Figure 4.4.2: Averaged P-wave isotropic velocity section of the upper mantle beneath the Siberian craton from Russian Deep Seismic Sounding experiments. The data are taken from Table 3 of Egorkin et al. [1984].

Figure 4.4.3: Sum of squared residuals (SSR) at each iteration. After 100 iterations, the SSR dropped from 59 to 26.

Figure 4.4.4: P-wave velocity model of the Baikal rift and adjacent regions from Bayesian inversion. The diagram on the top shows P-wave velocity at 300 km depth for rays with angle of incidence =  $28^\circ$ , which is the angle of event group 92L and is approximately the mid-value for all the groups (Table 2.2.3). The horizontal velocity variations, as indicated by horizontal variation of imaging brightness, is the effect of vertical anisotropy. The small insert on the right is a plot of isotropic  $V_p$  as a function of depth in the regions outside the upwarp area from Egorkin et al. [1984].

Figure 4.4.5: Inverted velocity model (upper-right insert), fitted (solid lines) and original (dots) data, as well as arrival direction of the rays (upper-left insert) for the 1992 (A) and 1991 (B) networks. The velocity model is plotted along the  $+Y$  direction, and the travel time residuals are plotted along the 1992 and 1991 profiles for figure (A) and (B), respectively.

Figure 4.4.6: Estimated vertical anisotropy at the top of the flat asthenospheric layer of anisotropy.

Figure 4.4.7: Cross correlation coefficients between final parameters computed from covariance matrix, which is a symmetric matrix with unit diagonal elements.

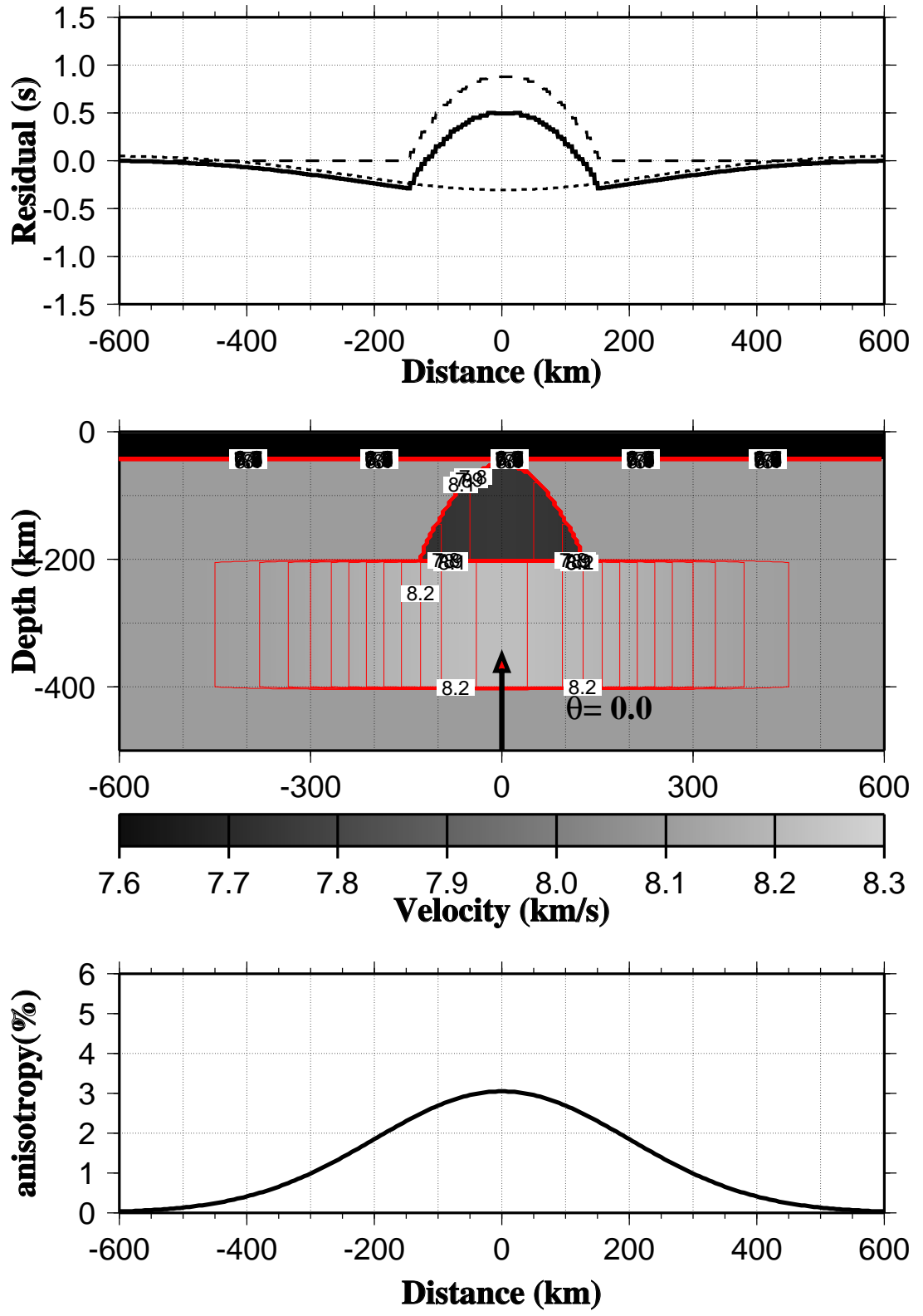


Figure 4.2.1

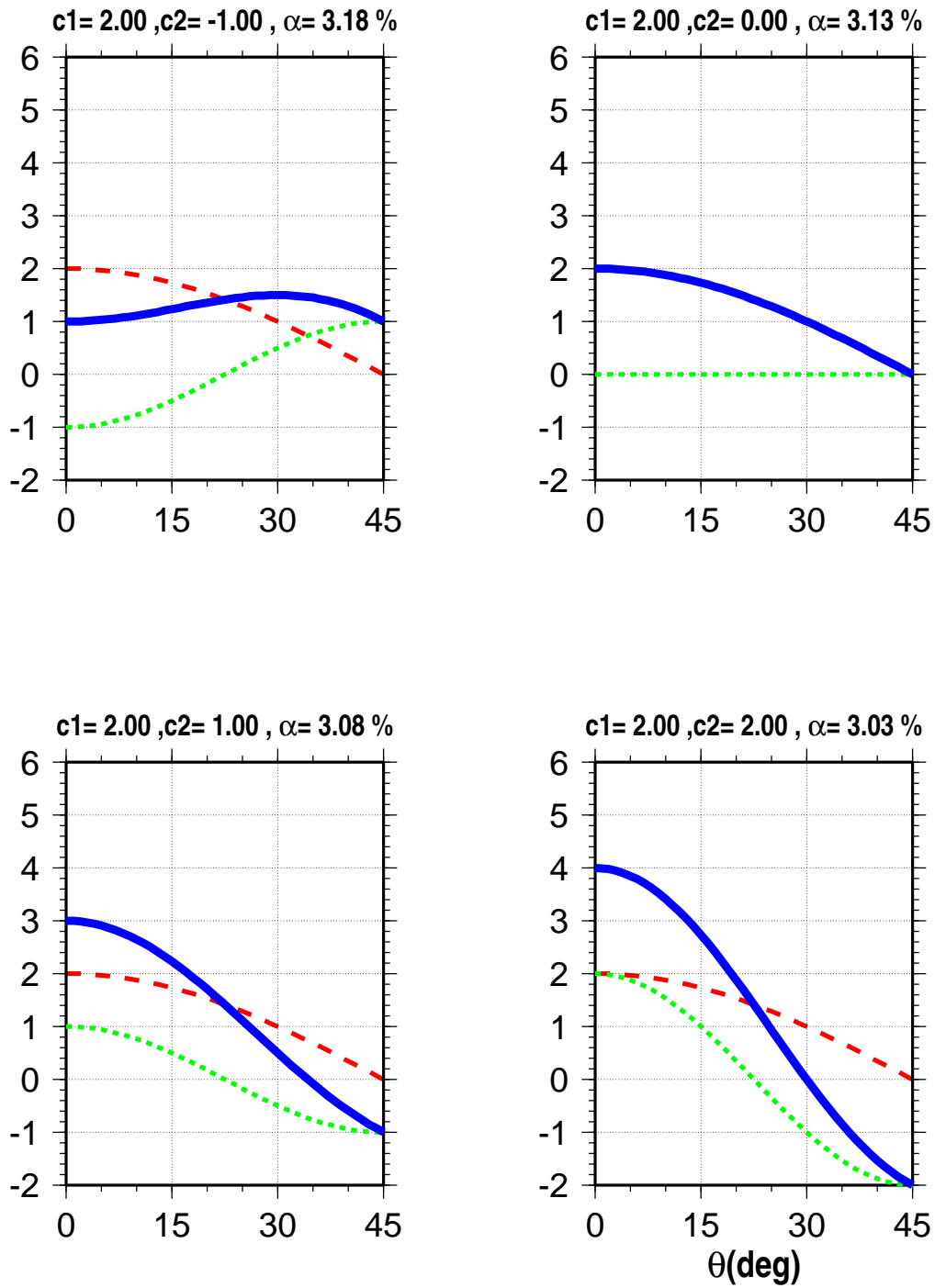


Figure 4.2.2 (A)

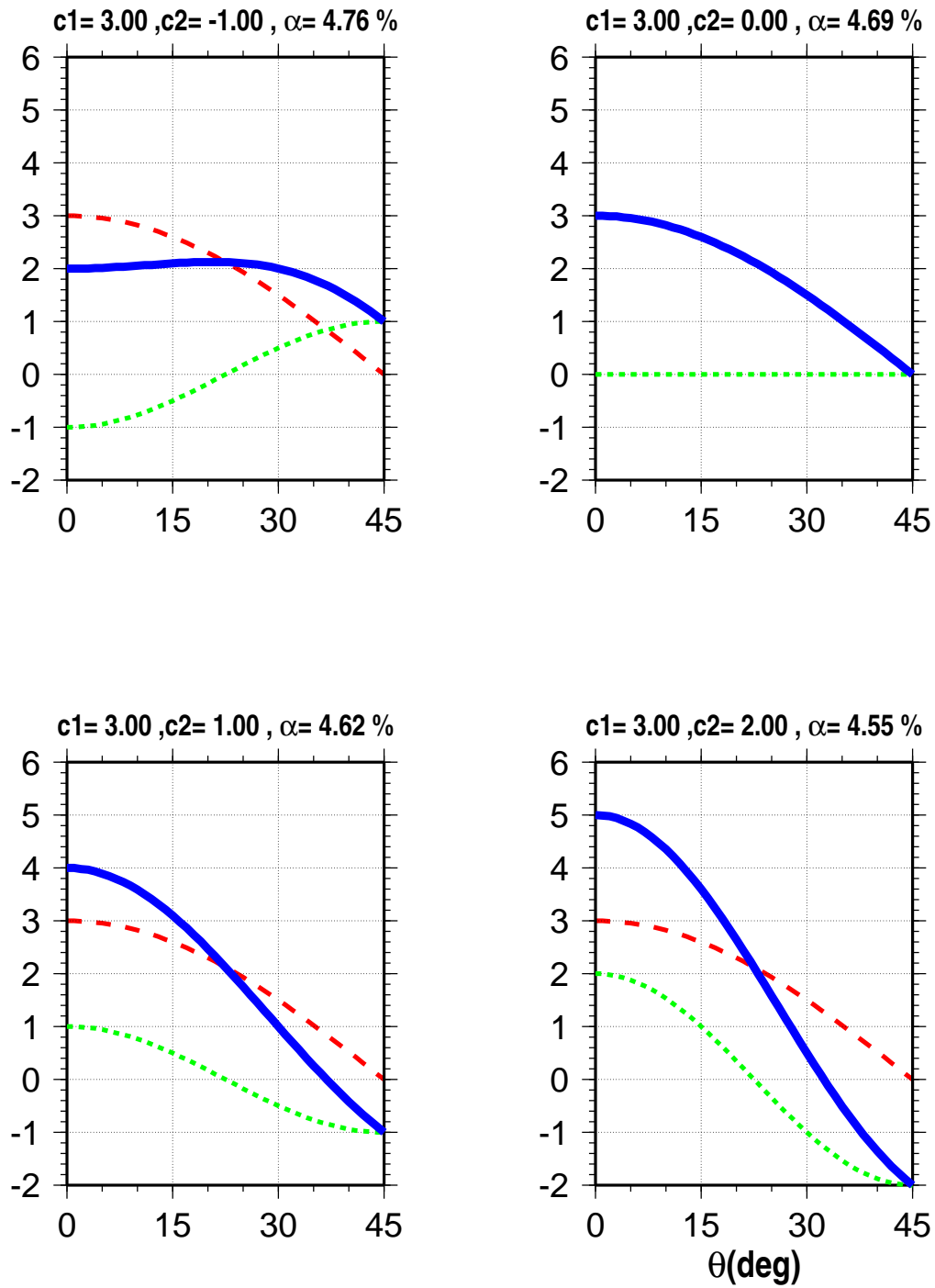


Figure 4.2.2 (B)

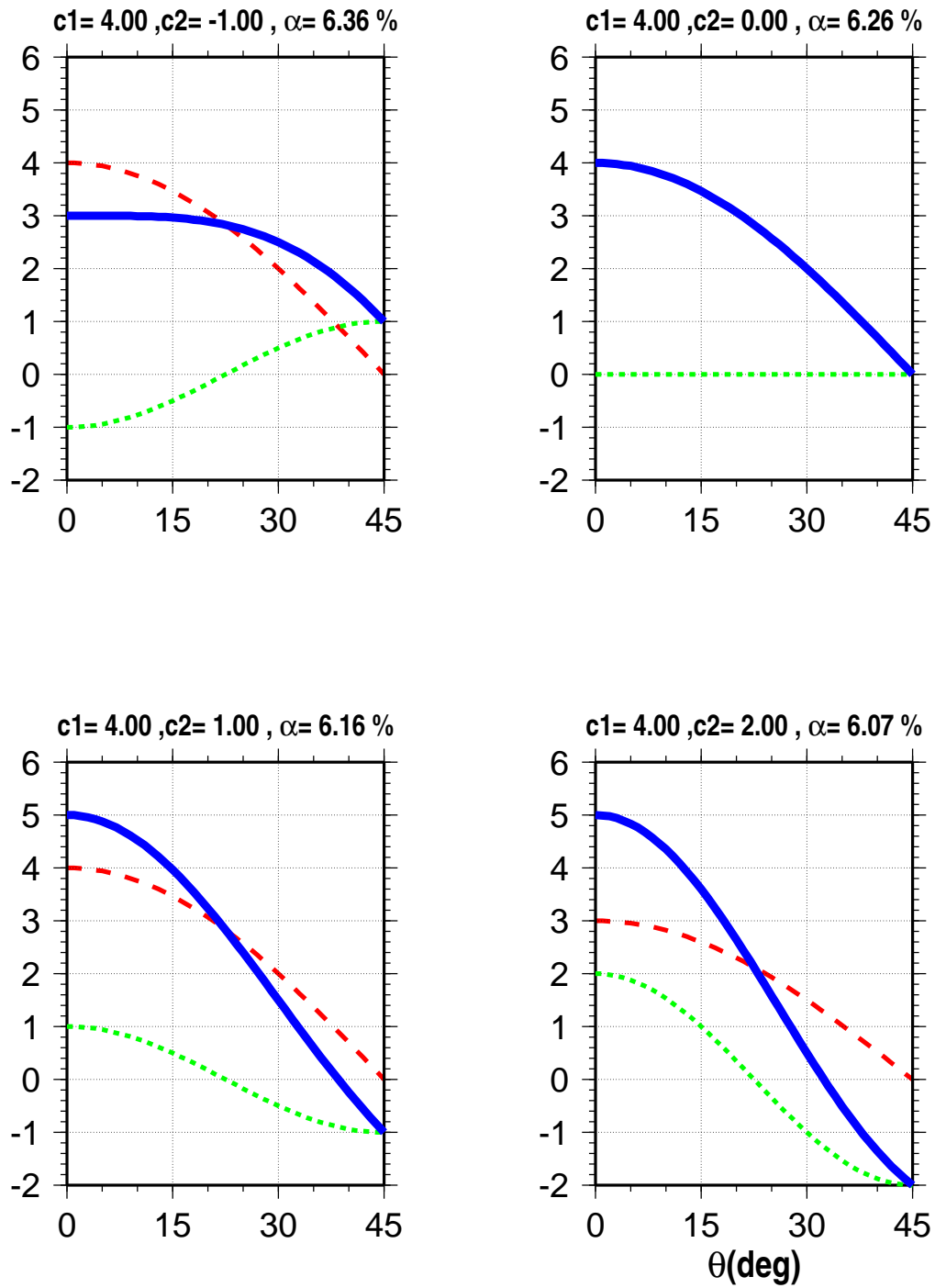


Figure 4.2.2 (C)

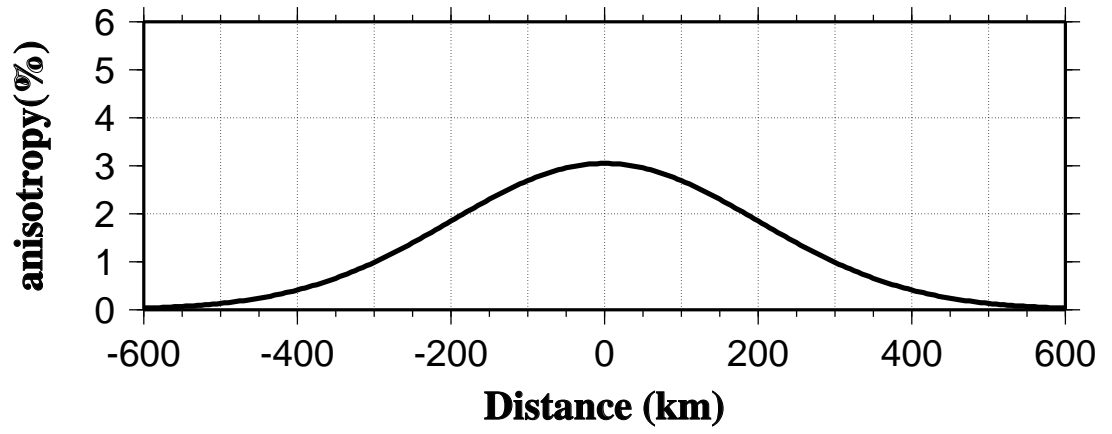
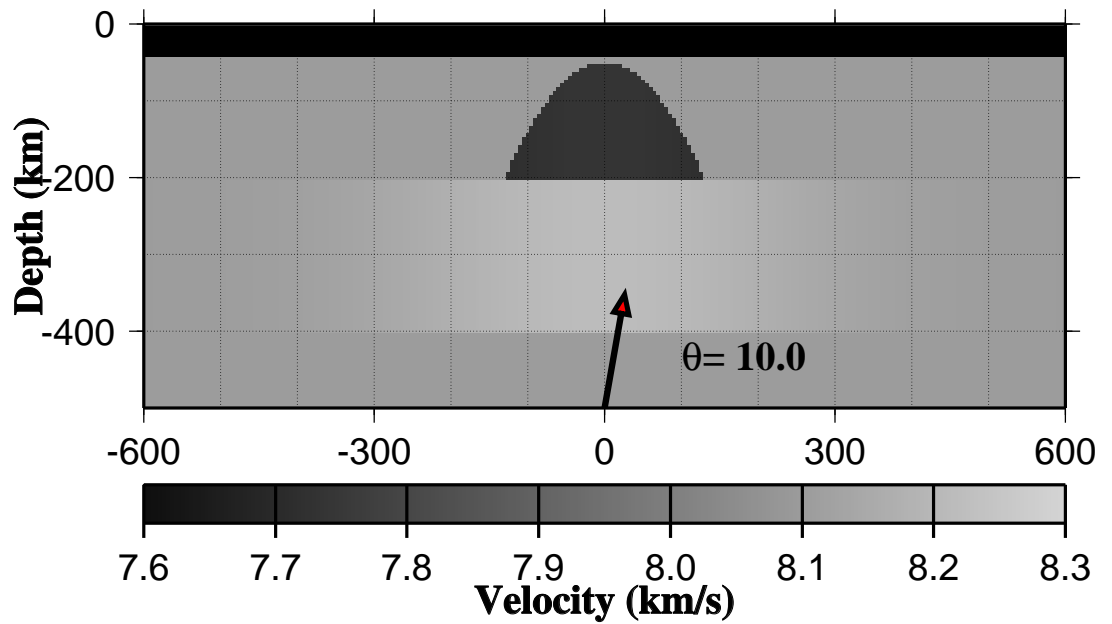
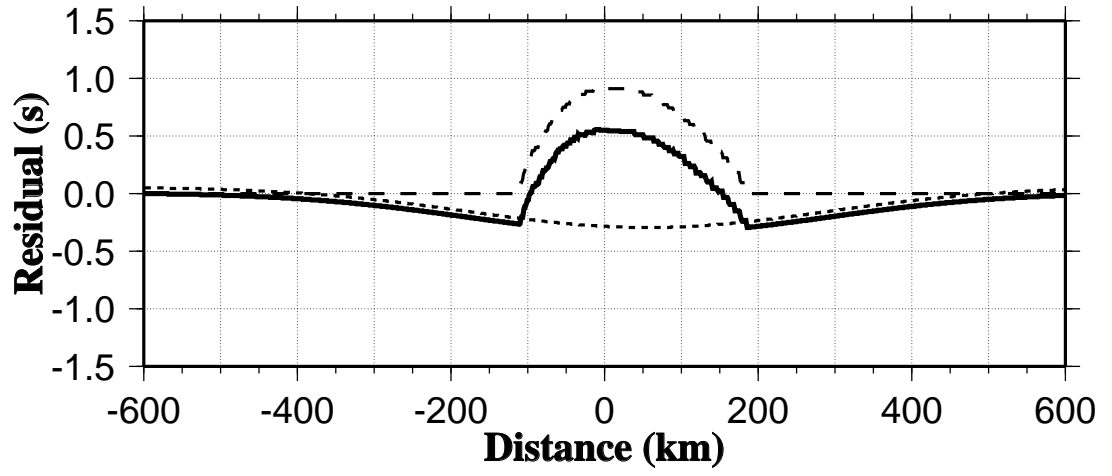


Figure 4.2.1

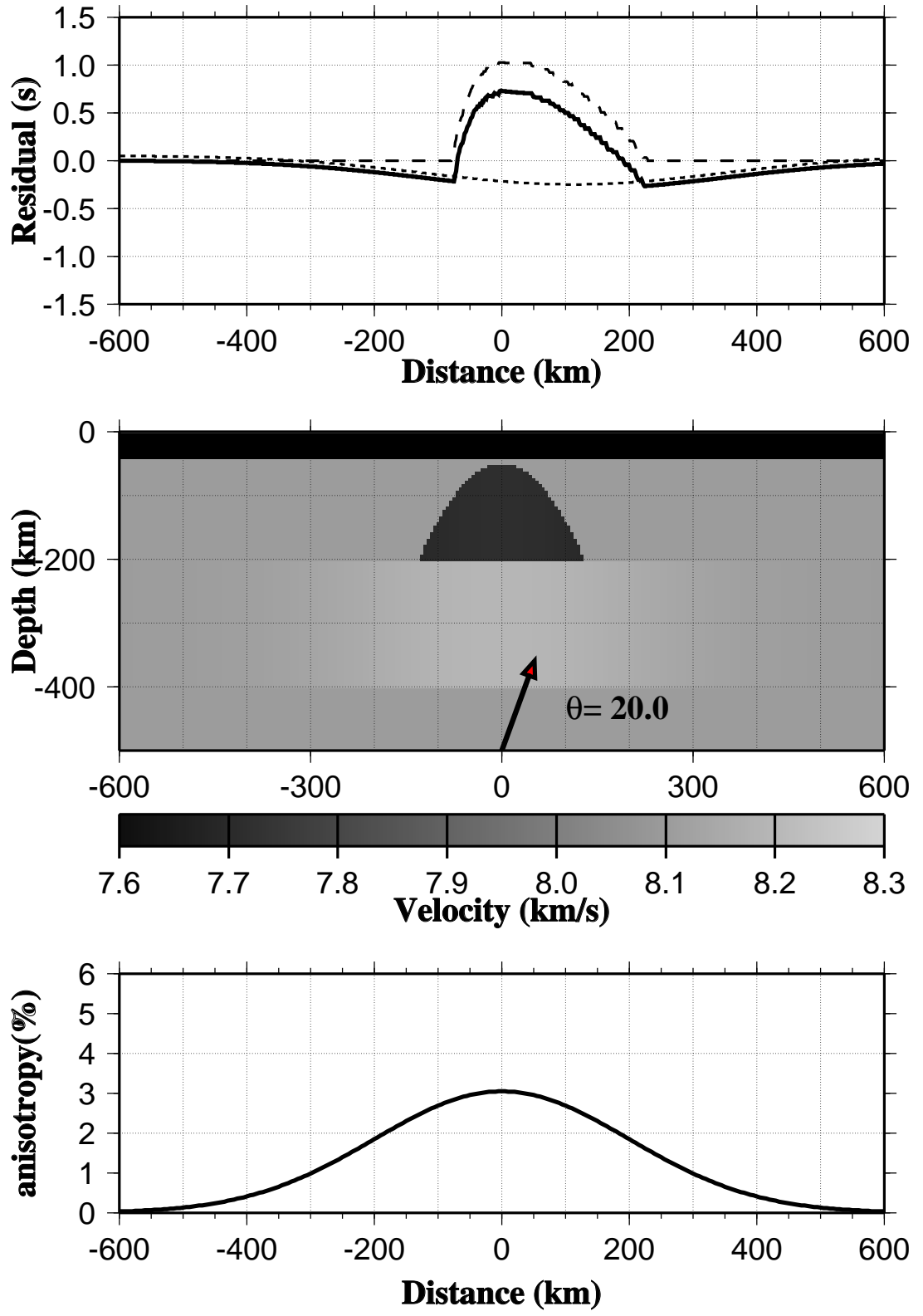


Figure 4.4.1 (B)

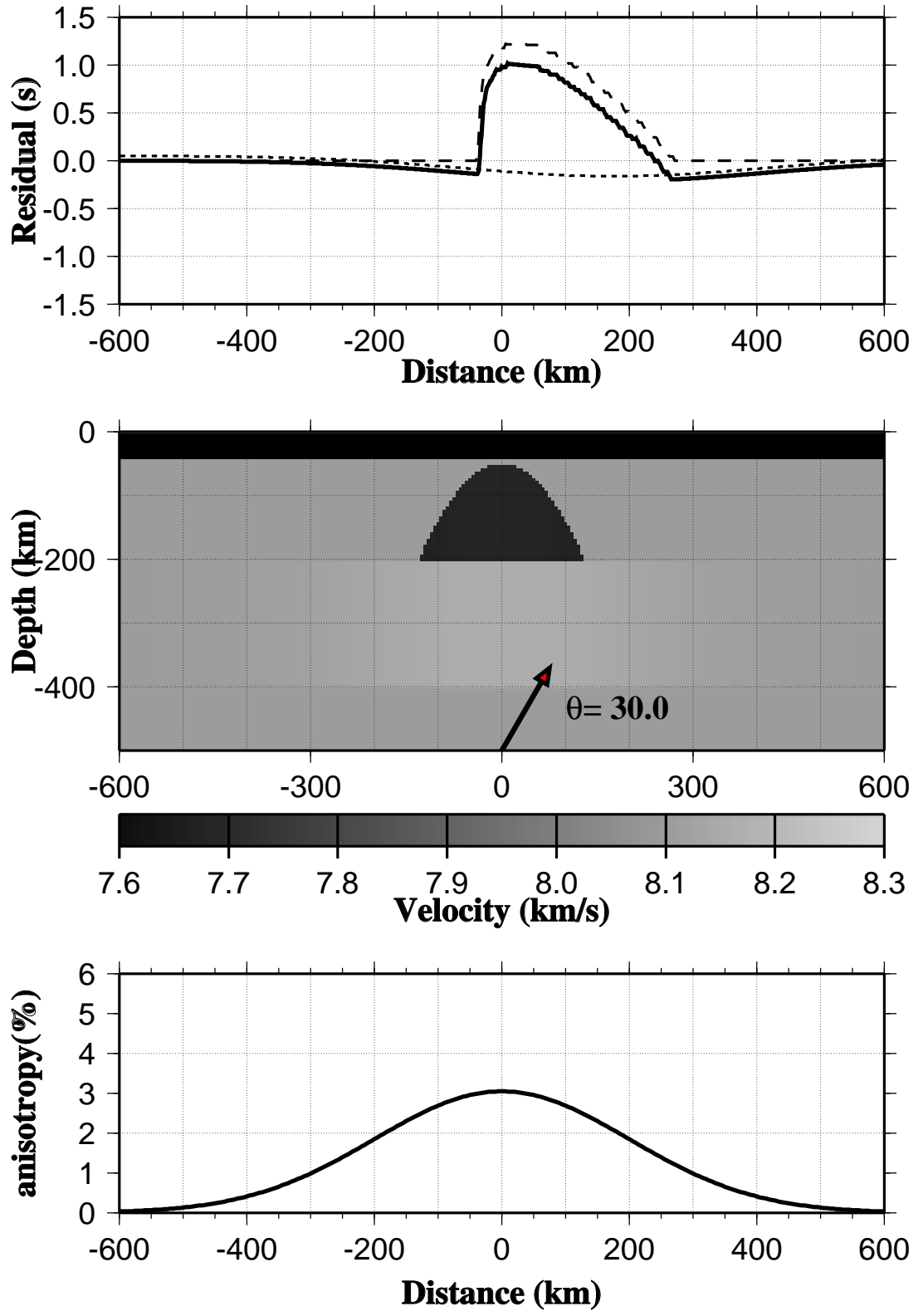
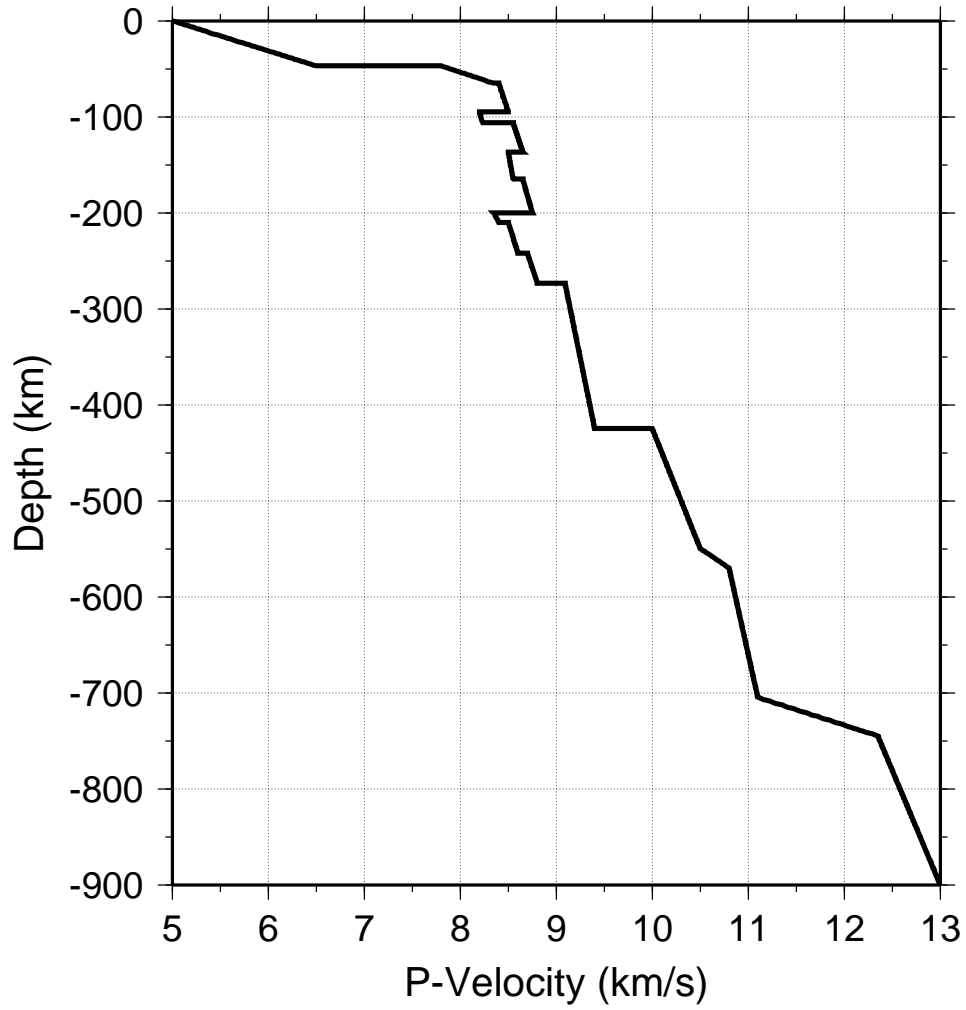
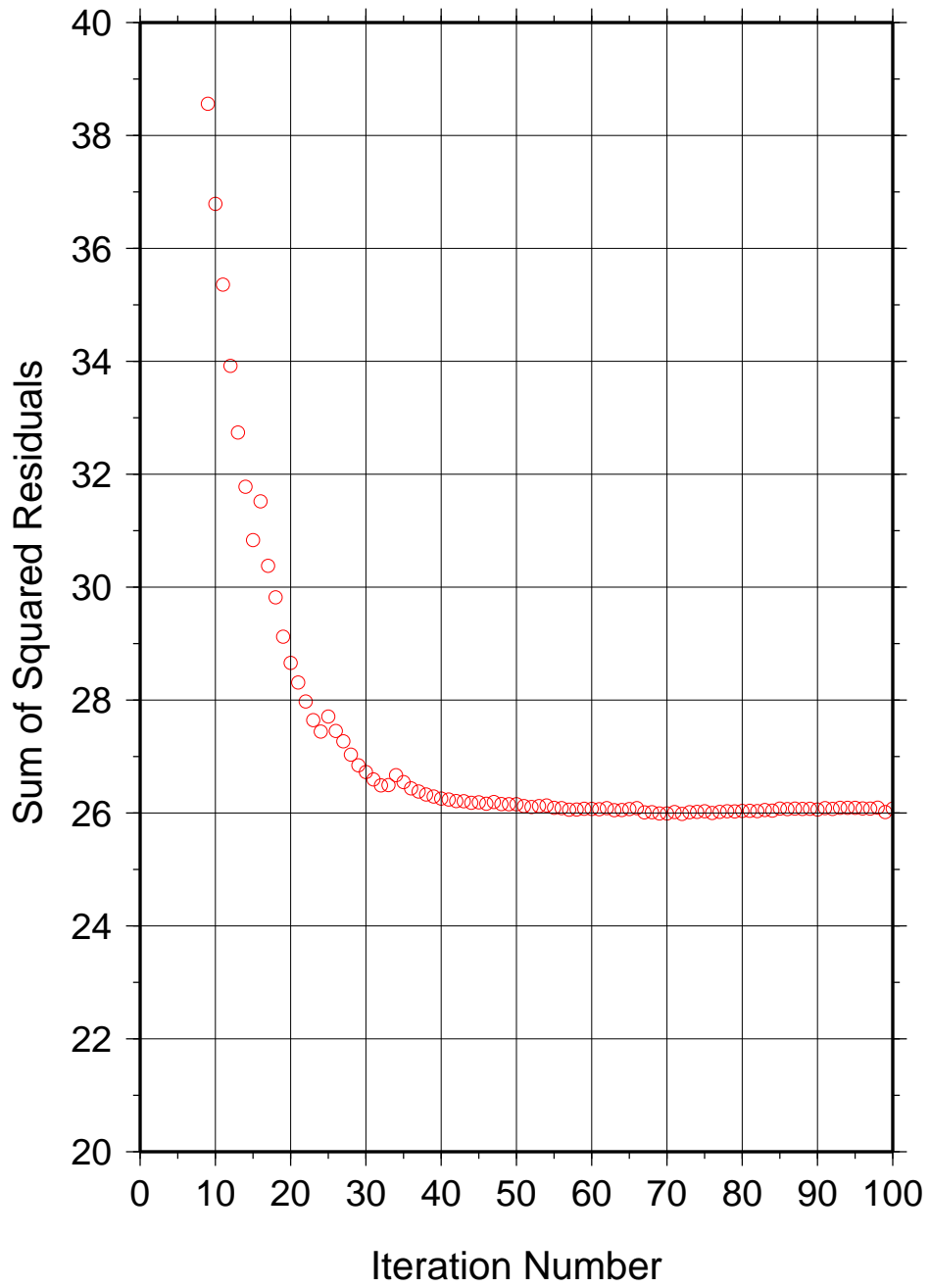


Figure 4.4.1 (C)

### Siberian Craton P-Velocity vs. Depth



**Figure 4.4.2**



**Figure 4.4.3**

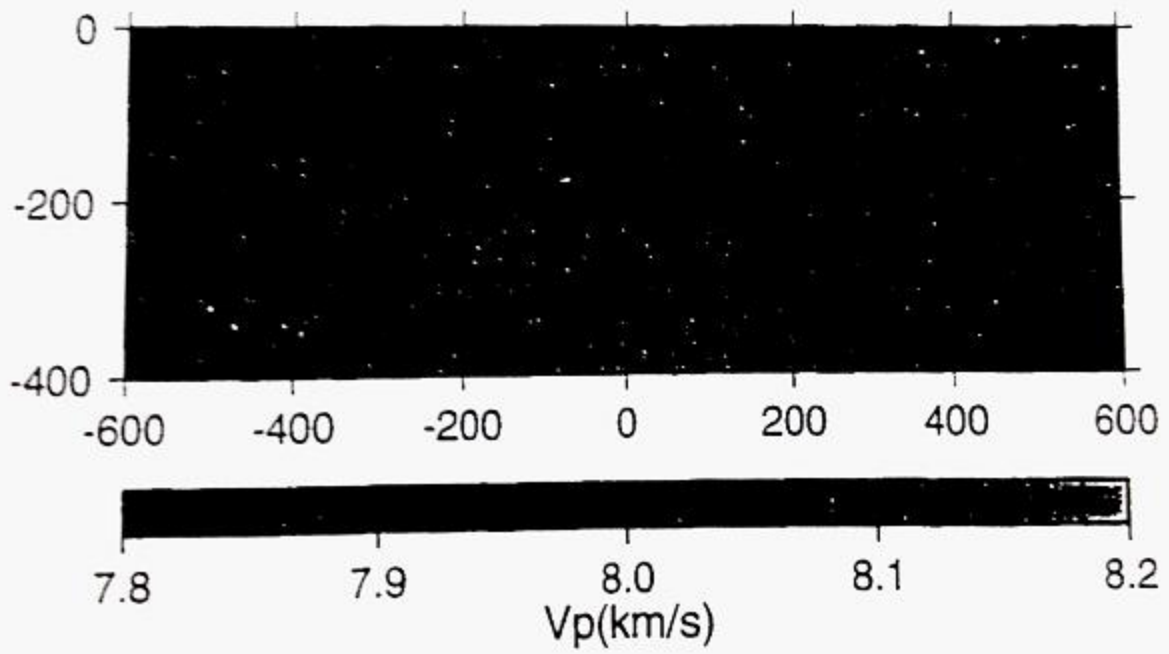
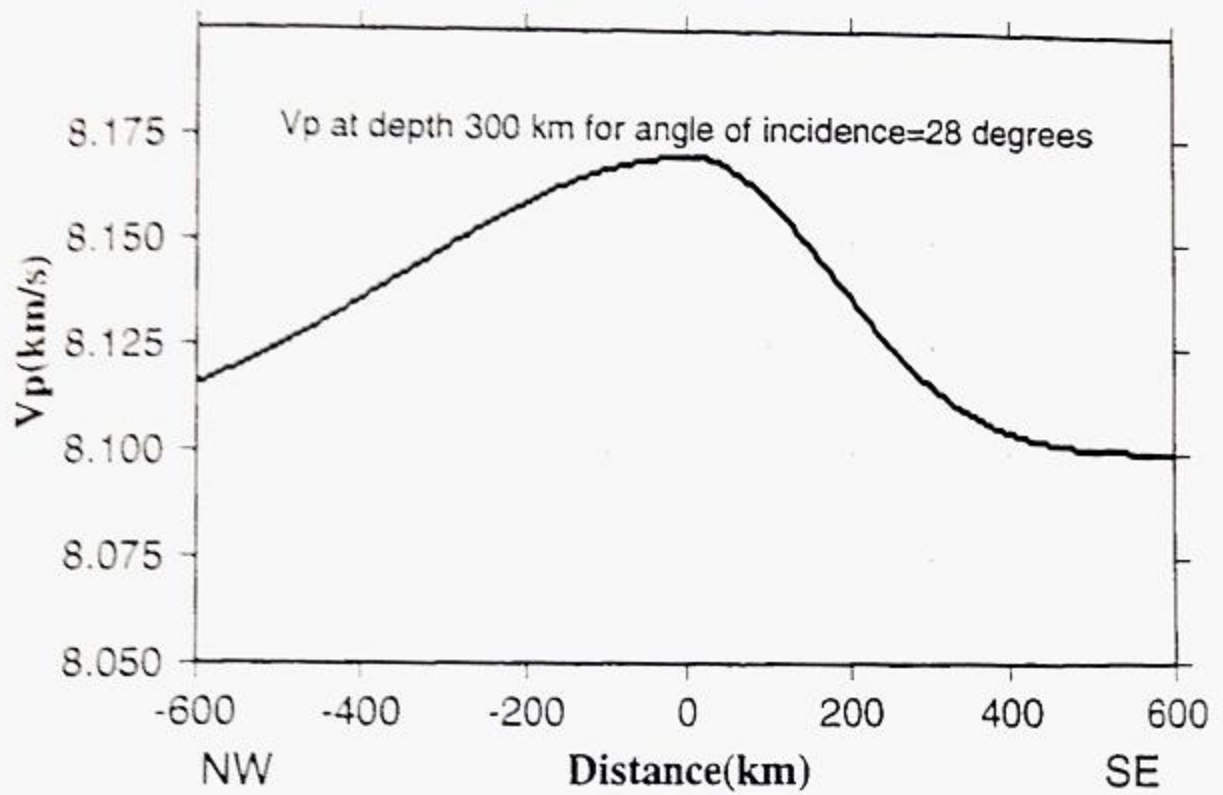


Figure 4.4.4

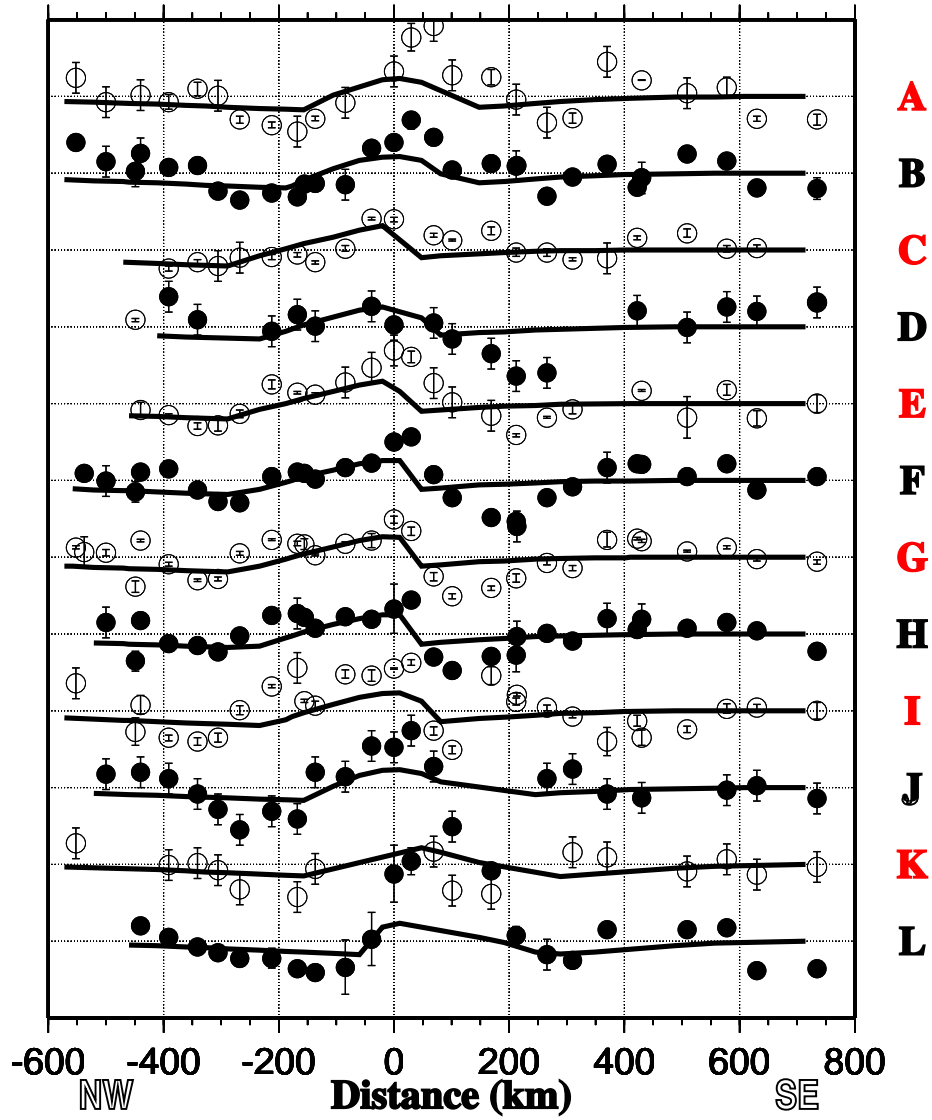
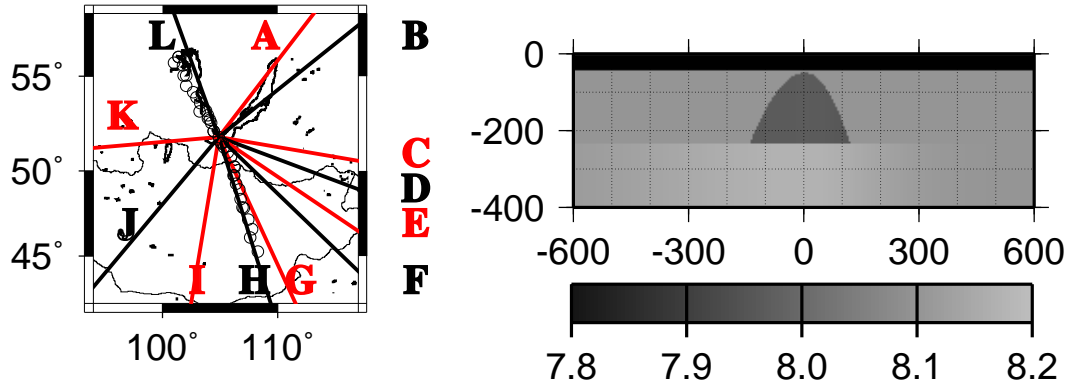


Figure 4.4.5 (a)

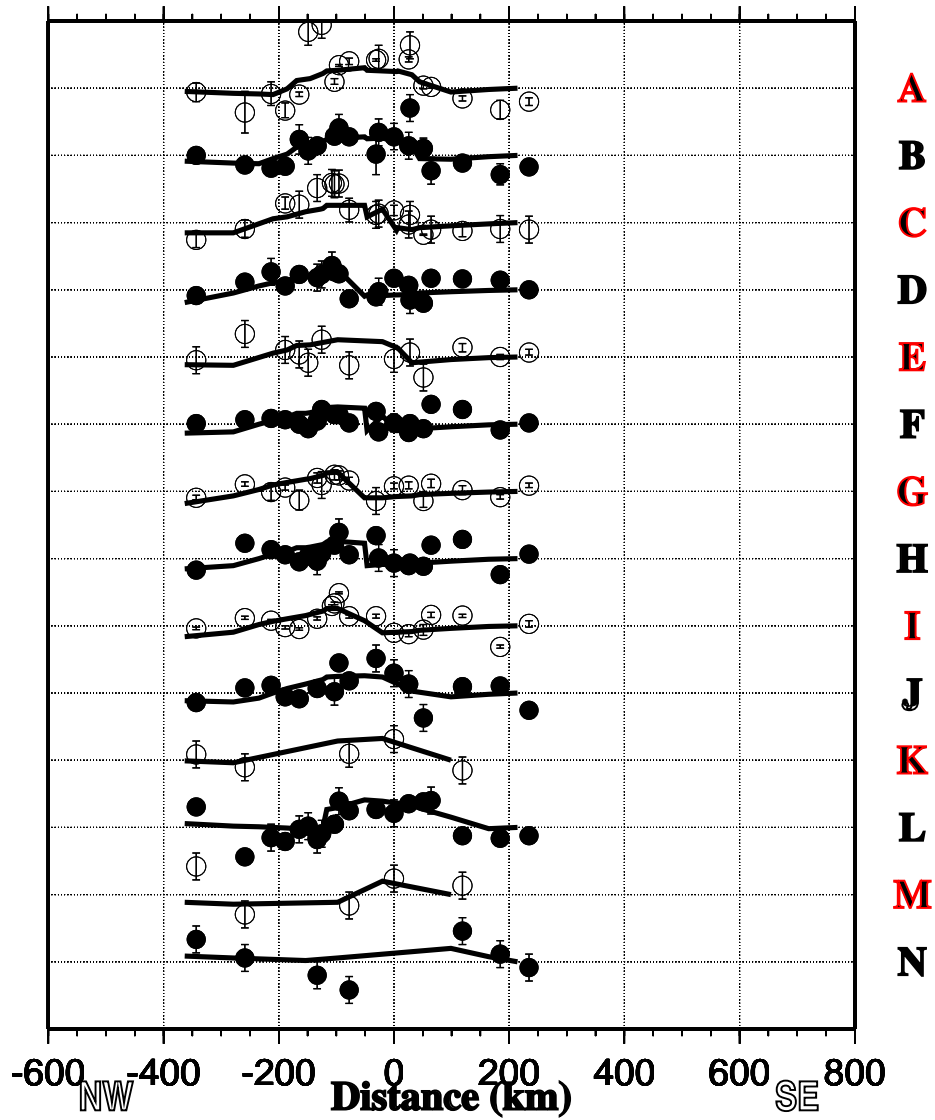
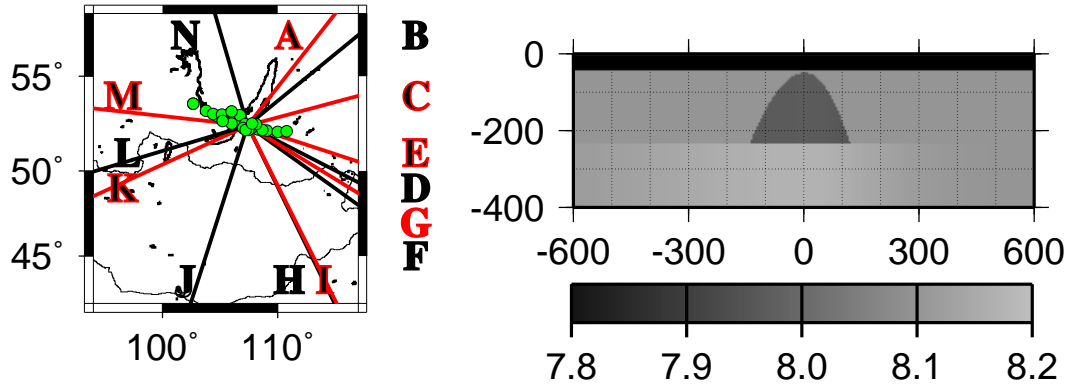
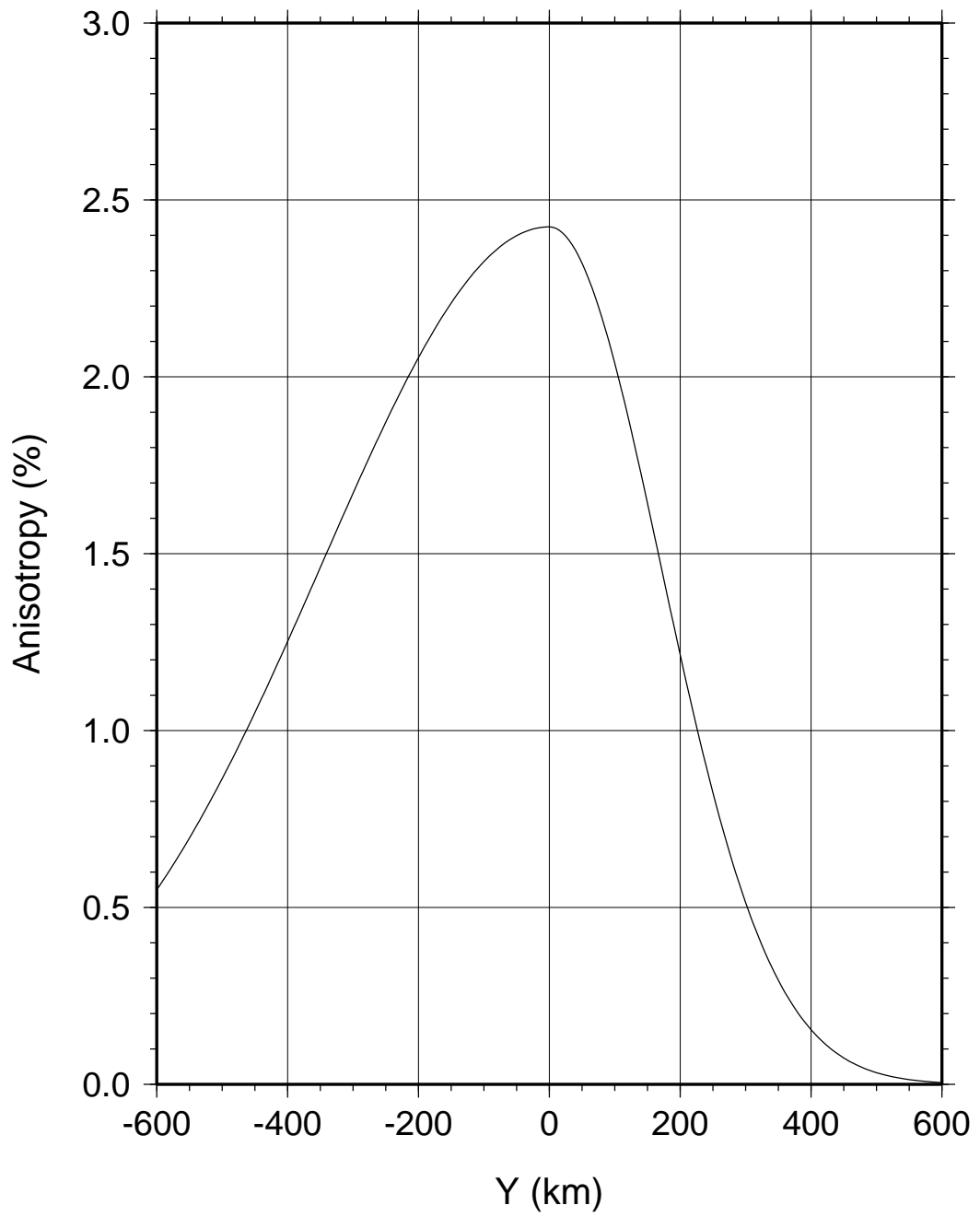


Figure 4.4.5 (b)



**Figure 4.4.6**

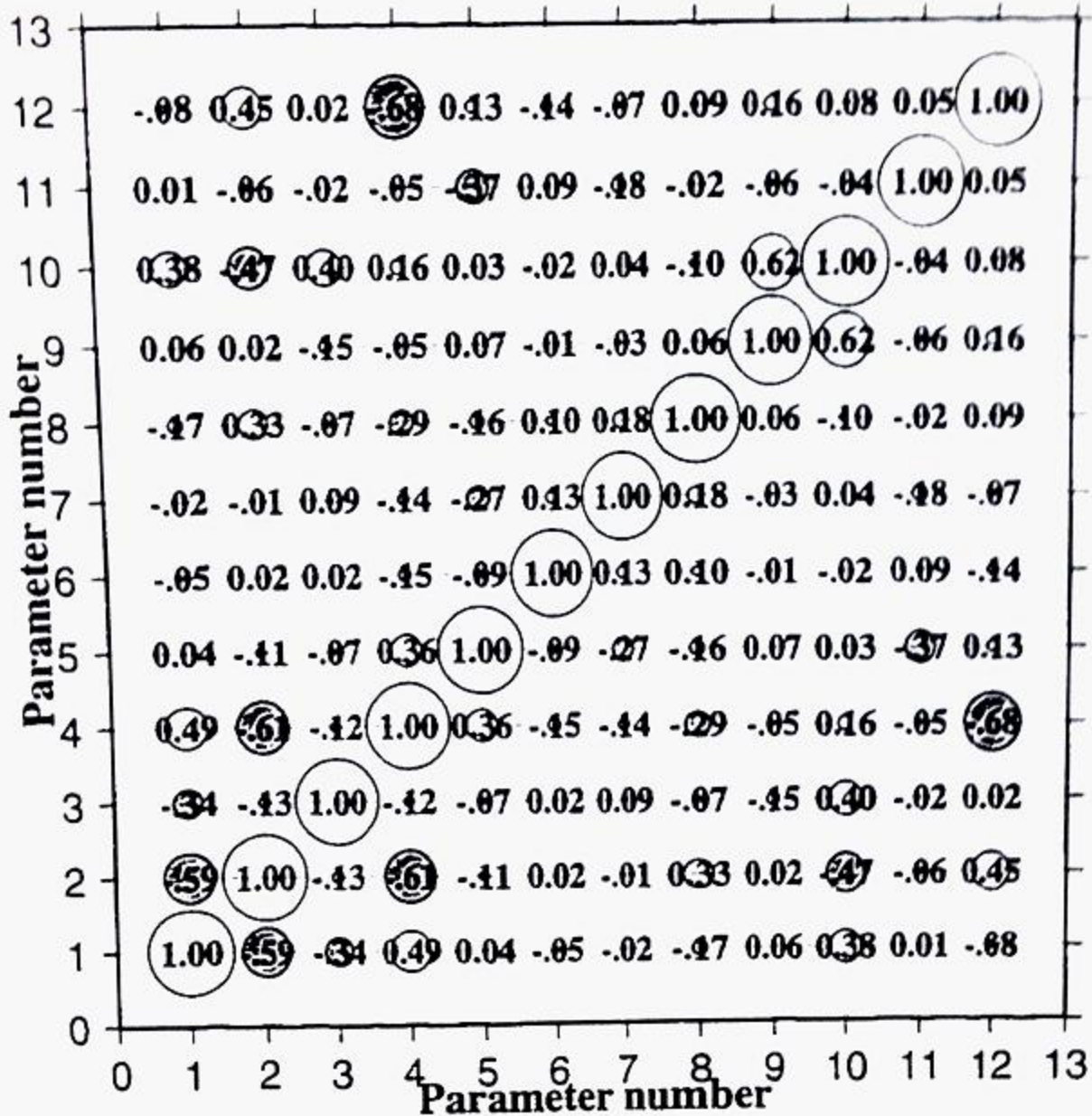


Figure 4.4.7

# **CHAPTER 5**

## **A Small Scale Mantle Convection Model for the Baikal Rift Zone**

### **5.1 Introduction**

The two most influential models are the so-called "active rifting" model [Logatchev and Zorin, 1983; 1992; Turcotte and Emerman, 1983] and the "passive rifting" model [Molnar and Tapponnier, 1975; Tapponnier and Molnar, 1979; Zonenshain and Savostin, 1981; Kiselev and Popov, 1992].

In an active rifting model the formation and development of the BRZ is thought to be the result of the active intrusion of the asthenospheric diapir. Small-scale convection in the the diapir causes thermal thinning of the subcrustal lithosphere [Logatchev and Zorin, 1992; Zorin, 1981].

The passive rifting model of Molnar and Tapponnier [1975] suggests that the India-Asia collision generated most of the large scale tectonics of Asia, and that the collision perhaps ripped open Lake Baikal more than 3000 km away. They suggest that Baikal rifting results from a mechanism equivalent to the development of tension cracks near the ends of and oblique to shear zones. They interpret the BRZ as a manifestations of the India-Eurasia collision, and therefore driven by the forces causing the collision, not by the forces directly beneath the rift.

### **5.2 A small-scale mantle convection model derived from the study**

Based on previous observations and those described in this thesis, a small-scale mantle convection model is constructed (Figure 5.2.1).

According to the model, there is an asthenospheric upwarp in the vicinity of the BRZ. The low velocity upwarp starts approximately at the base of the lithosphere, which has a thickness of about 200 km and reaches the base of the crust.

The upwarped and the normal asthenosphere beneath the entire study area is anisotropic. The source of the anisotropy is an upper mantle flow system that rises from beneath the rift zone and spreads out horizontally perpendicular to the rift axis, forming a small-scale convective system.

In the vicinity of the rift zone, vertical flow dominates and the flow plane is vertical and parallel to the rift axis; In the areas away from the rift zone the dominant flow direction is horizontal and perpendicular to the rift axis, and the flow plane is horizontal.

I assume that the strain in the upper mantle originating from the India-Eurasia collision dominates in the south, while that caused by the flow system decreases toward the south. The result is that the extensional direction gradually changes from SE-NW to E-W, in the area  $> 300$  km SE of the rift axis.

### **5.3 Application of the model**

In this section we deal with a geophysical forward problem: to interpret facts and observations using the model described in section 5.2. A successful model should be able to not only explain the data from which it was derived, but also other facts and observations.

- *The existence of the Baikal rift zone and lake Baikal.*

According to the model, the BRZ was initiated and its development has been dominated by the small-scale convection beneath the rift zone. The ascending asthenosphere created uplift at the early stage of the rifting; gravity instability

and extensional force exerted by the convecting asthenosphere at the base of the lithosphere have been the main source for the development of the rift zone.

The existence of lake Baikal is due to the fact that the subsidence of the main rift valley (lake Baikal) is greater than the net accumulation of the volume of sediments.

- *The existence of the peaks corresponding to the rift axis on most of the travel time residual curves (Figures 2.2.4 and 2.2.5).*

The low velocity asthenospheric thermal upwarp beneath the BRZ alone can cause positive relative travel time residuals.

On the other hand, the ascending flow beneath the BRZ aligns the axis of olivine crystals in the asthenosphere in the vertical direction. This anisotropy effect alone could cause negative relative travel time residuals. Across the Atlantic mid-oceanic ridge Blackman et al. [1993] observed earlier P-wave arrivals near the rift axis and interpreted them as the result of vertical anisotropy.

Therefore the observed travel time residuals are the result of a combination of thermal and anisotropic effects (Figure 4.2.1). The fact that near the axis of the BRZ the combined travel time residuals are positive relative to the platform suggests that the thermal effect on travel time is *relatively* greater than the anisotropic effect near the rift axis. The anisotropic effect exceeds the thermal effect beneath the Siberian platform and the Mongolian fold belt, as indicated by the negative travel time residuals.

Earlier P-wave arrivals near the Atlantic mid-oceanic ridge suggests that the anisotropic effect on travel times is *relatively* stronger than the thermal effect.

- *The existence of the negative travel time residuals on each side of the rift (Figures 2.2.6).*

Both the thermal and anisotropy effects decay away from the rift axis. However, the thermal effect, which causes positive travel time residuals decays faster than the anisotropy effect, which results in negative residuals. At a distance of about 250 km each side of the rift axis, the anisotropy effect exceeds thermal effect and causes valleys in the travel time residual curves.

- *Azimuthal variation of travel time residuals (Figures 2.2.6 and 2.2.7).*

If the velocity structure (isotropic and anisotropic) beneath the study area were radially symmetric, there would be no azimuthal variation of travel time residuals. Rays arriving from different azimuths travel through different parts of the model (Figure 5.2.1), which is not radially symmetric but two-dimensional, and results in azimuthal variation of travel time residuals.

- *The existence of SKS splitting in the entire study area (Figure 3.4.2).*

The asthenospheric flow system indicated in the model causes preferred orientation of upper mantle anisotropic crystals such as olivines and causes anisotropy, which results in SKS splitting.

In the southern part of the Mongolian fold belt I propose that the SKS splitting is the result of N-S contraction caused by continental collision.

- *The regional stress fields are characterized by tensional, shear-tensional, tension-shear, and shear stresses.*

Figures 5.3.1 and 5.3.2 shows the regional stress fields of the BRZ [Sherman, 1992]. The stress fields were obtained from geological structural analysis and from earthquake focal mechanisms. Sherman [1992] finds that the results from the two

approaches are consistent with each other. The stress fields are grouped into four types: tensional, shear-tensional, tension-shear, and shear (Figure 5.3.2). Extensional stress pattern can also be observed from the global stress map of Zoback [1992]. Shear-tensional and tension-shear stress fields are the transition states between tensional and shear stress fields. For instance, a shear-tensional stress field is composed of both shear and tensional stresses with the latter being dominant.

The SW and NE regions of the rift zone are dominated by shear at the center with a transition to tensional-shear, shear-tensional, and tensional stresses away from the center (Figure 5.3.2).

The central part of the BRZ is dominated by tensional stresses with NW-SE subhorizontal tensional axes (Figure 5.3.1), which is well-interpreted by our model (Figure 5.2.1). The observed tensional stresses in the central part of the BRZ are the result of the small-scale convection, which exerts NW-SE tensional stresses on the base of the lithosphere.

Subcrustal stresses have been inferred from satellite gravity data [Liu, 1983; 1977] in this area. A remarkable tensional stress field under the BRZ has been revealed. This is another indication of the presence of small-scale convection.

*•In the NE part of the rift zone (Area A in Figure 3.4.2) the fast directions are mostly E-W.*

The opening of the BRZ creates an E-W shear zone in the area. The  $a$ - axes of the olivine crystals in the upper mantle are oriented to the shear direction, i.e., E-W.

The results in this area are consistent with the stress model of Sherman [1992] (Figure 5.3.1). According to the model and results of stress measurements using

structural analysis and earthquake focal mechanism data (Figure 5.3.2), E-W shear stress dominates in a nearly E-W trending zone of about 50 km wide. Away from this shear zone, NW-SE tensional stress dominates. On stations inside or near the left lateral shear zone the fast directions are nearly E-W; on stations away from the shear zone (e.g., A01 and A11) the fast directions are perpendicular to the rift axis.

An alternative interpretation of the fast feature is related to vertical flow beneath this area. In this area the rift axis turns to be nearly E-W. When the vertical flow dominates beneath a station, the flow plane and the oriented olivine  $a$ -axis are vertical. The two horizontal axes are the  $b$ - and  $c$ -axes, which have the lowest and medium velocity, respectively. The  $b$ -axis is perpendicular to the flow plane which is parallel to the rift axis; therefore the  $b$ -axis orients nearly N-S. The  $c$ -axis is perpendicular to both the  $a$ - and  $b$ -axes and therefore is parallel to the rift axis, i.e., orients nearly E-W.

• *In the Siberian platform (Area C in Figure 3.4.2) the fast SKS polarization directions are mostly NW-SE, i.e., perpendicular to the rift axis.*

In this area horizontal flow is stronger than vertical flow and therefore the  $a$ -axes of olivine crystals are horizontal and parallel to the flow direction, i.e., in the NW-SE direction. The other horizontal axis is the  $c$ -axis, which is perpendicular to the flow direction and in the flow plane. The fast SKS polarization direction reflects the faster one of the two horizontal axes. Since shear waves polarized along the  $a$ -axis are faster than those polarized along the  $c$ -axis, the fast direction is the direction of oriented  $a$ -axis, which is NW-SE.

The fast directions are consistent with the observed stress fields (Figures 5.3.1 and 5.3.2).

•*In the central part of the rift zone (Area B in Figure 3.4.2) the fast SKS polarization directions are either parallel or perpendicular to the rift axis.*

In this area horizontal and vertical flows co-exist.

When the vertical flow dominates beneath a station, the flow plane and the oriented olivine  $a$ - axis are vertical. The two horizontal axes are the  $b$ - and  $c$ - axes, which have the lowest and medium velocity, respectively. Because the  $b$ - axis is perpendicular to the flow plane which is parallel to the rift axis, the  $b$ - axis is perpendicular to the rift axis (Figure 3.1.3). The  $c$ - axis is perpendicular to both the  $a$ - and  $b$ - axes and therefore is parallel to the rift axis. The fast SKS polarization direction reflects the faster one of the two horizontal axes. Since shear waves polarized along the  $c$ - axis is faster than those polarized along the  $b$ - axis, the fast direction observed by the station is the direction of oriented  $c$ - axis, which is along the rift axis.

When horizontal flow dominates beneath a station, the observed direction is perpendicular to the rift axis, i.e. in the NW-SE direction, similar to the Siberian platform.

The rapid change of the fast directions from  $46^\circ$  at station B17 to  $132^\circ$  at station B18 over a distance of 30 km indicates that the source of anisotropy in this area could be as shallow as 50 km. This is consistent with the travel time inversion result of Chapter four, which suggests that the asthenosphere reaches the base of the Crust in this area.

•*In the northern part of the Mongolian fold belt the fast direction is perpendicular to the rift axis; in the southern part it is nearly E-W (Area D in Figure 3.4.2).*

Similar to the Siberian platform, the northern part of this area is close to the BRZ and the  $a$ - axis of olivine crystals is aligned to be perpendicular to the rift axis by horizontal flow. Therefore the fast directions in the northern part are perpendicular to the rift axis.

In the southern part N-S contraction caused by the continental collision orients the  $a$ - axis of olivine to be nearly E-W and causes observed E-W fast directions. The E-W fast feature has been observed in the Tibet and Tian Shan areas [McNamara et al., 1994; Makeyeva et al., 1990] (Figure 5.3.3). A further example of contraction-caused anisotropy is the dominant E-W directions observed in Southern California [Liu et al., 1995].

• *A possible cause for rift-parallel fast direction observed in the Rio Grande and Kenya rifts*

The rift-parallel fast feature observed in the Rio Grande rift (Figure 3.1.4) has been interpreted as related to small-scale convection by Sandvol and others [1992]. According to their interpretation, the small-scale convection beneath the Rio Grande rift is three-dimensional with much of the flow being parallel rather than perpendicular to the rift axis.

Due to the fact that E-W extensional strain has been inferred using morphology and Quaternary normal faults in the vicinity of the the N-S trending rift [Aldridge et al., 1986], Sandvol and others [1992] indicated that the observed E-W extensional strain is affecting the crust (and perhaps the uppermost mantle) but not the mantle beneath it.

A rift-parallel fast feature was observed in the Kenya rift area [Gao et al., 1994c] (Figure 3.1.5). The 16 stations used were in a 400 by 200 km area centered

on (36.5°E, 0° N). Thirteen events were used for the SKS splitting study. Of the 16 stations, 14 of them have a fast direction of  $30 \pm 20$  degrees. Since the rift strikes nearly N-S, the measured fast directions cannot be interpreted by the E-W flow associated with opening of the rift.

A new interpretation for the rift-parallel fast features observed in the central part of the Rio Grande and the Kenya rift zones can be made by means of vertical flow.

For a vertical flow system, the flow plane and the oriented olivine  $a$ - axis are vertical (Figure 3.1.3). The two horizontal axes are the  $b$ - and  $c$ - axes, along which the P-wave velocity has the lowest and medium values, respectively. Because the  $b$ - axes are perpendicular to the flow plane which is vertical and parallel to the rift axis, the  $b$ - axes are perpendicular to the rift axis (Figure 3.1.3). The  $c$ - axes are perpendicular to both the  $a$ - and  $b$ - axes and therefore is parallel to the rift axis. The fast SKS polarization direction reflects the faster one of the two horizontal axes. Since shear waves polarized along the  $c$ - axes are faster than those polarized along the  $b$ - axes, the fast direction observed by the station is the direction of oriented  $c$ - axes, which is along the rift axis.

The existence of vertical flow must be accompanied by horizontal flows spreading out from the rift axis.

In the Rio grande and the Eastern African rift zones, the observed fast directions are mostly parallel to the rift axes, while in the BRZ they are either parallel or perpendicular to the rift axis. The reason for the difference might be that the vertical flows beneath the former two rifts are stronger than that beneath the BRZ.

• *An alternative explanation for trench-parallel fast direction SKS polarization directions observed in South and Central America.*

Russo and Silver [1994] measured S and SKS splitting along the western coast of South and Central America and found that the most of the fast directions were parallel rather than perpendicular to the local absolute plate motion (APM) directions. The observations were interpreted as the indication of "a significant component of trench-parallel flow" [Russo and Silver, 1994]. They also found that some of the fast directions were either normal or oblique to the local APM directions and interpreted these measurements, which were inconsistent with the trench-parallel flow hypothesis, as the effects of slab morphology that results in localized variation of flow directions.

An alternative interpretation of their observations can be made based on our small-scale convection model (Figure 5.2.1).

At locations where the vertical component of the descending asthenosphere flow along the trench is stronger than the horizontal component, the olivine  $a$ -axes are aligned to be more vertical than horizontal; the  $b$ -axes are aligned to be nearly horizontal and perpendicular to the flow plane, which is nearly vertical and parallel to the trench direction; and the  $c$ -axes to be horizontal and perpendicular to the APM direction. Since the  $c$ -axes have higher velocity than the  $b$ -axes, the observed fast directions are normal to the APM direction.

At locations where the horizontal component of the descending asthenosphere flow along the trench is stronger than the vertical component, the olivine  $a$ -axes are aligned to be more horizontal than vertical; the  $b$ -axes are aligned to be nearly vertical; and the  $c$ -axes to be horizontal and perpendicular to the APM direction.

Since the  $a$ - axes have higher velocity than the  $c$ - axes, the observed fast directions are parallel to the APM direction.

## FIGURE CAPTIONS

Figure 5.2.1: A small-scale mantle convection model for the Baikal rift zone.

The top diagram shows the fast SKS polarization directions along the 1992 profile. At distance  $\geq +300$  km the fast directions change from SE to E or NE. The middle diagram shows a NW-SE cross-section of the model. Arrows are flow and olivine  $a$ - axes directions. At distance  $\geq 300$  km, the direction of the  $a$ - axes changes to E-W or NE, as indicated by the  $\oplus$  sign. The diagram on the bottom shows the orientation of olivine crystallographic axes in vertical and horizontal mantle flows (same as Figure 3.1.3).

Figure 5.3.1: Generalized structures and stress fields of the Baikal rift zone [Sherman, 1992]. 1 = major faults (longer than 80 km); 2 = rift depressions in addition to lake Baikal and lake Khubsuqul; 3 = strike-slip faults; 4 = direction of tensional stresses.

Figure 5.3.2: Regional stress fields of the Baikal rift zone obtained from surface geological structure analysis and earthquake focal mechanism studies [Sherman, 1992]. The stresses are grouped into four types: 1 = shear; 2 = tension-shear; 3 = shear-tensional; 4 = tensional. Symbol 5 = Cenozoic depressions in addition to lake Baikal. The figure on the bottom is the same as Figure 3.4.2B.

Figure 5.3.3: Seismic anisotropy measurements in Asia. Stations represented by dots are from SKS splitting studies. Orientation of the bars going through the dots represents the fast SKS polarization direction. Stations represented by squares (in India) are from Pn velocity azimuthal

variation studies. The bars going through the squares represent the fast Pn direction. Most of the results are from the following studies: Gao et al., 1994a and this study (Siberia-Mongolia); Makeyeva et al., 1992 (Tian Shan area); McNamara et al., 1994 (part of Tibet); Zheng and Gao, 1994 (China).

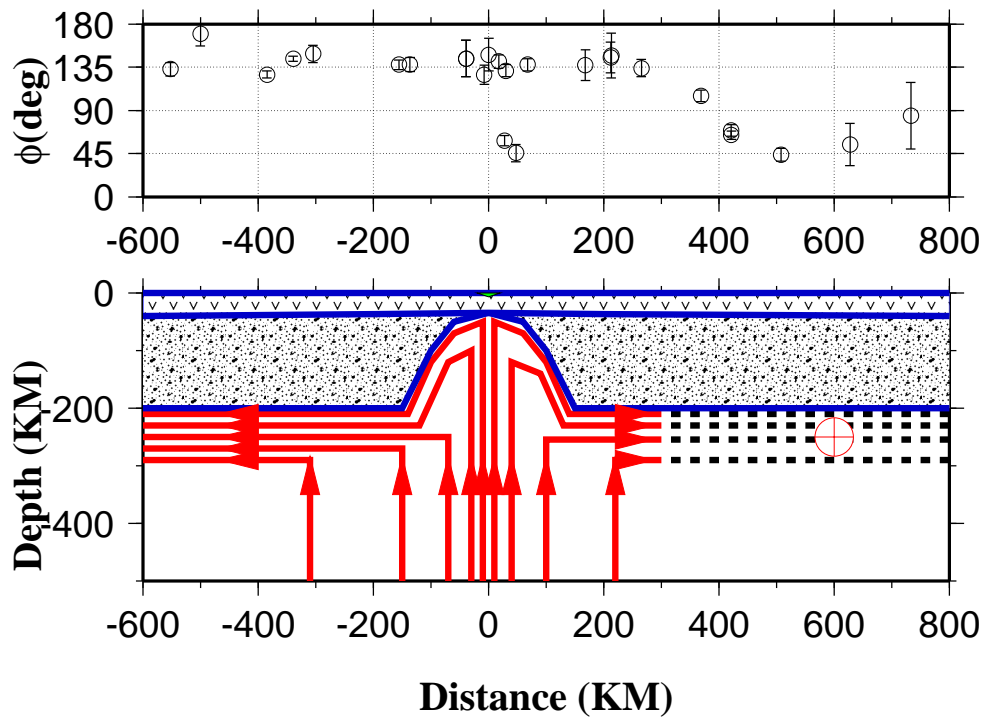


Figure 5.2.1

**Figure 5.3.1**

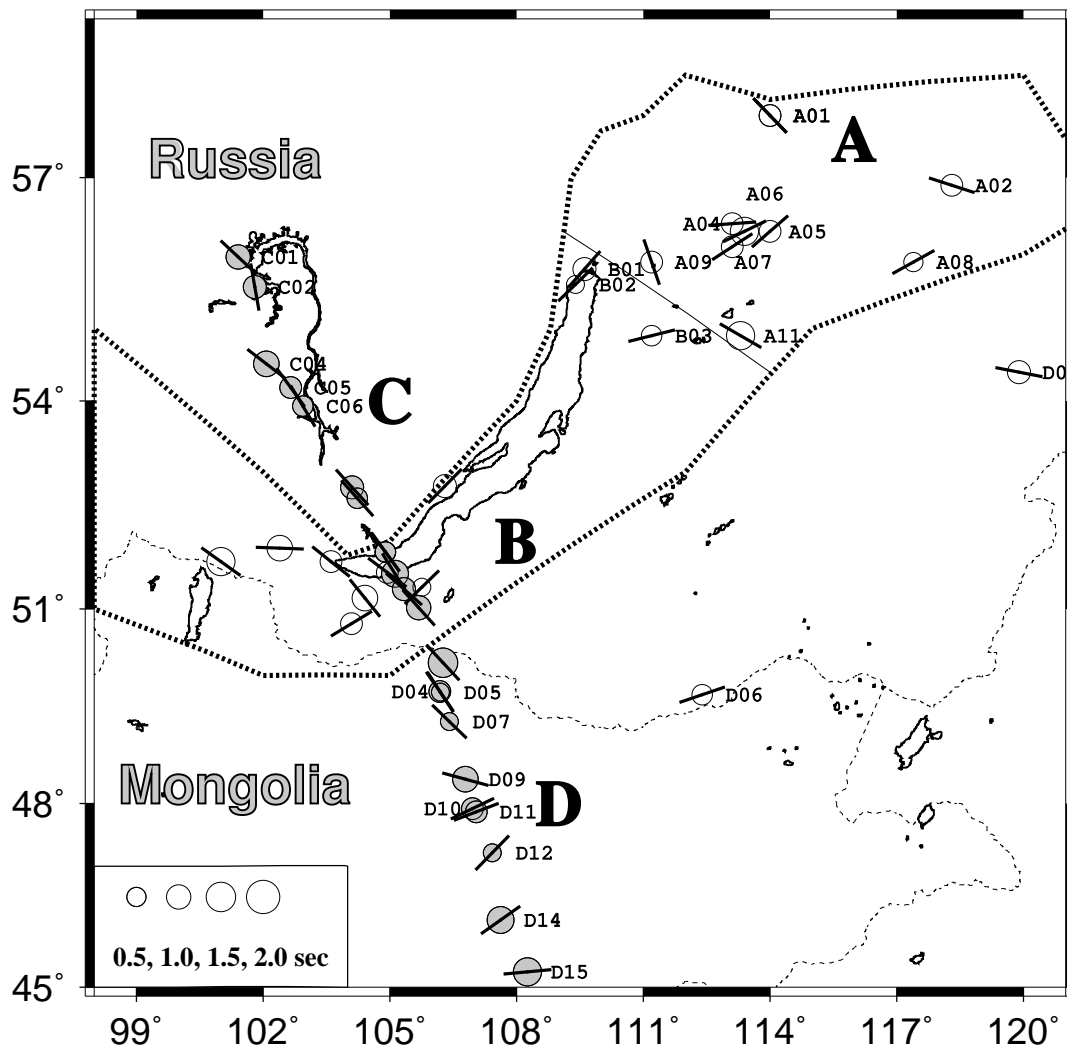
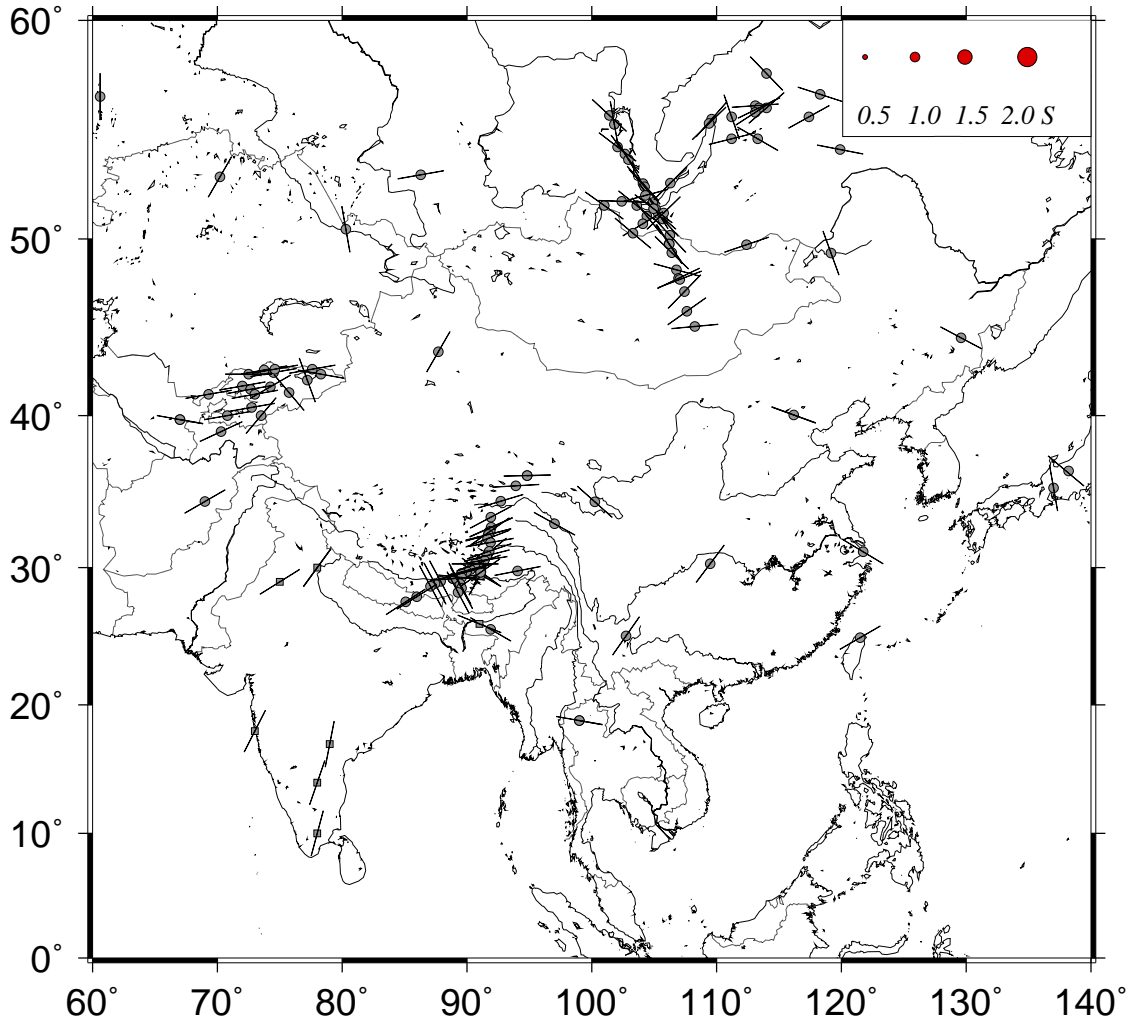


Figure 5.3.2



**Figure 5.3.3**

# CHAPTER 6

## Conclusions and Future Studies

### 6.1 Major conclusions

1. A new, high quality seismic data set recorded by approximately 100 digital stations in the Baikal rift and adjacent areas has been obtained and processed.

2. Positive teleseismic P-wave travel time residuals of about 0.7 s corresponding to the BRZ have been detected using 153 events. The location of the peak of the positive residuals is almost stationary with respect to arrival directions; Negative teleseismic P-wave travel time residuals of about 0.5 s at about 250 km on each side of the rift axis have been detected using 153 events. The location of the peaks of the negative residuals shifts as much as 200 km dependent on arrival directions.

3. The travel time residuals were interpreted by Bayesian nonlinear inversion using a traditional isotropic upper mantle model, and a new anisotropic upper mantle model. Thermal upwarp of the asthenosphere was required by both models. The P-wave lithosphere/asthenosphere velocity contrast ranges from 2 to 4%, depending on the model types (isotropic or anisotropic) and prior estimates of the parameters.

4. A lithospheric downwarp at about 250 km on each side of the rift axis is inferred from the isotropic model that gives rise to the observed negative travel time residuals. The downwarps have not been corroborated by DSS, gravity, and other observations.

5. In the anisotropic model, a vertical upper mantle flow system which orients the crystallographic axes of mantle anisotropic minerals such as olivine, and causes P-wave velocity anisotropy, is used to interpret the observed negative travel time residuals.

6. The upper mantle in the study area is anisotropic as revealed by SKS splitting of about 1 second.

7. In the Siberian platform and the northern part of the Mongolia fold belt, the fast SKS polarization directions are mostly perpendicular to the rift axis; in the southern part of the fold belt the fast directions are mostly E-W; in the central part of the BRZ the observed fast directions are either parallel or perpendicular to the rift; and in the shear zone of the NE part of the BRZ, the fast directions are approximately parallel to the shear direction.

8. The observed anisotropy is most probably the consequence of recent or present-day tectonic processes and is not fossil anisotropy.

9. A model was constructed and used for the interpretation of geological observations, such as the structure of the rift zone, and seismological observations such as travel time residuals and SKS splitting results. New interpretations for the rift-parallel fast directions observed in the Rio Grande and Kenya rift zones, and for the the trench-parallel fast directions observed in central and southern America are made based on the small-scale mantle convection model.

10. Several related future studies are proposed and the results are predicted based on the results from the current study.

11. The study indicates that traditional teleseismic P-wave tomography studies may result in incorrect results, if seismic anisotropy is not considered. For instance, in continental rift and hotspot areas where vertical flow exists, traditional travel time tomography underestimates the size and/or the velocity contrast of the accompanying low velocity body.

12. Small station spacing should be used for SKS splitting studies because anisotropy has rapid spatial variation.

## 6.2 Proposed future studies and predicted results

The Baikal experiment collected more than 20 Gigabytes of high quality digital seismic data. Many aspects of seismological studies can be carried out using this unique data set. For instance, abundant local events can be used to infer focal mechanism; numerous mining blasts and local earthquakes can be used for crustal tomography and for the discrimination of artificial and natural events; broadband records can be used for surface wave studies, for calculating receiver functions, and to study deeper structure such as the  $D''$  and major velocity discontinuities; the attenuation factors,  $Q_p$  and  $Q_s$  can also be obtained easily using the data set.

In this section I will describe in detail two topics that are related to the main task of this thesis, i.e., anisotropy, and predict the results by applying the small-scale convection model of Chapter 5.

### • *Surface wave azimuthal anisotropy*

Azimuthal anisotropy of surface waves has been use widely in finding large scale anisotropy in the mantle [e.g. Schlue and Knopoff, 1976; 1977; Tanimoto and Anderson, 1984; 1985].

Using fundamental mode Rayleigh and Love waves recorded by about 12 broadband sensors co-sited with short period sensors, it is possible to verify the anisotropy results derived using SKS and P waves.

Using 13 Love wave paths and 40 Rayleigh wave paths traversing Eurasia, Liao [1981] found that the S-wave velocity derived from both Rayleigh and Love wave data is  $4.34 \pm 0.02$  km/s in the channel ("asthenosphere"); for the lid ("lithosphere")

it is  $4.56 \pm 0.01$  km/s derived from Rayleigh wave data, and  $4.77 \pm 0.02$  km/s derived from Love wave data. It was also found that Rayleigh wave data did not require the presence of azimuthal anisotropy, and Love wave anisotropy might be marginally present for SH-velocities in both the channel and lid.

Since most of the paths used by Liao [1981] traveled through most of Eurasia, the observed velocities were averaged over great distances.

By applying a similar procedure to that of Liao [1981], high resolution results might be obtained using the Baikal data.

Polarization anisotropy derived from surface waves can be expected. According to our small-scale mantle convection model, In the rift zone area, SV wave velocities derived from Rayleigh waves should be higher than SH velocities derived from Love wave, due to the preferred orientation of the olivine  $a$ - axes along the vertical direction; In the areas outside the BRZ , SV wave velocities derived from Rayleigh waves should be lower than SH waves derived from Love wave, due to the preferred orientation of the olivine  $a$ - axes along the horizontal direction.

Azimuthal anisotropy derived from surface waves should be significant. For instance, in the areas that show NW-SE fast SKS directions, Rayleigh waves from the NW or SE should show higher velocity than those from the orthogonal directions; in the areas that show E-W fast SKS directions, Rayleigh waves from the E or W should show higher velocity than those from the orthogonal directions.

•  *$P_n$  azimuthal anisotropy*

$P_n$  azimuthal anisotropy has been observed in many situations [e.g., Hess, 1964; Bamford, 1977; Raitt et al., 1969; Morris et al., 1969; Sung and Jackson, 1992].

Abundant local and regional natural events and artificial mining blasts can be used for the study of azimuthal anisotropy of  $P_n$  velocity. The average fast directions revealed using  $P_n$  waves by Sung and Jackson [1992] for Southern California are  $\phi = 105^\circ \pm 4^\circ$ , which is very close to the results obtained using SKS phases beneath most of the individual stations by Liu et al. [1995]. Since the  $P_n$  wave results reflect the anisotropy of the uppermost mantle, while the SKS results reflect the anisotropy of both the asthenosphere and the lithosphere, the agreement in Southern California may indicate that the anisotropic layer revealed by the SKS measurements reaches the uppermost mantle.

If the  $P_n$  fast directions in the Baikal-Mongolian area are consistent with the SKS results, for a station in the BRZ or the Siberian platform, events from the NW or SE should have earlier arrivals than events from the NE or SW; for a station in central or southern Mongolia or in the shear zone of NE BRZ, events from the E or W has earlier arrivals than those from the N or S.

## References

- Aldridge, M. J., C. E. Chapin, and A. W. Laughlin, Stress history and tectonic development of the Rio Grande rift, New Mexico, *J. Geophys. Res.* *91*, 6199-6211, 1986.
- Anderson, D.L., *Theory of the Earth*, Blackwell Scientific Publications, 1989.
- Ansel, V., and H. C. Nataf, Anisotropy beneath 9 stations of the Geoscope broadband network as deduced from shear-wave splitting, *Geophys. Res. Lett.*, *16*, 409-412, 1989.
- Babuska, V., and M. Cara, *Seismic anisotropy in the Earth*, Kluwer Academic Publishers, 1991.
- Backus, G.E., Possible forms of seismic anisotropy of the upper-most mantle under oceans, *J. Geophys. Res.*, *70*, 3429-3439, 1965.
- Bamford, D., Pn Velocity anisotropy in a continental upper mantle, *Geophys. J. R. astr. Soc.*, *49*, 29-48, 1977.
- Bates, D. M., and D. G. Watts, *Nonlinear regression analysis and its applications*, John Wiley, New York, 1988.
- Blackman, D. K., J. A. Orcutt, D. W. Forsyth, and J. M. Kendall, Seismic anisotropy in the mantle beneath an oceanic spreading center, *Nature*, *366*, 675-677, 1993.
- Bowman, J. R., and M. Ando, Shear-wave splitting in the upper-mantle wedge above the Tonga subduction zone, *Geophys. J. R. astr. Soc.*, *88*, 25-41, 1987.

- Chastel, Y. B., P. R. Dawson, H. R. Wenk, and K. Bennett, Anisotropic convection with implications for the upper mantle, *J. Geophys. Res.*, *98*, 17,757-17,771, 1993.
- Christensen, N. I., and R. S. Crosson, seismic anisotropy in the upper mantle, *Tectonophysics*, *6*, 93-107, 1968.
- Christensen, N. I., and S. Lundquist, Pyroxene orientation within the upper mantle, *Bull. Geol. Soc. Am.*, *93*, 279-288, 1982.
- Crampin, S., and D. Bamford, Inversion of P-wave velocity anisotropy, *Geophys. J. R. astr. Soc.*, *49*, 123-132, 1977.
- Crosson, R. S., Symmetry of upper mantle anisotropy, *Earth Planet. Sci. Lett.*, *15*, 423-429, 1972.
- Dahlheim, H.-A., P. M. Davis, and U. Achauer, Teleseismic investigation of the East African Rift-Kenya, *J. Afr. Earth Sci.*, *8*, 2-4, 461-470, 1989.
- Davis, P. M., Continental rift structures and dynamics with reference to teleseismic studies of the Rio Grande and East African rifts, *Tectonophysics*, *197*, 309-325, 1991.
- Davis, P. M., E. C. Parker, J. R. Evans, H. M. Iyer, and K. H. Olsen, Teleseismic deep sounding of the velocity structure beneath the Rio Grande Rift, *Field Conf. Guide Book, N. M. Geol. Soc.*, *35th*, 29-38, 1984.
- Davis, P. M., The 1992 Baikal seismic array project, *submitted to DARPA*, November, 1992.
- Davis, P. M., S. Gao, H. Liu, and P. D. Slack, Baikal 1991 Seismic Array Project data report, *submitted to IRIS DMC and DARPA*, January, 1993a.

- Davis, P. M., P. Slack, H.-A. Dahlheim, W. V. Green, R. P. Meyer, U. Achauer, A. Glahn, and M. Granet, Teleseismic Tomography of Continental Rift Zones, in H. M. Iyer and H. Hirata (editors) *Seismic Tomography: Theory and Practice*, pp. 397-439, Chapman Hall, 1993b.
- Davis, P. M., S. Gao, H. Liu, P. D. Slack, M. Benthien, and D. Daniels Baikal 1992 Seismic Array Project data report, *submitted to IRIS DMC and DARPA*, July, 1994.
- Doser, D. I., Faulting within the western Baikal rift as characterized by earthquake studies, *Tectonophysics*, 196, 87-107, 1991.
- Dziewonski, A. M., and D. L. Anderson, Preliminary reference Earth model, *Phys. Earth Planet. Inter.*, 25, 297-356, 1981.
- Egorkin, A. V., S. K. Ziuganov, N. M. Chernyshev, The upper mantle of Siberia, *Proceedings of the 27th International Geological Congress*, 8, 29-26, 1984.
- Fowler, C. M. R., *The solid Earth, An introduction to global geophysics*, Cambridge Univ. Press, Cambridge, 1990.
- Fuchs, K., Seismic anisotropy and composition of the continental subcrustal lithosphere, *Proceedings of the 27th International Geological Congress*, Vol. 8, 1-27, Geophysics, VNU Science Press, 1984.
- Gao, S., P. M. Davis, H. Liu, P. D. Slack, Yu. A. Zorin, V. V. Mordvinova, V. M. Kozhevnikov, and R. P. Meyer, Seismic Anisotropy and Mantle Flow beneath the Baikal Rift Zone, *Nature*, 371, 149-151, 1994a.
- Gao, S., P. M. Davis, H. Liu, P. Slack, Y. A. Zorin, N. A. Logatchev, M. Kogan, P. Burkholder, and R. P. Meyer, Asymmetric upwarp of the

- Asthenosphere beneath the Baikal Rift zone, Siberia, *J. Geophys. Res.*, *99*, 15,319-15,330, 1994b.
- Gao, S., P.M. Davis, H. Liu, P.D. Slack, Yu.A. Zorin, V.V. Mordvinova, V.M. Kozhevnikov, and R.P. Meyer, Seismic Anisotropy beneath the Baikal and Kenya rift zones, *EOS, Trans. Am. Geophys. Union*, *75*, 67 (abstract), 1994c.
- Golenetsky, S. I., and L. A. Misharina, Seismicity and earthquake focal mechanisms in the Baikal rift zone, *Tectonophysics*, *45*, 71-85, 1978.
- Golenetsky, S. I., Problems of the seismicity of the Baikal rift zone, *J. of Geodynamics*, *11*, 293-307, 1990.
- Gornostaiev, V. P., V. I. Michailovskiy, and V. J. Pospelov, Deep magnetotelluric soundings on the south of the Siberian platform in the Baikal rift zone, *Geol. Geofiz.*, *4*, 111-118, 1970.
- Halderman, T. P., and P. M. Davis,  $Q_p$  beneath the Rio Grande and east African rift zones, *J. Geophys. Res.*, *96*, 10,113-10,128, 1991.
- Hess, H., Seismic anisotropy of the uppermost mantle under oceans, *Nature*, *203*, 629-631, 1964.
- Humphrey, N., and D. Helmberger, NXSCAN, *IRIS Data Management Center*, Seattle, Washington, 1993.
- Jackson, D. D., Interpretation of inaccurate, insufficient and inconsistent data, *Geophys. J. R. astr. Soc.*, *28*, 97-109, 1972.
- Jackson, D. D., and M., Matsu'ura, A Bayesian approach to nonlinear inversion, *J. Geophys. Res.*, *90*, 581-591, 1985.

- Jenkins, G. M., and D. G. Watts, *Spectral analysis and its applications*, Holden-Day, San Francisco, Calif., 1968.
- Karato, S., Seismic anisotropy: mechanisms and tectonic implications, in *Rheology of solids and of the Earth*, edited by S. Karato and M. Toriumi, Oxford Science Publications, 1989.
- Kendall, J. M., and C. J. Thomson, Seismic modelling of subduction zones with inhomogeneity and anisotropy— I. Teleseismic P-wavefront tracking, *Geophys. J. Int.*, *112*, 39-66, 1993.
- Kennett, B. L. N., and E. R. Engdahl, Travel times for global earthquake location and phase identification, *Geophys. J. Int.*, *105*, 429-465, 1991.
- Kind, R., G. L. Kosarev, L. I. Makeyeva, and L. P. Vinnik, Observations of laterally inhomogeneous anisotropy in the continental lithosphere, *Nature*, *318*, 358-361, 1985.
- Kiselev, A. I., and A. M. Popov, Asthenospheric diapir beneath the Baikal rift: petrological constraints, *Tectonophysics*, *208*, 287-295, 1992.
- Knopoff, L., *Q*, *Rev. Geophys.*, *2*, 625-660, 1964.
- Liao, A. H., Anisotropy in the upper mantle of Eurasia, Ph. D. thesis, University of California, Los Angeles, 1981.
- Lipson, S. G., and H. Lipson, *Optical Physics*, Cambridge Uni. Press, London, 1981.
- Liu, H., P. M. Davis, and S. Gao, SKS splitting beneath southern California, *Geophys. Res. Lett.* *22*, 767-770, 1995.
- Liu, H. S., Mantle convection pattern and subcrustal stress field under Asia, *Phys. Earth Planet. Inter.*, *16*, 247-256, 1978.

- Liu, H. S., Geodynamics of the Baikal-Stanovoy seismic belt, *Phys. Earth Planet. Inter.*, 31, 77-82, 1983.
- Logatchev, N. A., The Baikal rift system, *Episodes*, 7, No.1, 38-42, 1984.
- Logatchev, N. A., and N. A. Florensov, The Baikal system of rift valleys, *Tectonophysics*, 45, 1-13, 1978.
- Logatchev, N. A., and Yu. A. Zorin, Baikal rift zone: structure and geodynamics, *Tectonophysics*, 208, 273-286, 1992.
- Logatchev, N. A., Yu. A. Zorin, and V. A. Rogozhina, Cenozoic continental rifting and geologic formations (as illustrated by the Kenya and Baikal rift zones), *Geotectonics*, 17, No. 2, 83-92, 1983a.
- Logatchev, N. A., Yu. A. Zorin, and V. A. Rogozhina, Baikal rift: active or passive?— comparison of the Baikal and Kenya rift zones, *Tectonophysics*, 94, 223-240, 1983b.
- Logatchev, N. A., and Yu. A. Zorin, Evidence and causes of the two-stage development of the Baikal rift, *Tectonophysics*, 143, 225-234, 1987.
- Lubimova, E. A., Heat flow patterns in Baikal and other rift zones, *Tectonophysics*, 8, 457-467, 1969.
- Lysak, S. V., Terrestrial heat flow in the South of East Siberia, *Tectonophysics*, 103, 205-215, 1984.
- Lysak, S. V., Terrestrial heat flow of continental rifts, *Tectonophysics*, 143, 31-41, 1987.
- Makeyeva, L. I., A. Plesinger, and J. Horalek, Azimuthal anisotropy beneath the Bohemian Massif from broadband seismograms of SKS waves, *Phys. Earth Planet. Int.*, 62, 298-306, 1990.

- Makeyeva, L. I., L. P. Vinnik, and S. W. Roecher., Shear-wave splitting and small-scale convection in the continental upper mantle, *Nature*, *358*, 144-147, 1992.
- McNamara, D. E., T. J. Owens, P. G. Silver, and F. T. Wu, Shear wave anisotropy beneath the Tibetan Plateau, *J. Geophys. Res.*, *99*, 13,655-13,665, 1994.
- Minster, J. B., and T. H. Jordan, Present-day plate motions, *J. Geophys. Res.*, *83*, 5331-5354, 1978.
- Molnar, P., and P. Tapponnier, Cenozoic tectonics of Asia: Effects of a continental collision, *Science*, *189*, No.4201, 419-426, 1975.
- Mordvinova, V. V., Method of the ratio of amplitude spectra of seismic vibrations as applied to studying the Baikal region, *Izvestiya, Earth Physics*, *19*, 887-893, 1983.
- Mordvinova, V. V., Spectra of seismic vibrations and lithospheric thickness in southern Siberia, *Izvestiya, Earth Physics*, *24*, 340-346, 1988.
- Morgan, P., Heat flow in rift zones, *Geodynamics Series, Am. Geophys. Union*, *8*, 107-122, 1982.
- Morris, G. B., R. W. Raitt, and G. G. Shor, Velocity anisotropy and delay time maps of the mantle near Hawaii, *J. Geophys. Res.*, *74*, 4300-4316, 1969.
- Nicolas, A., F. Boudier, and A. M. Boullier, Mechanisms of flow in naturally and experimentally deformed peridotites, *Am. J. Sci.*, *273*, 853-876, 1973.

- Nicolas, A., and N. I. Christensen, Formation of anisotropy in upper mantle peridotites – a review, *Rev. Geophys.*, 25, 111-123, 1987.
- Nicolas, A. and J. P. Poirier, *Crystalline plasticity and solid state flow in metamorphic rocks*, Weley, London/New York, 1976.
- Novoselova, M. R., Magnetic anomalies of the Baikal rift zone and adjacent areas, *Tectonophysics*, 45, 95-100, 1978.
- Parker, E. C., P. M. Davis, J. R. Evans, H. M. Iyer, and K. H. Olsen, Upwarp of anomalous asthenosphere beneath the Rio Grande rift, *Nature*, 312, 354-356, 1984.
- Popov, A. M., A deep geophysical study in the Baikal Region, *Pageoph*, 134, 575-587, 1990.
- Puzyrev, N. N., M. M. Mandelbaum, S. V. Krylov, B. P. Mishenkin, G. V. Petrik, and G. V. Krupskaya, Deep structure of the Baikal and other continental rift zones from seismic data, *Tectonophysics*, 45, 15-22, 1978.
- Puzyrev, N. N., Bowels of Lake Baikal from seismic data, *Nauka*, Novosibirsk, 105pp. (in Russian), 1981.
- Raitt, R. W., G. G. Shor, Jr., T. J. G. Francis, and G. B. Morris, Anisotropy of the Pacific upper mantle, *J. Geophys. Res.*, 74, 3095-3109, 1969.
- Russo, R. M., and P. G. Silver, Trench-parallel flow beneath the Nazca plate from seismic anisotropy, *Science*, 263, 1105-1111, 1994.
- Sandvol, E., J. Ni, S. Ozalaybey, and J. Schlue, Shear-wave splitting in the Rio Grande rift, *Geophys. Res. Lett.*, 19, 2337-2340, 1992.

- Savage, M. K., P. G. Silver, and R. P. Meyer, Observations of teleseismic shear-wave splitting in the basin and range from portable and permanent stations, *Geophys. Res. Lett.*, *17*, 21-24, 1990.
- Savage, M. K., and P. G. Silver, Mantle deformation and tectonics; constraints from seismic anisotropy in the western United States, *Phys. Earth Planet. Inter.*, *78*, 207-227, 1993.
- Savage, M. K., Anisotropy and rift systems, *Nature*, *371*, 105-106, 1994.
- Schlue, J. W., and L. Knopoff, Shear wave anisotropy in the upper mantle of the Pacific basin, *Geophys. Res. Lett.*, *3*, 359-362, 1976.
- Schlue, J. W., and L. Knopoff, Shear-wave polarization anisotropy in the Pacific basin, *Geophys. J. R. astr. Soc.*, *49*, 145-165, 1977.
- Sherman, S. I., Faults and tectonic stresses of the Baikal rift zone, *Tectonophysics*, *208*, 297-307, 1992.
- Silver, P. G., and W. W. Chan, Implications for continental structure and evolution from seismic anisotropy, *Nature*, *335*, 34-39, 1988.
- Silver, P. G., and W. W. Chan, Shear wave splitting and subcontinental mantle deformation, *J. Geophys. Res.* *96*, 16,429-16,454, 1991.
- Silver, P. G., and S. Kaneshima, Constraints of mantle anisotropy beneath precambrian north America from a transportable teleseismic experiment, *Geophys. Res. Lett.*, *20*, 1131-1134, 1993.
- Slack, P. D., P. M. Davis, H. A. Dalheim, A. Glahn, J. R. R. Ritter, W. V. Green, P. K. H. Maguire, and R. P. Meyer, Attenuation and velocity of P-waves in the mantle beneath the East African rift, Kenya, *Tectonophysics*, *236*, 331-358, 1994.

- Slack, P. D., Teleseismic investigations of the East African and Rio Grande rifts, Ph. D. thesis, University of California, Los Angeles, 1994.
- Sun, R., and G. A. McMechan, Seismic modelling by Fresnel diffraction theory with application to wide-aperture data from SW Oklahoma, *Geophys. J.*, *98*, 603-612, 1989.
- Sung, L. Y., and D. D. Jackson, Crustal and uppermost mantle structure under southern California, *Bull. Seismol. Soc. Am.*, *82*, 934-961, 1992.
- Tanimoto, T., and D. L. Anderson, Mapping convection in the mantle, *Geophys. Res. Lett.*, *11*, 287-290, 1984.
- Tanimoto, T., and D. L. Anderson, Lateral heterogeneity and azimuthal anisotropy of the upper mantle: Love and Rayleigh waves 100-250 s, *J. Geophys. Res.*, *90*, 1842-1858, 1985.
- Tapponnier, P., and P. Molnar, 1979, Active faulting and cenozoic tectonics of the Tien Shan, Mongolia, and Baykal regions, *J. Geophys. Res.*, *84*, 3425-3459, 1979.
- Turcotte, D. L., and G. Schubert, *Geodynamics, Applications of continuum physics to geological problems*, John Wiley & Sons, 1982.
- Turcotte, D. L., and S. H. Emerman, Mechanisms of active and passive rifting, *Tectonophysics*, *94*, 39-50, 1983.
- Verma, R. K., Elasticity of several high-density crystals, *J. Geophys. Res.*, *65*, 757-766, 1960.
- Vinnik, L. P., V. Farra, and B. Romanowicz, Azimuthal anisotropy in the Earth from observations of SKS at Geoscope and NARS broadband stations, *Bull. Seismol. Soc. Am.*, *79*, 1542-1558, 1989.

- Vinnik, L. P., L. I. Makeyeva, A. Milev, and A. Yu. Usenko, Global patterns of azimuthal anisotropy and deformations in the continental mantle, *Geophys. J. Int.*, *111*, 433-447, 1992.
- Wessel, P., and W. H. F. Smith, Free software helps map and display data, *EOS Trans. Amer. Geophys. U.*, *72*, 441&445-446, 1991.
- Wylegall, K., P. Bormann, and M. Baumbach, Investigation of inhomogeneities and anisotropy in the crust and upper mantle of central Europe by means of teleseismic P waves, *Phys. Earth Plane. Interiors*, *51*, 169-178, 1988.
- Zamarayev, S. M., and V. V. Ruzhich, On relationships between the Baikal rift zone and ancient structures, *Tectonophysics*, *45*, 41-47, 1978.
- Zheng, S. H., and Y. Gao, Azimuthal anisotropy in lithosphere on the Chinese mainland from observations of SKS at CDSN, *Acta Seismologica Sinica*, *7*, 177-186, 1994.
- Zoback, M. L., First- and second-order patterns of stress in the lithosphere; the World Stress Map Project, *J. Geophys. Res.*, *97*, 11,703-11,728, 1992.
- Zonenshain, L. P., and L. A. Savostin, Geodynamics of the Baikal rift zone and plate tectonics of Asia, *Tectonophysics*, *76*, 1-45, 1981.
- Zonenshain, L. P., M. I. Kuzmin, and L. M. Natapov, *Geology of the USSR: A plate-tectonic synthesis*, Edited by B.M. Page. Geodynamics Series Vol. 21. Am. Geophys. Union, Washington, D.C. pp. 242, 1990.
- Zorin, Yu. A., 1971, *Recent structure and isostasy of the Baikal rift zone and adjacent areas*, Moscow, 168pp. (in Russian), 1971.

- Zorin, Yu. A., and V. A. Rogozhina, Mechanism of rifting and some features of the deep-seated structure of the Baikal rift zone, *Tectonophysics*, 45, 23-30, 1978.
- Zorin, Yu. A., Baikal rift: an example of the intrusion of asthenospheric material into lithosphere as the cause of disruption of lithospheric plates, *Tectonophysics*, 73, 94-104, 1981.
- Zorin, Yu. A., and S. V. Osokina, Model of the transient temperature fields of the Baikal rift lithosphere, *Tectonophysics*, 103, 193-204, 1984.
- Zorin, Yu. A., and S. V. Lepina, Geothermal aspects of development of asthenospheric upwelling beneath continental rift zones, *J. Geodyn.*, 3, 1-22, 1985.
- Zorin, Yu. A., V. M. Kozhevnikov, M. R. Novoselova, and E. K. Turutanov, Thickness of the lithosphere beneath the Baikal rift zone and adjacent regions, *Tectonophysics*, 168, 327-337, 1989.
- Zorin, Yu. A., and L. Cordell, Crustal extension in the Baikal rift zone, *Tectonophysics*, 198, 117-121, 1991.

## Some remarks from the author

Sep. 20, 2012, Stephen Shangxing Gao, Professor of Geophysics

Missouri University of Science and Technology

The original version of the dissertation was published in 1995 by UMI Dissertation Services. Given the level of technology and financial limits at that time, all the color figures were printed as black/white, and many figures were illegible. Over the past year, together with a graduate student of mine, we were able to locate all the original texts and the vast majority of the figures from the back up disks, and produced this version. A few missing figures were scanned from the original UMI version. No modifications to the texts and figures were applied.

*Materials in Chapters 2, 4, and 5 were published in the following refereed papers:*

**Paper 1:** Gao, S., P.M. Davis, H. Liu, P. Slack, Y.A. Zorin, N.A. Logatchev, M. Kogan, P. Burkholder, and R.P. Meyer (1994),  
Asymmetric upwarp of the asthenosphere beneath the Baikal rift zone, Siberia,  
**Journal of Geophysical Research**, vol. **99**: pp. 15,319-15,330. [pdf](#)

**Paper 2:** Gao, S.S., K.H. Liu, P.M. Davis, P.D. Slack, Y. A. Zorin, V.V. Mordvinova, and V.M. Kozhevnikov (2003),  
Evidence for small-scale mantle convection in the upper mantle beneath the Baikal rift zone,  
**Journal of Geophysical Research**, vol. **108(B4)** , 2194 (10 pages), doi:10.1029/2002JB002039.  
[pdf](#)

**Paper 3:** Zhao, D., J. Lei, T. Inoue, A. Yamada, and S. S. Gao (2006),  
Deep structure and origin of the Baikal rift zone,  
**Earth and Planetary Science Letters**, vol. **243**, pp. 681-691. [pdf](#)

*Materials in Chapter 3 were published in the following refereed papers:*

**Paper 4:** Gao, S., P.M. Davis, H. Liu, P.D. Slack, Yu.A. Zorin, V.V. Mordvinova, V.M. Kozhevnikov, and R.P. Meyer (1994),  
Seismic anisotropy and mantle flow beneath the Baikal rift zone,  
**Nature**, vol. **371**: pp. 149-151. doi:10.1038/371149a0 [pdf](#)

**Paper 5:** Gao, S., P.M. Davis, H. Liu, P.D. Slack, A.W. Rigor, Yu.A. Zorin, V.V. Mordvinova, V.M. Kozhevnikov, and N. A. Logatchev (1997),  
SKS splitting beneath continental rift zones,  
**Journal of Geophysical Research**, vol. **102(B10)** , pp. 22,781-22,797. [pdf](#)

**Paper 6:** Gao, S.S.; P.M. Davis, H. Liu, P.D. Slack, and others (1999),  
"SKS splitting beneath continental rifts zones" by Gao et al. - Reply.  
**Journal of Geophysical Research**, vol. **104**: pp.10,791-10,794. [pdf](#)